Max-Planck-Institut für Quantenoptik

Characterisation of Laser-Accelerated Proton Beams

Malte Christoph Kaluza

Vollständiger Abdruck der von der Fakultät für Physik der Technischen Universität München zur Erlangung des akademischen Grades eines

Doktors der Naturwissenschaften

genehmigten Dissertation.

Vorsitzender:		Univ.-Prof. Dr. Manfred Kleber
Prüfer der Dissertation:	1.	apl. Prof. Dr. Jürgen Meyer-ter-Vehn
	2.	Univ.-Prof. Dr. Dr. h.c. Alfred Laubereau

Die Dissertation wurde am 14.06.2004 bei der Technischen Universität München eingereicht und durch die Fakultät für Physik am 23.07.2004 angenommen.

Contents

Chapter 1

Introduction

The development of ultrahigh-power laser systems using the technique of chirped-pulse-amplification (CPA) [1] has sparked an enormous scientific activity in the field of laser-plasma interaction. Beyond intensities of a few times $10^{18}\,\mathrm{W/cm^2}$, the motion of electrons in the electromagnetic field of the laser becomes relativistic, as the electron velocity approaches the speed of light within only one oscillation period, and a large variety of new phenomena opens up. Worldwide, laser facilities delivering pulses with peak powers in excess of 1 petawatt ($1\,\mathrm{PW}=10^{15}\,\mathrm{W}$) have either been comissioned during the last few years [2–4] or are presently under construction. Such laser systems have pushed the limit of achievable intensities beyond $10^{21}\,\mathrm{W/cm^2}$ [5].

When laser pulses with these intensities interact with any kind of target material, the rising edge of the pulse is already sufficiently intense to transform matter into the plasma state. The main part of the pulse then interacts with a highly ionised and heated plasma. Due to collective effects of the freed electrons, such a plasma can support electric fields in excess of $10^{12}\,\mathrm{V/m}$. These fields are higher by several orders of magnitude compared to conventional particle accelerators that usually operate at $10^{8}\,\mathrm{V/m}$. Due to the higher fields the acceleration length for particles in the energy range of several 100's of MeV is of the order of 1 mm at most [6]. Therefore, high-power lasers are a promising alternative to conventional RF-accelerators.

During the last decade, a dramatic increase in particle energies accelerated in laser-plasma experiments could be witnessed. Primarily, the laser light efficiently couples its energy into the formation of collimated electron beams with peak kinetic energies in the range from several 100 keV to more than 200 MeV [6–10]. In secondary processes, it is possible to generate $\gamma-$rays in the MeV-range [9, 11], to accelerate protons [12–17], and also heavy ions [18] to MeV-energies, and to generate neutrons from fusion reactions [9, 19, 20]. Although most of the proof-of-principle experiments were carried out with large-scale Nd:Glass-laser systems generating pulses at a repetition rate of ~ 1 shot/hour at the 100 TW to 1 PW level, small-scale laser systems in the $1\ldots20$ terawatt (TW) regime operating at a much higher repetition rate allow experiments for the investigation of the physics underlying the associated acceleration processes in much greater detail. Using the 2-TW laser facility ATLAS at Max-Planck Institut für Quantenoptik operating at 10 Hz, it was possible for the first time to generate positrons with a table-top laser [21].

Although the generation of fast ions in the energy range of a few 10's or 100's of keV has already been observed in the late 1970's [22–25], the generation of MeV-proton beams during the interaction of high-intensity CPA-laser pulses with thin foils has attracted a great deal of attention due to the unique properties of such beams. Independent of the target material, a strong and well-collimated proton signal is observed in the experiments. These protons originate from water vapor and hydrocarbon contaminations on the target surfaces, as it has been observed in experiments carried out in the framework of the Los Alamos Helios program [26].

Using the NOVA-PW laser at Lawrence Livermore National Laboratory [27], a total number of 2×10^{13} protons has been accelerated to kinetic energies above $10\,\mathrm{MeV}$ [15]. The initial proton-pulse length is determined by the laser pulse duration ($\tau_\mathrm{L} = 500\,\mathrm{fs}$ in this experiment), and it is emitted from a spot of $\sim$ 100-μm diameter from the rear surface of the target. This yields an initial proton current as high as $6.4 \times 10^6\,\mathrm{A}$ and a proton-power density in excess of $10^{18}\,\mathrm{W/cm^2}$, what is higher by several orders of magnitude compared to conventional accelerators. Furthermore, the rear-side accelerated proton beam exhibits an extraordinary low emittance and an almost ideal laminar flow as a consequence of the acceleration process [28–30]. Such beams are therefore well suited for the imaging of μm-scale structures on the rear surface of the target. By appropriately shaping the target rear surface, the focusing of a proton beam has recently been demonstrated [31]. During the interaction of this beam with a secondary target, isochoric heating of the secondary-target material to temperatures of $20\,\mathrm{eV}$ has been observed[1]. As protons having MeV-energies can penetrate dense matter, they can be used to probe highly overdense plasmas that are non transparent for optical light [32]. Due to their electric charge the protons are also deflected by magnetic and electric fields in the plasma and carry information about the field distributions in the highly overdense regions [33,34]. Furthermore, laser-accelerated protons are envisaged as a possible ignition beam [35] in the fast-ignitor scenario for inertial confinement fusion [36].

For all the applications mentioned above, the generation of proton beams with controllable parameters such as energy spectrum, brightness, and spatial profile is crucial. Hence, for the reliable generation of proton beams, the physics underlying the acceleration process has to be understood as accurately as possible. After the first proof-of-principle experiments [12–16], systematical studies were carried out to examine the influence of target material and thickness [37–39]. To establish the influence of the main laser parameters such as intensity, pulse energy, and duration over a wide range, results from different laser systems have to be compared, as each system covers a small parameter range only. Besides these parameters, strength and duration of the laser prepulse due to amplified spontaneous emission (ASE) play an important role, too [37]. Until now, a detailed investigation has not been carried out but is expected to play a significant role in the acceleration process [40, 41].

Besides the influence of the experimental parameters mentioned above, the origin of the fastest protons is still debated. There are at least two acceleration scenarios able to explain the occurance of MeV-protons during the interaction of high-intensity lasers with thin foils. (i) These protons may come from the *front* surface of the target, i.e. the side irradiated by the laser [12–14] or (ii) from the *rear* surface [15, 18, 42]. Recent

---

[1] In laser-plasma physics, it is convenient to express temperatures not in Kelvin, but in eV. The equivalent temperature to the quasi-temperature of $1\,\mathrm{eV}$ is $11.600\,\mathrm{K}$.

results indicate that both mechanisms act simultaneously [43, 44], in accordance with the predictions of multi-dimensional particle-in-cell (PIC) codes [17, 45].

Special attention has also been paid to the spatial profile of the proton beam emitted from the target. Using the solid-state nuclear track detector CR 39, "ring"-like structures have been observed in different experiments [13, 14, 46]. These structures were the basis for conflicting interpretations about the origin of the proton beam.

Aiming at a global picture for the physics underlying the proton acceleration process, the influence of as many experimental parameters as possible has to be understood. Also the role and suitability of the diagnostics used in different experiments has to be investigated to be able to compare the results and interpretations. Therefore, this work is focused on the characterisation of proton beams accelerated in high-intensity laser-solid interactions and the influence of the different experimental parameters on the acceleration process.

During the course of this thesis, the following new and important aspects were discovered and described:

1. For the first time, a controlled variation of the laser-prepulse pedestal due to amplified spantaneous emission was achieved by implementing an ultra-fast Pockels cell into the laser chain. The prepulse was characterised in terms of intensity and duration.
2. Due to this unique possibility, the influence of the laser prepulse duration on the laser-driven acceleration of protons could be studied in great detail. It was found to have a huge effect on the emitted energy spectra of the protons [47].
3. By a controlled variation both of the prepulse duration and the thickness of the target foil used in the experiment, a clear distinction between the two different acceleration regimes mentioned above was possible. Furthermore, the controlled generation of a proton population stemming from the rear side of the target was possible for the first time.
4. By comparing the experimental results with numerical simulations, a quantitative explanation of the associated effects was possible. It was found that the prepulse-induced changes in the target properties not only influence the rear-side proton acceleration by the formation of an initial ion-density gradient as claimed in [37], but also the density distribution in the target itself strongly influences the electron propagation, which in turn affects the rear-side proton acceleration [48].

The results described in this thesis both have a high relevance for a comparison of existing experimental results as well as for future experiments aiming at an optimisation of the acceleration process. The thesis is structured as follows:

- Chapter 2 gives an overview over the physics of laser-plasma interactions at relativistic laser intensities. After a description of the interaction of a single electron with the laser field, the occurance of collective effects of electrons in the plasma are discussed. They give rise to charge separation in the plasma and generate quasi-static electric fields. These fields are responsible for the acceleration of protons and light ions to MeV-energies. The two acceleration scenarios from the two different target surfaces are described.

- Chapter 3 describes the ATLAS-laser system that was used for the experiments. The control of the laser prepulse by means of an ultra-fast Pockels cell and the significant enhancement of the laser focusability by adaptive optics are described in detail, as their comissioning and characterisation were major parts of this work [49] and were crucial for the feasibility of experiments on proton acceleration.
- Chapter 4 deals with the diagnostics used to characterise the proton beam accelerated during the laser-plasma interaction in terms of energy spectrum, spatial divergence, and angular distribution.
- Chapter 5 presents the experimental results investigating the dependence of the proton-beam properties on different experimental parameters as target thickness, prepulse duration, laser-pulse energy and emission angle. The profound effect of these parameters on the acceleration process could be demonstrated [47].
- To qualitatively describe the effect of the prepulse, hydrodynamic simulations using the code MULTI-FS [50] were carried out. The results from these simulations are discussed in chapter 6.
- Chapter 7 presents a 1-dimensional computer code that was newly developed within the course of this work. It describes the rear-side proton acceleration driven by a hot-electron population accelerated by the laser on the target front side. The code is used to include prepulse-induced changes as target expansion and formation of a plasma-density gradient at the target rear side in the description of the acceleration process and to obtain a more detailed insight into the underlying physics.
- Chapter 8 draws conclusions from the comparison of the experimental results with the predictions from numerical simulations and theory. A distinction between two proton populations accelerated on either of the two target surfaces is possible. It manifests the strong influence of target thickness and prepulse duration on these two mechanisms. A numerical code is used to describe the influence of the fast-electron transport on the rear-side acceleration of protons. Furthermore, the angularly resolved measurements are found to match the predictions made by three-dimensional particle-in-cell (PIC) simulations [45], giving an insight into the distributions of the electron density and the acceleration fields at the target rear surface.
- Finally, chapter 9 summarises this work and gives a perspective for the future, suggesting further experiments and numerical investigations concerning the acceleration of protons and light ions in relativistic laser-plasma interaction.
- Appendix A describes the setup of a novel, synchronised 2-colour probe beam that was set up during the course of this thesis and that was used for interferometric side-view images taken during the laser-target interaction.
- In appendix P, the publications about the most important parts of this work are attached.

Chapter 2

Laser-Plasma Interaction at Relativistic Laser Intensities

During the interaction of ultra-short laser pulses having peak intensities in excess of $10^{18}\,\mathrm{W/cm^2}$ with solid targets, the main part of the laser pulse with the highest intensities interacts with a highly ionised and strongly preheated plasma on the target front side. This preplasma has been formed by the unavoidable low-intensity prepulse pedestal of the laser due to amplified spontaneous emission (ASE) and by the leading edge of the main pulse itself. In this preplasma, the electrons are accelerated to velocities close to the speed of light by the laser fields and therefore their motion is dominated by relativistic effects. At these “relativistic” intensities, a large fraction of the laser-pulse energy is converted into kinetic energy of relativistic electrons. They are expelled from the focal region of the laser pulse due to its ponderomotive force and leave behind a space charge of positive ions close to the *front surface* of the target. Furthermore, the electrons having kinetic energies in the MeV-range are capable of propagating through the target. A strong space-charge field is generated at the *rear surface* due to electrons that have escaped the target. The electric fields arising from these regions of charge separations on both target surfaces vary on a time scale that is much longer than the laser period that dominates the electron motion. These quasi-static fields are capable of accelerating ions to kinetic energies in the MeV-range. To understand and interpret these two different mechanisms underlying the ion acceleration at the front and rear side of the target, the interaction of the laser pulse with the plasma electrons has to be described first.

This chapter starts with the interaction of a laser-light wave of relativistic intensity with a single electron. Subsequently, effects are discussed that arise from the collective behaviour of a large number of electrons, when the laser pulse interacts with the preplasma including the different collective electron-acceleration processes. Finally, the two different ion-acceleration mechanisms are introduced.

2.1 Interaction of Laser Light with Plasma Electrons

2.1.1 Treatment of a Single Electron in the Laser Field

First, the interaction of a single electron with a plane laser-light wave is investigated. The light wave is assumed to propagate in $\vec{e}_x$-direction and to be linearly polarised in $\vec{e}_y$-direction.

Description of the Laser Field

The light wave of the laser is described by its vector potential, $\vec{A}(x,t)$, that is parallel to the $\vec{e}_y$-direction and varies only in space, x, and time, t: [1]

$$\vec{A} = \vec{e}_y \cdot A_0 \sin(k_\mathrm{L} x - \omega_\mathrm{L} t), \tag{2.1}$$

where $\omega_\mathrm{L}/2\pi$ is the laser-light frequency, $k_\mathrm{L} = 2\pi\eta_\mathrm{r}/\lambda_\mathrm{L}$ the wave number, $\lambda_\mathrm{L} = 2\pi c/\omega_\mathrm{L}$ the laser-wave length in vacuum, η_r the refractive index, and c the speed of light. In the absence of any electrostatic potential, Φ_el, the electric and magnetic fields, $\vec{\mathcal{E}}_\mathrm{L}$ and $\vec{B}_\mathrm{L}$, are obtained from

$$\begin{aligned} \vec{\mathcal{E}}_\mathrm{L} &= -\frac{\partial \vec{A}}{\partial t} = \vec{\mathcal{E}}_0 \cos(k_\mathrm{L} x - \omega_\mathrm{L} t), \quad \text{with } \vec{\mathcal{E}}_0 = \vec{e}_y \cdot \omega_\mathrm{L} A_0 \quad \text{and} && (2.2)\\ \vec{B}_\mathrm{L} &= \vec{\nabla} \times \vec{A} = \vec{B}_0 \cos(k_\mathrm{L} x - \omega_\mathrm{L} t), \quad \text{with } \vec{B}_0 = \vec{e}_z \cdot k_\mathrm{L} A_0 = \vec{e}_z \frac{\eta_\mathrm{r}\mathcal{E}_0}{c}. && (2.3) \end{aligned}$$

In vacuum, where $\eta_\mathrm{r} = 1$, the laser intensity, I_L, which is the magnitude of the Poynting vector, $\vec{S}$, averaged over a laser period, $T_\mathrm{L} = 2\pi/\omega_\mathrm{L}$, what is denoted by $\langle \ldots \rangle$, can be written as

$$I_\mathrm{L} = \langle |\vec{S}| \rangle = \frac{1}{\mu_0} \langle |\vec{\mathcal{E}}_\mathrm{L} \times \vec{B}_\mathrm{L}| \rangle = \frac{\varepsilon_0 c}{2} \mathcal{E}_0^2, \tag{2.4}$$

where μ_0 is the permeability and ε_0 the permittivity of the vacuum.

Interaction of a Single Particle with the Laser Field

The interaction of an electron with charge $-e$ and rest mass m_e with external electric and magnetic fields, $\vec{\mathcal{E}}$ and $\vec{B}$, is described by its **equation of motion**

$$\frac{\mathrm{d}\vec{p}}{\mathrm{d}t} = \frac{\mathrm{d}}{\mathrm{d}t}(\gamma m_\mathrm{e} \vec{v}) = -e\left(\vec{\mathcal{E}} + \vec{v} \times \vec{B}\right), \tag{2.5}$$

where $\vec{v}$ and $\vec{p}$ are velocity and momentum of the electron, respectively. $\gamma = 1/\sqrt{1-\beta^2} = 1/\sqrt{1-v^2/c^2} = \sqrt{1+(p/m_\mathrm{e}c)^2}$ is the relativistic Lorentz factor, $\beta = v/c$. Multiplying

---

[1] Note that all field quantities of the light wave depend on space, x, and time, t, what will be omitted for clarity.

eq. (2.5) with $\vec{p}$ and using $\vec{p}\cdot(\vec{v}\times\vec{B})=0$ and $\vec{p}\cdot\mathrm{d}\vec{p}=\frac{1}{2}\mathrm{d}p^2$, one obtains the **evolution of the kinetic energy**, $E_{\mathrm{kin}}=m_{\mathrm{e}}c^2(\gamma-1)$, of the electron to

$$\frac{\mathrm{d}E_{\mathrm{kin}}}{\mathrm{d}t}=m_{\mathrm{e}}c^2\frac{\mathrm{d}\gamma}{\mathrm{d}t}=-e\vec{\mathcal{E}}\cdot\vec{v}. \tag{2.6}$$

In the classical regime, i.e. for velocities $v\ll c$, where $\gamma\approx 1$, the electron motion is dominated by the electric field, as the magnetic term is smaller by a factor of v/c and in the first order can be neglected. Integrating the equation of motion (2.5) for this case with initial conditions $x_0=0, y_0=0$, and $v_0=0$ leads to the velocity $\vec{v}=\vec{e}_y\cdot e\mathcal{E}_0/\omega_{\mathrm{L}}m_{\mathrm{e}}\cdot\sin(k_{\mathrm{L}}x-\omega_{\mathrm{L}}t)$ and the displacement $y=e\mathcal{E}_0/\omega_{\mathrm{L}}^2 m\cdot[\cos(k_{\mathrm{L}}x-\omega_{\mathrm{L}}t)-1]$ of the electron. In the classical case, the electron oscillates driven by the external electric field with amplitudes $y_0=e\mathcal{E}_0/\omega_{\mathrm{L}}^2 m_{\mathrm{e}}$ and $v_0=e\mathcal{E}_0/\omega_{\mathrm{L}}m_{\mathrm{e}}$ parallel to the electric field only[2].

The amplitude of the velocity, v_0, approaches c, when the so-called **normalised vector potential**

$$a_0=\frac{e\mathcal{E}_0}{\omega_{\mathrm{L}}m_{\mathrm{e}}c}=\frac{eA_0}{m_{\mathrm{e}}c} \tag{2.7}$$

approaches unity. In this case, a purely classical description is no longer valid. Using a_0, the amplitudes of the electric and magnetic fields can be rewritten as

$$\mathcal{E}_0 = \frac{a_0}{\lambda_{\mathrm{L}}}\cdot 3.21\times10^{12}\frac{\mathrm{V}}{\mathrm{m}}\cdot\mu\mathrm{m} \quad \text{and} \tag{2.8}$$

$$B_0 = \frac{a_0}{\lambda_{\mathrm{L}}}\cdot 1.07\times10^{4}\mathrm{T}\cdot\mu\mathrm{m}. \tag{2.9}$$

The laser-light intensity, I_{L}, is given by

$$I_{\mathrm{L}}=\frac{a_0^2}{\lambda_{\mathrm{L}}^2}\cdot 1.37\times10^{18}\,\mathrm{W/cm^2}\cdot\mu\mathrm{m}^2. \tag{2.10}$$

The normalised vector potential, a_0, delimits the interaction of laser light with matter into three regimes. For $a_0\ll 1$, the electron motion is classical and the regime is called non-relativistic. For $a_0\approx 1$, the electron approaches the speed of light already during a laser-half cycle and the interaction has to be treated fully relativistic, for $a_0\gg 1$, the regime is called ultra-relativistic. For a wave length of $\lambda_{\mathrm{L}}=790\,\mathrm{nm}$, the normalised vector potential a_0 equals 1 for an intensity of $2.2\times10^{18}\,\mathrm{W/cm^2}$. In the experiments described in this thesis, the maximum intensity on target was $I_{\mathrm{L}}=1.5\times10^{19}\,\mathrm{W/cm^2}$ with a wave length of $\lambda_{\mathrm{L}}=790\,\mathrm{nm}$. This results in a normalised vector potential of $a_0=2.6$.

In the relativistic regime, the solution of the equation of motion (2.5) leads to different results compared to the classical case [51–53]. Using the vector potential from eq. (2.1)

---

[2] As the amplitude of the velocity scales with the inverse particle mass, it is obvious that during the interaction with a plasma the laser mainly couples to the electrons in the first place, as their mass is much lower than the mass of even the lightest ions. Except for extremely high intensities (see below), the ions in a plasma are not directly affected by the laser fields but the forces of the laser light are mediated by the plasma electrons.

and the expressions (2.2) and (2.3) for the electric and magnetic field one finds

$$\frac{\mathrm{d}p_y}{\mathrm{d}t} = e\frac{\mathrm{d}A}{\mathrm{d}t}$$

$$\Longrightarrow \quad \boxed{p_y - eA = C_1,} \tag{2.11}$$

where $\partial\vec{A}/\partial t = \mathrm{d}\vec{A}/\mathrm{d}t - (\vec{v}\cdot\vec{\nabla})\vec{A}$, $\vec{v}\times(\vec{\nabla}\times\vec{A}) = \vec{\nabla}(\vec{v}\cdot\vec{A}) - (\vec{v}\cdot\vec{\nabla})\vec{A}$, and $\partial\vec{A}/\partial y = \partial\vec{A}/\partial z = 0$ were used. The constant C_1 is the **first invariant** of the electron motion. It is related to the electron's initial momentum in $\vec{e}_y-$direction.

Together with eq. (2.6) and considering that $\vec{\mathcal{E}}_0||\vec{e}_y$ and $\vec{B}_0||\vec{e}_z$, one obtains from eq. (2.5)

$$\frac{\mathrm{d}p_x}{\mathrm{d}t} = -ev_yB_0 = m_\mathrm{e}c\frac{\mathrm{d}\gamma}{\mathrm{d}t}$$

$$\Longrightarrow \quad \boxed{\gamma - \frac{p_x}{m_\mathrm{e}c} = C_2.} \tag{2.12}$$

C_2 is the **second invariant** of the electron motion. Using $\gamma^2 = 1 + (p/m_\mathrm{e}c)^2$, one finds the following relation between longitudinal and transversal momentum, p_x and p_y:

$$\frac{p_x}{m_\mathrm{e}c} = \frac{1 - C_2^2 + (p_y/m_\mathrm{e}c)^2}{2C_2}. \tag{2.13}$$

Considering an electron that is at rest at $t = 0$ and at $x = 0$, i.e. $\vec{p} = 0$, when the electric field is maximal, one finds $C_1 = 0$ and $C_2 = 1$. This leads to

$$p_y = eA_y \quad \text{and} \tag{2.14}$$

$$E_\mathrm{kin} = cp_x = \frac{p_y^2}{2m_\mathrm{e}}, \tag{2.15}$$

and one obtains the following form of the relativistic Lorentz factor for a single electron in a laser wave: $\gamma = 1 + a^2/2$. To derive the $x-$ and $y-$coordinates of the electron, $\Phi = k_\mathrm{L}x - \omega_\mathrm{L}t$ and $\mathrm{d}\Phi/\mathrm{d}t = v_xk_\mathrm{L} - \omega_\mathrm{L} = \omega_\mathrm{L}(\beta_x - 1) = -\omega_\mathrm{L}/\gamma$ are used, what leads to

$$\vec{p} = \gamma m_\mathrm{e}\frac{\mathrm{d}\vec{r}}{\mathrm{d}t} = \gamma m_\mathrm{e}\frac{\mathrm{d}\vec{r}}{\mathrm{d}\Phi}\cdot\frac{\mathrm{d}\Phi}{\mathrm{d}t} = -m_\mathrm{e}\omega_\mathrm{L}\frac{\mathrm{d}\vec{r}}{\mathrm{d}\Phi}. \tag{2.16}$$

Using eqs. (2.14) and (2.15), the integration of the $x-$ and $y-$component of eq. (2.16) leads to the spatial components of the electron trajectory:

$$x = \frac{c}{\omega_\mathrm{L}}\frac{a_0^2}{4}\left(\Phi - \frac{1}{2}\cos(2\Phi)\right) \quad \text{and} \tag{2.17}$$

$$y = \frac{c}{\omega_\mathrm{L}}a_0\left(1 - \cos\Phi\right). \tag{2.18}$$

While the $y-$component is identical to the classical case, the electron is strongly pushed forward in laser direction for $a_0 \geq 1$. This forward motion in the laboratory frame consists of a drift in laser direction with the velocity

$$\vec{v}_\mathrm{D} = \left\langle\frac{x}{t}\right\rangle = \frac{a_0^2}{4 + a_0^2}c\cdot\vec{e}_x \tag{2.19}$$

arising from the first part in eq. (2.17). This drift velocity approaches c for $a_0 \longrightarrow \infty$. The second part describes a rapid oscillation of the electron in $\vec{e}_x-$direction with twice the frequency as in $\vec{e}_y-$direction. This gives rise to a "figure-8" motion of the electron in a frame of reference co-moving with $\vec{v}_\mathrm{D}$.

For the case of an infinitely long laser pulse with an infinite lateral extension, the electron motion in the laboratory frame is sketched in Fig. 2.1 (a). For the case of a laser pulse of finite duration as shown in Fig. 2.1 (b), where eqs. (2.14) and (2.15) are still valid, the electron is pushed forward by the laser as in (a). But when the pulse is over, the electron comes to a stop again (red line). In this case, the electron is only displaced in laser direction but gains no net energy. However, the electron can be ejected from a laser focus of finite diameter, if this diameter is comparable to or smaller than the amplitude of the electron's quiver motion. It leaves the focus under an angle, θ, to the laser axis with a finite velocity (green line) by so-called *ponderomotive scattering* (see below) [54–57]. This can be understood qualitatively, as the electron starting on the laser axis, where the fields are maximal, is displaced sideways during the first laser-half cycle into regions of reduced intensity. Thus the restoring force acting on the electron is smaller, when the fields change sign. Hence, it does not return to its initial position in the next laser-half period, and finally leaves the focus with a finite velocity.

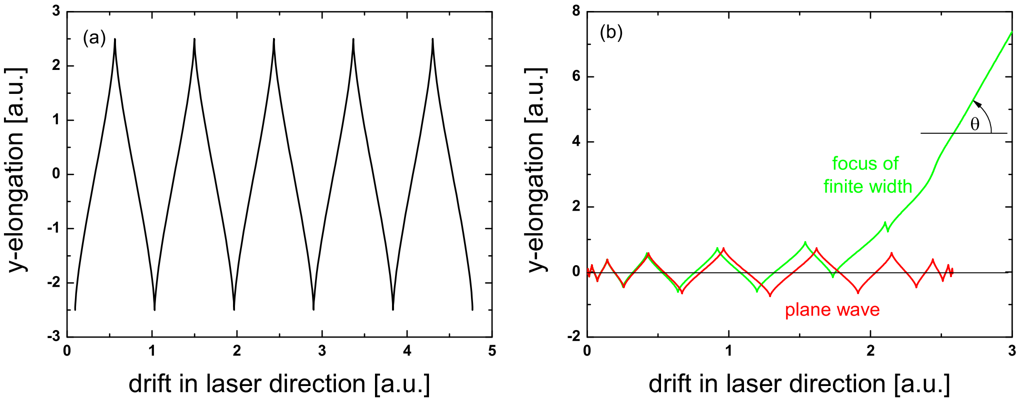

Figure 2.1: Relativistic electron motion in the laser field. In (a), the laser is a plane wave of infinite length. In (b), the laser has a finite duration and is either a plane wave (red line) or it is focused to a Gaussian spot of finite diameter (green line).

The Ponderomotive Force

If one is not interested in the detailed trajectory but only the final energy and the scattering angle of the electron, an elegant description of the acceleration is obtained by introducing the ponderomotive force, $\vec{F}_\mathrm{pond}$, of the laser acting on the electron [58, 59]. To derive this non-linear force, one again starts from the equation of motion (2.5), first assuming $\gamma \approx 1$ for the classical case:

$$m\frac{\mathrm{d}\vec{v}}{\mathrm{d}t} = -e(\vec{\mathcal{E}} + \vec{v} \times \vec{B}). \tag{2.20}$$

In the first order, only contributions that depend linearly on the electric field, $\vec{\mathcal{E}}(x,t) = \vec{\mathcal{E}}_\mathrm{s}(\vec{r}) \cdot \cos(\omega_\mathrm{L} t)$, are used, where $\vec{\mathcal{E}}_\mathrm{s}(\vec{r})$ contains the spatial dependence. For the velocity, $\vec{v}_1$, and the displacement, $\delta\vec{r}_1$, of the electron from its initial position, $\vec{r}_0$, one finds

$$\begin{aligned} \vec{v}_1(\vec{r}_0) &= -\frac{e}{m_\mathrm{e}\omega_\mathrm{L}} \vec{\mathcal{E}}_\mathrm{s}(\vec{r}_0) \cdot \sin(\omega_\mathrm{L} t) = \frac{\mathrm{d}\vec{r}}{\mathrm{d}t} \quad \text{and} && (2.21) \\ \delta\vec{r}_1(\vec{r}_0) &= \frac{e}{m_\mathrm{e}\omega_\mathrm{L}^2} \vec{\mathcal{E}}_\mathrm{s}(\vec{r}_0) \cdot \cos(\omega_\mathrm{L} t). && (2.22) \end{aligned}$$

To proceed to the second order, the electric field, $\vec{\mathcal{E}}(\vec{r})$, is expanded around the electron's initial position, $\vec{r}_0$, to

$$\vec{\mathcal{E}}(\vec{r}) = \vec{\mathcal{E}}(\vec{r}_0) + (\delta\vec{r}_1 \cdot \vec{\nabla})\, \vec{\mathcal{E}}\Big|_{\vec{r}=\vec{r}_0} + \dots \tag{2.23}$$

Using now only terms that quadratically depend on the electric field and deriving the magnetic field, $\vec{B}_1$, from Maxwell's equation $\vec{\nabla} \times \vec{\mathcal{E}} = -\partial\vec{B}/\partial t$, what leads to $\vec{B}_1(\vec{r}_0) = -\omega_\mathrm{L}^{-1} \vec{\nabla} \times \vec{\mathcal{E}}\Big|_{\vec{r}=\vec{r}_0} \cdot \sin(\omega_\mathrm{L} t)$, the second-order equation of motion reads

$$\begin{aligned} m_\mathrm{e}\frac{\mathrm{d}\vec{v}_2}{\mathrm{d}t} &= -e\left[\left(\delta\vec{r}_1(\vec{r}_0) \cdot \vec{\nabla}\right) \vec{\mathcal{E}}(\vec{r}_0) + \vec{v}_1(\vec{r}_0) \times \vec{B}_1(\vec{r}_0)\right] \\ &= -\frac{e^2}{m_\mathrm{e}\omega_\mathrm{L}^2}\left[\left(\vec{\mathcal{E}}_\mathrm{s}(\vec{r}_0) \cdot \vec{\nabla}\right) \vec{\mathcal{E}}_\mathrm{s}(\vec{r}_0) \cdot \cos^2(\omega_\mathrm{L} t) + \right. \\ &\qquad \left. + \vec{\mathcal{E}}_\mathrm{s}(\vec{r}_0) \times \left(\vec{\nabla} \times \vec{\mathcal{E}}_\mathrm{s}(\vec{r}_0)\right) \cdot \sin^2(\omega_\mathrm{L} t)\right]. \end{aligned} \tag{2.24}$$

Temporally averaging over the fast oscillations of the laser field ($\langle \sin^2(\omega_\mathrm{L} t)\rangle = \langle \cos^2(\omega_\mathrm{L} t)\rangle = \frac{1}{2}$) and using $\vec{\mathcal{E}}_\mathrm{s} \times (\vec{\nabla} \times \vec{\mathcal{E}}_\mathrm{s}) = \frac{1}{2}\vec{\nabla}(\mathcal{E}_\mathrm{s}^2) - (\vec{\mathcal{E}}_\mathrm{s} \cdot \vec{\nabla})\vec{\mathcal{E}}_\mathrm{s}$, this finally leads to

$$\vec{F}_\mathrm{pond} = m_\mathrm{e}\left\langle \frac{\mathrm{d}\vec{v}_2}{\mathrm{d}t} \right\rangle = -\frac{e^2}{4 m_\mathrm{e}\omega_\mathrm{L}^2} \vec{\nabla}(\mathcal{E}_\mathrm{s}^2). \tag{2.25}$$

A fully relativistic description gives an additional factor of $1/\langle\gamma\rangle$ [60], where γ is also averaged over the fast oscillations of the laser field

$$\vec{F}_\mathrm{pond} = -\frac{e^2}{4\langle\gamma\rangle m_\mathrm{e}\omega_\mathrm{L}^2} \vec{\nabla}(\mathcal{E}_\mathrm{s}^2). \tag{2.26}$$

According to this equation, an electron is expelled from high-intensity regions of the laser focus along the gradient of the laser-intensity distribution, which is proportional to $\mathcal{E}_\mathrm{s}^2$. Finally, the scattering angle, θ, is determined by the ratio of transversal and longitudinal momentum of the electron [55] that are determined by eq. (2.14) and eq. (2.15):

$$\theta = \arctan\left(\frac{p_y}{p_x}\right) = \arctan\left(\sqrt{\frac{2}{\gamma - 1}}\right). \tag{2.27}$$

This relation has been verified experimentally by Moore *et al.* [54], where the scattering of single electrons from the laser focus was observed.

Note that all the relations derived up to this point describe the interaction of a single electron in the electromagnetic fields of a laser pulse. Any electrostatic potentials arising from laser-induced charge separations during the interaction of the laser with a plasma have been neglected so far. It will be shown in the next section, how the situation changes, when such effects are taken into account.

Up to now, only electrons were concerned, while the ions were assumed to form an immobile, positively charged background. Due to their much higher rest mass, the laser intensities presently available are by far not high enough to trigger a relativistic ion quiver motion in the laser field. The relativistic threshold for protons with mass $m_\mathrm{p} \approx 1836\, m_\mathrm{e}$ is at $a_0 = 1836$ and therefore at an intensity of $I_\mathrm{L}\lambda_\mathrm{L}^2 = 1836^2 \cdot 1.37 \times 10^{18}\,\mathrm{W/cm^2{\cdot}\mu m^2} = 4.62 \times 10^{24}\,\mathrm{W/cm^2{\cdot}\mu m^2}$, which is far beyond the present laser technology. However, *collective* effects of a large number of plasma electrons interacting with an intense laser pulse give rise to strong electric fields that vary on the time scale of the pulse duration and not of the laser period. On these much longer time scales, also the ions in the plasma can be accelerated to MeV-energies. These collective effects of the plasma electrons will be discussed in the next section.

2.1.2 Collective Effects of Plasma Electrons

This section concentrates on collective effects of the plasma electrons that occur during the interaction with laser pulses of relativistic intensities ($a_0 \geq 1$). While collective electron acceleration mechanisms in a plasma are discussed in section 2.2, this section is dedicated to the relativistic equation of motion in a plasma, Debye-shielding, the plasma frequency, and relativistic effects concerning the propagation of laser pulses in a plasma.

Relativistic Equation of Motion in a Plasma

To derive the relativistic equation of motion in a plasma, the electrons are treated as a fluid at zero temperature with density and velocity distributions, $n_\mathrm{e}(\vec{r},t)$ and $v_\mathrm{e}(\vec{r},t)$, that depend on space and time. Due to their significantly higher rest mass, the plasma ions are assumed to form an immobile, positively charged background.

As in the case for a single electron, the behaviour of this electron fluid is described by the equation of motion as eq. (2.5), the electric and magnetic fields can now also be modified by charge distributions and currents in the plasma

$$\vec{B} = \vec{\nabla} \times \vec{A}, \tag{2.28}$$

$$\vec{\mathcal{E}} = -\vec{\nabla}\Phi_\mathrm{el} - \frac{\partial \vec{A}}{\partial t}, \tag{2.29}$$

what leads to an equation of motion of the form

$$\left(\frac{\partial}{\partial t} + \vec{v}\cdot\vec{\nabla}\right)\vec{p} = -e\left[-\frac{\partial \vec{A}}{\partial t} - \vec{\nabla}\Phi_\mathrm{el} + \vec{v} \times (\vec{\nabla} \times \vec{A})\right]. \tag{2.30}$$

Using the relations $\gamma = \sqrt{1+(p/m_\mathrm{e}c)^2}, \vec{\nabla}\gamma = (2\gamma)^{-1}\cdot\vec{\nabla}(p/m_\mathrm{e}c)^2$, and $\vec{v}\times(\vec{\nabla}\times\vec{p}) = m_\mathrm{e}c^2\vec{\nabla}\gamma - (\vec{v}\cdot\vec{\nabla})\vec{p}$, one obtains the **relativistic equation of motion of the plasma** [61] to

$$\boxed{\frac{\partial}{\partial t}\left(\vec{p}-e\vec{A}\right) - \vec{v}\times\vec{\nabla}\times\left(\vec{p}-e\vec{A}\right) = \vec{\nabla}\left(e\Phi_\mathrm{el} - \gamma m_\mathrm{e}c^2\right).} \tag{2.31}$$

This equation has a trivial solution $\vec{p} = e\vec{A}$ and therefore $e\vec{\nabla}\Phi_\mathrm{el} = m_\mathrm{e}c^2\vec{\nabla}\gamma$, in which the ponderomotive force, $m_\mathrm{e}c^2\vec{\nabla}\gamma$, is balanced by the electrostatic force, $e\vec{\nabla}\Phi_\mathrm{el}$, arising from the laser-induced charge separation in the plasma. This implies $\gamma = \sqrt{1+a^2}$, what differs from the expression for a single electron derived in section 2.1.1, and leads to the ponderomotive potential in a plasma,

$$\Phi_\mathrm{pond} = m_\mathrm{e}c^2(\gamma-1) = m_\mathrm{e}c^2\left(\sqrt{1+a^2}-1\right). \tag{2.32}$$

The ponderomotive potential depends on the local laser intensity that scales with a^2. In the focus of the laser pulse, where the intensity is maximal and $a = a_0$, the ponderomotive potential can be expressed in units of the laser intensity, I_L, and the laser wave length, λ_L, according to eq. (2.10):

$$\Phi_\mathrm{pond} = 511\,\mathrm{keV}\times\left(\sqrt{1+\frac{I_\mathrm{L}\lambda_\mathrm{L}^2}{1.37\times10^{18}\,\mathrm{W/cm^2}\cdot\mu\mathrm{m}^2}}-1\right). \tag{2.33}$$

Debye Shielding

One of the key characteristics of a plasma is its tendency to shield externally applied electric fields. The differently charged particles arrange in a way that an electric field of opposite orientation is generated that tends to cancel the external field on a macroscopic scale, where the plasma appears to be quasi-neutral. On a microscopic scale, the positive ions are surrounded by plasma electrons that shield the electric potential of the ions. For a single ion with charge, Ze, this shielding modifies the pure Coulomb potential by an exponential drop [59]

$$\Phi_\mathrm{ion}(r) = \frac{1}{4\pi\varepsilon_0}\frac{Ze}{r}\cdot\exp\left(-\frac{r}{\lambda_\mathrm{D}}\right) \tag{2.34}$$

with the characteristic shielding length, λ_D, that depends on the temperature, T_e, and the density, n_e, of the surrounding plasma electrons:

$$\lambda_\mathrm{D} = \sqrt{\frac{\varepsilon_0 k_\mathrm{B} T_\mathrm{e}}{n_\mathrm{e}e^2}}. \tag{2.35}$$

λ_D is called the **Debye length** of the plasma and k_B denotes the Boltzmann constant. In an undisturbed plasma, charge neutrality is provided on scales larger than the plasma Debye length.

Light Propagation in a Plasma

If the plasma electrons are displaced from the positive ion background by an external perturbation, a restoring force builds up due to the electric fields arising from the charge separation. When the perturbation is over, the electrons start to oscillate around the position of charge equilibrium with a characteristic frequency, ω_{pe}, that only depends on the density, n_{e}, of the plasma electrons [58]:

$$\omega_{\mathrm{pe}} = \sqrt{\frac{n_{\mathrm{e}} e^2}{\varepsilon_0 m_{\mathrm{e}}}}. \tag{2.36}$$

ω_{pe} is called the **electron plasma frequency.** The plasma electrons can also follow periodic external perturbations, that are varying with frequencies $\omega < \omega_{\mathrm{pe}}$. A light wave with $\omega < \omega_{\mathrm{pe}}$ cannot propagate in a plasma, as the electrons shield the oscillating light field. If the electric field of the external perturbation is that strong that the electron quiver velocity approaches c within the oscillation, the effective electron mass, γm_{e} increases, what in turn changes the electron plasma frequency. Due to the variation of the effective electron mass during an oscillation cycle, the electron motion becomes unharmonious. Then the electron plasma frequency is given by

$$\omega_{\mathrm{pe}} = \sqrt{\frac{n_{\mathrm{e}} e^2}{\varepsilon_0 \langle\gamma\rangle m_{\mathrm{e}}}}, \tag{2.37}$$

where $\langle\gamma\rangle$ is averaged both over the fast oscillation of the laser field and locally over a large number of electrons. However, when the external frequency exceeds ω_{pe}, the electrons are too inert to follow the varying field, and the external wave can propagate in the plasma. If on the other hand an electromagnetic wave with frequency ω_{L} propagates through a plasma density gradient, it is stopped at that electron density, n_{cr}, where the light frequency, ω_{L}, matches the local plasma frequency, ω_{pe}. This density is called the **critical plasma density**

$$n_{\mathrm{cr}} = \frac{\varepsilon_0 \langle\gamma\rangle m_{\mathrm{e}} \omega_{\mathrm{L}}^2}{e^2} = \frac{1.11 \times 10^{21} \mathrm{cm}^{-3}}{\lambda_{\mathrm{L}}^2} \cdot \langle\gamma\rangle \cdot \mu\mathrm{m}^2. \tag{2.38}$$

For a laser-wave length of $\lambda_{\mathrm{L}} = 790\,\mathrm{nm}$ and low intensities, i.e. $\langle\gamma\rangle \approx 1$, the critical density is $n_{\mathrm{cr}} = 1.79 \times 10^{21} \mathrm{cm}^{-3}$. Plasmas with electron densities above this limit are called *overcritical*, below this density they are referred to as *undercritical*.

The propagation of an electromagnetic wave with frequency ω_{L} in an underdense plasma is described by the **plasma dispersion relation**

$$\omega_{\mathrm{L}}^2 = k_{\mathrm{L}}^2 c^2 + \omega_{\mathrm{pe}}^2. \tag{2.39}$$

Using the refractive index, η_{r}, of the plasma, that is defined by

$$\eta_{\mathrm{r}} = \sqrt{1 - \left(\frac{\omega_{\mathrm{pe}}}{\omega_{\mathrm{L}}}\right)^2} = \sqrt{1 - \left(\frac{n_{\mathrm{e}}}{n_{\mathrm{cr}}}\right)}, \tag{2.40}$$

the group and phase velocity of the electromagnetic wave, v_{gr} and v_{ph}, in the plasma read

$$v_{\mathrm{gr}} = \frac{\partial \omega_{\mathrm{L}}}{\partial k} = \eta_{\mathrm{r}} \cdot c \quad \text{and} \quad v_{\mathrm{ph}} = \frac{\omega_{\mathrm{L}}}{k} = \frac{1}{\eta_{\mathrm{r}}} \cdot c. \tag{2.41}$$

As the refractive index η_{r} in a plasma with $n_{\mathrm{e}} < n_{\mathrm{cr}}$ is always smaller than 1, the group velocity is smaller and the phase velocity larger than c.

The intensity dependence of the refractive index η_{r} via the Lorentz factor, that is averaged both over the fast laser oscillations and a large number of plasma electrons, $\langle\gamma\rangle = (1+a^2)^{1/2}$, has several consequences for the propagation of laser pulses of relativistic intensities in plasmas.

- The plasma frequency decreases for increasing laser intensity. Therefore, a plasma layer with an electron density n_{e}, that is overcritical and therefore non transparent for a sub-relativistic light wave with $a_0 \ll 1$, can become transparent for a laser pulse with $a_0 \leq 1$, when the condition

  $$\frac{\varepsilon_0 \omega_{\mathrm{L}}^2 m_{\mathrm{e}}}{e^2} < n_{\mathrm{e}} < \frac{\varepsilon_0 \omega_{\mathrm{L}}^2 m_{\mathrm{e}}}{e^2} \cdot \sqrt{1+a_0^2} \tag{2.42}$$

  is fulfilled. This phenomenon is called **self-induced transparency** [62].

- If a laser pulse with a *moderate intensity*, that is on the one hand low enough to be treated classically but on the other hand sufficiently high to significantly enhance the ionisation degree of the plasma by optical field ionisation, the electron density in the center of the focus is increased due to the ionisation, while the density remains unchanged outside the focus. This leads to a lower refractive index in the center of the beam, what in turn increases the phase velocity, $v_{\mathrm{ph}} = c/\eta_{\mathrm{r}}$, of the laser wave in the center compared to the wings of the focus. Therefore, the plasma acts as a negative lens, defocusing the laser beam. This effect is called **ionisation defocusing**.

  When a *relativistic* laser pulse is focused into a plasma, the averaged electron mass, γm_{e}, increases the more during the oscillation in the laser field, the higher the local intensity is. This leads to a reduction of the refractive index on the laser axis compared to the wings of the focus. If this effect dominates the ionisation defocusing, the plasma acts as a positive lens further increasing the intensity compared to the focusing in vacuum. This effect is called **relativistic self-focusing**. Furthermore, the electrons are ponderomotively scattered out of the center of the focus where the intensity is higher, decreasing the local electron density. This effect, that further enhances the laser-beam focusing, is referred to as **ponderomotive self-focusing**. The power threshold above which relativistic self-focusing dominates over the ionisation defocusing is given by [63]

  $$P_{\mathrm{RSF}} = 2 \frac{m_{\mathrm{e}} c^2}{e} \frac{4\pi\varepsilon_0 m_{\mathrm{e}} c^3}{e} \cdot \left(\frac{n_{\mathrm{cr}}}{n_{\mathrm{e}}}\right) = 17.4\,\mathrm{GW} \cdot \left(\frac{n_{\mathrm{cr}}}{n_{\mathrm{e}}}\right), \tag{2.43}$$

  where $m_{\mathrm{e}} c^2/e = 511\,\mathrm{kV}$ is the voltage corresponding to the electron rest energy and $4\pi\varepsilon_0 m_{\mathrm{e}} c^3/e = 17\,\mathrm{kA}$ is the Alfvén current [64], which is the maximum current that can be transported through vacuum (see below).

2.2 Electron Acceleration Mechanisms in a Plasma

When a high-intensity laser pulse interacts not only with a single electron, as it was discussed in section 2.1.1, but with a plasma, the situation becomes much more complex as a large variety of nonlinear effects associated with the collective behaviour of the electrons opens up. It turns out that a fraction of the plasma electrons can very effectively – in total number as well as in kinetic energy – be accelerated by high-intensity laser pulses. A fraction of several tens of percent of the laser pulse energy can be converted into electrons in the MeV-range forming a *directed* electron beam – in contrast to the pure heating of a plasma resulting in an almost *isotropic* velocity distribution. As all these different collective effects potentially influence each other, a description of the whole picture as complete as possible can only be achieved by using numerical simulations.

Depending on the experimental conditions, different acceleration mechanisms can become dominant. In general, they can be divided into two groups. First, electrons are accelerated at or close to the surface of the overcritical plasma layer, where the laser pulse is stopped and partly reflected. These effects play a role in experiments with solid targets, where such a layer exists. Second, electrons are accelerated in underdense-plasma regions, as they occur in gas targets or in long-scale length preplasmas in front of a solid target. These effects become dominant, when the laser pulse can propagate through underdense plasma regions over a distance that is much longer compared to its minimal diameter in the focus.

2.2.1 Electron Acceleration at the Critical Surface

In experiments with solid targets, the intrinsic laser prepulse due to amplified spontaneous emission is intense enough to generate a preplasma at the target front side, in which the electron density rises from 0 in vacuum to the solid density ($\sim 10^{23}\,\mathrm{cm}^{-3}$) over a scale length that depends on the prepulse characteristics. When the main pulse is incident on the overdense plasma surface ($\sim 10^{21}\,\mathrm{cm}^{-3}$) that is parallel to the initial target surface, it is partially reflected. As the beam cannot propagate beyond this overcritical surface, the field gradient is maximal here and it is directed normal to the overcritical surface. The ponderomotive force directed along the steepes field gradient drives electrons perpendicular to the surface of the overcritical-plasma layer into the target. While this surface is initially parallel to the target surface, it is deformed during the interaction with the laser as the laser pulse pushes electrons and hence also the critical surface sideways and in forward direction. This effect is referred to as laser hole boring. In the context of relativistic laser-plasma interaction, it has been identified in 2-D PIC simulations [65]. Due to this effect, the direction of electron acceleration is no longer only perpendicular to the target surface, but occurs in a direction between target normal and laser direction [66]. The mean energy or the effective temperature, $k_\mathrm{B}T_\mathrm{e}$, of the electron population accelerated in that way can be estimated by the ponderomotive potential of the laser to

$$k_\mathrm{B}T_\mathrm{e} \;=\; m_\mathrm{e}c^2\left(\sqrt{1+a_0^2}-1\right)$$

$$= \quad 0.511\,\mathrm{MeV} \cdot \left(\sqrt{1 + \frac{I_\mathrm{L}\lambda_\mathrm{L}^2}{1.37\times 10^{18}\mathrm{W/cm^2}\mu\mathrm{m}^2}} - 1 \right). \qquad (2.44)$$

This relation has first been deduced from PIC simulations carried out by S. Wilks *et al.* [67] and verified experimentally by G. Malka *et al.* [8]. Typically, a fraction of $\eta \approx 25\%$ of the laser energy, E_L, is converted into electrons having such a Boltzmann temperature [9]. Laser pulses from ATLAS, delivering an energy of $E_\mathrm{L} = 850\,\mathrm{mJ}$ on the target with $\lambda_\mathrm{L} = 790\,\mathrm{nm}$ at an averaged intensity of $I_\mathrm{L} = 1.5 \times 10^{19}\,\mathrm{W/cm^2}$, generate an electron population with a quasi-temperature of $k_\mathrm{B}T_\mathrm{e} \approx 920\,\mathrm{keV}$. The total number, N_e, of this population can be estimated to be the total energy of the population divided by their mean energy:

$$N_\mathrm{e} \approx \frac{\eta E_\mathrm{L}}{k_\mathrm{B}T_\mathrm{e}} = 1.44 \times 10^{12}. \qquad (2.45)$$

Brunel Heating

In this scenario, a *p*-polarised[3] laser pulse is focused under oblique incidence onto a solid target with a steep density gradient, i.e. a short scale length, L_p, of the order of the laser-wave length [68]. As in vacuum, the transverse electric field of the laser accelerates electrons sideways. While in vacuum the electrons would oscillate symmetrically around the laser axis, in regions close to the critical surface of the solid the electrons only experience the electric field of the laser in areas of undercritical density. They are accelerated towards the vacuum in the first laser-half cycle, turn round and are accelerated into the solid, where they feel no restoring forces any more as the laser fields cannot penetrate into overdense regions. Via this mechanism the electrons can gain energy and enter the solid along the direction of the gradient, but the acceleration is only effective for steep gradients (otherwise the necessary differences in the forces acting on the electron during the two laser-half cycles are too small).

2.2.2 Electron Acceleration in Underdense Plasma

Laser Wake-Field Acceleration

When a short laser pulse is focused into an underdense plasma, the ponderomotive force acting at the leading edge of the pulse expells electrons from the focal region. This charge separation excites a plasma wave that follows the laser pulse in its wake and copropagates with the group velocity, $v_\mathrm{gr} = c \cdot \eta_\mathrm{r} < c$, of the laser pulse in the plasma. The longitudinal electric field in the plasma wave can trap electrons that can gain a large amount of kinetic energy, when they travel with the wave. This acceleration mechanism, that is called laser wakefield acceleration (LWFA), was proposed by T. Tajima *et al.* [69]. It is most efficient,

---

[3] For *p*-polarisation, the electric field vector of the laser pulse incident on the target under oblique incidence lies in the plane defined by the *k*-vector of the wave and the target normal. For *s*-polarisation, the electric field vector is perpendicular to this plane. Here, the laser electric field vector has no component parallel to the target normal, as it is the case for *p*-polarisation.

when the laser-pulse duration is half as long as a period of the plasma oscillation, i.e. if $\tau_{\mathrm{L}} = \pi/\omega_{\mathrm{pe}}$. The problem is to trap electrons efficiently; large trapping occurs when the plasma wave breaks, i.e. when groups of wave electrons move faster than the wave's phase velocity.

Direct Laser Acceleration

During the interaction of a relativistic laser pulse with a plasma of undercritical density self-focusing of the laser pulse can occur, when the power threshold, eq. (2.43), is passed. This reduces the focal diameter of the laser and increases the intensity compared to the focusing in vacuum. A plasma channel is formed along the laser axis, that extends over a distance of many Rayleigh lengths of the vacuum-laser focus. In this channel, the ponderomotive forces of the laser radially expell electrons and additionally drive a strong electron current along the channel. This leads to the formation of strong radial electric fields due to the lack of plasma electrons in the channel and strong azimuthal magnetic fields due to the high current. An electron running under small initial pitch angles to the axis of the channel is bent back by the strong electric and magnetic fields and starts to oscillate in these fields. If this electron oscillation is in resonance with the Doppler-shifted laser-light oscillation, and if the phases between electron and laser field match, the electron can gain a large amount of energy directly from the laser fields. This mechanism is called direct laser acceleration (DLA) and has been described by Z. M. Sheng, A. Pukhov, and J. Meyer-ter-Vehn [70,71]. In an experiment carried out by C. Gahn at the MPQ using the ATLAS laser system, it has been demonstrated clearly [10]. It is capable of accelerating electrons to very high energies, but it requires a long region of underdense plasma as present in a gas jet or in a long-scale length preplasma that a plasma channel can build up. For the "ideal" conditions of a gas jet, where a self-focused channel of 400-μm length was observed, a conversion efficiency of 5% was measured in [10].

To estimate the efficiency of this mechanism in experiments with solid targets, the possible length over which a plasma channel can form, has to be determined. This is the length of the region, where the electron density is above the density for self focussing, given by eq. (2.43) and below the critical density, n_{cr}, where the laser pulse is reflected. Depending on the preplasma conditions, this region can be as short as several tens of micrometers only for very short laser prepulses or as long as several 100's of μm for very long and intense prepulses. In the experiments of this thesis, this length was of the order of 10 μm to 50 μm. Hence, it can be estimated that the efficiency of electron acceleration via DLA will be less than 5% in the experiments reported here. For the case of a long-scale length preplasma formed by a second, synchronised ns-laser pulse as in [72], the efficiency of this acceleration mechanism might increase again. In appendix A, some results from an experiment are described, where electrons were accelerated in a plasma channel via direct laser acceleration. In this experiment, a long-scale length preplasma was generated by a ns-Nd:Glass laser pulse, the channel extended over more than 400 μm.

Concluding Remarks

Although these are only some examples for different possible scenarios to accelerate electrons on the target front side, multi-dimensional PIC-simulations show that the electron injection into the target mainly occurs in a direction between target normal direction and laser propagation direction [66]. Here, the deformation of the critical surface due to hole-boring is important, too. The direction of the electron injection into the target also depends on the preplasma conditions [73]. For scale lengths above $10\ldots15\,\mu$m, the direction of the electron beam is mainly directed in laser forward direction, for scale lengths below $3\ldots5\,\mu$m, the electron injection into the target is mainly parallel to the target normal direction. Recent experiments carried out at MPQ showed a clear distinction between the two acceleration directions, one in laser direction the other one in target normal direction [74].

By these effects, a large number of high-energetic electrons is generated capable of propagating through the target. During their passage through the overdense part of the target, collective effects of the beam electrons play a role, too. They will be discussed in the next section.

2.3 Electron-Beam Transport Through Overdense Plasma

In the last section, mechanisms to accelerate $\sim10^{12}$ electrons (cf. eq. 2.45) with a temperature of $\sim1\,$MeV were described. As the acceleration process occurs within the laser pulse duration only, the corresponding hot-electron current entering the target is of the order of $10^6\,$A. This value exceeds by far the Alfvén limit for electron currents, $I_\mathrm{A} = \beta\gamma\cdot 17\,\mathrm{kA}$ [64]. No electron current above this limit can freely propagate in vacuum, as for such a current the beam electrons are forced on bent trajectories by the self-induced magnetic field that no net current above this limit can be transported in the initial beam direction. However, in a plasma the transport of currents above the Alfvén limit is possible, when the hot-electron current is compensated locally by a suitable return current. This return current is driven by electric fields induced by magnetic field build-up due to the fast-electron current itself and by the charge separation in the target. While the hot-electron beam is generated at the critical density, n_cr, and the beam density is of the same order ($\sim10^{21}\,\mathrm{cm}^{-3}$), the electron density of the return current, n_ret, is of the order of the solid density ($\sim10^{23}\,\mathrm{cm}^{-3}$). Consequently, the return current consists of a slow drift of the background electrons. For conductors, the return current can be carried by the free electrons. In insulators however, free electrons first have to be generated by field or collisional ionisation [75]. These ionisation processes strongly reduce the energy of the hot-electron beam.

The configuration of two counter-streaming electron currents is highly unstable with respect to the Weibel instability [76], as small local perturbations in the current densities that violate the exact balancing of the two currents give rise to azimuthal magnetic fields generated by the arising net current that tend to pinch this net current and to expell the return current out of this beam filament. This can lead to the formation of beam filaments, each carrying up to one Alfvén current, that is cylindrically surrounded by a return current almost cancelling the magnetic field outside the filament. When two of these filaments coalesce afterwards due to residual attraction, a part of the energy carried by the hot-electron current is converted into transversal heating of the surrounding plasma, until the current carried by the merged filament is reduced to one Alfvén current again. If this effect, that was described by M. Honda [77], sets in, it leads to a significant dissipation of energy, the electron beam undergoes so-called anomalous stopping.

While the distance between the filaments described above is on a sub-μm scale, the electron beam as a whole having an initial diameter of several micrometers can undergo beam pinching, too. This can be understood qualitatively as follows. The background plasma is ohmically heated by the return current [41, 75] leading to a non uniform temperature distribution of the background plasma producing a spatial variation of the resistivity of the plasma that strongly depends on the temperature [78]. This gives rise to a spatial variation of the electric field driving the return current that generates an azimuthal magnetic field that can pinch the electron beam as a whole [79]. This scenario is investigated in detail in chapter 8.2 using a fast-electron-transport code developed by J. J. Honrubia [80] .

2.4 Proton-Acceleration Mechanisms

As described at the end of section 2.1.1, the *direct* interaction of protons and all the more heavier ions with laser light of presently achievable intensities is by far not strong enough to accelerate these ions to MeV-energies. However, the plasma electrons can mediate the forces of the laser fields to the ions by the generation of strong and quasi-static electric fields arising from local charge separations. These fields can be of the same magnitude as the fast-oscillating laser fields, but they vary on a time scale comparable to the laser-pulse duration giving the ions a significantly longer time to be accelerated.

In this section, the two main proton-acceleration scenarios will be described, that can both provide sufficiently strong electric fields over a sufficiently long time. According to these two scenarios, protons can either be accelerated in the laser focus at the **target front side**, where the ponderomotively expelled electrons leave behind a positive space charge of ions, or at the **target rear side**, where the electrons, that have been accelerated by the laser on the front side and have propagated through the target, form a thin Debye-sheath, that also provides strong and long-lasting electric fields.

2.4.1 Proton Acceleration at the Target Front Side

The first possible mechanism accelerates protons at the front side of the target in the vicinity of the laser focus due to electrostatic fields arising from the ponderomotive expulsion of plasma electrons from regions of high laser intensities. The front-side proton acceleration has recently been studied by Y. Sentoku *et al.* using a 1-D PIC code [81]. In these simulations, the laser pulse is focused into a preplasma having a μm-scale length, that has been formed by the intrinsic prepulse of the laser. This preplasma is assumed to be quasi-neutral before the arrival of the main pulse, i.e. electron and ion densities balance each other: $n_{\mathrm{e0}}(x) \approx n_{\mathrm{i0}}(x)$, as it is sketched in Fig. 2.2 (a). When the main pulse of relativistic

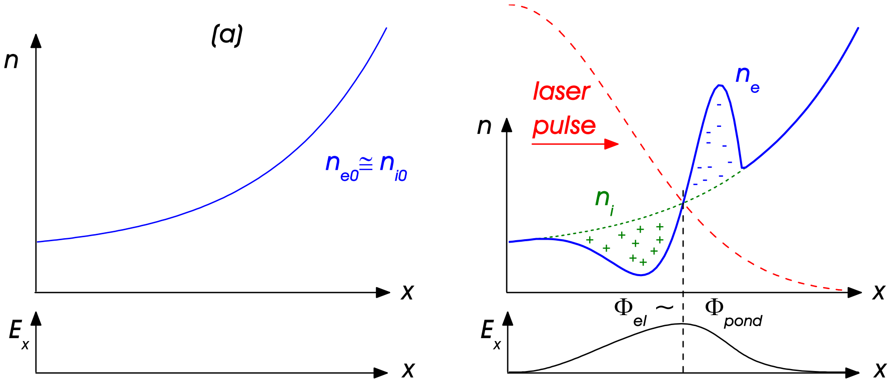

Figure 2.2: Electron and ion densities, n_{e0} and n_{i0}, at the target front side immediately before (a) and during (b) the interaction of a relativistic laser pulse with the preformed plasma. Due to the ponderomotive force, electrons are piled up at the laser-pulse front, until the electrostatic potential of the charge separation, Φ_{el}, balances the ponderomotive potential of the laser, Φ_{pond}.

intensity with a normalised vector potential $a_0 > 1$ arrives at the relativistic critical surface, electrons are ponderomotively expelled out of the focal region, until the electrostatic potential, Φ_{el}, arising from the charge separation balances the ponderomotive potential, Φ_{pond}, of the laser, that was given in eq. (2.32), what leads to

$$\Phi_{\mathrm{el}} \approx \Phi_{\mathrm{pond}} = m_{\mathrm{e}}c^2(\gamma - 1) = m_{\mathrm{e}}c^2\left(\sqrt{1+a^2} - 1\right). \tag{2.46}$$

This situation is shown in Fig. 2.2 (b). When a single proton experiences this potential, it can gain a maximum kinetic energy equal to the potential difference. This holds true, as long as the acceleration field lasts long enough for the proton to be accelerated to this energy. The life-time of the field can be estimated to be the laser pulse duration, τ_{L}. The necessary proton-acceleration time, τ_{acc}, that has to be compared to the field duration, τ_{L}, will now be derived – following the paper by Sentoku.

The 1-D equation of motion for a proton in the front-side acceleration field, $\mathcal{E}_x$, reads

$$m_{\mathrm{p}}\frac{\mathrm{d}v_{\mathrm{p}}}{\mathrm{d}t} = \frac{\mathrm{d}E_{\mathrm{p}}}{\mathrm{d}x} = e\mathcal{E}_x, \tag{2.47}$$

where m_{p} and v_{p} are proton mass and velocity, respectively, and $E_{\mathrm{p}} = \frac{1}{2}m_{\mathrm{p}}v_{\mathrm{p}}^2$ is its kinetic energy. To integrate this equation, it is assumed that the electrostatic field, $\mathcal{E}_x$, is constant with an averaged value of $\mathcal{E}_{x0}/2$ over an acceleration length x_{max}, that will be determined below. Then the kinetic energy as a function of distance, x, is given by

$$E_{\mathrm{p}}(x) = e\frac{\mathcal{E}_{x0}}{2}x. \tag{2.48}$$

As the maximum proton energy reached at the end of the acceleration length, x_{max}, equals the ponderomotive potential, i.e. $E_{\mathrm{p}}(x_{\mathrm{max}}) = \Phi_{\mathrm{pond}} = k_{\mathrm{B}}T_{\mathrm{e}}$, and as the maximum value of the electric field is $\mathcal{E}_{x0} \approx k_{\mathrm{B}}T_{\mathrm{e}}/e\lambda_{\mathrm{D}}$, (see next section), the acceleration length is $x_{\mathrm{max}} = 2\lambda_{\mathrm{D}}$. Note that this differs from the assumptions made by Sentoku [81], where $x_{\mathrm{max}} \approx$

$\lambda_D/2$ and $\mathcal{E}_{x0} \approx 2m_e c^2\langle\gamma\rangle/e\lambda_D$ were assumed. With these values, the protons do not gain the maximum energy equal to the ponderomotive potential. Therefore, the different values as described above are used here to fulfill this requirement and to obtain a coherent picture of the front-side acceleration.

To obtain the acceleration time, τ_{acc}, the relation

$$\frac{m_p}{2}\left(\frac{dx}{dt}\right)^2 = e\frac{\mathcal{E}_{x0}}{2}x \quad \rightarrow \quad dt = \frac{dx}{\sqrt{(e\mathcal{E}_{x0}/m_p)x}} \tag{2.49}$$

is used and integrated from $x = 0$ to $x_{max} = 2\lambda_D$, where $\mathcal{E}_{x0}$ was assumed to be constant:

$$\tau_{acc} = \int_0^{2\lambda_D} \frac{dx}{\sqrt{(e\mathcal{E}_{x0}/m_p)x}} = \sqrt{\frac{8m_p\lambda_D}{e\mathcal{E}_{x0}}} \approx \sqrt{\frac{8m_p\lambda_D^2}{k_B T_e}}. \tag{2.50}$$

The Debye length at the critical density, that is given in eq. (2.38), can be written as

$$\lambda_D^2 = \frac{\varepsilon_0 k_B T_e}{n_{cr}e^2} = \frac{k_B T_e}{\omega_L^2 m_e\langle\gamma\rangle} = \frac{k_B T_e}{4\pi^2 m_e c^2}\cdot\frac{\lambda_L^2}{\langle\gamma\rangle}. \tag{2.51}$$

This finally leads to the following expression for the proton-acceleration time

$$\tau_{acc} = \sqrt{\frac{8m_p}{m_e\langle\gamma\rangle}}\cdot\frac{T_L}{2\pi} \approx 20\times\frac{T_L}{\sqrt{\langle\gamma\rangle}}, \tag{2.52}$$

where T_L denotes the laser period. For the ATLAS conditions (T_L=2.63 fs and $\langle\gamma\rangle \approx 2.8$), one finds $\tau_{acc} \approx 32$ fs, what is significantly shorter than the laser-pulse duration of $\tau_L =$ 150 fs. It can therefore be concluded that during the interaction of the laser pulse with the preplasma on the target-front side, a proton can be accelerated to the maximal energy determined by the ponderomotive potential of the laser. Note that eqs. (2.51) and (2.52) differ from [81], where $\lambda_D \sim \lambda_L$ was assumed. The acceleration time predicted by Sentoku for the ATLAS conditions would be 70 fs. Nevertheless, both estimates for τ_{acc} are well below the laser-pulse duration in the experiments described in this thesis.

Further investigations of the front-side acceleration process carried out by Sentoku in [81] with 1-D PIC simulations revealed an additional collective effect of the protons, that increases the maximum proton energies. Immediatetly after the interaction with the laser pulse, a proton front with a very sharp density peak is formed. As the local electron temperature is too high (and thus the local Debye length too long) to shield the strong electrostatic repulsion forces within this front, it explodes afterwards further accelerating the fastest protons. In the simulations an increase of the maximum proton velocity by a factor of 1.5 is observed. This further increases the maximum proton energy by a factor of $(1.5)^2$.

Taking all these considerations into account, an analytical estimate for the maximum energy of the front-side accelerated protons for laser pulses with $\tau_L \geq \tau_{acc}$ can be given. It is

$$\begin{aligned} E_{p,front} &= (1.5)^2\cdot k_B T_e \\ &= 1.15\,\mathrm{MeV}\cdot\left(\sqrt{1+\frac{I_L\lambda_L^2}{1.37\times10^{18}\,\mathrm{W/cm^2}\cdot\mu\mathrm{m}^2}}-1\right), \end{aligned} \tag{2.53}$$

and for $I_\mathrm{L} = 1.5 \times 10^{19}\,\mathrm{W/cm^2}$ and $\lambda_\mathrm{L} = 790\,\mathrm{nm}$ as in the experiments described in chapter 5, the maximum energy for protons accelerated at the front side of the target is

$$E_\mathrm{p,front} = 2.1\,\mathrm{MeV}. \tag{2.54}$$

All the assumptions and conclusions discussed above are based on 1-D geometry. However, as the laser focus in a real experiment has a finite diameter and as the charge-separation sheath in which the acceleration occurs will no longer be plane but convex-shaped, the protons will consequently be accelerated in a large opening angle around the target normal direction, which is the initial direction of the electron density gradient as discussed above.

2.4.2 TNSA-Mechanism for Proton Acceleration from the Target Rear Side

The second possible mechanism also providing strong and slowly-varying electric fields for an effective proton and ion acceleration acts at the target rear surface. In this section, the physical picture of the mechanism will be described and an analytical description for the evolution of the electrical field driving the acceleration is presented.

The Physical Picture

MeV-electrons that have been generated in the laser focus propagate through the target as discussed above. After the fastest electrons have left the target at the rear side, a strong electrostatic potential is built up due to the charge separation in the vicinity of the rear-side target-vacuum boundary. As soon as the subsequently arriving electrons pass this boundary, they are held back and forced to return into the target. Due to this mechanism an electron sheath is formed at the rear surface of the target. An estimation for the initial electric-field strength shows that the fields are by far strong enough to ionise atoms at the target rear surface (see below). These ions can subsequently be accelerated by the same fields. Due to unavoidable contaminations of water or pump-oil vapor on the target surfaces, the favorably accelerated ion species are protons, as they have the highest charge-to-mass ratio. They leave the target together with comoving electrons forming a quasi-neutral plasma cloud. As the plasma density in this cloud quickly drops after the detachment from the target and as the temperature remains high in this cloud, recombination effects are negligible for propagation lengths in the range of several meters [82]. The situation for the rear-side acceleration mechanism is sketched in Fig. 2.3.

The electric-field lines are parallel to the normal vector of the target rear surface and also the ion acceleration is aligned along this direction. Therefore, the mechanism is called **T**arget-**N**ormal-**S**heath **A**cceleration (TNSA). It has first been described by Snavely and Wilks [15, 17] in short-pulse experiments using the Nova-Petawatt laser at Lawrence Livermore National Laboratory, where the emission of protons normal to both rear surfaces of a wedge-shaped target was observed. Since then it has been widely accepted as a possible mechanism to accelerate protons to kinetic energies well above 1 MeV.

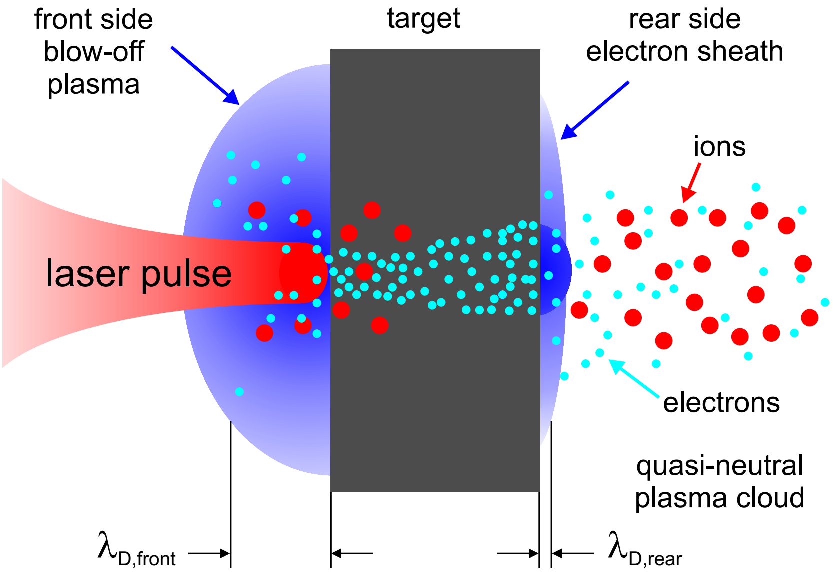

Figure 2.3: Sketch of the TNSA-mechanism. The laser pulse coming from the left is focused into a preplasma on the target front side having a long Debye length, $\lambda_{\mathrm{D,front}}$, which has been formed by the laser prepulse. Electrons are accelerated in the laser focus. They propagate through the target setting up an electrical field due to charge separation, when they leave the target at the rear surface, forming a thin electron sheath with a very short Debye length, $\lambda_{\mathrm{D,rear}}$. This electrical field ionizes atoms at the rear surface and accelerates them in target normal direction. The ions leave the target in a quasi-neutral cloud together with comoving electrons.

The pyhsical model underlying the TNSA-mechanism has already been described in the early 1970's for the acceleration of ions using ns-laser pulses [83–85]. The significant differences to present-day experiments are the much shorter laser-pulse durations, the much higher electron temperatures, and the associated different temporal evolution fo the electric fields driving the acceleration process. For long-pulse experiments, the plasma at the target rear surface slowly expands. Due to the expansion of the positive ion distribution (see below), the electric fields at the ion front are reduced during the expansion. Therefore, the acceleration becomes almost ineffective already during the laser pulse duration. For short-pulse experiments however, the life-time of the acceleration field is dominated by the laser pulse duration and not by the ion expansion itself. The acceleration process is terminated, when the laser pulse is over.

The TNSA-mechanism works as well at the target front surface, as the MeV-electrons that were initially accelerated in laser direction, are reflected at both target surfaces due to the space charge fields. They can travel through the target to and fro several times, while they loose their energy and quickly spread out sideways, heating up the bulk of the target. Protons accelerated at the target-front side by TNSA leave the target along the front-side normal direction into the front-side half space[4]. This effect has been observed by G. D. Tsakiris *et al.* [24] and recently by E. Clark *et al.* [13]. Due to the much longer

---

[4] Note that the front-side acceleration described in the last section accelerates the protons *into* the target, while the TNSA-mechanism described here accelerates ions into the front half space, i.e. *away from* the target.

scale length in the front-side blow-off plasma, that has been generated by the laser prepulse, the electric fields are much lower here. Although the *potential difference* is equal for both target surfaces, the electric fields, that are proportional to the *potential gradient*, are inversly proportional to the Debye length in the plasma sheaths at each target surface. As the potential difference and the electric fields are only kept up as long as the electron temperature remains high, ions accelerated at the target-front side gain much lower energies by the TNSA-mechanism.

The initial TNSA-model by S. Wilks [17] provides an analytical estimate only for the electric field at the beginning of the acceleration process, which was also derived in earlier papers that described the plasma expansion into a vacuum driven by a hot electron population. The evolution during the expansion of the proton distribution could only be studied with multi-dimensional computer codes, that quickly reached the limits of even the most powerful computer systems. P. Mora recentyl provided an analytical description of the evolution of the peak electric field in the expanding plasma cloud during the whole acceleration process for planar geometry [86]. These formulas can exactly be reproduced by numerical but time-consuming simulations, as it will be shown in chapter 7. If one is interested in the peak energy of the protons only, these formulas can be used to accurately predict the peak proton energies achieved during the acceleration process from the target rear side.

Estimation for the Initial Electric Field

To derive an expression for the initial electric field, $\mathcal{E}_0$, at the target rear side, the simplest case of a pre-ionised hydrogen plasma with a step-like hydrogen-density distribution at the rear surface, $x = 0$, is investigated. When an electron population with a Boltzmann-like temperature, T_e, and an initial electron density, $n_{\mathrm{e}0}$, exits the target at the rear side, an electrostatic potential, $\Phi_\mathrm{el}(x)$, is generated that is in thermal equilibrium with the electron-density distribution:

$$n_\mathrm{e}(x) = n_{\mathrm{e}0} \cdot \exp\left(\frac{e\Phi_\mathrm{el}(x)}{k_\mathrm{B}T_\mathrm{e}}\right). \tag{2.55}$$

Furthermore, the Poisson equation provides another potential-dependence of the charge densities, and one obtains

$$\frac{\partial^2}{\partial x^2}\Phi_\mathrm{el}(x) = -\frac{\rho(x)}{\varepsilon_0} = \frac{e n_{\mathrm{e}0}}{\varepsilon_0} \cdot \begin{cases} \exp\left(\frac{e\Phi_\mathrm{el}(x)}{k_\mathrm{B}T_\mathrm{e}}\right) - 1 & \text{for } x \leq 0, \quad \text{(I)} \\ \exp\left(\frac{e\Phi_\mathrm{el}(x)}{k_\mathrm{B}T_\mathrm{e}}\right) & \text{for } x \geq 0, \quad \text{(II)} \end{cases} \tag{2.56}$$

where $\rho(x)$ is the total charge distribution and $n_\mathrm{p} = n_{\mathrm{e}0}$ for $x \leq 0$ is assumed, which implies charge neutrality for $x \to -\infty$. Case (II) can be integrated analytically to

$$\frac{e\Phi_\mathrm{el}(x)}{k_\mathrm{B}T_\mathrm{e}} = -2\ln\left(1 + \frac{x}{\sqrt{2e_\mathrm{E}}\lambda_\mathrm{D}}\right) - 1 \qquad \text{for } x \geq 0. \tag{2.57}$$

Here, $e_\mathrm{E} = 2.71828\ldots$ denotes the basis of the natural logarithm. From this expression for the potential, the electric field, $\mathcal{E}_\mathrm{fr}$, that has its peak value at the target-vacuum interface, $x = 0$, at the time $t = 0$, can be derived by

$$\mathcal{E}_\mathrm{fr} = -\left.\frac{\partial \Phi_\mathrm{el}}{\partial x}\right|_{x=0} = \sqrt{\frac{2}{e_\mathrm{E}}} \cdot \frac{k_\mathrm{B} T_\mathrm{e}}{e\lambda_\mathrm{D}} = \sqrt{\frac{2}{e_\mathrm{E}} \cdot \frac{k_\mathrm{B} T_\mathrm{e} n_\mathrm{e0}}{\varepsilon_0}} = \sqrt{\frac{2}{e_\mathrm{E}}} \cdot \mathcal{E}_0 \tag{2.58}$$

with $\mathcal{E}_0 = \sqrt{k_\mathrm{B} T_\mathrm{e} n_\mathrm{e0}/\varepsilon_0}$. Note that the initial value of the electric field at the rear surface depends on the initial electron density, n_e0, and the electron temperature, T_e, only. For an electron density of $n_\mathrm{e0} = 7.3 \times 10^{20}\,\mathrm{cm}^{-3}$ and an electron temperature of $T_\mathrm{e} = 920\,\mathrm{keV}$, the peak value of the electric field is $\mathcal{E}_\mathrm{fr} = 3.0 \times 10^{12}\,\mathrm{V/m}$, which lies well above the threshold for field-ionisation of atomic hydrogen, $3.2 \times 10^{10}\,\mathrm{V/m}$ [87]. This justifies the assumption of a pre-ionised hydrogen target at the rear surface. Note that this field is of the same order of magnitude as the fast-oscillating electric field in the laser focus. If one would assume this field to be constant over the laser-pulse duration, $\tau_\mathrm{L} = 150\,\mathrm{fs}$, this would lead to a maximum proton energy of 9.6 MeV.

The integration of eq. (2.56) inside the target, i.e. for case (I), can only be carried out numerically. A simulation code, that calculates the potential in both regions (I) and (II) for times $t \geq 0$ during the expansion of the proton distribution at the target rear side, will be described in chapter 7.

Description of the Proton Expansion into the Vacuum

Starting from these initial conditions shown in Fig. 2.4 (a), the proton distribution is expanding into the vacuum, as it can be seen in Fig. 2.4 (b). The expansion is driven by the electric field that is generated by the hot electrons leaking out of the back of the target and forms the rear-side Debye sheath. This electric field is kept up as long as the electron temperature remains high, i.e. as long as the laser pulse accelerates electrons at the target front side. But already during the laser pulse duration, where the electron temperature remains high, the peak electric field is decreasing due to the expansion of the proton distribution, as the positive charge distribution of the protons, which is no longer step-like during the expansion, partly shields the electric field.

The plasma expansion into the vacuum is described by the equations of continuity and motion of the protons

$$\left(\frac{\partial}{\partial t} + v_\mathrm{p}\frac{\partial}{\partial x}\right) n_\mathrm{p} = -n_\mathrm{p}\frac{\partial v_\mathrm{p}}{\partial x} \quad \text{and} \tag{2.59}$$

$$\left(\frac{\partial}{\partial t} + v_\mathrm{p}\frac{\partial}{\partial x}\right) v_\mathrm{p} = -\frac{e}{m_\mathrm{p}}\frac{\partial \Phi_\mathrm{el}}{\partial x}, \tag{2.60}$$

where $v_\mathrm{p} = v_\mathrm{p}(x,t)$ is the local velocity, $n_\mathrm{p} = n_\mathrm{p}(x,t)$ the local density of the protons. Using the ion-acoustic velocity, $c_\mathrm{s} = \sqrt{(Zk_\mathrm{B}T_\mathrm{e} + k_\mathrm{B}T_\mathrm{i})/m_\mathrm{p}} \approx \sqrt{k_\mathrm{B}T_\mathrm{e}/m_\mathrm{p}}$ for protons with $T_\mathrm{i} \ll T_\mathrm{e}$ and $Z = 1$, a self-similar solution is found for $x + c_\mathrm{s}t > 0$ [88], if quasi-neutrality is assumed in the expanding plasma with

$$n_\mathrm{e} = n_\mathrm{p} = n_\mathrm{e0} \cdot \exp\left(-\frac{x}{c_\mathrm{s}t} - 1\right), \tag{2.61}$$

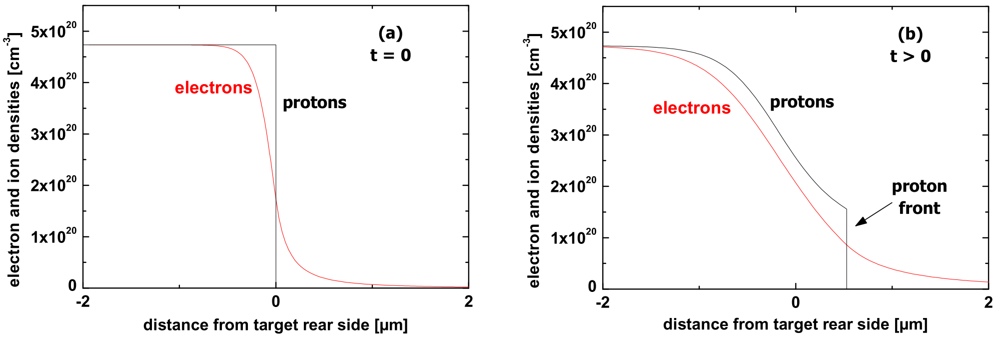

Figure 2.4: Electron and proton densities at the target rear side immediately before (a) and during (b) the expansion, that is driven by the electric field set up by the hot-electron population exiting the target rear surface. During the expansion, the protons that were initially situated at $x = 0$ form a well-defined front at the leading edge of the proton distribution. In this situation, the laser comes from the left and interacts with the target front side, what is not shown here.

$$v_p = c_s + \frac{x}{t}, \qquad \text{and} \tag{2.62}$$

$$\mathcal{E}_{ss} = \frac{k_B T_e}{e c_s t} = \frac{\mathcal{E}_0}{\omega_{pp} t}. \tag{2.63}$$

Here, $\omega_{pp} = \sqrt{n_e e^2/\varepsilon_0 m_p}$ is the proton-plasma frequency. This self-similar solution has no meaning as long as the *initial* Debye length, $\lambda_{D0} = \sqrt{\varepsilon_0 k_B T_e / n_{e0} e^2}$, is larger than the proton-density scale length in the self-similar solution, $c_s t$, that is for $\omega_{pp} t < 1$ [86]. Furthermore, this solution predicts a proton distribution that extends to infinity with a non-converging proton velocity for $x \longrightarrow \infty$, what contradicts the real situation, where protons originally situated at the target surface at $x = 0$ form a well defined front at the leading edge of the expanding proton distribution [84]. To solve this discrepancy and to account for the large differences in the charge distributions of electrons and protons that set up the strong electric fields, the proton distribution is assumed to extend up to the proton front only. The position of the front is (first empirically) defined by the condition, that the *local* Debye length, $\lambda_D = \lambda_{D0} \cdot \sqrt{n_{e0}/n_e} = \lambda_{D0} \cdot \exp[(1 + x/c_s t)/2]$, equals the self-similar density scale length, $c_s t$. At this position, the self-similar solution predicts a proton velocity of $v_{p,fr} = 2 c_s \ln(\omega_{pp} t)$, implying that the electric field at the proton front has a value of

$$\mathcal{E}_{fr}(t) \cong 2\mathcal{E}_{ss} = 2\frac{\mathcal{E}_0}{\omega_{pp} t}, \tag{2.64}$$

which is obtained by integrating eq. (2.63) over time. Together with eq. (2.58), one has two asymptotic solutions for the electric field at the proton front for $t = 0$ and for $\omega_{pp} t \gg 1$. Mora showed by comparison with 1-D simulations [86] that the peak value of the electric field at the proton front is very accurately described **for all times $t \geq 0$** by

$$\mathcal{E}_{fr}(t) \cong \frac{2\mathcal{E}_0}{\sqrt{2 e_E + \omega_{pp}^2 t^2}} = \sqrt{\frac{2}{e_E}} \cdot \frac{\mathcal{E}_0}{\sqrt{1+\tau^2}}, \tag{2.65}$$

with $\tau = \omega_{\mathrm{pp}} t / \sqrt{2 e_{\mathrm{E}}}$. Obviously, this expression has the exact asymptotic behaviour both for $t = 0$ and for $\omega_{\mathrm{pp}} t \gg 1$. In chapter 7, the exact validity of these assumptions will be shown by comparing the fields predicted by this formula with results obtained from a numerical simulation.

Maximum Proton Energy and Spectrum for the Rear-Side Acceleration

Based on the expression (2.65) for the electric field, analytic formulas for the velocity and the position of the proton front are found by integrating the proton equation of motion $\mathrm{d}v_{\mathrm{fr}}/\mathrm{d}t = e\mathcal{E}_{\mathrm{fr}}/m_{\mathrm{p}}$ and $\mathrm{d}x_{\mathrm{fr}}/\mathrm{d}t = v_{\mathrm{fr}}$ over time:

$$\begin{aligned} v_{\mathrm{fr}}(t) &\cong 2c_{\mathrm{s}} \cdot \ln\left(\tau + \sqrt{\tau^2+1}\right) \qquad \text{and} & (2.66)\\ x_{\mathrm{fr}}(t) &\cong 2\sqrt{2e_{\mathrm{E}}} \cdot \lambda_{\mathrm{D0}} \left[\tau \cdot \ln\left(\tau + \sqrt{\tau^2+1}\right) - \sqrt{\tau^2+1} + 1\right]. & (2.67)\end{aligned}$$

If the proton-acceleration time, t, is assumed to be the laser-pulse duration, τ_{L}, what is a good approximation for the duration where the electron temperature remains high, one finally obtains the maximum proton energy as

$$E_{\mathrm{p,rear}} \cong \frac{1}{2} m_{\mathrm{p}} v_{\mathrm{fr}}^2 = 2k_{\mathrm{B}} T_{\mathrm{e}} \cdot \left[\ln\left(\frac{\omega_{\mathrm{pp}}\tau_{\mathrm{L}}}{\sqrt{2e_{\mathrm{E}}}} + \sqrt{1 + \frac{\omega_{\mathrm{pp}}^2 \tau_{\mathrm{L}}^2}{2e_{\mathrm{E}}}}\right)\right]^2. \qquad (2.68)$$

Here, the maximum energy of protons accelerated from the rear side of the target, $E_{\mathrm{p,rear}}$, only depends on the laser-pulse duration, τ_{L}, the hot-electron temperature, T_{e}, and the initial hot-electron density, n_{e0}, at the target-rear surface. For the same parameters that were used before to estimate the maximum proton energy from the target-rear side, eq. (2.68) yields to a maximum energy of 4.5 MeV, which is smaller by more than a factor of 2 compared to the case, where a constant electric field was assumed. This shows that a correct description of the rear-side proton acceleration has to take into account the real evolution of the electric field including shielding effects by the expanding proton distribution itself.

The proton-energy spectrum predicted by the self-similar solution has the following form [86]:

$$\begin{aligned}\frac{\mathrm{d}N_{\mathrm{p}}}{\mathrm{d}E_{\mathrm{p}}} &= n_{\mathrm{i0}} \cdot \frac{c_{\mathrm{s}} t}{\sqrt{2k_{\mathrm{B}} T_{\mathrm{e}} E_{\mathrm{p}}}} \cdot \exp\left(-\sqrt{\frac{2E_{\mathrm{p}}}{k_{\mathrm{B}} T_{\mathrm{e}}}}\right)\\ &= \frac{n_{\mathrm{i0}} t}{\sqrt{m_{\mathrm{p}}}} \cdot \frac{1}{\sqrt{E_{\mathrm{p}}}} \cdot \exp\left(-\sqrt{\frac{2E_{\mathrm{p}}}{k_{\mathrm{B}} T_{\mathrm{e}}}}\right). \qquad (2.69)\end{aligned}$$

This energy spectrum would extend to infinite proton energies in the pure self-similar model and it would only increase in number for longer interaction times. However, as it was discussed above, the protons show a sharp energy cutoff due to the formation of a proton front during the acceleration process. Therefore, also the energy spectrum only extends up to the peak energy of the protons situated at the front. It was shown in [86] that the real spectrum calculated from simulations only weakly deviates from the self-similar solution, if it is assumed that the self-similar spectrum only extends to the cutoff energy.

Electron Populations with Two Temperatures

Up to now, the rear-side proton acceleration was assumed to be driven by a one-temperature electron distribution only. However, the laser-plasma interaction on the target front side is quite complex, as it was discussed above, and results in a total electron-energy spectrum having more than only one quasi-temperature. As also the modification of the electron spectrum during the passage of the electron beam through the target is a complex problem, numerical simulations are the only tool to approximately describe the propagation and the resulting electron spectrum at the target rear side that is responsible for the proton acceleration. To analytically estimate the influence of an electron spectrum exhibiting more than only one temperature, M. Passoni *et al.* [41] have investigated the effect of a two-temperature electron distribution on the initial field strength, $\mathcal{E}_0$, that drives the proton acceleration. Depending on the ratio of the quasi-pressures, $p_{\mathrm{cold}}/p_{\mathrm{hot}}$, of the electron populations, where $p_{\mathrm{cold}} = n_{\mathrm{cold}}T_{\mathrm{cold}}$ and $p_{\mathrm{hot}} = n_{\mathrm{hot}}T_{\mathrm{hot}}$, the authors conclude that even for the case of equal quasi-pressures, the hot-electron component dominates the initial electric field strength, $\mathcal{E}_0$. This is consistent with recent numerical simulations carried out by P. Mora, where the proton acceleration with a two-temperature electron population was investigated [89]. Here, the increase of the proton-peak energy due to the cold electron component was estimated to be of the order of 10% only. This allows to neglect the effect of a colder electron component, when $p_{\mathrm{cold}}/p_{\mathrm{hot}} \leq 1$ is satisfied. Considering an additional, hotter electron population (e.g generated by DLA) but with a significantly lower conversion efficiency (only a few percent compared to 25% for that one generated at the critical density), one can assume that this hotter population also has a negligible effect on the proton acceleration, because here $p_{\mathrm{cold}}/p_{\mathrm{hot}} \gg 1$ is fulfilled. For this case, the acceleration is dominated by the colder component, i.e. again that one accelerated at the critical density as described in section 2.2.1.

Concluding Remarks

Although the assumption that the rear-side acceleration terminates when the laser pulse is over might underestimate the maximum kinetic energies of the protons, the electric field quickly drops as both the electron temperature drops and also the rear-side density decreases, as the electrons, that oscillate through the target, quickly spread out sideways from the center of the electron beam, reducing the electron densities in the rear-side sheath. Finally, the electric field has already dropped significantly due to the expansion of the proton distribution when the laser pulse terminates. Taking all these aspects into account, it appears to be a good estimate that the main part of the proton acceleration occurs during the laser-pulse duration only.

This analytical description for the rear-side acceleration is only valid for an initially step-like proton distribution before the expansion starts. The reduction of the electric fields due to an initial ion-density scale length at the *rear side* of the target, as it can be formed by a prepulse-launched shock [37] or by a second laser beam incident on the target rear surface [42], cannot be taken into account. These effects are discussed in chapter 7, where a 1-D simulation code will be introduced that was developed during the course of this thesis to include such preplasma effects.

Chapter 3

Experimental Setup

This chapter describes the ATLAS laser system and the characterisation of the generated laser pulses used for the experiments of this thesis. After a short general description of the whole laser system and the target chamber, the wave-front correction by adaptive optics and the control of the prepulse pedestal are described in detail, as their implementation into the beamline was a major part of this work and indispensable for the experiments presented in chapter 5.

3.1 The Multi-Terawatt Titanium:Sapphire Laser System ATLAS

The experiments described in this thesis were carried out using the laser system ATLAS at Max-Planck-Insitut für Quantenoptik in Garching [90]. ATLAS is a 3-table-top solid-state laser system using titanium-doped sapphire crystals (Al_2O_3) as an amplification medium. Titanium:sapphire is well suited for the generation and amplification of ultra-short laser pulses due to its broad amplification bandwidth between 650 and 1050 nm. In an oscillator, pulses of a few nJ energy as short as 6.5 fs [91] have been obtained, the generation of mJ-laser pulses shorter than 10 fs has been demonstrated [92].

Pulses with much higher energies in the multi-terawatt (TW) or even petawatt (PW) regime [93] need to be amplified in a chain of several amplifiers. In the laser chain, the power and intensity of the pulses have to remain below the thresholds for self-phase modulation and small-scale self focusing to preserve the otical elements from damage. To reduce these quantities, either the diameter of the beam or its duration have to be increased. While the first method is limited by the size of amplification crystals that can be fabricated with good optical quality (in terms of doping homogeniety and surface flatness), the latter method is employed in the technique of chirped-pulse amplification (CPA) [1]. Here, the short pulses having a finite frequency bandwidth enter a grating stretcher, in which the different frequencies have to cover optical paths of different length. Such a stretcher imprints a so-called positive chirp onto the pulse, i.e. the pulse components with lower frequencies leave the stretcher earlier than the high-frequency components. While the spectral shape of the pulse remains unchanged, its duration is increased by up to 5 orders of magnitude. The power and intensity of the pulses are reduced by the same factor. After the amplification, the pulses enter a grating compressor that imprints a negative chirp onto the pulses that exactly cancels the positive chirp from the stretcher. Gain narrowing during the amplification process prevents from reaching the original pulse duration after

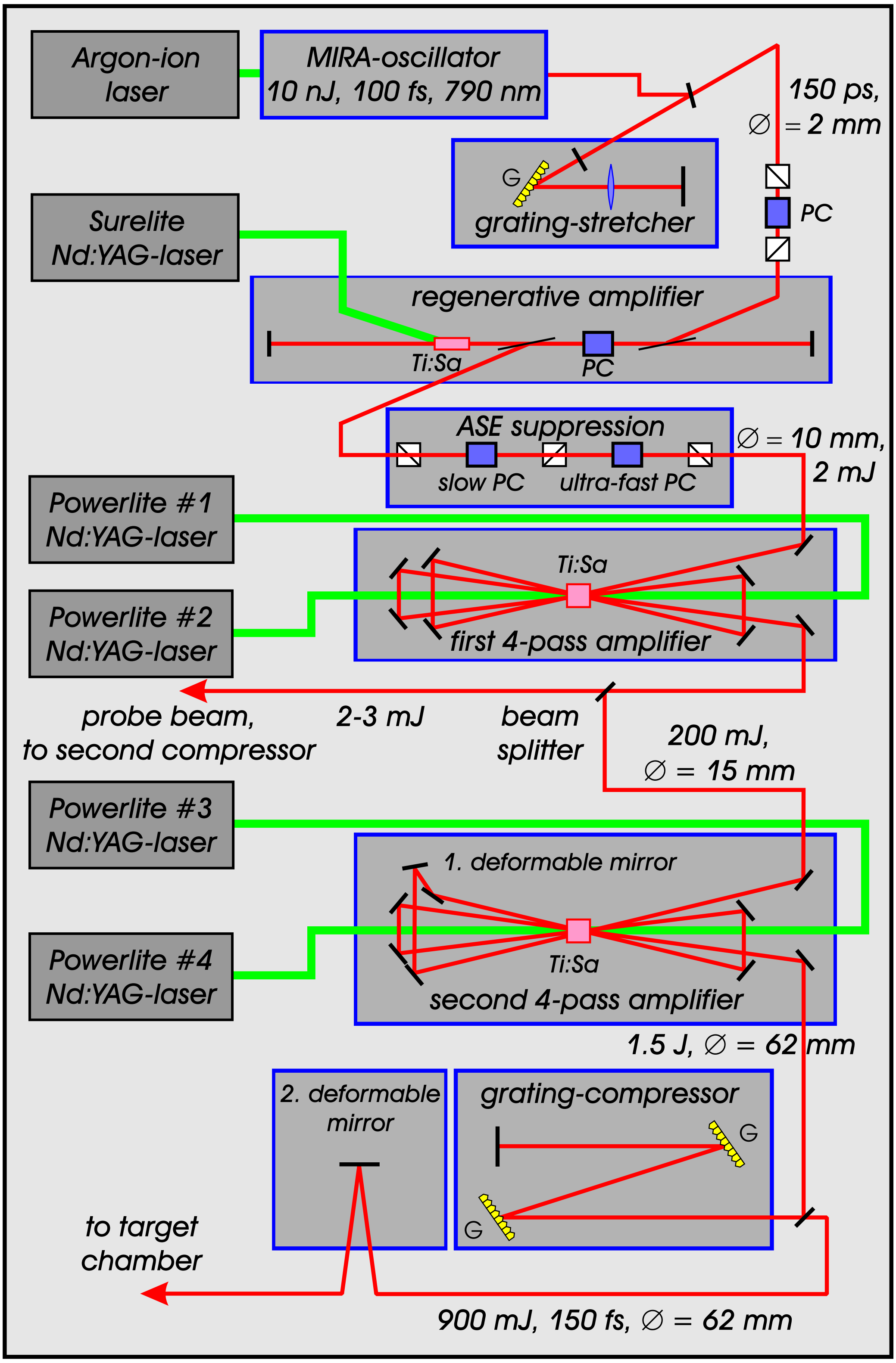

Figure 3.1: Schematic setup of the CPA-based laser system ATLAS. The diameters and energies characterise the laser pulse at the different amplification stages.

recompression. At output energies between several 100's of mJ and several 10's of J, a duration of $\sim 25\,\mathrm{fs}$ appears to be practically reliable [3, 94, 95], reaching peak powers close to 1 PW[1].

Based on the principle of CPA, ATLAS generates output laser pulses of $\tau_\mathrm{L} = 130...160\,\mathrm{fs}$ duration (FWHM) delivering an energy of up to $E_\mathrm{L} = 900\,\mathrm{mJ}$ onto the target resulting in peak powers exceeding 6 TW. A system of two adaptive mirrors enhaces the focusability of the laser pulses and allows nearly diffraction-limited focal spots with peak intensities in excess of $10^{19}\,\mathrm{W/cm^2}$ [49]. Furthermore, ATLAS is the first laser system that allows a controlled variation of the prepulse pedestal. While producing moderate pulses in terms of pulse duration, output energy, and peak intensities, ATLAS is a highly reliable laser system well suited for systematic studies of relativistic laser-plasma physics.

The laser is built in modules comprising a fs-pulse oscillator (COHERENT MIRA 900), a four-pass grating stretcher, three amplification stages, and finally an evacuated four-pass grating compressor. After their recompression, the amplified laser pulses are transported to the experiments through an evacuated tube system. Movable mirrors allow the guiding of the pulses into different vacuum chambers. Here, the pulses are focused to a micrometer spot by a high-quality off-axis parabolic mirror to achieve the highest possible intensities on the target. Fig. 3.1 shows the schematic setup of ATLAS.

Oscillator and Grating Stretcher

In the front-end of ATLAS, a 76-MHz train of laser pulses of 100-fs duration and 10-nJ pulse energy is generated in a commercial Kerr-lens mode-locked oscillator [96], that is pumped by an Argon-ion laser. After stabilising the beam pointing with a closed-loop system consisting of two pairs of quadrant detectors and piezo-driven mirrors, the pulses enter a four-pass grating stretcher, where their duration is increased by a factor of 1.5×10^3 to 150 ps. After the stretching and before the pulses are amplified in the subsequent stages of the laser, pulses at a repetition rate of 10 Hz are picked out of the initial 76-MHz train by a Pockels cell (PC) located between two crossed polarisers.

Regenerative Amplifier and Prepulse-Control Unit

The first amplification stage is a regenerative amplifier built in the form of a linear laser cavity. The vertically polarised laser pulses are deflected into the cavity by a polarising beam splitter. A PC located behind this first beam splitter rotates the plane of polarisation of the pulses by 90°, that can now pass a second polarising beam splitter behind the PC without being reflected. The pulses make 13 round-trips in the cavity being amplified by more than 5 orders of magnitude to an energy of 2 mJ. At appropriate time, the PC again rotates the plane of polarisation by 90°, and the pulses are reflected out of the cavity by the second polarising beam splitter.

---

[1] Another approach to generate PW-laser pulses is realised in large-scale CPA-Nd:Glass laser systems. Due to the relatively narrow bandwidth of this amplification medium, the pulse durations are significantly longer (between 400 fs and 1 ps), but the achievable energies are in the range of several 100's of J [2,4,27].

After the regenerative amplifier, the pulses pass two Pockels cells again located between crossed polarisers, that strongly reduce the prepulse pedestal originating from amplified spontaneous emission (ASE) generated in the regenerative amplifier. This prepulse-control unit will be described in section 3.3.

Multi-Pass Amplifiers and Grating Compressor

Then the ASE-cleaned laser pulses enter two four-pass disk amplifiers, where they reach their final energy. After the first multi-pass stage, where the pulses are amplified to an energy of 340 mJ having a Gaussian spatial fluence distribution, the outer regions of the beam are cut off by an 8-mm aperture and further amplified in the second multi-pass stage in order to obtain a top-hat like spatial beam profile. Due to the poor optical quality of the final titanium:sapphire crystal, that produces a near-field beam profile with two sharp intensity peaks, the first deformable mirror is installed into the second multi-pass amplifier, significantly smoothing the fluence pattern. After the amplification, the pulses are recompressed by a four-pass grating compressor to a final duration of 150 fs.

Before the amplified and recompressed laser pulses are guided into the target chamber, the pulse wave front, that shows strong aberrations due to the amplification process in the last amplifier and to the smoothing of the near-field fluence pattern by the first DM, is corrected by a computer-controlled closed-loop system consisting of a Shack-Hartmann wave-front sensor and a second DM. The two deformable mirrors and their effect on the optical properties of the laser pulses will be described in detail in section 3.2.

The laser pulses lose a significant part of their energy on their way from the last amplifier to the target. Due to reflection losses mainly in the grating compressor only 60% of the pulse energy is delivered onto the target. A laser pulse of initially 1.5-J energy entering the compressor delivers an energy of only 900 mJ onto the target that can be used in the experiment.

Setup in the Target Chamber

Coming from the compressor chamber and the second deformable mirror, the laser pulses of 62-mm diameter are guided through an evacuated tube system over movable mirrors into different target chambers. The compressor chamber, the tube system, and each vacuum chamber are equipped with separate pump systems, each producing a vacuum pressure below 10^{-5} mbar. In the target chamber, the laser pulses are deflected under an angle of 30° to the horizontal plane by a last plane mirror, before they are focused by a 4"-off-axis parabolic mirror with an effective focal length of 162 mm onto thin foils that are glued onto a target holder. Two synchronised probe beams of 790-nm and 395-nm wave length pass the target parallel to its surface from the side. The laser-target interaction area is side-imaged by a $f/4-$lens with a magnification of $\sim$10 onto two CCD cameras separated by a dichroic mirror. This allows a positioning of the target front surface with respect to the main-pulse focus within an accuracy determined by the spatial resolution of the side-view image, which is $\approx 10\,\mu$m. The setup of these two probe beams and the possibility to measure the electron density of a preformed plasma on the target front surface is described in Appendix A. The paths of the different laser beams in the target chamber are shown in Fig. 3.2.

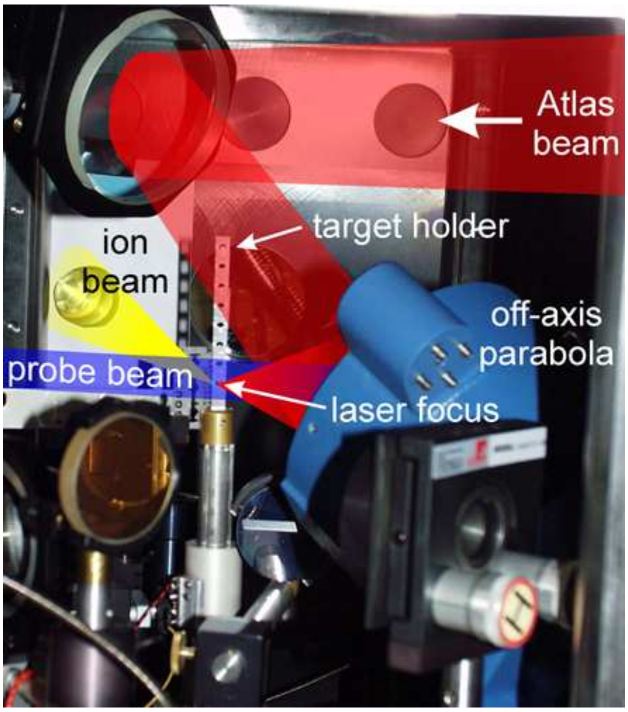

Figure 3.2: Setup in the vacuum chamber. The ATLAS-pulses indicated by the red beam, are deflected by a last plane mirror (top left corner) onto the off-axis parabola, which is seen from the back. The laser pulses are focused onto thin foils that are glued onto the target holder. The target is side-illuminated by two synchronised probe beams (coming from the left) that can be used to position the target and to measure preplasma formation on both target surfaces. The ion beam accelerated from the target is depicted by the yellow cone emerging from the target. Behind the hole in the rear chamber wall, a Thomson parabola detects the ion beam.

For an ideal top-hat like near-field profile with a plane wave front, the radius, r_f, of the first Airy disk in the focal plane is determined by the beam diameter, D_L, the focal length of the focusing optics, f, and the laser wave length, λ_L [97]

$$r_\mathrm{f} \approx 1.22 \cdot \frac{f}{D_\mathrm{L}} \lambda_\mathrm{L} \approx 2.5\,\mu\mathrm{m}. \tag{3.1}$$

The confocal parameter of the laser focus in vacuum, which is twice the Rayleigh length, x_R, is given by

$$2 \cdot x_\mathrm{R} = 2 \cdot \frac{\pi r_\mathrm{f}^2}{\lambda_\mathrm{L}} \approx 50\,\mu\mathrm{m}. \tag{3.2}$$

Within the confocal parameter, the laser intensity is reduced by a factor of 2 compared to the peak intensity exactly in the focal plane. Again for an ideal top-hat like beam, a fraction of $\approx 84\%$ of the total pulse energy is contained within this first Airy disk. An averaged intensity, I_L, is obtained from dividing the fraction of energy, ηE_L, contained within the inner Airy disk by the product of the disk area, πr_f^2, and the pulse duration, τ_L:

$$I_\mathrm{L} = \frac{\eta E_\mathrm{L}}{\tau_\mathrm{L} \cdot \pi r_\mathrm{f}^2}. \tag{3.3}$$

Compared to this averaged intensity, the peak intensity in the center of the inner focal spot is higher by a factor of ≈ 4.38. However, the laser pulses delivered by ATLAS are neither ideally top-hat like, nor Gauss-shaped. A detailed characterisation of the pulses and the focusability is presented at the end of the next section.

3.2 Improvement of the Optical Quality of the Laser Pulses using Adaptive Optics

In this section, we will describe the method of improving the optical quality of the amplified laser pulses in order to obtain as high laser intensities on the target as possible. In a first step, the near-field fluence distribution has to be flattened and, in a second step, the wave-front abberations have to be eliminated. This is done by means of two deformable mirrors.

3.2.1 Smoothing of the Near-Field Beam Profile

Due to severe growth defects and doping inhomogenieties in the final 40-mm disk amplifier of ATLAS 10, the quality of the amplified laser pulses is quite poor. In the near-field beam profile two intensive peaks show up as it can be seen in Fig. 3.3 (a). When the pulses are amplified to an energy of 1.4 J before they enter the vacuum compressor, the laser fluence within these peaks exceeds $\sim 300\,\mathrm{mJ/cm^2}$. This peak fluence lies well above the damage threshold of $150\,\mathrm{mJ/cm^2}$ of the compressor gratings. Under these conditions, the energy of the laser pulses transmittable through the compressor is limited to 0.5 J to preserve the gratings from damage. This reduction of the pulse energy in turn significantly reduces the laser performance.

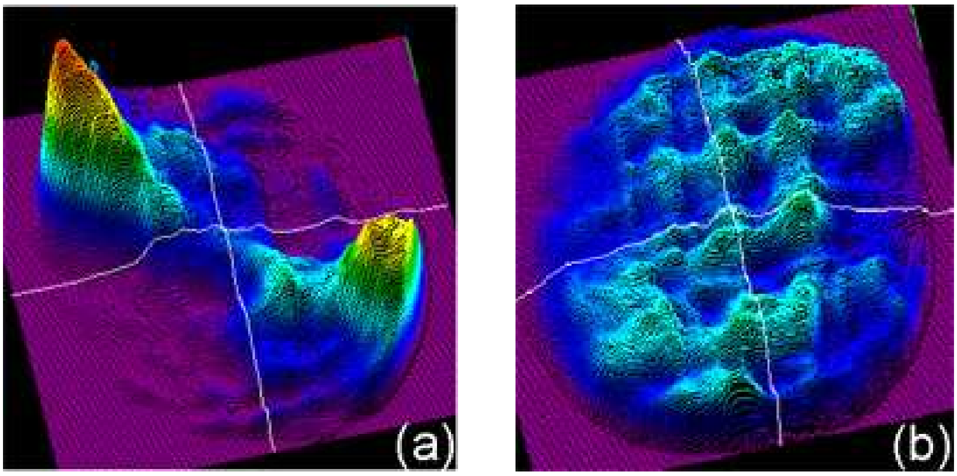

(a) Near-field profile without DM1 (b) Near-field profile with DM1

Figure 3.3: Near-field profiles of the ATLAS pulse in the plane of the last compressor grating. While in (a) no adaptive optics are used, resulting in two strong peaks with fluences of $\sim 300\,\mathrm{mJ/cm^2}$, the profile in (b) is significantly flattened to peak fluences of $\sim 90\,\mathrm{mJ/cm^2}$ by means of a first deformable mirror.

To smooth the near-field profile of the laser pulses, a first bimorph deformable mirror (DM) was installed just before the final pass of the laser pulse through the 40-mm disk amplifier, as it is sketched in Fig. 3.1. This first DM with a diameter of 30 mm has 17 active piezo electrodes. By applying voltages between -300 V and $+200$ V to the different electrodes, the surface of the mirror can be deformed locally. This changes the fluence distribution in the near-field profile in a plane of the last compressor grating (which is ≈ 11 m downstream in the laser chain) and it can be controlled on-line by a CCD camera. As a result, the strong peaks in the beam profile are flattened and the profile is nearly top-hat like as it is shown in Fig. 3.3 (b). With this fluence pattern, the laser pulses can enter the compressor with a maximal energy of up to 1.5 J without damaging the gratings.

3.2.2 Correction of the Laser-Pulse Wave Front

On the other hand, the profile is flattened at the expense of additional wave-front distortions of the laser pulses leading to a very poor focusability. Fig. 3.4 shows the fluence distribution in the focal plane as it is optained, when the first DM is optimised to give a flat beam profile as shown in Fig. 3.3 (b).

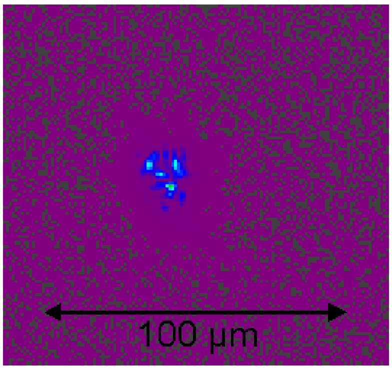

Figure 3.4: Fluence distribution of the laser pulses in the focal plane of the off-axis parabolic mirror in the target chamber. The first DM is optimised to obtain a smooth fluence pattern, but due to the strongly disturbed wave front, the focusability is quite poor and the pulse energy is scattered over a large area in the focal plane, resulting in low peak intensities.

To obtain laser pulses with a plane wave front and thus an improved focusability, the wave-front distortions have to be measured and then corrected in a controlled manner. This is done in the ATLAS laser by a closed-loop system consisting of a Shack-Hartmann sensor and a second computer-controlled DM. In the Shack-Hartmann sensor, the laser beam passes through a 2-D array of small lenses. Each lens focuses a small local part of the beam onto a computer-read CCD resulting in a 2-D pattern of focal spots in the plane of the CCD chip. Any local wave-front distortion of the laser beam causes a sideways shift of the associated spot in the focal plane. After the focal-spot pattern of an expanded beam from a 790-nm laser diode of 75 mm diameter with a wave-front distortion smaller than $\lambda/20$ was taken as a reference pattern, the wave-front distortion of any other laser beam can be quantified with this sensor by comparing its focal spot pattern with the pattern of the reference beam.

The wave-front abberations in the ATLAS pulses are corrected by a second DM located behind the compressor in the evacuated tube system. This bimorph mirror of 80-mm diameter has 33 active piezo electrodes. The voltages applied to each of these electrodes are controlled by the same computer, that is connected to the Shack-Hartmann sensor. First, the response of the wave front on changes in the voltage applied to each single electrode of the DM is determined. After that, the necessary voltages for all the electrodes to correct the focal-spot pattern and therefore the wave front are calculated by the computer and applied to the second DM. In the next iteration, the corrected wave front is again measured and compared to the reference. From this new difference, the new voltages for the DM are calculated. This iterative algorithm converges after three or four steps. Then the set of voltages is fixed and the flatness of the wave front, which is of the order of $\lambda/4$, remains constant for hours within small shot-to-shot fluctuations of the laser. The drastic improvement of the laser-pulse focusability is demonstrated in the next section.

As mentioned above, the near-field (NF) intensity distribution[2] of ATLAS is not exactly top-hat like but shows a less steep decay at the edges of the profile, as it is shown in Fig. 3.3 (b). To quantitatively investigate the influence of such a NF profile on the far-field (FF) intensity distribution, the NF profile was averaged within concentrical rings giving an averaged NF intensity distribution, $I_{\mathrm{NF}}(r)$, only depending on the radius, r. The associated electrical field distribution, $\mathcal{E}_{\mathrm{NF}}(r) \propto [I_{\mathrm{NF}}(r)]^{1/2}$, is shown by the red line in Fig. 3.5 (a). For such a radially symmetric NF distribution, that can be described by $\mathcal{E}_{\mathrm{NF}}(r)$, the FF distribution of the electrical field, $\mathcal{E}_{\mathrm{FF}}(\rho)$, is obtained from the following integration [97]

$$\mathcal{E}_{\mathrm{FF}}(\rho) \propto \frac{1}{\rho^2} \int\limits_{w=0}^{w=\infty} \mathcal{E}_{\mathrm{NF}}(w) \cdot w \cdot J_0(w)\, \mathrm{d}w, \tag{3.4}$$

where $w = 2\pi\rho r/f\lambda_{\mathrm{L}}$ is the normalised radius in the NF and $J_0(w)$ is the Bessel function (of the first kind) of order zero. This calculation only holds true for an ideally flat wave front. For a top-hat like profile, eq. (3.4) can be solved analytically and one obtains the Airy pattern. The NF distribution of ATLAS is shown in Fig. 3.5 (a) by the red line compared both to a top-hat profile (black line) and a Super-Gaussian approximation of 6th order (blue line). The FF distributions of the electric field for the three different NF profiles are given in Fig. 3.5 (b). A weak dependence on the initial NF distribution is found for the three cases. The radius of the first minimum differs from 2.5 μm for the top-hat profile to 2.6 μm for the real profile. For the real ATLAS-profile a peak intensity in the center of the focal spot is found that is higher by a factor of ≈ 4.78 compared to the intensity averaged over the area within the first minimum. A 2-D Fourier transformation of the NF distribution carried out by R. Tommasini [98] gives the theoretical FF distribution of the laser pulse, that is shown in Fig. 3.6. This distribution is not exactly radially symmetric, as the NF profile also deviates from radial symmetry. However, the radii of the minima are well reproduced by the symmetrical approximation as depicted in Fig. 3.5 (b).

From these considerations, we can conclude that a top-hat approximation for the NF distribution of the ATLAS pulses is sufficient to derive the FF distribution and to calculate the laser intensity.

---

[2] For the spatial distribution pulse intensity and fluence are equivalent, the latter is the first time-integrated over the pulse duration.

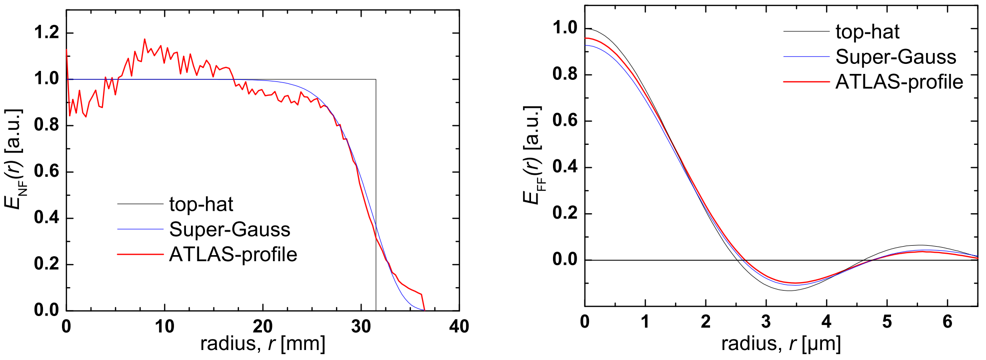

(a) Near-field intensity distributions (b) Far-field intensity distributions

Figure 3.5: Comparison of the radial electrical field distributions of the near-field of ATLAS (red line) with a top-hat like (black line) and a Super-Gaussian distribution of 6th order (blue line) in (a). (b) gives the corresponding radial distributions of the electrical field in the far field. The radii of each first minimum in the far-field distributions differ between 2.5 μm for the top-hat profile and 2.6 μm for the real profile.

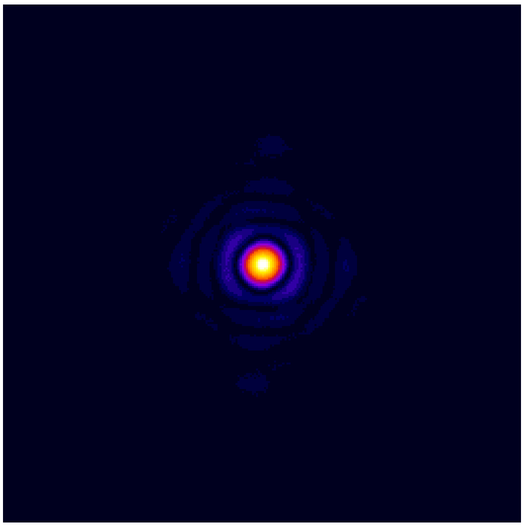

Figure 3.6: Theoretical far-field distribution calculated from the ATLAS profile shown in Fig. 3.3 (b) assuming a flat wave front.

3.2.3 Measurement of the Intensity Distribution in the Focal Plane

For the measurement of a fluence distribution in the laser focus as they are shown in Figs. 3.4 and 3.7, the laser pulses were guided into the target chamber and focused by the f/2.6 off-axis parabolic mirror as in the real experiment. A high-quality $f/2-$lens imaged the focal plane with a magnification of ~ 50 onto an 8-bit CCD. To increase the dynamical range of this measurement, differently filtered images of the focus were subsequently taken. After these measurements, the images were added, taking into account the different filter transmissions and thereby increasing the dynamical range of the measurement to more than 12 bits.

As on the one hand the imaging lens cannot sustain the high fluences occuring with the

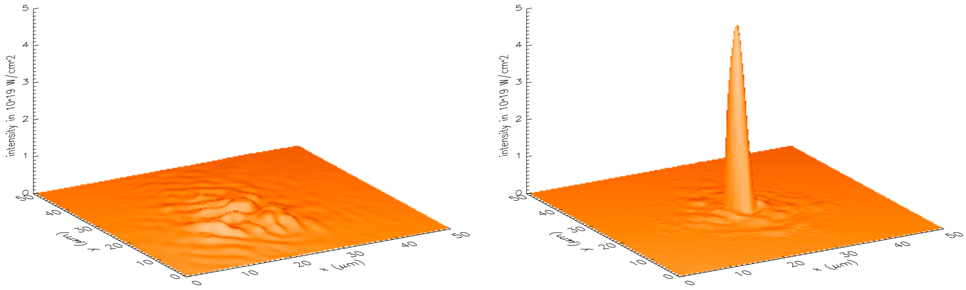

(a) Focal intensity distribution without CL

(b) Focal intensity distribution with CL

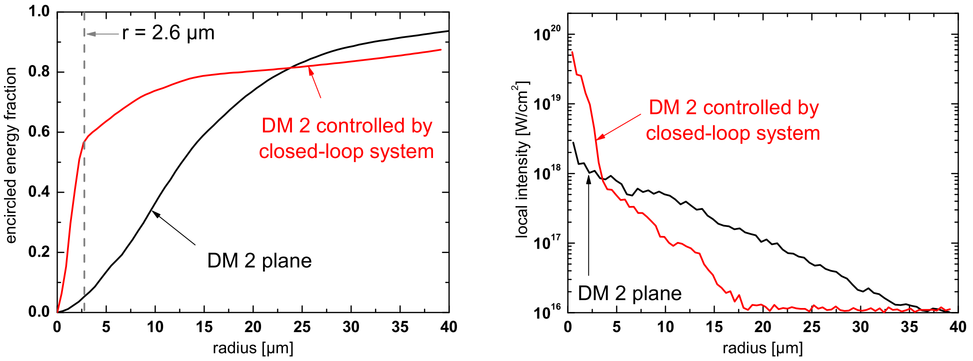

(c) Encircled fraction of total energy within a certain radius

(d) Local laser intensity

Figure 3.7: Comparison of the far-field intensity distributions in the focal plane, (a) and (b), the fraction of energy encircled within a certain radius (c), and the local intensities (d) for a plane second DM and for the case of DM 2 controlled by the closed-loop system described in the text. For pulses of 150-fs duration and 900-mJ energy on the target, the intensities are given in units of $10^{19}\,\mathrm{W/cm^2}$ in (a) and (b). In (b), the intensity averaged over the first Airy-disk ($r_\mathrm{f} = 2.6\,\mu\mathrm{m}$) is $1.7 \times 10^{19}\,\mathrm{W/cm^2}$.

full laser energy but on the other hand the wave-front distortions become maximal only when the pulses are fully amplified, a mirror with a high-reflecting coating located behind the final multi-pass amplifier was replaced by an uncoated wedge with a reflectivity of only $\sim 2\%$. Most of the laser pulse energy was transmitted through this wedge into a beam dump. Due to the tilt between the two wedge surfaces, the rear-side reflection was deflected under a different angle and thus could not enter the compressor chamber avoiding any ghost images. By this technique, the fluence in the imaging lens was reduced without changing the wave-front distortions of the fully amplified laser pulse. This enabled us to measure the equivalent focal-intensity distribution of a full-energy laser shot.

The fluence distributions in the focal plane were first measured with a plane second DM (the first DM was always in operation) and then with the voltages determined by the closed-loop system applied to DM 2. The measurements are shown in Fig. 3.7 (a) and (b). Fig. 3.7 (c) and (d) compare the fraction of the total laser-pulse energy encircled within a certain radius and also the local intensities in the focal plane for the two different cases.

While in (a), the laser-pulse energy is scattered over a large area resulting in several small peaks with low intensities, the energy in (b) is concentrated within a single narrow peak having only a weak low-intensity halo around it. The fraction of laser energy encirceled within a spot of 2.6-μm radius, which corresponds to the first Airy-disk in the focal plane[3], is increased from $\sim 5.5\%$ in (a) to $\sim 60\%$ in (b), the peak intensity is increased by a factor of ~ 20 to a peak value approaching $6 \times 10^{19}\,\mathrm{W/cm^2}$ and an intensity averaged over the first Airy-disk of $1.7 \times 10^{19}\,\mathrm{W/cm^2}$. The measured peak value gives a Strehl-ratio[4] of ~ 0.7. The corresponding averaged intensity for the case of a second DM corrected to be plane is only $1.6 \times 10^{18}\,\mathrm{W/cm^2}$. Note that all these intensities correspond to normal incidence of the laser pulse onto the target. They are reduced for oblique incidence under the angle α by a factor of $\cos\alpha$.

3.3 Control and Characterisation of the ASE Pedestal

In present CPA-laser systems as ATLAS, amplified spontaneous emission (ASE) from the pumped amplification crystals generates a low-intensity prepulse pedestal underneath the short high-intensity pulse. The main contribution to this pedestal originates in the oscillator and the regenerative amplifier, and it is further amplified in the laser chain. Usually extending over several ns, the ASE pedestal is incoherent and passes the grating compressor unchanged typically resulting in an on-target intensity ratio of the order of 10^7 between main pulse and prepulse pedestal. When the main pulse is focused onto the target to intensities in excess of $10^{19}\,\mathrm{W/cm^2}$, the pedestal reaches an intensity of the order of $10^{12} \ldots 10^{13}\,\mathrm{W/cm^2}$ on a time scale of several ns preceding the peak intensity. This is sufficient to preheat and ionise the surface of a solid target producing an expanded plasma on the target-front side. In addition, a shock wave is launched by the ASE prepulse that propagates through the target, preheats the bulk of the material and – especially with thin foils – destroys the target before the main pulse arrives at the surface, what is highly unwanted. We will concentrate on this fact and its consequences for experiments in a later chapter. Therefore, the characterisation of the prepulse pedestal is of great importance for precise laser-plasma experiments. Intensity and especially the duration of the ASE prepulse have to be known or – even better – controlled as accurately as possible.

Within the framework of this thesis, the characterisation and controllability of the prepulse pedestal in ATLAS was significantly enhanced by implementing an additional ultrafast Pockels cell into the laser chain. This enabled us for the first time to do systematic studies of prepulse dependent effects on the acceleration of protons and ions from thin foils [47]. While the results from these measurements will be presented in chapter 5, we will describe the setup of the Pockels cell and demonstrate its effect on the ASE pedestal in the next sections.

---

[3] Here we used the far-field distribution associated to the real near-field profile of ATLAS.

[4] The Strehl-ratio is defined as the ratio between real peak intensity and theoretical peak intensity, which is 4.78-times higher than the averaged intensity as we have shown above.

3.3.1 Pockels Cells used as Optical Shutters

To reduce the intensity and duration of the pedestal preceding the main pulse, appropriately gated Pockels cell (PC) shutters are used in the laser chain. A PC contains an uniaxial electro-optical crystal (e.g. Potassium di-Hydrogen Phosphate, KDP) with the optical axis aligned along the direction of laser propagation. It becomes an optically biaxial crystal, when an external voltage is applied along the optical axis. For a certain voltage, $U_{\lambda/2}$ of the order of 5 kV, the crystal acts like a $\lambda/2$-wave plate for the wave length λ, rotating the plane of polarisation of the incident light wave by 90°. If the PC is positioned between two crossed polarisers, it can be used as an optical shutter. The incoming light wave passes the first polariser (e.g. a Glan prism) and the PC. It is blocked by the second polariser when no voltage is applied to the PC, but it can pass when the voltage matches $U_{\lambda/2}$. In a laser system, $U_{\lambda/2}$ is applied by means of a high-voltage (HV) pulser just before the arrival of the main pulse. The preceding ASE pedestal is blocked and only the main pulse can pass, as its polarisation is rotated by the PC. Nevertheless, the minimal duration of the pedestal preceding the main pulse is limited by the following factors:

- The optical shutter has to be opened completely before the main pulse passes through to avoid its clipping. Therefore, the *electronic* rise time of the HV signal applied to the crystal is a lower limit for the minimal duration of the ASE pedestal.
- The *optical* rise time of the PC scales with the diameter of the electro-optical crystal, additionally increasing the *total* opening time of the optical shutter.
- As the PC is located at a position in the laser chain, where the main pulse is still stretched to $\sim$150 ps to avoid optical damages in the material, the pedestal within this time window cannot be reduced without clipping a part the main pulse. After recompression, which leaves the incoherent pedestal unchanged, the main pulse sits in the middle of this pedestal, which then starts $\sim$75 ps before the peak intensity.
- The suppression factor of a single PC is limited to $\sim 500 \ldots 1000$ due to non-ideal polarisation and parallelism of the incoming laser beam.

3.3.2 System of Pockels Cells in ATLAS

In ATLAS two PCs are used to control the ASE pedestal preceding the main pulse. The setup is sketched in Fig. 3.8. While PC 3 is controlled by a slow HV pulser having a signal-rise time of $\sim 5 \ldots 6$ ns, an ultra-fast HV pulser (KENTECH Pulse Generator GPS3/S [99]) is used for PC 4. It delivers a rectangular HV signal with a rise time of $\sim$120 ps and a duration of 5 ns. The total rise time of the optical gate is increased to $\sim 250 \ldots 300$ ps due to the finite diameter and response time of the PC, the duration of the gate is increased to 6 ns. Due to the jitter of the electronic trigger for the KENTECH pulser ($\tau_{\text{jitter}} \sim 150$ ps), the duration of the pedestal was chosen to be longer by τ_{jitter} to avoid clipping of the main pulse at the expense of shortening the prepulse. After recompression, the minimum achievable duration of the ASE pedestal at an intensity level of $\sim 10^{12}\,\mathrm{W/cm^2}$ on the target

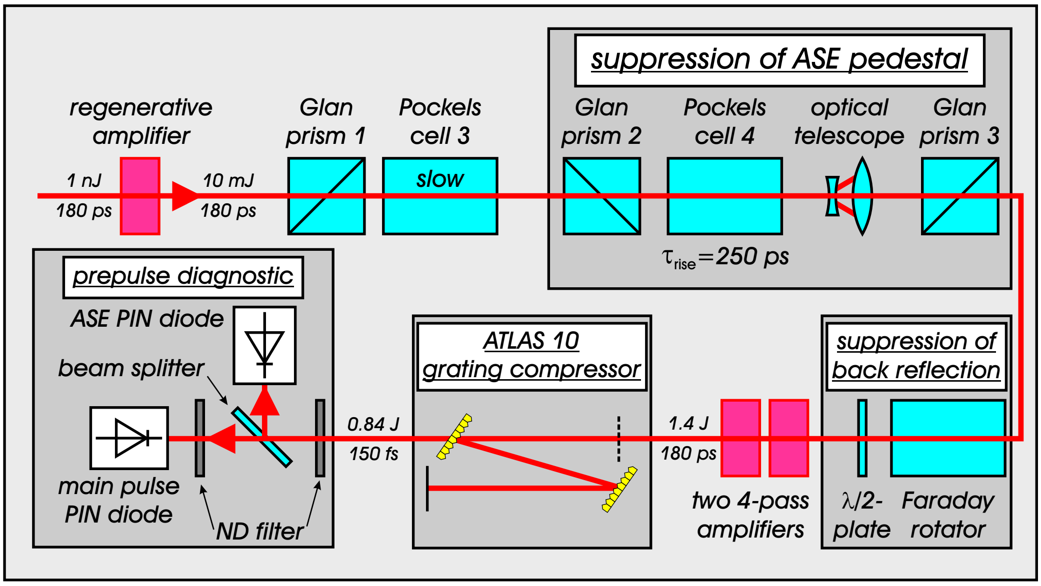

Figure 3.8: Setup of the ASE-suppression system using a combination of different Pockels cells and polarisers in the ATLAS laser. The prepulse diagnostic consists of a pair of differently filtered PIN diodes connected to a fast oscilloscope.

was therefore

$$\tau_{\mathrm{ASE,min}} = (500 \pm 150)\,\mathrm{ps}.$$

It is preceded by a 6-ns ASE pedestal with an intensity ratio below 10^{-10} due to the finite suppression level of the ultra-fast PC. This results in an intensity of $\sim 10^9\,\mathrm{W/cm^2}$ on the target, which can be neglected for preplasma creation [100]. The intensity evolution on the target is depicted in Fig. 3.9.

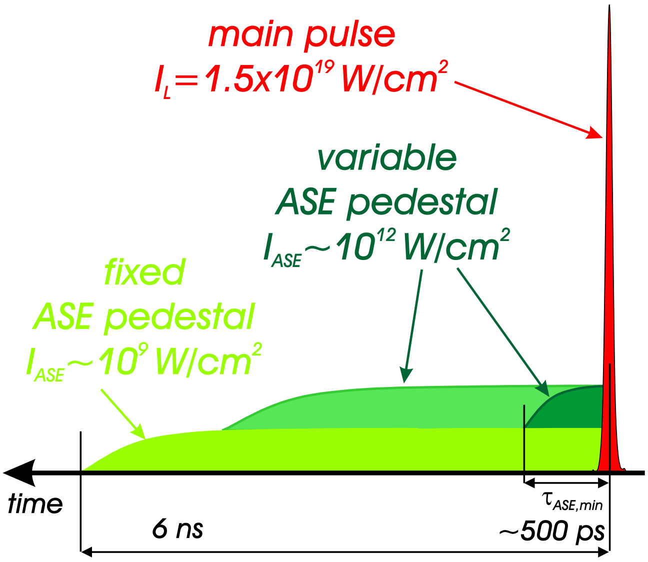

Figure 3.9: Schematic intensity evolution on the target after suppression of the pedestal with two Pockels cells (PCs). The main pulse (red) is preceded by a variable ASE pedestal (dark green) with an intensity of $\sim 10^{12}\,\mathrm{W/cm^2}$. This pedestal has a minimum duration of $\tau_{\mathrm{ASE,min}} \sim 500 \pm 150\,\mathrm{ps}$, and its duration can be increased up to 6 ns. As the ultra-fast PC reduces the pedestal only by a factor of ~500, the variable ASE pedestal is preceded by a fixed ASE pedestal (light green) with an intensity of $\sim 10^9\,\mathrm{W/cm^2}$ and a duration of 6 ns.

By changing the trigger delay for the KENTECH pulser with respect to the main laser pulse, the duration of the variable ASE pedestal at an intensity level of $\sim 10^{12}\,\mathrm{W/cm^2}$ on the target could be varied in steps of 100 ps between the minimum value of 500 ps and the maximum value of ∼6 ns.

3.3.3 Measurement of Level and Duration of the ASE Prepulse

The prepulse level and its temporal evolution were measured with a combination of two Centronic AEPX 65 PIN diodes [101], which were separated by a beam splitter as it is sketched in Fig. 3.8. The diodes were connected to a fast oscilloscope (a 1-GHz Tektronix TDS 684 B with a sampling rate of 5 GS/s [102]). The part of the laser beam entering the "main-pulse" PIN diode was sufficiently strong filtered, that the main pulse could be recorded without overexposing the diode. The amount of filters in front of the "ASE" diode was reduced to record the energy level of the ASE pedestal, although the signal of the main pulse was strongly overexposed here. After adjusting the relative timing and sensitivity of the two diodes including the different filtering, time-resolved measurements of the energy ratio between main pulse and ASE pedestal were possible – at least within the time resolution of the combination of oscilloscope and PIN diodes ($\tau_{\mathrm{osci}} \approx 1.25\,\mathrm{ns}$). As the compressed pulses have a much shorter duration of $\tau_{\mathrm{L}} \approx 150\,\mathrm{fs}$ (FWHM), that cannot be resolved, the intensity level of the main pulse is higher by a factor of $\tau_{\mathrm{osci}}/\tau_{\mathrm{L}} \approx 8330$ multiplied with the inverse filter transmission. Assuming the same focusability of the ASE pedestal and the main pulse, the upper level for the intensity ratio on the target can be deduced from this measurement. It was found to be $2\ldots4\times10^{-8}$ just before the arrival

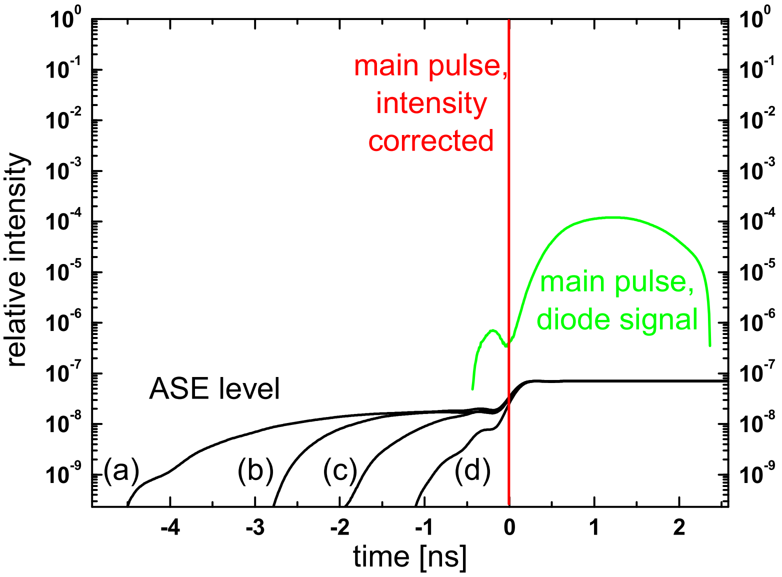

Figure 3.10: Measurement of the prepulse level with two PIN diodes for four different delays of the KENTECH pulser. The four black lines give the ASE levels for prepulse durations of 5.5 ns (a), which is the unsuppressed ASE level, 3.5 ns (b), 2.5 ns (c), and 1.5 ns (d). The green line gives the filter-corrected, the red line the filter- and intensity-corrected signal of the main-pulse diode.

of the main pulse. Results from the measurement are shown in Fig. 3.10.

As the rise time of the ASE pedestal was expected to be much shorter ($\sim 300\ldots500\,$ps) than the time resolution of the 1-GHz oscilloscope and the Centronic PIN diodes, we carried out a separate measurement with a 4-GHz oscilloscope (Tektronix CSA 7404 B [102]) having a sample rate of 20 GS/s and an extremely fast GaAs-PIN diode (ET-4000 [103]) together having a time resolution of $\sim 130\,$ps. In this measurement, the time-resolved increase of the prepulse intensity could be recorded, and the results are shown in Fig. 3.11.

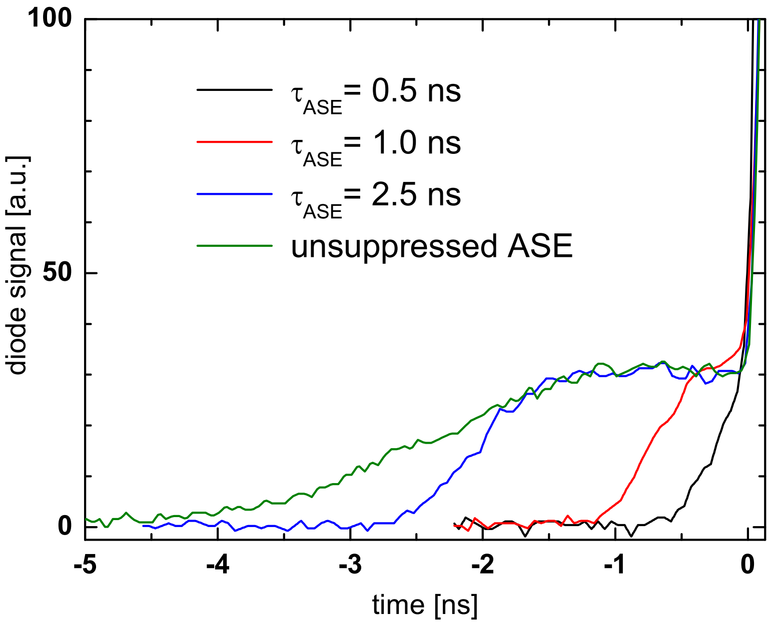

Figure 3.11: Temporal evolution of the ASE prepulse measured with a 4-GHz oscilloscope and a GaAs-PIN diode with four different trigger delays for the ultra-fast Pockels cell. The green line gives the unsuppressed ASE, the other three lines give the measured (solid) ASE evolutions for prepulse durations of $\tau_{\mathrm{ASE}} = 2.5\,$ns (blue), $1.0\,$ns (red), and $0.5\,$ns (black), respectively. The main pulse starts at $t = 0$.

For the shortest prepulse duration of $\tau_{\mathrm{ASE}} = 500\,$ps (solid black line), the rise time of the ASE pedestal is also on the order of $500\,$ps. The rise time appears to increase for longer prepulse durations, but the changes are only marginal. After the linear increase of the ASE intensity, it remains constant at an intensity level of $(2\ldots4)\times10^{-8}$ until the arrival of the main pulse increases the intensity by several orders of magnitude. For a prepulse duration of $2.5\,$ns (blue line), the rise time is increased to $\sim 1.0\,$ns, as the unsuppressed ASE level (green line) is also not constant.

Taking the results of these two measurements together, we could exactly characterise the temporal evolution of the ASE prepulse. The maximum ASE level is $(2\ldots4)\times10^{-8}$. The prepulse duration could be controlled by changing the trigger delay for the ultra-fast

PC. The rise-times for different trigger delays could be resolved and are approximately linear. This measurement allows an exact numerical modeling of the preplasma formation on both target surfaces. The corresponding simulations will be presented in chapter 6.

Chapter 4

Detection of Laser-Accelerated Protons and Light Ions in the Experiment

This chapter describes the diagnostics used in the experiments to characterise the ion beam formed during the interaction of the high-intensity laser pulse from ATLAS 10 with a thin foil. Three different diagnostics were employed:

1. the plastic nuclear track detector CR 39,
2. a time-of-flight (TOF) detector coupled to a fast oscilloscope, and
3. a Thomson parabola magnetic spectrometer.

These three different types of detectors will now be described in detail.

4.1 Ion Detection with CR 39 Nuclear Track Detectors

Preliminary measurements using a simple setup were performed to show that protons can be accelerated to MeV-energies in thin-foil experiments using the ATLAS 10 laser. For that purpose pieces of CR 39 were used to detect the protons. CR 39 is a solid state nuclear track detector fabricated of polymeric plastic. The pieces of CR 39 used in this thesis were produced by TASL in Bristol, UK [104]. When an energetic particle propagates through the plastic, it deposits certain amounts of its kinetic energy along its path in the material depending on the particle's cross-section and its momentary energy while it is decelerated and finally stopped. If the amount of locally deposited energy exceeds a certain threshold, the polymeric chains of the detector material break up at this position. Thus the energetic particle leaves a trace along its path in the material until it is stopped. As the cross-sections for electrons and γ-rays are much lower than that for ions, and as the locally deposited energy therefore remains below the threshold for chain break-up[1], the detector is sensitive to ion impacts only. Furthermore, protons with kinetic energies between 100 keV and 5 MeV leave significant traces at the front surface of the detector material, where they can

---

[1] This holds true as long as the flux of electrons and γ-rays is not too high. In the experiments reported on in this thesis, no detectable effect of electrons or γ-rays on CR 39 could be observed, as the fluxes were too low.

be detected afterwards. This predestines CR 39 as an ideal ion detector in laser-plasma experiments, as also very small ion signals can be detected within the "noise" generated by any other energetic radiation occurring in high-intensity interactions.

The most common way to make the ion hits visible is to etch the plastic in hot NaOH solution [105]. As the etching rates of the plastic differ between regions with undisturbed polymeric structure and regions where an ion broke up the polymeric chains, while it lost part of its kinetic energy, small pits on the scale of several μm are formed on the surface of the CR 39 plastic. These pits can easily be detected under an optical microscope [82].

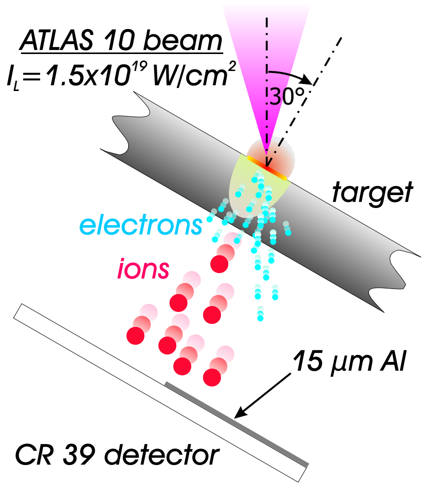

Figure 4.1: Setup for the preliminary detection of protons using CR 39 plates partly wrapped with a 15-μm aluminum foil standing ~9 cm behind the target. The minimum kinetic energies for the protons that can be detected by the two parts of the detector are 1 MeV and 100 keV for the wrapped and unwrapped part of the detector, respectively.

The experimental setup for the preliminary proton detection is shown in Fig. 4.1. The CR 39 plates were positioned ~9 cm behind the target around its normal direction. One part of the CR 39 was covered with a 15-μm aluminum foil, the other part remained unshielded providing a detector sensitive to protons with two different minimum energies. Using the CSDA stopping ranges of protons in aluminum published by the National Institute of Standards and Technology (NIST, [106]), the stopping ranges, d, for protons with kinetic energies, E_{kin}, between 300 keV and 4 MeV can be approximated by

$$d \approx 16\,\mu\mathrm{m} \times (E_{\mathrm{kin}}/1\,\mathrm{MeV})^{1.45}\,. \tag{4.1}$$

Thus the minimum proton energies detected by the CR 39 are 1 MeV and 100 keV for the shielded and unshielded part of the detector, respectively. The minimum proton energy detectable by bare CR 39 is determined by the threshold that has to be overcome to cause significant damage in the polymeric structure of the detector material.

Figure 4.2: Magnified picture of a CR 39 plate after etching. The left part was unshielded, the right part was covered with a 15-μm aluminum foil. While the left part is saturated with pits from ions with kinetic energies above 100 keV, in the right part single pits of 1 . . . 2 μm diameter can be distinguished.

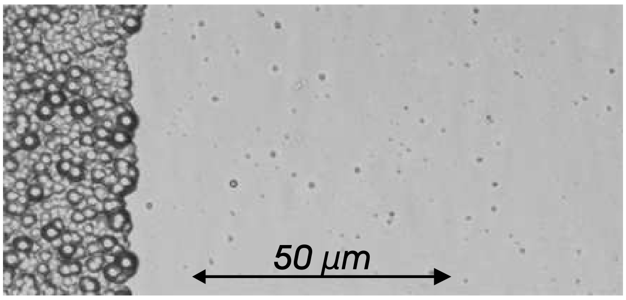

A magnified section of a piece of CR 39 is shown in Fig. 4.2. The plate has been etched for 2 hours in 6-molar NaOH solution at ~80°C. We show the boundary between the two differently shielded parts of the detector. The left side was unshielded and thus sensitive to any ion with a kinetic energy above 100 keV, the right side was wrapped with a 15-μm aluminum foil. In this part, single pits can be distinguished. They can only originate from protons with kinetic energies exceeding 1 MeV.

After this first experimental proof of the acceleration of MeV-protons with the ATLAS laser, a more precise diagnostic was needed to characterise the proton beam and its energy spectrum. For this purpose, we used a time-of-flight detector described in the next section.

4.2 Spectral Characterisation of the Ion Beam using a Time-Of-Flight Detector

4.2.1 Setup of the Detector

A time-of-flight (TOF) detector realised as a Faraday cup [107], as it is depicted in Fig. 4.3, is sensitive to the total electric current, $I(t_{\mathrm{TOF}})$, impinging at time t_{TOF} on the charge collector of the detector. The temporal evolution of the current can be recorded by means of an ultra-fast oscilloscope connected to the detector. As the detector is standing at a defined distance, d_{TOF}, from the target, where the ions are generated, the ions are temporally dispersed due to their different velocities, v_{i}, or kinetic energies, E_{kin}. If the flying time of the ions, t_{TOF}, is much longer than the time interval within which they are generated[2], we find a direct relation between E_{kin} and t_{TOF}:

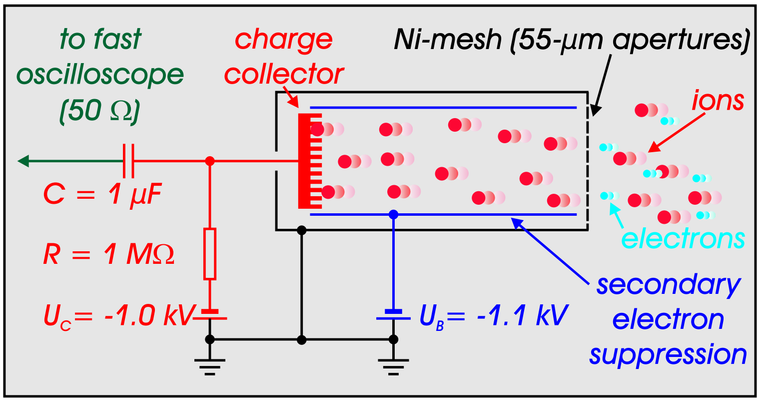

Figure 4.3: Schematic diagram of an ion TOF detector including a mesh to shield the charge collector against co-propagating electrons and a metallic cylinder to suppress the effect of secondary electrons generated at the charge collector.

$$E_{\mathrm{kin}} = \frac{m_{\mathrm{i}}}{2} \cdot {v_{\mathrm{i}}}^2 = \frac{m_{\mathrm{i}} \cdot d_{\mathrm{TOF}}^2}{2} \cdot t_{\mathrm{TOF}}^{-2}, \tag{4.2}$$

where m_{i} is the ion mass. As the maximum kinetic energies of the ions measured in the experiments are well below their rest mass (for protons with rest mass m_{p} we obtain $E_{\mathrm{max}} \sim 5\,\mathrm{MeV} \ll m_{\mathrm{p}}c^2 = 938\,\mathrm{MeV}$), the classical treatment is sufficient.

---

[2] The flying time of the ions for our detector setup is of the order of 10 ns and longer, as it will be shown below, while the generation time is of the order of the laser pulse duration, $\tau_{\mathrm{L}} = 150\,\mathrm{fs}$.

To record the positive ion current only, several technical precautions have to be taken. The ion beam flying away from the target is charge-neutralised by a co-propagating cloud of thermalised electrons, which have approximatly the same velocity. As the TOF detector is sensitive to the *total* current impinging on its charge collector, the ions have to be separated from the electrons. This is done by means of a 10-μm thick Ni-mesh with quadratic apertures of $55\,\mu$m that stands in front of the charge collector. It is connected to a high-voltage supply that generates a potential barrier of $1\,$kV between the mesh and the charge collector what is sufficient to hold back 1-keV electrons that co-propagate with protons having kinetic energies of up to $1.8\,$MeV.

As γ-rays and MeV-electrons generated in the laser-plasma interaction are not held back by this potential barrier, they can reach the charge collector and knock out *secondary electrons* from the collector material [108]. If these can leave the collector, a positive current is detected that is not generated by ions. To suppress these secondary electrons having kinetic energies of $\sim 50\ldots100\,$eV, the collector has a rake-like surface on a mm scale, to recollect secondary electrons immediately after their generation. Additionally, a long metallic cylinder is positioned in front of the collector where the ions can fly through, but it is lying on a potential that repells the secondary electrons and sends them back to the collector, generating a short positive peak in the detector. The onset of this so-called photo peak can be used afterwards to calibrate the flying time of the ions hitting the collector, as the γ-rays responsible for this peak propagate with the speed of light.

Additionally, the TOF signal is strongly disturbed by the electro-magnetic pulse (EMP) from the high-intensity interaction. Therefore, the connecting cables between detector and oscilloscope, and also the oscilloscope itself were carefully shielded against electromagnetic radiation, but the charge collector itself could not be shielded completely without blocking the ion beam. Fortunately, the EMP arrives earlier at the detector and is already decreasing, when the ion beam arrives. Nevertheless, the EMP limits – together with the high voltage to separate the ions from co-propagating electrons – the maximum detectable ion energy, as these ions reach the detector immediately after the EMP.

4.2.2 Measurement of Ion Spectra

Fig. 4.4 shows a typical TOF signal recorded with the circuit shown in Fig. 4.3 and a fast oscilloscope (a 1-GHz Tektronix TDS 684 B with a sampling rate of $5\,\mathrm{GS/s}$ and a time resolution of $\sim$900 ps [102]). The signal was attenuated by a factor of 11 to prevent the oscilloscope from saturation, but in Fig. 4.4 the real voltages are shown. As the detector stood $d_{\mathrm{TOF}} = 182\,$mm behind the target and its radius was $10\,$mm, the covered solid angle was $\Delta\Omega = 9.5\,$msr. The inset shows the ion signal recorded over $2.8\,\mu$s, while only the early part of the signal corresponding to the fastest ions is used to deduce the ion spectrum. The photo peak is clearly visible and can be used to define $t = 0$ on the time axis.

The ion spectrum, $\mathrm{d}N/\mathrm{d}E$, can be deduced from the TOF signal, $U(t_{\mathrm{TOF}})$, in the following way[3]. If one assumes protons with mass, m_{p}, and charge, $+e$, to be the main

---

[3] The oscilloscope gives a voltage, $U(t_{\mathrm{TOF}})$, that is associated to the ion current $I(t_{\mathrm{TOF}}) = U(t_{\mathrm{TOF}})/R$, where $R = 50\Omega$ is the resistance of the channel of the oscilloscope.

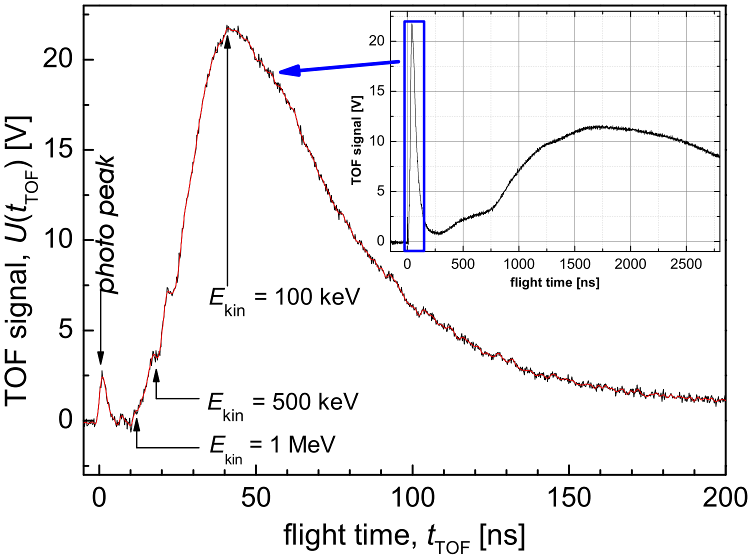

Figure 4.4: Ion TOF signal, $U(t)$, obtained with a 8-μm Mylar foil. The early part of the signal is zoomed in from the total time window of $2.8\,\mu$s given in the inset. The red line gives the signal after applying a low-pass filter to reduce the EMP-noise. This filtered signal is used to deduce the ion spectrum (see text). The onset of the photo peak defines $t = 0$. The indicated arrival times hold for protons with kinetic energies of 1 MeV, 500 keV, and 100 keV. The signal extending over several μs in the inset is associated with the plasma blow-off.

contribution to this ion signal (carbon and oxygen ions can only be distinguished with a Thomson parabola, what will be discussed later), one obtains with help of eq. (4.2)

$$\begin{aligned}\left|\frac{\mathrm{d}N}{\mathrm{d}E}\right| &= \frac{\mathrm{d}N}{\mathrm{d}t}\cdot\left|\frac{\mathrm{d}t}{\mathrm{d}E}\right| = \frac{I_{\mathrm{prot}}(t_{\mathrm{TOF}})}{q}\cdot\left|\frac{\mathrm{d}t}{\mathrm{d}E}\right| = \frac{1}{e}\frac{U(t_{\mathrm{TOF}})}{R}\cdot\frac{d_{\mathrm{TOF}}}{2}\sqrt{\frac{m_{\mathrm{p}}}{2E(t_{\mathrm{TOF}})^3}} = \\ &= \frac{1}{e\cdot m_{\mathrm{p}}}\cdot\frac{1}{d_{\mathrm{TOF}}^2\cdot R}\cdot U(t_{\mathrm{TOF}})\cdot t_{\mathrm{TOF}}^3, \end{aligned} \tag{4.3}$$

where $I_{\mathrm{prot}}(t_{\mathrm{TOF}})$ is the proton current impinging on the charge collector, $R = 50\,\Omega$ is the resistance of the channel of the fast-oscilloscope, and $U(t_{\mathrm{TOF}})$ is the voltage detected by the oscilloscope. Using this expression, the proton spectrum is easily obtained. The spectrum per solid angle corresponding to the TOF signal in Fig. 4.4 is shown in Fig. 4.5.

In this spectrum, protons with kinetic energies up to 1.5 MeV are detected. The spectrum shows two distinct proton populations, one with a Boltzmann-like temperature of $T_{\mathrm{cold}} = 65\,\mathrm{keV}$ and a second one with $T_{\mathrm{hot}} = 200\,\mathrm{keV}$.

The spectrum in Fig. 4.5 was deduced assuming protons being the only ion species in the detected beam. Any additional ion species (e.g. carbon or oxygen) would also affect the spectrum, especially for higher charge states. If one assumes that carbon ions with the same kinetic energy as the protons, i.e. $E_{\mathrm{kin}} = 1.5\,\mathrm{MeV}$, are also accelerated from the target, they have a velocity smaller by a factor of $1/\sqrt{12}$ due to their higher

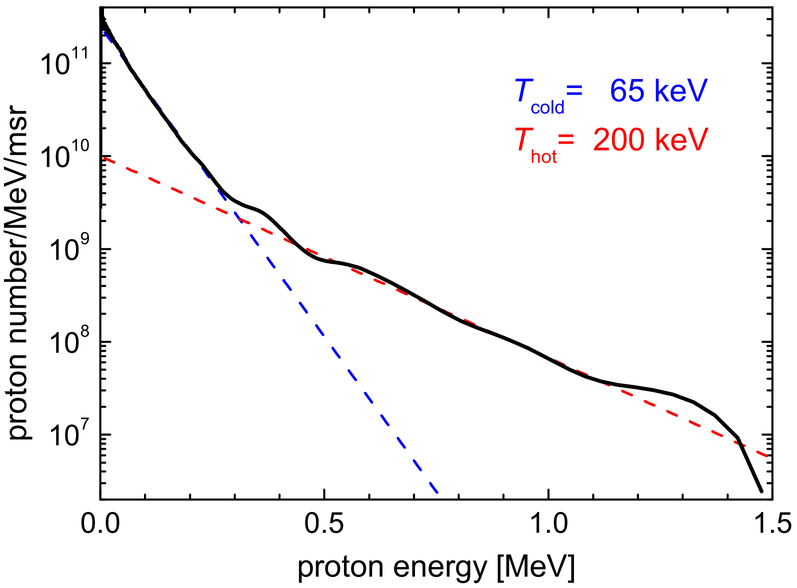

Figure 4.5: Proton spectrum normalised to a solid angle of 1 msr deduced from the TOF signal given in Fig. 4.4. The spectrum consists of two distinct proton distributions with $T_{\mathrm{cold}} = 65\,\mathrm{keV}$ and $T_{\mathrm{hot}} = 200\,\mathrm{keV}$. It shows a clear cutoff at $E_{\mathrm{kin}} = 1.5\,\mathrm{MeV}$.

mass, and they are delayed by a factor of $\sqrt{12} \approx 3.46$ compared to the protons and arrive after $t_{\mathrm{TOF}} \approx 37\,\mathrm{ns}$ at the TOF detector. This arrival time is associated to a proton kinetic energy of $\approx 120\,\mathrm{keV}$. The signal corresponding to higher proton energies cannot originate from carbon ions, as they would need to have a higher kinetic energy than 1.5 MeV. If these simple considerations hold true, one can conclude that the spectrum deduced from the TOF signal above a kinetic energy of $\approx 120\,\mathrm{keV}$ originates from protons only. For a detailed investigation of the different ion species in the beam, a Thomson parabola spectrometer was employed. This is described in the next section.

4.3 Measurement of Ion Spectra with a Thomson Parabola

The only diagnostic used in the experiment, that was able to distinguish between ion species having different charge-to-mass ratios and record their energy spectra separately, was a Thomson parabola spectrometer equipped with CR 39 plates as a detector [82, 109]. In such a spectrometer, ions are dispersed due to their different charge-to-mass ratios and kinetic energies, while they fly through parallel electric and magnetic fields, that are perpendicular to the initial propagation direction of the ions.

The initial kinetic energy of the ions can be deduced from their deviation in the fields. It is assumed that an ion with charge, q_{i}, and mass, m_{i}, propagating in $\vec{e}_z$-direction with velocity, v_{i}, enters a homogeneous electric and magnetic field distribution, as it is depicted

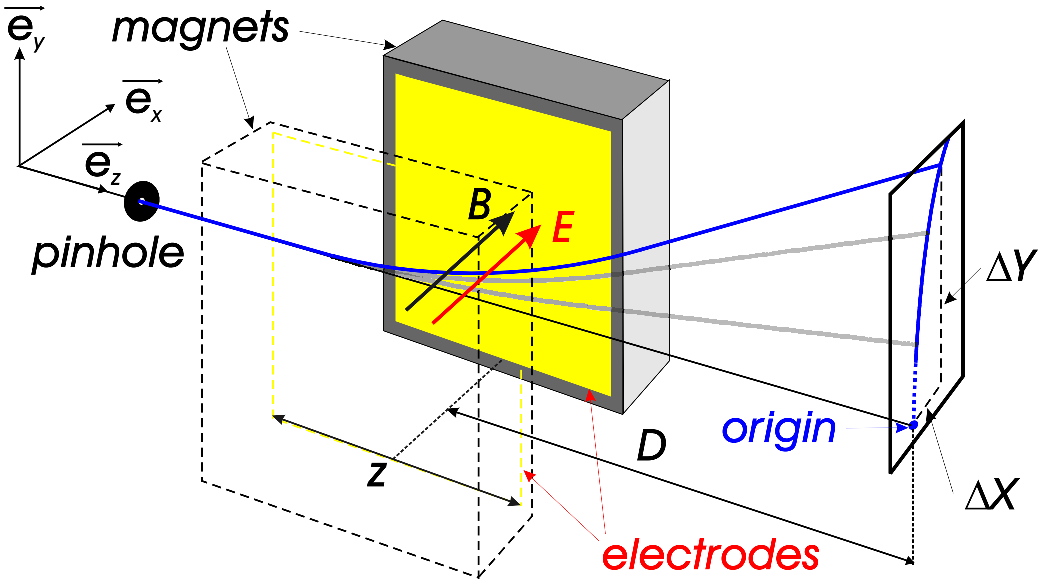

Figure 4.6: Schematic layout of a Thomson parabola. Ions coming from the target pass through a small pinhole and fly through parallel electric and magnetic fields generated by two pairs of electrodes and magnets. In these fields, they are dispersed onto distict parabola traces in the plane of the detector. In this sketch, only ions of the same species but with different velocities are shown.

in Fig. 4.6. The field lines are parallel to $\vec{e}_x$. After the ion has moved through the field distribution in $\vec{e}_z$-direction, it has been deflected sideways by the fields. If one assumes a constant field strength over the total extension, z, of the fields and neglects fringe effects, the deflection parallel to $\vec{e}_x$ due to the electric field, $\mathcal{E}$, is for small deviations given by

$$\Delta x \sim \frac{1}{2}at^2 = \frac{\mathcal{E}z^2}{2} \cdot \frac{q_\mathrm{i}}{m_\mathrm{i}{v_\mathrm{i}}^2}, \tag{4.4}$$

which is inversely proportional to the ion kinetic energy, $E_\mathrm{kin} = m_\mathrm{i}{v_\mathrm{i}}^2/2$. The deflection in $\vec{e}_y$-direction due to the magnetic field, $\mathcal{B}$, can be written as

$$\Delta y \sim \frac{1}{2}at^2 = \frac{\mathcal{B}z^2}{2} \cdot \frac{q_\mathrm{i}}{m_\mathrm{i}v_\mathrm{i}} \tag{4.5}$$

and is thus inversely proportional to the momentum, $p_\mathrm{i} = m_\mathrm{i}v_\mathrm{i}$, of the ion. Here we assume a constant velocity, v_i, when the ion passes through the fields, although it is slightly increased by the electric field. When the ion hits the detector which is positioned in distance, D, from the center of the fields, the total deviations are then given by

$$\Delta X \sim \mathcal{E}Dz \cdot \frac{q_\mathrm{i}}{m_\mathrm{i}{v_\mathrm{i}}^2} \qquad \text{and} \qquad \Delta Y \sim \mathcal{B}Dz \cdot \frac{q_\mathrm{i}}{m_\mathrm{i}v_\mathrm{i}}. \tag{4.6}$$

Taking these two equations together, ΔX can be written as

$$\Delta X \sim \frac{\mathcal{E}}{\mathcal{B}^2Dz} \cdot \frac{m_\mathrm{i}}{q_\mathrm{i}} \cdot (\Delta Y)^2, \tag{4.7}$$

which is a parabolic equation with the inverse charge-to-mass ratio as a parameter. Note that the deflection along a single parabola trace in the plane of the detector depends on the ion velocity, but different ion species lie on parabolas with different slopes. The ion species with the highest charge-to-mass ratio (in our experiments protons with $q_\mathrm{i}/m_\mathrm{i} = 1 \cdot e/u$) forms the parabola trace, which is least bent in $\vec{e}_x$-direction.

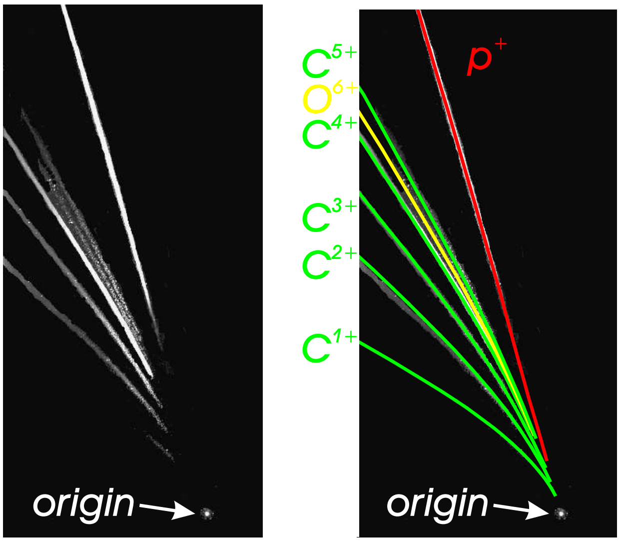

Figure 4.7: Digital photograph of a CR 39 plate after etching. The left side shows the bare detector with parabola traces from seven different ion species. The origin of the parabolas is formed by neutral atoms that pass through the Thomson parabola unaffected by the fields. On the right side, the traces obtained by a 3-D tracking routine are compared to the measured traces. A very good agreement is found that allows a clear determination of the ion species.

Fig. 4.7 shows a piece of CR 39, that has been etched in hot NaOH solution after a single laser shot. Seven different parabola traces are visible. The origin of all traces in the lower right corner is generated by ions that have recombined with co-propagating electrons before entering the spectrometer. As they are electrically neutral, they are not deflected by the fields and form a spot on the detector which would also correspond to a charged ion with infinite velocity.

To identify the ion species with a certain charge-to-mass ratio forming a single parabola trace, a 3-D tracking routine for different ion species and different velocities through the real electric and magnetic fields was carried out by J. Schreiber [110]. The magnetic field distribution was measured with a Hall-sensor, the electric field distribution and the ion trajectories through the fields were simulated using the program EM STUDIO$^{\mathrm{TM}}$ [111]. The excellent agreement between the calculated and measured traces, as it can be seen in the right part of Fig. 4.7, allows a definite assignment of the different traces on the detector to protons, C^{1+} to C^{5+}, and O^{6+} ions.

Each parabola trace consists of a large number of ion pits. They can be separated under an optical microscope, as it is shown in Fig. 4.8. The microscope having a $x-y$ translation stage and a connected CCD are controlled by a computer. A pattern-recognition software fits ellipses to the pits and stores their diameters and positions. Starting from the origin on the detector, the deviations of the charged ions can be measured easily. With the dispersion relations obtained by the tracking routine, the energy spectra of the different ion species can be deduced from the stored deviations of the ion pits. The energy spectra for the protons and the different Carbon-species deduced from the CR 39 plate shown in Fig. 4.7 are presented in Fig. 4.9.

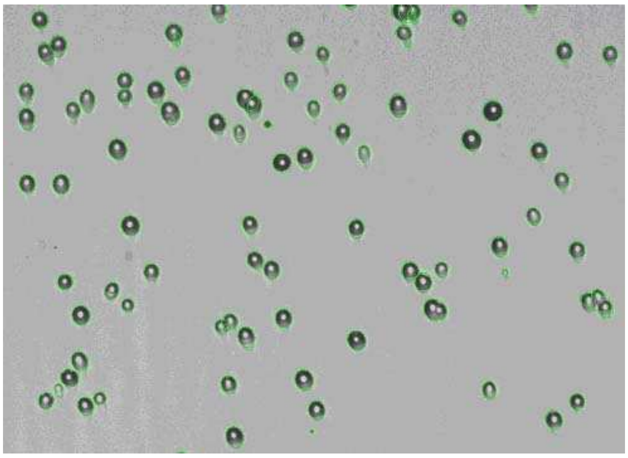

Figure 4.8: Magnified part of the proton parabola trace on a piece of CR 39 after etching. The green ellipses were fitted to the proton pits by the computer software. Their positions and diameters are stored for subsequent spectral analysis. Even slightly overlapping pits can be resolved. The fitting of pits essentially smaller than the proton pits (e.g. from dust) is either suppressed, or the ellipses can be excluded afterwards due to their smaller diameters.

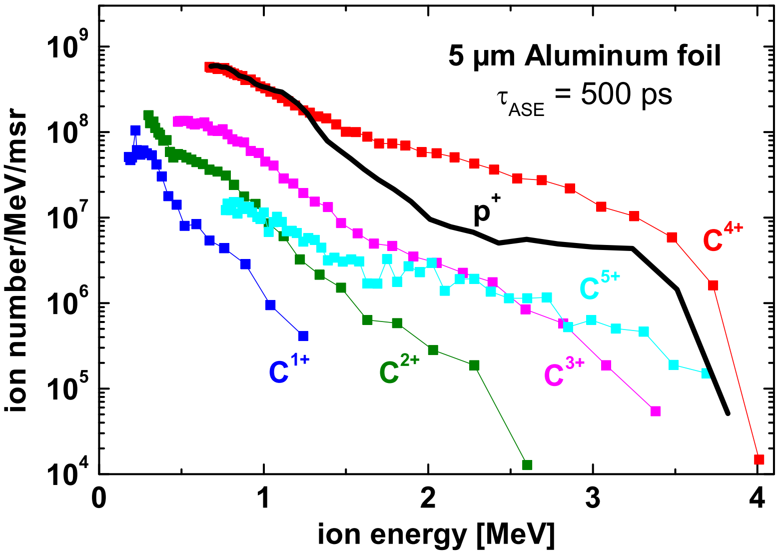

Figure 4.9: Proton and carbon spectra corresponding to the CR 39 plate shown in Fig. 4.7.

Different Methods for Deduction of Ion-Energy Spectra

To obtain an energy spectrum, $\mathrm{d}N(E)/\mathrm{d}E \approx \Delta N(E)/\Delta E$, of a certain ion species, the number of ions, $\Delta N(E)$, within the energy interval, $[E, E+\Delta E]$, has to be determined. In the plane of the CR 39 detector, the ion pits are spread according to their kinetic energy, E, on a parabola trace. An energy interval, $[E, E+\Delta E]$, corresponds to an interval, $[y, y+\Delta y]$, along the $\vec{e}_y-$axis deviation on the detector, described by the ion-dispersion relation, $\mathrm{d}E/\mathrm{d}y$. $\Delta N(E)$ can either be taken within a *constant energy interval*, ΔE, or within a *constant deviation interval*, Δy, over the whole parabola trace. In the first case of constant ΔE, the corresponding $\Delta y(E)$-interval becomes smaller, in the second case of constant Δy, the energy interval, $\Delta E(E)$, becomes larger for increasing ion energy, E. As ions having exactly the same kinetic energy are scattered within the parabola trace at least over an area

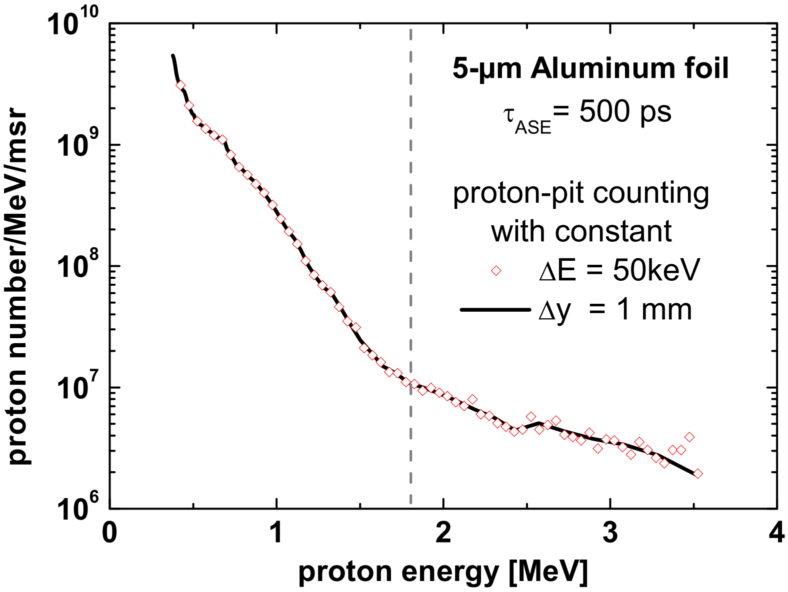

Figure 4.10: Proton energy spectra from the same laser shot obtained with two different counting methods. For the case of the solid line, the number of ions were detected within a constant deviation interval $\Delta y = 1\,\mathrm{mm}$ on the CR 39 detector. The red diamonds show the spectrum obtained with a constant energy interval $\Delta E = 50\,\mathrm{keV}$. For kinetic energies above 2 MeV, this second spectrum becomes noisy. This is an artefact, as here the counting intervals are smaller than the size of the pinhole image in the plane of the detector.

corresponding to the size of the image of the Thomson-parabola pinhole, a separation into Δy-intervals smaller than the pinhole diameter during the counting procedure generates artificial noise in the ion spectra. This behaviour is shown in Fig. 4.10, where the proton spectrum of the same laser shot is deduced using the two different methods described above. For this shot, a 450-μm pinhole was used in the Thomson parabola. The image of this pinhole on the CR 39 detector has a diameter of $\sim 600\,\mu$m. While the spectrum obtained by counting with a constant $\Delta y = 1\,\mathrm{mm}$ (solid black line), which is slightly above this diameter, is smooth over the whole energy range, the spectrum becomes noisy for energies above 1.8 MeV for the case of constant $\Delta E = 50\,\mathrm{keV}$ (red diamonds). Above this energy indicated by the dashed grey line, the corresponding interval, $\Delta y(E)$, becomes smaller than the diameter of the pinhole image. For high energies, the scattering amounts up to a factor of 2. To avoid this, all ion spectra were deduced from the CR 39 plates with the counting method using a constant interval, $\Delta y = 1\,\mathrm{mm}$. This increases the error for high kinetic energies, given by the energy distance of the data points in the spectrum, but correctly mirrors the real error arising from the limited energy resolution of the Thomson parabola.

4.4 Measurement of the Spatial Profile of the Proton Beam

Finally, the spatial profile of the generated proton beam was measured to have an estimate of the divergence of the beam. Both the energy spectrum and the profile of the proton beam had to be measured from the same laser shot to eliminate shot-to-shot fluctuations on the one hand and to be able to valuate these fluctuations quantitatively on the other hand. For this purpose, a piece of CR 39 was again positioned behind the target at a distance of 82 mm. Its front side was completely wrapped with a 12-μm aluminum foil to block protons with energies below 900 keV. A part of the ion beam could pass through a small hole both in the detector and the aluminum foil to be detected in the Thomson parabola simultaneously. Fig. 4.11 shows a typical spatial profile of the proton beam, that was accelerated from a 5-μm aluminum foil. Around the target normal direction, indicated by the small hole in the middle of the detector, a collimated proton feature appears that has a half opening angle of $\sim 10^{\circ}$.

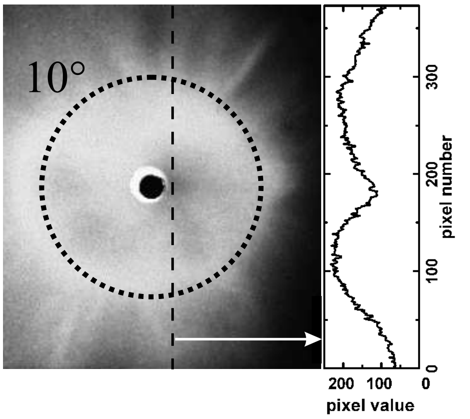

Figure 4.11: Spatial profile of the proton beam obtained with a 5-μm Al foil recorded on a piece of CR 39. The dotted circle corresponds to a half-opening angle of 10°. The main part of the proton beam appears to be collimated around the target normal direction, indicated by the hole in the detector. Any pits on this CR 39 plate originate from protons with kinetic energies exceeding 900 keV. The right part gives the line-out of the photographic image along the dashed vertical line suggesting a ring-like beam profile (see text).

As the diameter of the hole was only 3.5 mm, the alignment of this detector plate was crucial to avoid any clipping of the ion beam along its path from the target to the Thomson parabola. Therefore, a Helium-Neon laser was aligned through the pinhole of the Thomson parabola pointing onto the target rear surface. This laser beam thus had the same path as the ion beam coming from the target and entering the Thomson parabola through the pinhole. Before a shot with the main pulse, the hole of the CR 39 plate was positioned around the Helium-Neon laser beam.

For the photograph shown in Fig. 4.11, the CR 39 piece was positioned in front of a black screen and illuminated under oblique incidence from the back by a strong lamp avoiding direct light from the lamp into the camera. From a region on the CR 39 covered with ion pits, light is scattered into the camera resulting in a bright region on the photograph. From regions with a plane surface, i.e. without ion pits, no light is scatterd into the camera resulting in a dark region. On the photograph in Fig. 4.11, there appears to be a ring-like region with higher pit-densities (around the dashed circle), while the central region appears to be darker aggain suggesting a lower pit density here. The right part of Fig. 4.11 gives the line-out of the picture along the dashed vertial line illustrating the brightness distribution that also suggests a ring-like beam profile. Such ring-like features on CR 39 detectors have been observed in several experiments and have been interpreted as signatures of a ring-like spatial profile of the proton beam caused by magnetic fields in the target [13, 14, 44] or at the rear surface of the target [46]. The combination of the two proton diagnostics (Thomson parabola and CR 39 plates) enabled us to carry out a detailed spectral characterisation of the proton beam over the whole profile by slightly rotating the target around its vertical axis. Our results shed a totally new light onto the interpretation of these rings. The results will be discussed in the next chapter.

Chapter 5

Experimental Characterisation of Laser-Accelerated Protons

This chapter concentrates on the experimental results concerning the acceleration of protons during the interaction of the ATLAS-laser pulse with thin aluminum foils. Strong dependencies of the energy spectra and the spatial distribution of the proton beam on the target thickness and the duration of the ASE prepulse were found. Only the experimental findings and their qualitative explanation will be reported, while a quantitative interpretation, that will allow a clear connection of different features both in the energy spectra and in the beam profiles to different proton-acceleration mechanisms, will follow in chapter 8. After a description of the experimental setup for the proton measurements in the first section, the following two sections will concentrate on the spectral measurements using the Thomson parabola and discuss the influence of the target thickness and the prepulse duration on the spectra. In a last section, angularly resolved measurements both of the spectra and beam profiles of the protons will be presented.

5.1 Experimental setup

Fig. 5.1 shows the experimental setup for the proton measurements, which is similar to the setup shown in Fig. 4.1. Here, we used a CR 39 detector wrapped in a 12-μm aluminum foil to measure the spatial beam profile of the protons with kinetic energies exceeding 900 keV. Through a small hole both in the CR 39 plate and the aluminum foil, that was aligned around target normal direction, ions could pass and enter the Thomson parabola, where their energy spectra were measured simultaneously. The synchronised $2\omega-$probe beam that is described in Appendix A was used to align the target before the laser shot. The target was rotated with respect to the laser axis by 30° to suppress the reflection of the pulse back into the laser chain, as such a back reflection can severly damage optical elements in the laser system. However, the emission cone of the protons is aligned along target normal direction, as the field gradients on both target surfaces that are responsible for the acceleration of the protons are parallel to the density gradient and therefore perpendicular to the target surfaces.

Fig. 5.2 shows a typical proton spectrum measured with the Thomson parabola. For this shot, a 5-μm aluminum foil was used as a target, the prepulse duration was $\tau_{\mathrm{ASE}} = 500\,\mathrm{ps}$, and the laser intensity was $I_{\mathrm{L}} = 1.3 \times 10^{19}\,\mathrm{W/cm^2}$. The pinhole of the Thomson parabola

Figure 5.1: Experimental setup for the detection of protons using both CR 39 plates and the Thomson parabola. The CR 39 plates were positioned 82 mm behind the target. Through a small hole in the CR 39 sheet aligned along the target normal direction originating in the focal spot center ions could pass to be detected in the Thomson parabola. The 2ω-probe beam was used to align the thin target foil.

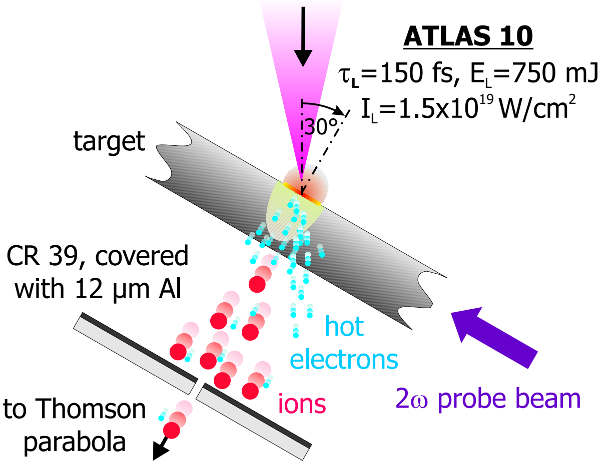

with a diameter of 300 μm was positioned at a distance of 82 cm from the target, covering a solid angle of $\sim 10^{-7}$ sr. The spectrum was measured in target normal direction (further defined as $\varphi = 0°$) with an accuracy of $\pm 1°$. In the spectrum, the proton numbers are given per MeV and msr. The low-energy cutoff, $E_{\text{min}} = 300$ keV, is determined by the setup of

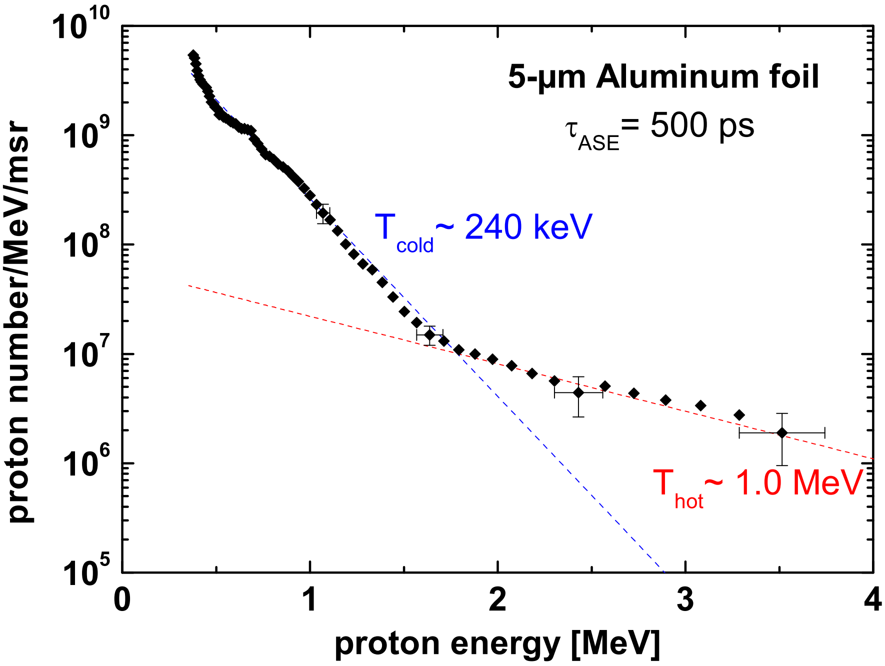

Figure 5.2: Proton energy spectrum measured with the Thomson parabola. The target was a 5-μm aluminum foil irradiated with an intensity of $I_L = 1.3 \times 10^{19}$ W/cm^2 and a prepulse of $\tau_{\text{ASE}} = 500$ ps duration.

the Thomson parabola itself, as slower protons do no longer hit the CR 39 detector because they are that strongly deflected by the fields in the spectrometer.

Again, two proton populations with different Boltzmann-like quasi-temperatures can be identified: (i) a cold component with a temperature of $T_{\text{cold}} = (240 \pm 30)\,\text{keV}$ and (ii) a hot one with $T_{\text{hot}} = (1.0 \pm 0.2)\,\text{MeV}$. The spectrum extends up to a sharp energy cutoff at, $E_{\text{p,max}} = 3.5\,\text{MeV}$. The appearance of such a typical well-defined maximum energy in the proton spectrum (as it was also seen during the TOF measurements[1]) was discussed in Chapter 2. The error bars in the energy that are only given exemplarily for four data points in the spectrum are mainly defined by the (constant) size of the intervals for the proton pit counting as it was discussed in section 4.3. Due to the dispersion relation the energy range within such a counting interval becomes larger for increasing energy resulting in larger error bars for higher proton energies. The error bars in the proton numbers are estimated from the accuracy of the proton-pit counting to 10% for low energies and up to 50% for the highest energies[2].

5.2 Proton Spectra for Different Target Thicknesses

Figs. 5.3 (a) and (b) show proton spectra measured with differently thick aluminum targets. During these measurements, the laser intensity and the prepulse duration were kept constant ($I_{\text{L}} = 1.0 \times 10^{19}\,\text{W}/\text{cm}^2$ and $\tau_{\text{ASE}} = 700\,\text{ps}$) within the unavoidable shot-to-shot fluctuations of the laser. The target thickness was varied between 0.75 and $86\,\mu$m. The aluminum foils used in the experiment were fabricated by Goodfellow [112].

It is obvious that in Fig. 5.3 (a) the cutoff energy, as well as the quasi-temperature of the hottest component, and also the total number of the protons between the lower cutoff energy of 300 keV and the maximum energy in each spectrum increases steadily with the target thickness up to the 3-μm foil. When the target thickness is further increased, as it is shown in Fig. 5.3 (b), the temperature and the cutoff energy of the protons drop again. This behaviour is depicted in Fig. 5.4.

There is a slightly different behaviour of the cutoff energy and the hot-temperature component of the protons on the one hand shown in Fig. 5.4 (a) and of the total proton number on the other hand in Fig. 5.4 (b). While the first two quantities both reach their maximum at a target thickness of $3\,\mu$m, the total proton number is peaked at a foil thickness of $5\,\mu$m. This difference is due to the much higher proton number of the cold component, that indeed peaks for a somewhat thicker target (cf. Fig. 5.3). Note that for the 86-μm thick target only a very small number of protons could be detected exactly at the lower cutoff energy of the Thomson parabola ($E_{\text{min}} = 300\,\text{keV}$). Therefore, only the cutoff energy of these protons can be given but not their temperature or total number.

---

[1] The lower cutoff energy measured with the TOF detector is due to the upper limit of detectable proton energies determined by the high voltage applied to the detector to suppress the co-moving electrons. Furthermore, aluminum targets are studies here, whereas the TOF measurements were carried out with thin Mylar foils.

[2] Counting errors can arise, e.g., from dust particles, that were also counted and could not be distinguished from the real proton pits afterwards. These errors are maximal for the highest proton energies, as here the proton pits density in the parabola trace becomes small. If the pits overlap within the parabola trace, the software does not recognise two separated proton pits, but counts two as one.

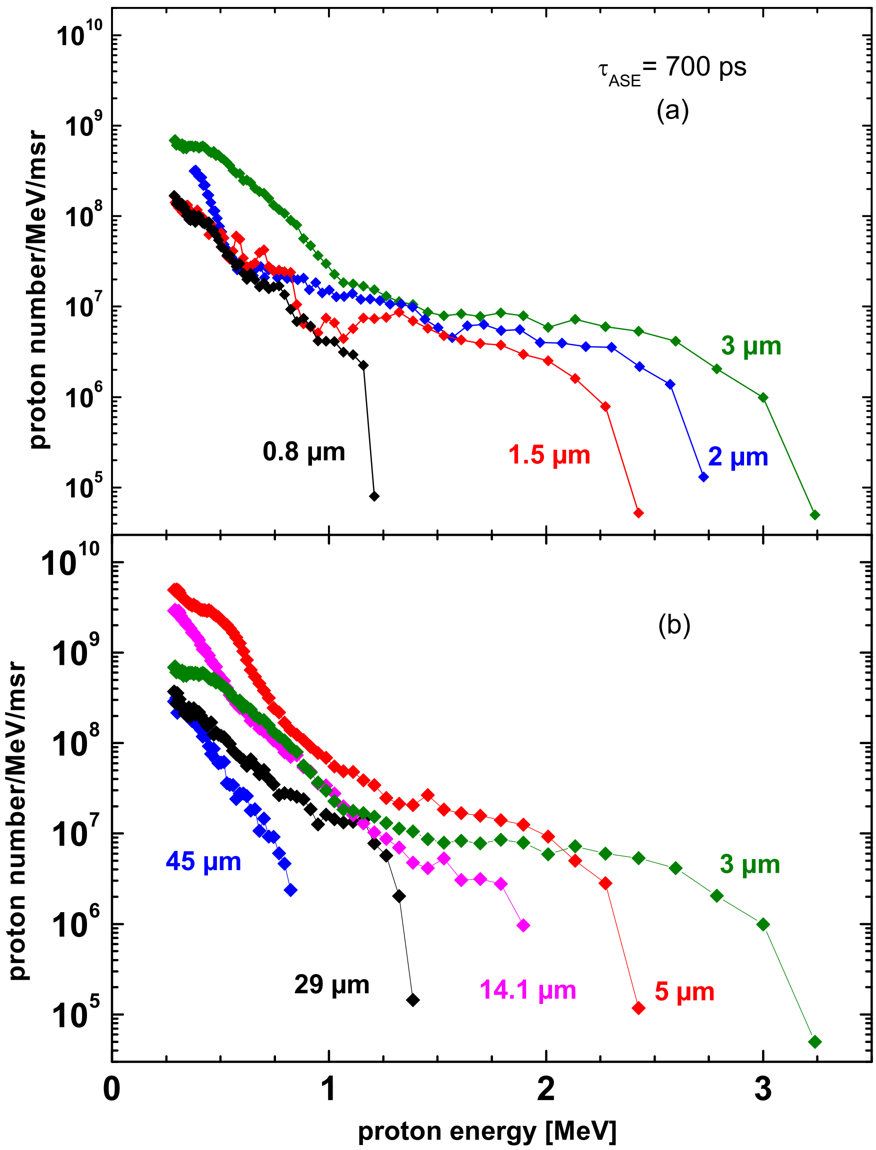

Figure 5.3: Proton spectra from the Thomson parabola. The aluminum foils of different thickness were irradiated by a laser intensity of I_L=1.0 × 10^{19} W/cm^2 and a prepulse duration of τ_{ASE} = 700 ps.

The **optimal target thickness**, d_{opt}, is defined as the value, where the highest proton cutoff energies are achieved. For all spectra presented in this section measured with a prepulse duration of $\tau_{ASE} = 700\,\mathrm{ps}$ and a laser intensity of $I_L = 1.0 \times 10^{19}\,\mathrm{W/cm^2}$

$$d_{opt}(\tau_{ASE} = 700\,\mathrm{ps}) = 3\,\mu\mathrm{m} \tag{5.1}$$

is found.

The proton spectra depicted in Fig. 5.4 (a) and (b) resolve into two regimes which are

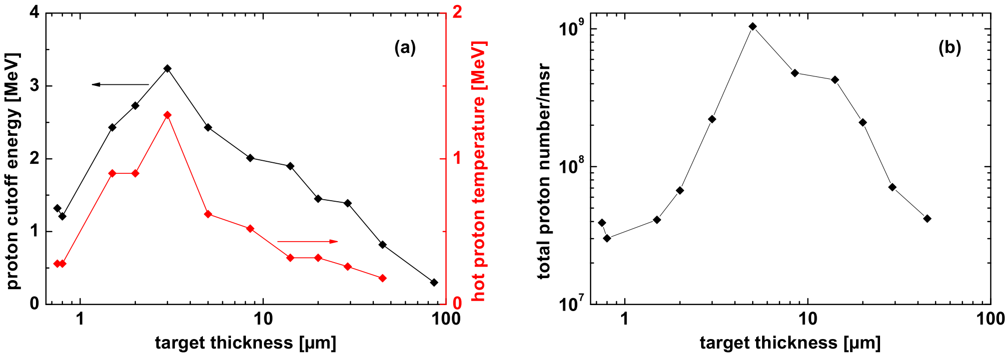

Figure 5.4: Cutoff energies, quasi-temperature of the hottest component (a), and total number between 300 keV and the maximum energy of each spectrum (b) of the protons as a function of the target thickness. The aluminum foils were irradiated at a laser intensity of I_L=1.0 × 10^{19} W/cm^2 and a prepulse duration of $\tau_{ASE} = 700$ ps. In (a) the arrows indicate the corresponding ordinate.

separated by the optimal target thickness. This phenomenon can be explained qualitatively by the following **model assumption** that is similar to the explanation given in [39]:

1. Below the optimal target thickness, d_{opt}, a plasma has been formed at the target rear side, before the main-pulse accelerated hot electrons arrive there and initiate the proton acceleration. The rear-side plasma formation and expansion are initiated by the ASE prepulse on the target front side, both are reduced for thicker foils. When the scale length of this rear-side plasma exceeds the Debye-length of the hot-electron sheath, the electric fields for the rear-side proton acceleration are the more reduced, the longer the plasma scale length is [17, 42]. For a constant prepulse duration it is therefore found that the thinner the target is, the flatter is the rear-side density gradient, and the stronger are the proton cutoff energies reduced. This notion well explaines the experimental observations below the optimal target thickness, d_{opt}.

2. For thicker foils, the rear surface has remained undisturbed, when the rear-side proton acceleration starts, as the effect of the prepulse on the rear side is weaker for thicker foils. But, due to the divergence of the electron beam in the target, the electron spot size at the rear surface increases with increasing target thickness, which in turn reduces the electron density and therefore the acceleration fields. In addition, energy losses of the electrons during their passage through the target reduce the mean energy or the temperature, T_e, of the hot-electron component arriving at the target rear side. Either of these two scenarios can explain the reduction of the acceleration fields and the corresponding drop in proton cutoff energy for an increasing target thickness.

In this model assumption, there are two counteracting target-thickness dependencies of the maximum proton energy. Due to the prepulse-induced plasma formation at the back of the target, the maximum proton energy increases with increasing target thickness up to the optimal value, d_{opt}, and then drops again due to the divergence of the electron beam in the target. While the second regime should remain almost unaffected by changes of the prepulse, its duration, τ_{ASE}, is crucial for the behaviour in the first regime. The longer τ_{ASE}, the thicker the target has to be to provide an undisturbed rear surface and therefore d_{opt} increases. As a consequence of this model assumption, the fastest protons, that are accelerated from targets of optimal thickness, come from the *rear* side of the target.

5.3 Proton Spectra for different ASE Prepulse Durations

5.3.1 Measurements with a constant laser intensity

To further test the model assumption introduced in the last section, the ASE prepulse duration was changed. This was accomplished by varying the trigger delay for the ultrafast Pockels cell as described in chapter 3.3. In addition to the results obtained by the thickness variation with $\tau_{\mathrm{ASE}} = 700\,\mathrm{ps}$ and described in the last section, thickness scans were performed with prepulse durations of $\tau_{\mathrm{ASE}} = 500\,\mathrm{ps}$, which is the minimal ASE duration achievable with the ATLAS-laser system, $\tau_{\mathrm{ASE}} = 1.5\,\mathrm{ns}$, and $\tau_{\mathrm{ASE}} = 2.5\,\mathrm{ns}$. The proton cutoff energies obtained during the thickness scans for the shortest and longest ASE durations are compared with the results of $\tau_{\mathrm{ASE}} = 700\,\mathrm{ps}$ in Fig. 5.5.

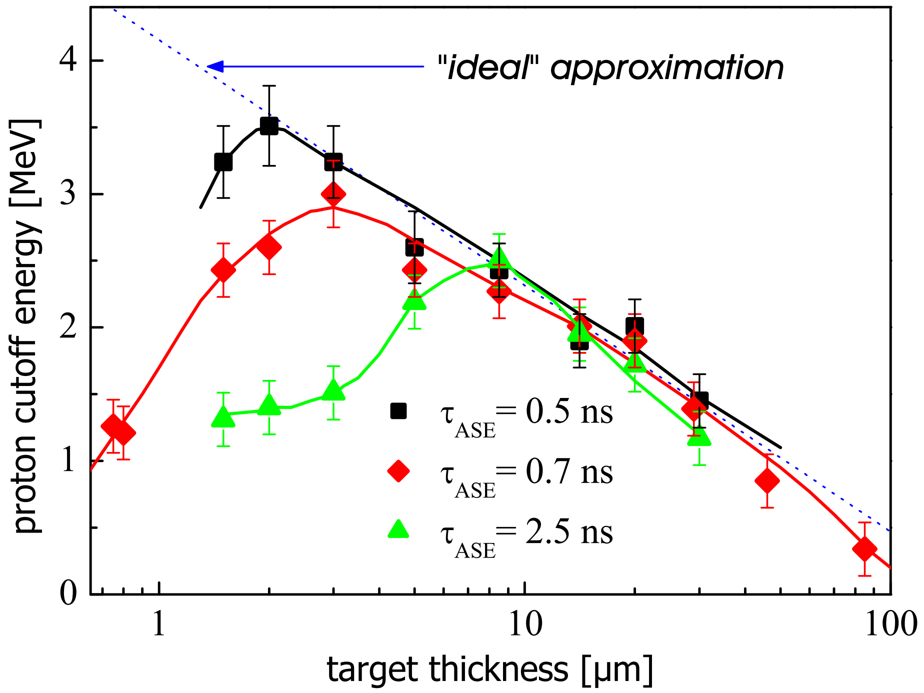

Figure 5.5: Proton cutoff energies obtained during scans of the target thickness for three different prepulse durations, $\tau_{\mathrm{ASE}} = 500\,\mathrm{ps}$ (black line), $700\,\mathrm{ps}$ (red line), and $2.5\,\mathrm{ns}$ (green line). The intensity for all laser shots was $I_{\mathrm{L}} = 1.0 \times 10^{19}\,\mathrm{W/cm^2}$. The dotted blue line represents the "ideal" approximation for the proton cutoff energies corresponding to the case of no prepulse ($\tau_{\mathrm{ASE}} = 0\,\mathrm{ps}$).

The qualitative behaviour of the maximum proton energy as a function of the target thickness is the same for all the three ASE durations, but the optimal target thickness, d_{opt}, strongly depends on the prepulse duration, τ_{ASE}. Note, that only the cutoff energies below each optimal target thickness are affected by changes of the prepulse duration. They are the more reduced the longer the ASE prepulse is. On the other hand, the cutoff energies appear to be independent on the prepulse duration above each optimal thickness. They seem to converge to an "ideal" approximation suggested by the dotted blue line. This ideal case would correspond to $\tau_{\mathrm{ASE}} = 0\,\mathrm{ps}$, i.e. no ASE prepulse, as long as no other effects start to play a role when the prepulse becomes even shorter. Results published by A. Mackinnon *et al.* [38] obtained at the JANUSP-laser system at Lawrence Livermore National Laboratory (LLNL) show that electron recirculation in the target increases the proton cutoff energy even more for the thinnest targets compared to the "ideal" approximation in Fig. 5.5, if the ASE prepulse is even shorter and/or the pulse cotrast is substantially higher ($\sim 10^{-10}$ in [38] obtained with a saturable absorber in the laser chain compared to 4×10^{-8} for the ATLAS laser). Nevertheless, within the prepulse regime achievable with our system, which is comparable to most other state-of-the-art CPA lasers, this effect of electron recirculation in the target appears to play no significant role.

5.3.2 Influence of the laser intensity

In a next step, the influence of the laser pulse energy or the laser intensity is investigated. This was achieved by slightly changing the laser pulse energy[3], while the prepulse duration and all other experimental parameters (especially the main-pulse duration of 150 fs) were kept constant.

Fig. 5.6 shows the measured cutoff energies of the protons for three different laser intensities ($I_{\mathrm{L}} = 1.0 \times 10^{19}\,\mathrm{W/cm^2}, 1.3 \times 10^{19}\,\mathrm{W/cm^2}$, and $1.5 \times 10^{19}\,\mathrm{W/cm^2}$). While the maximum proton energies depend sensitively on the laser pulse energy/intensity for every thickness, the optimal thickness remains constant within the accuracy limited by the available target thicknesses.

Together with the results for different prepulse durations shown in Fig. 5.5, it can be concluded that the value of the optimal target thickness appears to depend on the prepulse duration only, while it is unaffected by relatively small changes of the laser energy/intensity. Therefore, the optimal target thickness, d_{opt}, is plotted versus the ASE prepulse duration, τ_{ASE} (Fig. 5.7). Within the error bars determined by the jitter of the trigger for the ultra-fast Pockels cell on the one hand ($\pm 150\,\mathrm{ps}$) and the available foil thicknesses on the other hand, this correlation can be approximated linearly with an effective quasi-velocity, $v_{\mathrm{pert}} \approx (3.6 \pm 0.6)\,\mu\mathrm{m/ns}$. Since this velocity can be interpreted as the speed of a perturbation launched by the prepulse on the front side, travelling through the foil and creating a plasma at its back side that affects the rear-side proton acceleration, it is obvious to compare it to the sound speed in cold aluminum, $c_{\mathrm{s}} = 6.4\,\mu\mathrm{m/ns}$ [113], which is a lower limit for the speed of the perturbation. Simulations using the hydrocode MULTI-FS [50, 114], that will be presented in chapter 6, will resolve this discrepancy.

---

[3] A change in the laser pulse energy was accomplished by varying the delay between the Nd:YAG-lasers pumping the amplification crystals in the laser chain and the Ti:Sa-pulse.

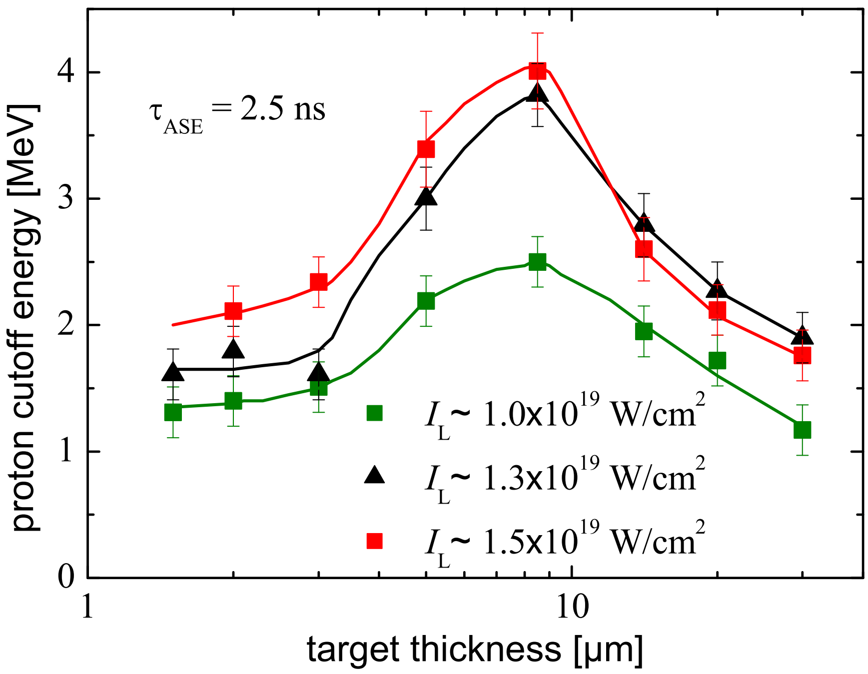

Figure 5.6: Proton cutoff energies for three different laser intensities achieved by changing the main-pulse energy. While the prepulse duration for all the laser shots was kept constant at $\tau_{\mathrm{ASE}} = 2.5\,\mathrm{ns}$, the laser intensity was varied between $I_{\mathrm{L}} = 1.0 \times 10^{19}\,\mathrm{W/cm^2}$ and $I_{\mathrm{L}} = 1.5 \times 10^{19}\,\mathrm{W/cm^2}$. Although the cutoff energies strongly depend on the laser intensity, the optimal target thickness remains unaffected.

5.3.3 Correlated Changes in the Spatial Profiles of the Proton Beam

To describe two further aspects concerning the energy spectra and the beam profiles of the protons, that also change when approaching the optimal target thickness, the results obtained with a prepulse duration of $\tau_{\mathrm{ASE}} = 2.5\,\mathrm{ns}$ and a laser intensity of $I_{\mathrm{L}} = 1.3 \times 10^{19}\,\mathrm{W/cm^2}$ are investigated in more detail. In section 5.2, target-thickness dependencies both for the cutoff energy and the temperature of the hot proton component were already found (cf. Fig. 5.4).

For the longer prepulse duration of $\tau_{\mathrm{ASE}} = 2.5\,\mathrm{ns}$, this behaviour is even more pronounced, as a longer prepulse is capable of producing a rear-side plasma with a longer density-scale length. The proton spectra for three foil thicknesses approaching the optimal target thickness ($d_{\mathrm{opt}} = 8.5\,\mu\mathrm{m}$ for this prepulse duration) are shown in Fig. 5.8 (a) together with the spatial beam profiles (b)–(d), that were recorded simultaneously. The inset of Fig. 5.8 (a) compares the cutoff energies with the temperature of the hottest proton component for all foils used with thicknesses between 1.5 and 30 μm.

Starting at the foil thickness of 5 μm, a second hotter component appears in the proton spectra having its highest quasi-temperature of $(4.0 \pm 0.6)\,\mathrm{MeV}$ at the optimal target thickness. At and above this thickness, a clear two-temperature distribution is obtained in the energy spectrum. The cutoff energies match the temperature of the hot component

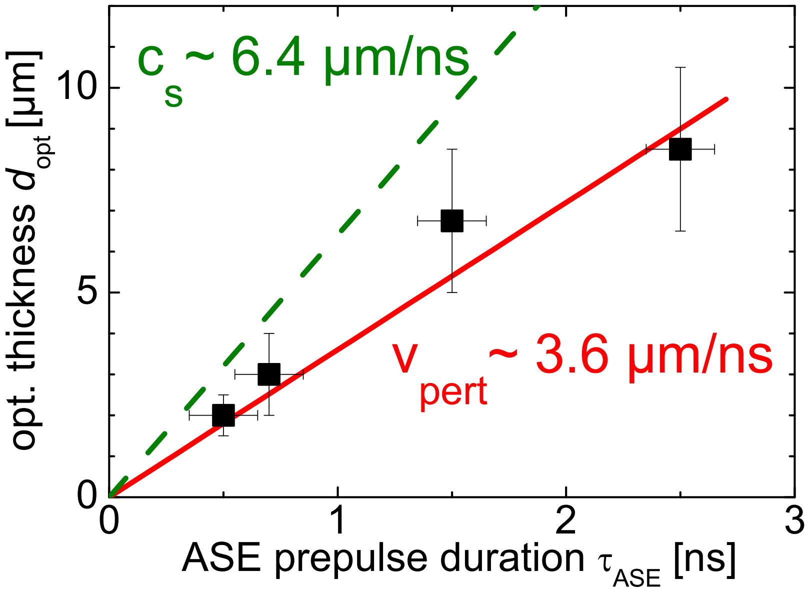

Figure 5.7: Correlation between optimal target thickness, d_{opt}, and ASE prepulse duration, τ_{ASE}. The experimentally found quasi-velocity of $v_{\text{pert}} = (3.6 \pm 0.6)\,\mu$m/ns given by the red line is compared to the sound speed, $c_s = 6.4\,\mu$m/ns, in cold aluminum indicated by the dashed green line.

within the error bars, while for thinner targets there is only one proton population in the energy spectrum. Its temperature of (250 ± 40) keV is always well below the maximum energy. This is due to the fact that the hotter proton component always shows a sharp energy cutoff, while the colder component does not.

Simultaneously with the appearance of an additional hotter component in the proton spectra, drastical changes in the spatial profile of the proton beam are also observed, when the target thickness is changed. This is shown in Fig. 5.8 (b)–(c). Note that, as the CR 39 detector was wrapped in a 12-μm aluminum foil, these far-field profiles correspond to those protons only, that have kinetic energies exceeding 900 keV. While for thinner foils (1.5, 2, and 3 μm) the beam profiles look similar to Fig. 5.8 (b), i.e. they are rather blurred and do not show any clear structure across the beam, the profiles appear well-collimated for thicker targets. To give an estimation of the proton-beam divergence, the corresponding half-opening angles are given in (b). They also apply for the other profiles. The collimation apparent in (c) and (d) persists in the proton beam for all thicker foils.

Due to the non-linear response of CR 39 on high proton fluxes, which will be described in the last section of this chapter, only qualitative conclusions can be drawn from such beam profiles. There appears to be a “ring”-like structure in the profile, i.e. coming from outer regions of the beam and moving towards its center, the proton flux seems to increase first and then to decrease again as it is described in chapter 4.4. The pictures shown here are brightness-inverted photographic images taken with a digital camera. On the first sight, brighter regions appear to correlate to higher proton fluxes. Such rings on CR 39 plates have also been observed by E. Clark *et al.* [13, 14] and M. Zepf *et al.* [44] and were interpreted as a signature of protons coming from the target *front* side and being deflected

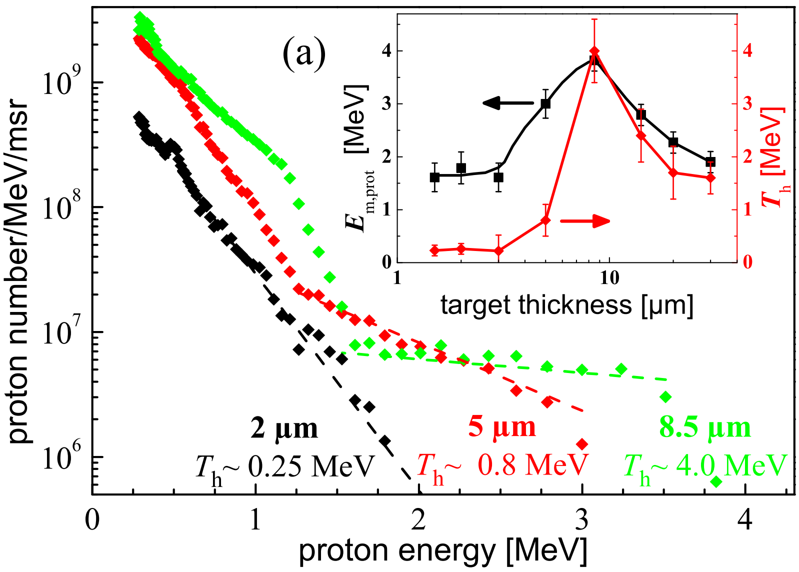

(a) Proton energy spectra

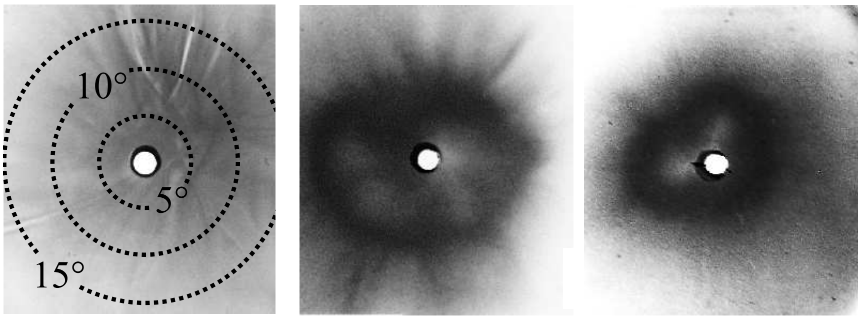

(b) 2-μm foil (c) 5-μm foil (d) 8.5-μm foil

Figure 5.8: Energy spectra (a) and spatial beam profiles on CR 39 plates (b)–(d) of protons accelerated from aluminum foils of 2 (b), 5 (c), and 8.5 μm (d) thickness, respectively. The targets were irradiated at a laser intensity of $I_L = 1.3 \times 10^{19}\,\mathrm{W/cm^2}$ and a prepulse duration of $\tau_{ASE} = 2.5\,\mathrm{ns}$. The inset in (a) gives the quasi-temperature of the hottest proton component for all foil thicknesses used. For the three given spectra the dashed lines correspond to these quasi-temperatures. The circles in (b) give half-opening angles of 5°, 10°, and 15° of the proton beam with respect to the target normal indicated by the white hole in the CR 39 plates. These angles apply for all profiles.

inside the target by the azimuthal magnetic fields associated with the hot-electron current. This interpretation does not comply with the model assumption about the origin of the fastest protons, according to which this hottest component appears only at and above the optimal target thickness and is accelerated at the target *rear* side. Y. Murakami *et al.* [46] report on similar rings observed on CR 39 plates that also recorded the spatial profile of proton beams accelerated from plastic targets. In this paper, the formation of such ring-like beam profiles is explained by toroidal magnetic fields at the rear surface of the target. These magnetic fields are generated by hot electrons that exit the target and are pulled back by the arising electrostatic fields forming a fountain structure as it will be described in Chapter 8.3. These magnetic fields in turn deflect the rear-side accelerated protons sideways from target normal direction. This gives rise to the ring-like beam profiles.

These two conflicting interpretations make different predictions about the origin of the ring-like beam profile. Therefore, the exact proton distribution within the "ring" has to be investigated by spectral measurements over the whole extension of the beam using the Thomson parabola. The results from these investigations will be presented in the next section proving that the ring structure is not real and but rather due to an artefact arising from the non-linear response of CR 39 on high proton fluxes. In the measurements presented here, it could be shown that the proton beam has no ring-like structure but a distribution with the peak of the proton flux exactly on its axis along the target normal direction.

5.4 Angularly Resolved Measurement of the Proton Spectra

This last section concentrates on angularly resolved spectral measurements of the proton beam, to obtain a characterisation of the protons as complete as possible, including changes of the energy spectra over the whole spatial extension of the beam. This provides a better understanding of the underlying acceleration processes. On the other hand, it allows a clarification of the origin of the "ring"-like features in the spatial profiles that were observed in the experiments and described in the last section.

5.4.1 Changes in the Experimental Setup

For this purpose, the target was rotated around its vertical axis as depicted in Fig. 5.9, while the position of all other diagnostics and in particular the angle between the main pulse and the Thomson parabola remained constant. This allowed an easy variation of the angle, φ, during the experiment without any changes in the target chamber or the setup of the diagnostics. The angle, φ, was limited to $\sim +13^\circ$ due to back reflection of the laser pulse as mentioned above.

On the other hand, a rotation of the target changed the laser intensity on the front side. During these measurements using an on-target energy of $\sim 700\,\mathrm{mJ}$, the averaged intensity on the target depending on the angle, φ, is estimated as

$$I_\mathrm{L}(\varphi) = \frac{\eta \cdot E_\mathrm{L}}{\tau_\mathrm{L} \cdot \pi r_\mathrm{f}^2 / \cos(30^\circ - \varphi)} = 1.34 \times 10^{19}\,\mathrm{W/cm^2} \cdot \cos(30^\circ - \varphi), \tag{5.2}$$

where $\eta \cdot E_\mathrm{L}$ is the fraction of the laser energy that is contained within the (elliptical) area $\pi r_\mathrm{f}^2 / \cos(30^\circ - \varphi)$, that corresponds to the first Airy-disc in the focal plane (cf. chapter 3.1). The case of $\varphi = 30^\circ$ corresponds to normal incidence with a circular focal spot on the target. As the target was rotated between the angles $\varphi = -9^\circ$ and $\varphi = +13^\circ$, the intensity varied between 1.04 and $1.29 \times 10^{19}\,\mathrm{W/cm^2}$, the higher intensity corresponding to a larger value of φ. A counteracting process arises due to the fact that the absorption of the *p*-polarised laser light and its conversion into hot electrons via resonance absorption is

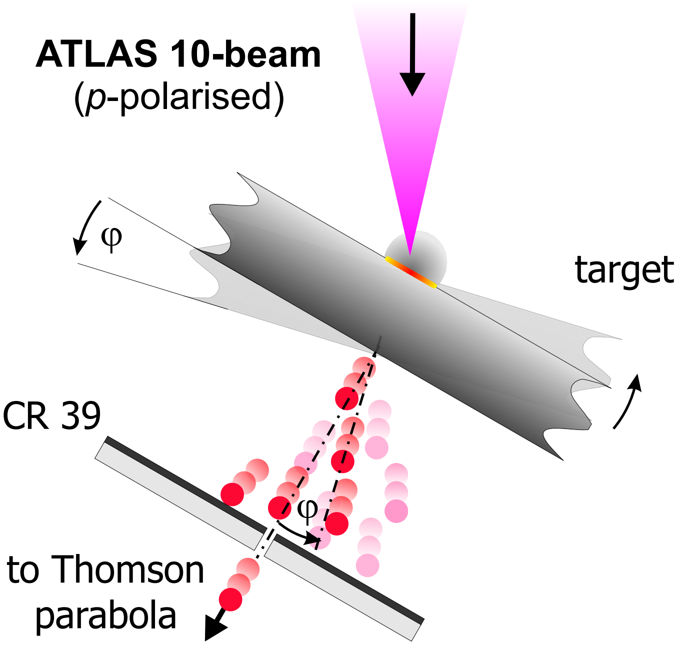

Figure 5.9: Experimental setup for the angularly resolved measurements of the proton spectra. While the angle between main pulse and Thomson parabola remains fixed, the target is rotated around its vertical axis by the angle, φ. The rotated target corresponds to $\varphi = +13°$. As the proton beam is emitted along the target normal direction, its imprint on the CR 39 plates is shifted correspondingly. The Thomson parabola then measures the spectrum under an angle, φ, from target normal direction.

enhanced for larger incident angles [59]. To some extent, this increased absorption might balance the associated reduction of the laser intensity. Furthermore, as the preplasma evolution on the target front side is a mixture of both a plane and a radial expansion, resulting in a convex sphere of the critical density where the laser light is absorbed, any effects associated with a rotation of the target are additionally reduced.

5.4.2 Measurement of Proton-Energy Spectra and Beam Profiles

Fig. 5.10 shows both the energy spectra (a) and the beam profiles (b)−(e) of the protons obtained for four different angles φ ($-7°, 0°, +5°$, and $+13°$). It is obvious that the beam profiles move as to follow the target rotation. The center of the profile is always rotated by the same angle as the target with an accuracy of $\pm 1°$, which was also the accuracy of the target alignment. This is in full agreement with the fact that similar proton features observed in different experiments [15,28] always appeared in the direction of the rear-side target normal.

The energy spectra of the protons were measured simultaneously in a direction corresponding to the position in the spatial profile that is indicated by the hole in the CR 39 plate. These holes are either in the center of the beam (c) where the proton flux appears to be lower or in the outer regions (b), (d), and (e) with apparently higher fluxes. But when comparing the beam profiles with the exact energy spectra (a), it can be concluded unambigously that in the center of the beam, i.e. for $\varphi = 0°$, the highest proton numbers are obtained and the larger the deviation from the center is, the more is the total proton number reduced. This clearly rules out a ring-like beam profile as in [13, 14, 46]. A detailed investigation of the CR 39 plates under an optical microscope reveals that coming from outer regions (i.e. from large angles φ), the proton pits are well separated in the beginning but then start to overlap corresponding to a region on the CR 39 which appears

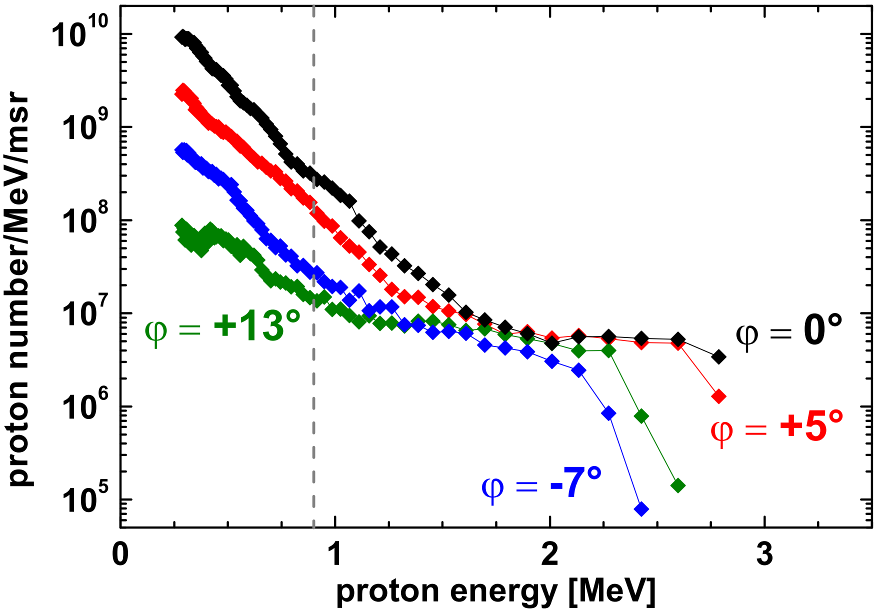

(a) Proton energy spectra

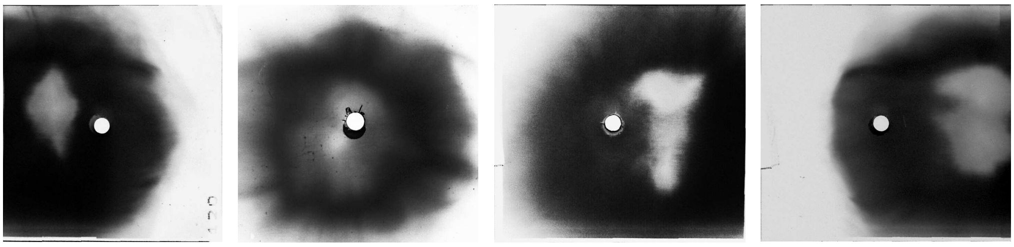

(b) $\varphi = -7°$ (c) $\varphi = 0°$ (d) $\varphi = +5°$ (e) $\varphi = +13°$

Figure 5.10: Energy spectra (a) and spatial beam profiles (b)–(e) of protons accelerated from 5-μm aluminum foils. The targets were irradiated at laser intensities, I_L, between 1.04 and $1.29 \times 10^{19}\,\mathrm{W/cm^2}$ depending on the rotation angle, φ, and with a constant prepulse duration of $\tau_\mathrm{ASE} = 500\,\mathrm{ps}$. The rotation angle was varied between $-7°$ (b) and $+13°$ (e). The center of the beam profile moves corresponding to the rotation of the target. This motion can be traced with an accuracy of $\pm 1°$. As the CR 39 was shielded with 12-μm aluminum foils, the profiles correspond to protons with $E_\mathrm{kin} \geq 900\,\mathrm{keV}$, indicated by the dashed vertical line in (a).

duller or darker when looked at with the bare eye or a digital camera. The proton flux increases further when approaching the center of the beam, as the spectral measurements reveal. But the CR 39 detector shows a different behaviour, namely a region appearing brighter or more transparent again. In this region, the proton pits are close together and therefore strongly overlap so that the surface appears to be plane again. This gives rise to the illusion of lower proton numbers when the plates are viewed by naked eye, although the real flux is maximal here.

More specifically, a much stronger reduction of the cold proton component is observed than of the hot one. While for the latter component, the temperature, the total number, and the cutoff energy only show a weak dependence on the angle φ, the cold component is much more affected. The lower the kinetic energy of the protons is, the stronger is the reduction for larger deviations from $\varphi = 0^\circ$. For the lowest detected proton energy of 300 keV, a reduction by two orders of magnitude is found for $\varphi = +13^\circ$ compared to $\varphi = 0^\circ$. In other words, the lower the proton energy, the stronger they are collimated along the target normal direction.

Figure 5.11: Photographic picture of a CR 39 plate, that was wrapped with two different aluminum filters during the exposure to the proton beam. While the upper part was covered with a 12-μm foil, showing a ring-like structure as on the previous CR 39 plates, corresponding to a strong increase in proton flux towards the center of the beam, the lower part was shielded with a 62-μm foil, that blocks protons below $E_\mathrm{kin} = 2.5\,\mathrm{MeV}$. In this part, we do not observe any ring, but a homogeneous disc that has a slightly smaller diameter. This beam profile exactly reproduces the spectral measurements presented in Fig. 5.10.

The different divergences of slower and faster protons are also seen in Fig. 5.11, where two parts of the beam profile were recorded with a differently filtered CR 39 plate, giving the spatial distribution of protons in two different energy intervals. While the upper part is dominated by the low-energy protons with $E_\mathrm{kin} \geq 900\,\mathrm{keV}$, that have much higher total numbers, the lower part was only sensitive to protons with $E_\mathrm{kin} \geq 2.5\,\mathrm{MeV}$. In the upper part, a clear “ring”-like dependence, which – as it was shown before – corresponds to a strong increase in the proton flux towards the center of the beam. In the lower part, a very even proton distribution is obtained, that matches the observations of the energy spectra for high proton energies.

5.4.3 Determination of the Energy-Resolved Divergence of the Protons

To gain a deeper insight into the spatial distribution of the electric field at the target rear side, that drives the proton acceleration, the proton-energy spectra measured under different angles from the target normal direction, φ, were examined in more detail. Each energy spectrum is subdivided into discrete energy intervals around a set of fixed energy values, E_j. Within each interval, the total number of protons, $N(E_j)$, is counted, giving an energy spectrum, $\mathrm{d}N(E_j)/\mathrm{d}E$, with a much lower energy resolution, smearing out shot-to-shot fluctuations. This is done for all proton spectra measured under different angles, φ, with a prepulse duration of $\tau_\mathrm{ASE} = 500\,\mathrm{ps}$. Then, the total proton numbers within a certain energy interval around E_j are compared for the different angles, φ, leading to a divergence of protons with kinetic energies exactly within this energy interval around E_j. Fig. 5.12 shows the deduced divergence angles (FWHM), α, for the different energies, E_j. A clear increase of the divergence angle, α, up to a maximum value of 20° is observed, when the proton energy increases to $\approx 1.8\,\mathrm{MeV}$. Beyond this energy, the divergence decreases again. This first behaviour exactly reproduces the observations in the energy spectra, that were already described above, where the low-temperature component has a significantly

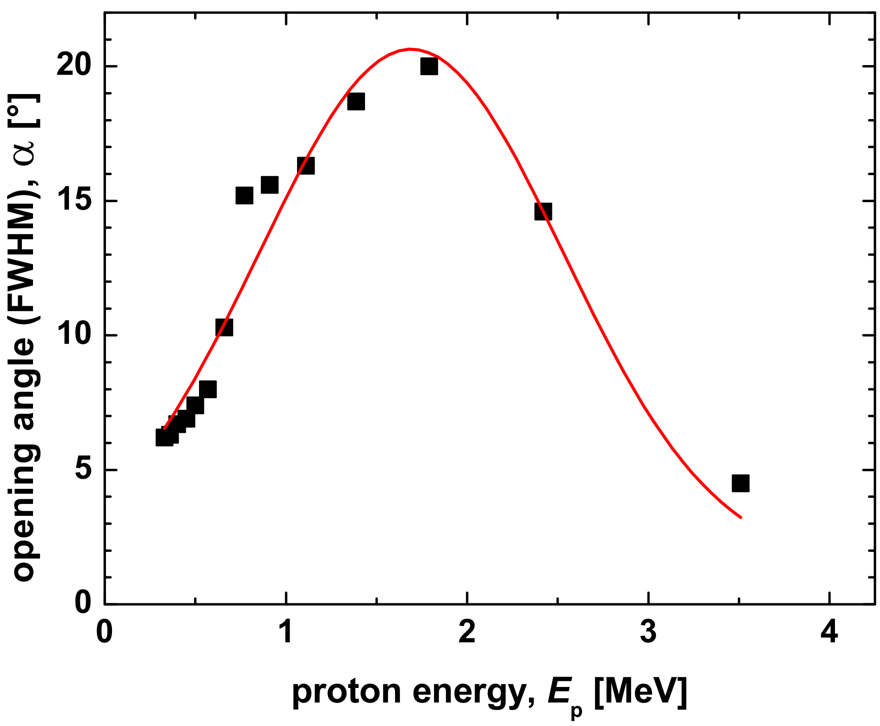

Figure 5.12: Half-opening angles, α, of protons of a certain energy, E_p. The black squares give the experimentally measured values, the red line is to guide the eye.

lower divergence than the hot component. However, for the highest proton energies, the divergence decreases again, which is in exact agreement with measurements carried out at the LULI laser published by M. Roth *et al.* [28] (for a detailed description of these measurements see e.g. [82]). In these experiments, the divergence of protons with kinetic energies between 2 MeV and 12 MeV was determined by measuring the opening angle of the spatial beam profiles obtained in a stack of radiochromic films and filter foils. Each film layer corresponded to a narrow proton-energy gap. Roth *et al.* found a continuous decrease of the divergence angle with increasing proton energy. However, this measurement was limited by the lower energy cutoff of 2 MeV in the experiment. This was the energy of protons detectable in the first film layer. In the experiments described here, the energy range could be extended down to 300 keV. In this range, again a strong decrease of the divergence is found. This behaviour can be explained by the spatial distribution of the electric field at the target rear side. It will be described in chapter 8.

5.4.4 Measurement with Different Prepulse Durations

Similar angular scans were carried out with a prepulse duration of $\tau_{ASE} = 2.5$ ns. The measured spectra are shown in Fig. 5.13. It is obvious from the spectra that for this case of a longer prepulse duration, the cold proton component is less strongly collimated than in the case of a short prepulse as it was discussed in the last section. Furthermore, the hot

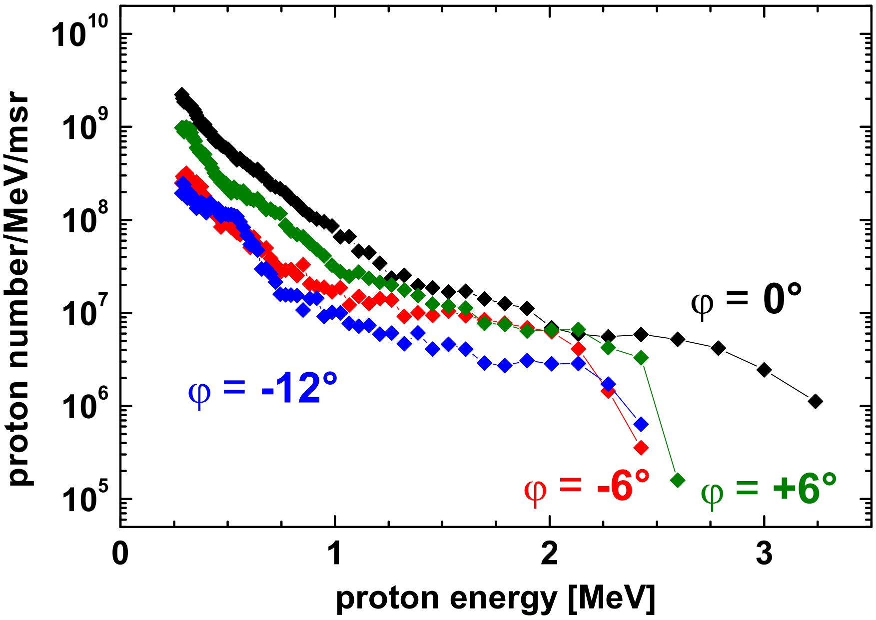

Figure 5.13: Proton energy spectra measured under different emission angles, φ, for a prepulse duration of $\tau_{\mathrm{ASE}} = 2.5\,\mathrm{ns}$. The foil thickness was again $5\,\mu\mathrm{m}$. The collimation of the cold proton component is weaker than for a shorter prepulse duration, as it is shown in Fig. 5.10.

proton component also decreases for larger deviation angles, φ.

The difference between the two prepulse durations is summarised in Fig. 5.14, where the proton numbers per msr (a) as well as the energy of the protons contained in the spectrum per msr (b) are given as a function of the emission angle, φ, for the two different prepulse durations. The experimental values are fitted by Gaussian distributions with different divergences (FWHM) of $\sim 11.5°$ and $\sim 15°$ for the prepulse durations of $0.5\,\mathrm{ns}$ and $2.5\,\mathrm{ns}$, respectively. For negative angles, φ, lower proton numbers and integrated energies are obtained for both prepulse durations compared to positive angles. This can be explained by the slightly higher intensity on the target front surface for positive angles, as it was estimated in the beginning of this section. Nevertheless, the differences in the proton spectra for the same deviation, $|\varphi|$, from the target normal in positive and negative direction arising from intensity variations on the target front side, appear to be small compared to the changes in the spectra arising when the emission angle is changed from $\varphi = 0°$ to larger angles.

Based on the Gaussian fits that are shown in Fig. 5.14, the total proton numbers and the total energy carried by the protons in the beam can be estimated by integration over the angle. For the prepulse duration of $\tau_{\mathrm{ASE}} = 500\,\mathrm{ps}$ one obtains

$$\begin{aligned} N_{\mathrm{ges}}(500\,\mathrm{ps}) &= 5.7 \times 10^{10} \qquad \text{and} \\ E_{\mathrm{ges}}(500\,\mathrm{ps}) &= 3.1 \times 10^{16}\,\mathrm{eV} = 4.9\,\mathrm{mJ}, \end{aligned}$$

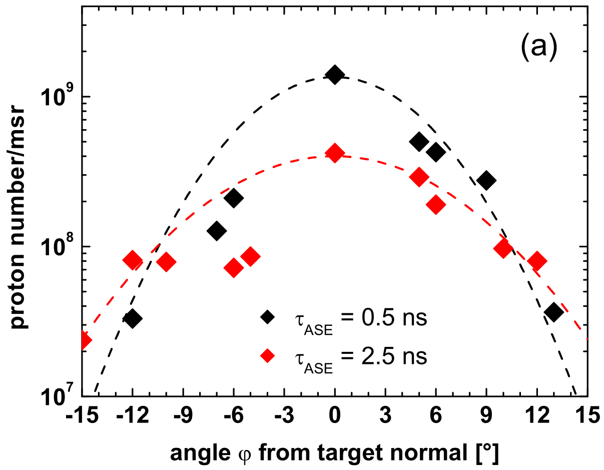

(a) Proton number per solid angle

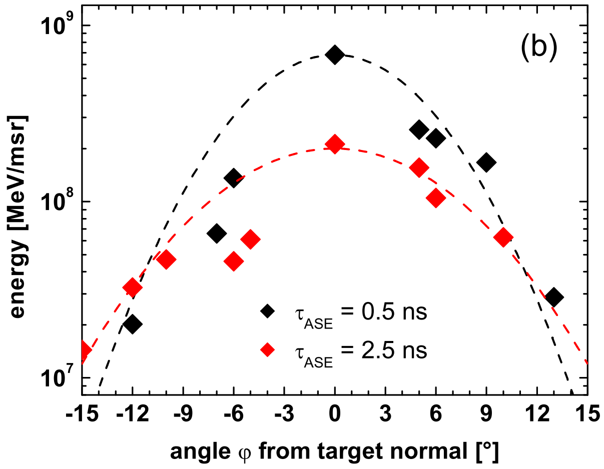

(b) Energy carried by the protons per solid angle

Figure 5.14: Proton number per solid angle (a) and energy carried by the protons per msr (b) as a function of the emission angle, φ, for two prepulse durations of 500 ps (black diamonds) and 2.5 ns (red diamonds). The dashed lines are Gaussian fits to the experimental data, yielding in both plots divergences (FWHM) of 11.5° and 15° for the prepulse durations of 500 ps and 2.5 ns, respectively.

while for the longer prepulse of $\tau_{\mathrm{ASE}} = 2.5\,\mathrm{ns}$

$$\begin{aligned} N_{\mathrm{ges}}(2.5\,\mathrm{ns}) &= 3.0\times 10^{10} \qquad\qquad \text{and} \\ E_{\mathrm{ges}}(2.5\,\mathrm{ns}) &= 1.5\times 10^{16}\,\mathrm{eV} = 2.4\,\mathrm{mJ} \end{aligned}$$

is found. The conversion efficiency of laser-pulse energy ($E_{\mathrm{L}} \approx 700\,\mathrm{mJ}$ for these shots) into protons with kinetic energies exceeding 300 keV is therefore 0.7% and 0.34% for the prepulse durations of 500 ps and 2.5 ns, respectively.

5.5 Summary of the Experimental Observations

The experimental findings concerning the characterisation of the laser-accelerated proton beam can be summarised as follows:

- A strong dependence of the appearance of one or more temperatures in the energy spectra, the total number, and the maximum kinetic energy of the protons on the aluminum-foil thickness was demonstrated. An optimal target thickness, d_{opt}, was found at which the proton cutoff energy and the temperature of the hottest component in the spectrum are maximal.
- By a controlled variation of the ASE prepulse duration, τ_{ASE}, a clear correlation between the optimal target thickness and the prepulse duration was found. This correlation is approximately linear.
- While the proton cutoff energy strongly depends on the laser-pulse energy and the combination of target thickness and prepulse duration, the optimal target thickness, d_{opt}, depends on the prepulse duration only.
- The proton spectra and the spatial beam profiles change significantly around d_{opt}, a correlated appearance both of a significantly hotter proton component in the energy spectrum and of a collimated feature in the beam profiles, exactly aligned along the target normal direction was observed.
- The “ring”-like structure in the beam profiles recorded on CR 39 plates is not real but an artefact of the non-linear response of the detector on high proton fluxes. This was proven by angularly resolved measurements of the proton spectra revealing a strong collimation of the cold proton component and a large divergence of the hotter component for short prepulses.
- The proton divergence strongly depends on their kinetic energy. While for energies above 2 MeV the divergence decreases with the proton energy, what is in exact agreement with measurements from other groups, a strong collimation of the low energy protons could be demonstrated for the first time.
- The total number of protons accelerated from a 5-μm aluminum foil to energies above 300 keV is 5.7×10^{10} and 3.0×10^{10} for the prepulse durations of 500 ps and 2.5 ns, respectively. These protons carry a total energy of 4.9 mJ ($\tau_{\mathrm{ASE}} = 500\,\mathrm{ps}$) and 2.4 mJ ($\tau_{\mathrm{ASE}} = 2.5\,\mathrm{ns}$) yielding a conversion efficiency of 0.7% and 0.34% from a laser-pulse energy of $E_{\mathrm{L}} \approx 700\,\mathrm{mJ}$ into protons.

Chapter 6

Influence of the Laser Prepulse: Simulations with the Code MULTI-FS

In the experiments described in chapter 5, a strong influence of the laser prepulse duration, τ_{ASE}, on the acceleration of protons was observed. The highest kinetic proton energies were achieved with foils having an optimal thickness, d_{opt}. This optimal thickness was found to increase with increasing prepulse duration (cf. Figs. 5.5 and 5.7). This behaviour could be explained qualitatively by assuming that prepulse-induced changes in the target properties such as an expansion of the target and a formation of a rear-side ion-density gradient strongly influence the rear-side acceleration. Triggered by the prepulse impinging on the front side, it appears natural that the changes at the rear side of the target depend on its thickness. This chapter deals with the quantitative description of prepulse-induced effects on the target properties by means of numerical simulations.

6.1 Motivation for Hydro Simulations

The effect of the ASE prepulse on the rear-side acceleration of protons was observed for the first time by M. Roth *et al.* in experiments using gold targets, that were irradiated with slightly higher laser intensities [37]. In these experiments, the number of protons with kinetic energies above the detection threshold of $\sim 2\,\mathrm{MeV}$ were compared for two different prepulse durations using targets with a constant thickness of $48\,\mu\mathrm{m}$. For a prepulse of $5\,\mathrm{ns}$ duration having an intensity level of $\sim 5 \times 10^{12}\,\mathrm{W/cm^2}$, a strong proton signal was observed, while for a 10-ns prepulse, no protons with energies exceeding $2\,\mathrm{MeV}$ could be detected. These two experimental values only allow a rough estimate of the influence of the prepulse. Based on results from MULTI simulations [114], the authors concluded that the break-out of a shock wave at the back of the target that has been launched by the prepulse on the front side and has travelled through the target was responsible for the diminution of the proton cutoff energy below the detection threshold of $2\,\mathrm{MeV}$.

For the experiments presented in this thesis with slightly different laser conditions, especially a much lower prepulse intensity level, which could be carried out in much greater detail and with higher accuracy, the shock wave propagating through the material alone is not sufficient to explain the results. To gain a deeper insight into the processes involved, detailed simulations using the code MULTI-FS [50] were carried out. These simulations give a plausible explanation for the experimental results.

6.2 The 1-D Hydrodynamic Code MULTI-FS

The one-dimensional hydrodynamic code MULTI-FS [50] is an extended version of the code MULTI [114] developed to describe the radiation hydrodynamics in experiments relevant for inertial confinement fusion. Both versions of the code describe the hydrodynamic processes in solid targets triggered by laser irradiation. The code uses Lagrangian coordinates [115] including electronic heat conduction and multigroup radiation transport. In Lagrangian coordinates the density, pressure, and velocity of the target material are not determined at a *fixed position in space* as in Eulerian coordinates, but the changes of these quantities are described for a *fluid element* that moves in space. Initially, the target foil is subdivided into thin layers, each representing such a 1-D fluid element. The temporal evolution of each layer is described by the basic equations of hydrodynamics [115] that express the conservation of mass, momentum, and total energy in each layer. The internal energy of each fluid element can be changed by changing its volume, by electronic heat conduction, and by the absorption and emission of radiation. The hydrodynamic equations have to be completed by equations of state (EOS) for the internal energy and the pressure as functions of the local density and temperature. This is implemented into the code by tabulated values obtained from the Los Alamos SESAME EOS [116]. The code treats radiative effects by using tabulated values for the (frequency-dependent) radiative absorption and emission coefficients that are also functions of density and temperature. These tabulated values (also called opacity tables) are obtained from the SNOP atomic physics code, as it is described in [117].

While in MULTI, the laser-light absorption is described by Beer's law that only holds true for shallow plasma gradients (density-scale length $L_\mathrm{p} \gg \lambda_\mathrm{L}$), MULTI-FS explicitly solves Maxwell's equations to correctly describe the light absorption also in steep-gradient plasmas. Furthermore, MULTI-FS includes a more realistic model for the electrical and thermal conductivity in the target covering a wide range of densities and temperatures. As the intensity of the ASE prepulse as well as the initial temperature of the target material were very low in the experiments described in this thesis, a correct description of the cold solid state in the simulation is of great importance. The energy exchange between electrons and ions as well as the thermal conductivity of the material depend on the electron-collision frequency, ν_e. In a plasma at high temperatures, the electron collisions are Coulomb-like, and ν_e is described by Spitzer's law. Here, ν_e is proportional to $T_\mathrm{e}{}^{-3/2}$, but for low electron temperatures, the collision frequency would diverge in this model. However, in a solid below the Fermi temperature, T_F, which is 11.7 eV for aluminum, the electrons are in a degenerate state, and the collision frequency no longer depends on the electron temperature, but it is governed by the scattering of electrons by lattice vibrations (phonons). In this case, ν_e is proportional to the temperature of the ions, T_i. Here, ν_e converges for low temperatures. In MULTI-FS, a formula interpolated between these two regimes is utilized to correctly describe the thermal conductivity in aluminum in all states ranging from the solid state at room temperature up to the plasma state. Furthermore, MULTI-FS uses separate SESAME EOS for electrons and ions, what becomes the more important, the lower the initial temperatures are. This allows realistic simulations with intensities and initial temperatures as low as in the experiments reported here.

6.3 Details of the Simulations

The simulation starts with an aluminum target that is initially at room temperature ($k_B T_e = k_B T_i = 0.03\,\mathrm{eV}$). The laser pulse implemented into the code follows the measured ASE-prepulse evolution that is again shown in Fig. 6.1. For the different prepulse durations, τ_{ASE}, used in the experiment, the ASE prepulse is modeled in the following way. Its intensity rises linearly from 0 to $8 \times 10^{11}\,\mathrm{W/cm^2}$ within a certain rise time, τ_{rise}, that slightly changes for the different prepulse durations. The peak ASE intensity corresponds to a relative ASE level of 4×10^{-8} for a main pulse intensity of $I_L = 2 \times 10^{19}\,\mathrm{W/cm^2}$, which was the peak intensity on the target in our experiments assuming the same focusability of prepulse and main pulse. After the time equivalent to the prepulse duration, the simulation gives the target properties at the moment of the main pulse arrival.

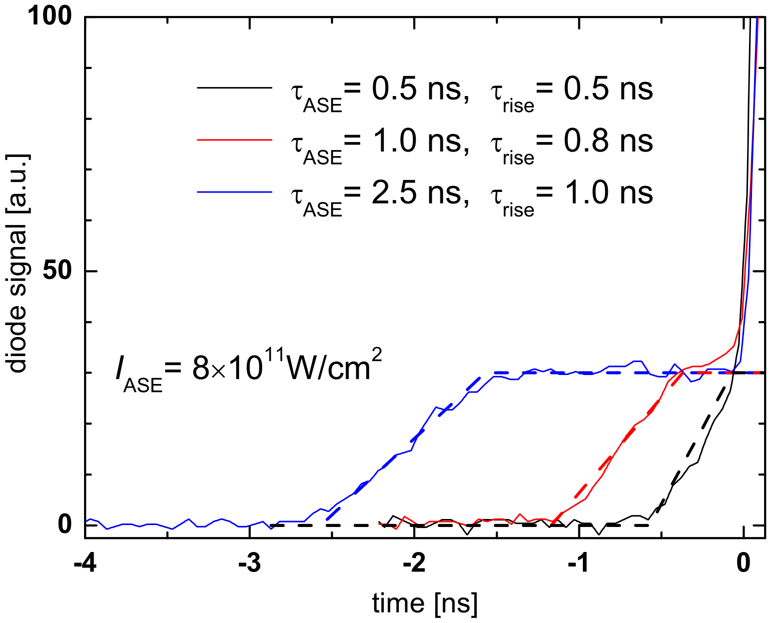

Figure 6.1: Linear fits (dashed lines) to the measured (solid lines) temporal evolution of the ASE intensity for different prepulse durations. The three solid lines correspond to $\tau_{\mathrm{ASE}} = 2.5\,\mathrm{ns}$ (blue), $1.0\,\mathrm{ns}$ (red), and $0.5\,\mathrm{ns}$ (black), respectively. At $t = 0$ the main pulse starts, what is no longer included in the MULTI-FS simulations. During τ_{rise}, the prepulse-intensity increases linearly to its maximum value of $8 \times 10^{11}\,\mathrm{W/cm^2}$.

Fig. 6.2 shows the schematic initial cell layout used in the simulations. The laser impinges onto the target from the left. The cell widths in the front- (A) and rear-side part (C) of the target decrease towards the surfaces to describe the laser-target interaction at the front and the rear-side plasma evolution at the back of the target with higher accuracy. The central part (B) has a constant cell width, the cell number is varied to obtain different total target thicknesses.

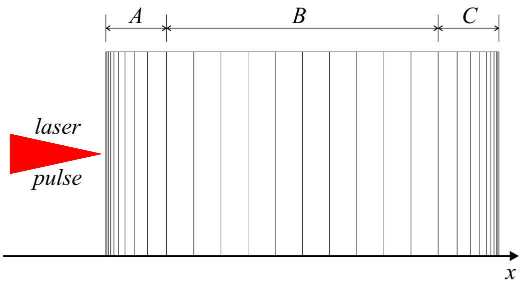

Figure 6.2: Initial configuration of the Lagrangian cells in the target used in the MULTI-FS simulations.

6.4 Simulation Results from MULTI-FS

Fig. 6.3 shows results from MULTI-FS calculations for the temporal evolution of the target foil under the influence of the ASE prepulse. The lines give the position of the interfaces of the Lagrangian cells as a function of time. The prepulse coming from the bottom impinging on the target front side at $x = 0$ deposits its energy in the first layers. Here, the target material is heated up to temperatures of $\sim 100\,\mathrm{eV}$, generating a low-density blow-off plasma expanding into the vacuum, as it is indicated in the plot by the lines bending down to negative $x-$values.

As a consequence of the front-side plasma expansion into the vacuum and the associated repulsion, a shock wave is launched into the target, as it is indicated by the dashed blue line. The front of this shock wave travels exactly with the sound speed in cold aluminum, $c_s = 6.4\,\mu\mathrm{m}/\mathrm{ns}$ [113]. However, when this shock front arrives at the target rear side, the caused changes remain small here, as the shock itself is only weak. The simulations reveal that the target material is only heated by $\sim 100°\mathrm{K}$, when the shock front passes. The pressure difference in front of and behind the shock front is of the order of $0.1\,\mathrm{Mbar}$ only. Furthermore, the simulations show that the shock-wave arrival does not trigger the formation of an ion density gradient at the rear side, as the whole foil is accelerated in laser direction after the shock break-out due to the repulsion from the blow-off plasma. However, when the entire foil starts to move in laser direction, the effective thickness, which is the thickness of the overdense plasma layer, increases. While the *relative* increase of the effective thickness is small for thicker foils, it is not negligible for the thinnest foils. Here, the arrival of the shock wave at the rear side appears to have a significant effect.

Additionally, the bulk of the target is radiatively heated by X-rays generated in the focus of the ASE prepulse on the target front side. As mentioned above, the emission of this radiation on the front side is determined by the local temperature and pressure of the material. The radiation penetrates the entire target material, a part of it is locally absorbed, again depending on the local target density and temperature but also on the frequency of the radiation. A comparison between the radiation intensities on the target front and rear side is shown in Fig. 6.4. While in (a), the evolution of the front- and rear-side intensities integrated over the intire frequency spectrum are shown, (b) gives the spectral intensities at the front- and rear-side at $t = 1\,\mathrm{ns}$ for different initial target thicknesses. Obviously the effect of radiative heating is strongly diminished for thicker foils, where the total radiation intensity is lower by more than one order of magnitude compared to the thinnest foil, as shown in (a). Figure 6.4 (b) shows that only the radiation from the $K-$shell emission

($E_{\text{photon}} \approx 1.5\,\text{keV}$) in the high-temperature layers on the target front side heats the bulk

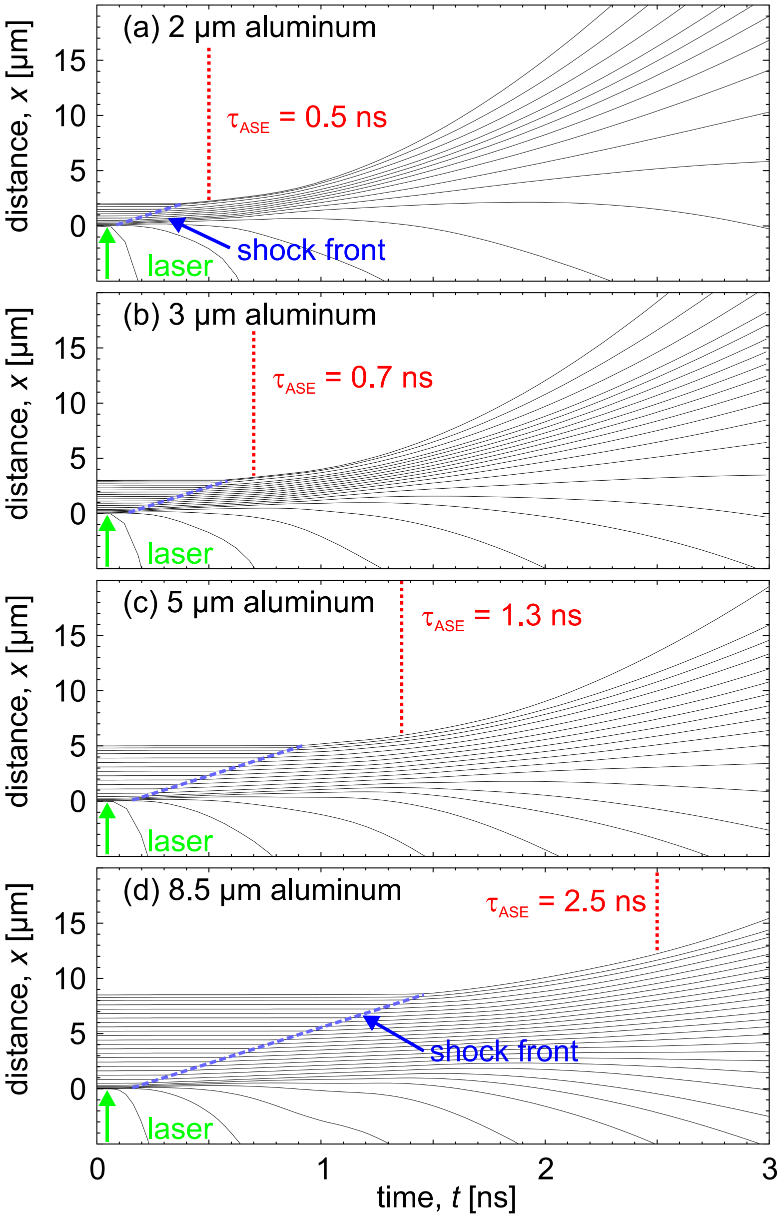

Figure 6.3: Motion of the Lagrangian cell interfaces in the target foil under the irradiance of the ASE prepulse for foils of 2-μm (a), 3-μm (b), 5-μm (c), and 8.5-μm thickness (d). The ASE prepulse is incident on the target front side at $x = 0$ from below. The position of the shock-wave front propagating through the target is indicated by the dashed blue lines. The dotted red lines indicate the prepulse durations for which each target thickness is the optimal value as measured in the experiment. These durations approximately correlate with the onset of the rapid expansion of the target rear side.

of the target, as it is optically thin for these photon energies. Photons with energies below 700 eV (mainly from $L-$shell emission) have a significantly shorter mean free path and cannot reach the rear surface, for these photons the target is optically thick.

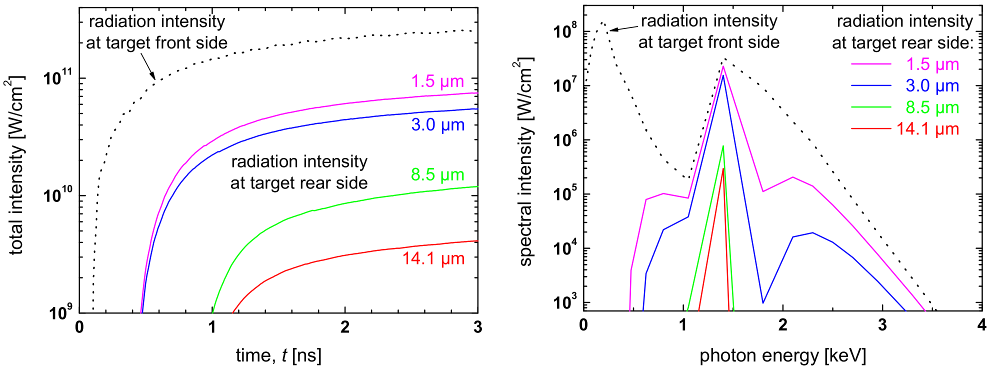

(a) Comparison of the evolution of the total X-ray intensity between target front and rear side for differently thick aluminum targets.

(b) Comparison of the spectral X-ray intensity at $t = 1\,\mathrm{ns}$ between target front and rear side for differently thick aluminum targets.

Figure 6.4: X-ray radiation intensities calculated with MULTI-FS simulations. The dotted lines give the intensity at the front side, the solid lines indicate the intensities at the rear surface of targets with different thicknesses.

Due to the local absorption of radiation the temperature is increased. At the target rear surface, this results in the formation of an ion-density gradient that can be described by a self-similar solution at the target rear surface as discussed in chapter 2. The expanison of the aluminum ions with mass $m_{\mathrm{ion}} = 27u$ is driven by the electrons with the temperature T_{e}. The ion density follows eq. (2.61), its scale length is given by $L_{\mathrm{p}} = c_{\mathrm{s}}t = t\sqrt{(Zk_{\mathrm{B}}T_{\mathrm{e}} + k_{\mathrm{B}}T_{\mathrm{i}})/m_{\mathrm{ion}}} \approx t\sqrt{(Z+1)k_{\mathrm{B}}T_{\mathrm{e}}/m_{\mathrm{i}}}$, where $T_{\mathrm{i}} \approx T_{\mathrm{e}}$. For a 3-$\mu$m foil, MULTI-FS predicts a rear-side temperature that is assumed – for these simple considerations – to be constant at a value of $0.5\,\mathrm{eV}$ over the time of $\sim 1.3\,\mathrm{ns}$ between the increase of the rear-side temperature above the boiling point of $0.24\,\mathrm{eV}$ and the arrival of the main pulse at the front side, when the proton acceleration sets in. This results in a density-scale length of $L_{\mathrm{p}} \approx 2.5\,\mu\mathrm{m}$. As it will be shown in chapter 7, the formation of a rear-side plasma causes a significant reduction of the rear-side acceleration fields.

The heating of the rear side is strongly reduced for thicker targets, as the radiation is already absorbed inside the target resulting in a lower intensity at the back, as shown in Fig. 6.4. Consequently, the expansion and the associated formation of a density gradient are much slower compared to thinner foils. Therefore, the prepulse-induced changes of the rear-side properties are significantly weaker and set in at a later time for thick foils. This agrees well with the experimental observations, where the ASE prepulse can be longer before the proton acceleration is affected. In Fig. 6.3 the experimentally found prepulse duration, for which each target has the optimal thickness, is indicated by vertical dotted red lines. For the first three thicknesses shown here, this agrees with the onset of the expansion of the target, while for the 8.5-μm foil, the rear-side expansion already starts earlier. One possible explanation for this fact could be the planar geometry the code is based on. When the focal spot of the prepulse is larger than or comparable to the target thickness, as it is the case for the first three thicknesses, the planar description is valid. For thicker targets, however, the effect due to radiative heating is overestimated in planar geometry. A 2-dimensional description would lead to a lower radiation intensity and thus a lower expansion velocity. This would lead to a later onset of the rear-side target expansion as it is expected from the experimental findings.

Finally, the electron density distributions for different initial target thicknesses after a 2.5-ns irradiation by the ASE prepulse is determined. This is shown in Fig. 6.5. All the

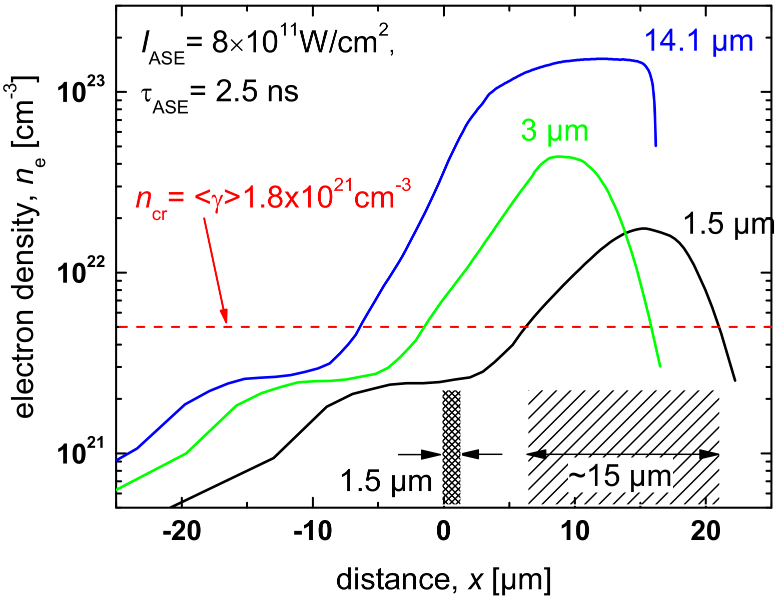

Figure 6.5: Electron-density distributions in targets of different initial thicknesses after the irradiation with an ASE prepulse of 2.5-ns duration and of $8 \times 10^{11}\,\mathrm{W/cm^2}$ peak intensity from the left. The targets had initial thicknesses of 1.5 μm (black line), 3 μm (green line), and 14.1 μm (blue line). The red line indicates the (relativistic) critical density. The two shaded regions depict the initial and the effective thickness for the 1.5-μm foil.

targets no longer have their initial thickness, but they have expanded on both sides. The front side expansion due to the laser irradiation extends far into the front-half space for all three targets. When the high-intensity main pulse having a wave length of 790 nm and an intensity that corresponds to an averaged Lorentz factor of $\langle\gamma\rangle \approx 2.8$ is interacting with the front-side plasma, it propagates up to the relativistic critical density of $n_e = 5.0 \times 10^{21}\,\mathrm{cm^{-3}}$, where the major part of its energy is converted into fast electrons. This density defines the effective thickness of the foil. At the rear side, a plasma gradient has been formed due to radiative heating for the foils of 1.5-μm and 3-μm thickness, the foil of 14.1 μm thickness still shows a sharp density drop[1]. For all three foils, the effective target thickness has increased. The initially 1.5-μm thick target has an effective thickness of $\sim$15 μm and a rear-side ion-density gradient with a scale length of $\sim$2.0 μm. For the 3-μm target, the effective thickness is $\sim$18 μm and the rear-side scale length is $\sim$1.5 μm. This approximately matches the simple estimation for the scale length of $L_p \approx 2.5\,\mu$m that was given above. For the initially 14.1-μm thick foil, the relative increase of the effective

---

[1] As MULTI-FS predicts a constant ionisation degree at the target rear surface, the ion and electron densities have the same spatial distributions and density gradients.

thickness to $\sim 22\,\mu$m is much smaller and the rear-side gradient is much steeper with a scale length smaller than $0.2\,\mu$m.

At the target front side, the electron density gradient depends only very weakly on the target thickness. For all different thicknesses used in the experiment, the front-side electron-density gradient varies between $3.5\,\mu$m for the thickest foils and $4.5\,\mu$m for the 1.5-μm foil for the prepulse duration of $\tau_{\text{ASE}} = 2.5\,$ns (these cases are shown in Fig. 6.5). For the shortest prepulse duration of $\tau_{\text{ASE}} = 0.5\,$ns, MULTI-FS predicts a constant value of $0.5\,\mu$m for all target thicknesses. Furthermore, the position of the critical density is only shifted within $\approx 15\,\mu$m, what is below the Rayleigh length of the focusing optics. This strongly suggests that the process of electron acceleration at the target front side remains unaffected *for a constant prepulse duration*, when the target thickness is changed. It might change for different prepulse duration also leading to a different injection angle of the electron beam into the target, as it was discussed in chapter 2.2. This effect was recently observed in an ongoing experiment using the same laser system at MPQ [118].

6.5 Summary of the MULTI-FS Simulations

- The ASE prepulse impinging on the target heats up the front surface and increases the effective target thickness. A shock wave is launched into the target.
- Additionally, the target material is radiatively heated due to X-rays generated in the focus of the prepulse. Due to the heating of the target rear side an ion-density gradient is formed. The rear-side heating is strongly reduced for thicker targets due to absorption of the radiation in the target. Furthermore, the relative increase of the target thickness due to the prepulse is much less pronounced for thicker foils.
- Assuming a cold and unexpanded target and a shock wave propagating with the sound speed of the cold material as in [37] is not sufficient to explain our experimental observations, as in our experiments the shock wave is too weak. Here, the radiative heating has to be taken into account.
- The front-side electron-density gradient remains almost constant for a fixed prepulse duration and all target thicknesses used in the experiments implying that the electron acceleration remains unaffected for a scan of the target thicknesses with a fixed value of τ_{ASE}.

Chapter 7

A One-Dimensional Simulation Code for the Rear-Side Acceleration of Protons

In this chapter, a one-dimensional simulation code will be introduced that was newly developed to describe the process of proton acceleration at the target rear side. After a detailed description of the simulation code itself the validity of the analytical formulas derived in chapter 2 is shown and the effect of an initial proton-density gradient at the target rear side is investigated.

7.1 Description of the Simulation Code

The process of proton acceleration at the rear side of the target is described by means of a 1-dimensional simulation code, that is based on a 1-D model by Crow *et al.* [84]. Published in 1975, it was developed to describe the ion acceleration in laser-plasma interactions using ns-pulses, which were the shortest pulses available at that time.

The physical picture of the rear-side acceleration is the same, as it was already described in chapter 2. The gradient of the rear-side potential, which initiates the proton acceleration, depends on the initial density, n_{e0}, and the temperature, T_e, of the hot-electron component, as it was shown in chapter 2. But furthermore, it depends on the initial density distribution of the protons at the rear side before the acceleration starts. The analytical solution derived in chapter 2 is valid for an initially step-like distribution only. The case of a preformed plasma at the target rear surface having an exponential drop in the proton density cannot be treated analytically. Such a case corresponds to a plasma formation due to the prepulse-launched heat wave arriving at the back of the target. This case will therefore be investigated using this simulation code. After the acceleration of the protons has started, the proton distribution expands away from the target-rear surface, additionally affecting the gradient of the rear-side potential. All these effects are included in the simulation, giving a detailed insight into the acceleration process.

7.1.1 Set of Equations Solved by the Code

The proton acceleration is described by the following set of equations including the Poisson equation, the equation of motion, and the equation of continuity for the protons:

$$\begin{aligned}
\varepsilon_0 \frac{\partial^2 \Phi_{\mathrm{el}}(x,t)}{\partial x^2} &= e\Big[n_{\mathrm{e}}(x,t) - n_{\mathrm{p}}(x,t)\Big], && (7.1)\\
\mathcal{E}(x,t) &= -\frac{\partial}{\partial x}\Phi_{\mathrm{el}}(x,t), && (7.2)\\
\frac{\partial v_{\mathrm{p}}(x,t)}{\partial t} + v_{\mathrm{p}}(x,t)\frac{\partial v_{\mathrm{p}}(x,t)}{\partial x} &= \frac{e}{m_{\mathrm{p}}}\mathcal{E}(x,t), \qquad \text{and} && (7.3)\\
\frac{\partial n_{\mathrm{p}}(x,t)}{\partial t} + \frac{\partial}{\partial x}\Big[n_{\mathrm{p}}(x,t)\cdot v_{\mathrm{p}}(x,t)\Big] &= 0. && (7.4)
\end{aligned}$$

Here, $\Phi_{\mathrm{el}}(x,t)$ is the potential and $\mathcal{E}(x,t)$ the electric field arising from the charge separation, that is described by the electron and proton densities, $n_{\mathrm{e}}(x,t)$ and $n_{\mathrm{p}}(x,t)$. During the acceleration process the proton-velocity distribution, $v_{\mathrm{p}}(x,t)$, changes. This set of equations is integrated numerically at discrete times, t_k, leading to new proton-density and -velocity distributions for the next time step, t_{k+1}.

7.1.2 Initial Conditions

The acceleration of the protons, that is driven by the electrostatic field set up by the hot electrons leaking out of the back of the target, is described by the evolution of the density and velocity distributions, $n_{\mathrm{p}}(x,t)$ and $v_{\mathrm{p}}(x,t)$, of the protons. These quantities are numerically calculated at discrete time steps, t_k, that are separated by a constant time interval, Δt. The electron distribution, $n_{\mathrm{e}}(x,t)$, with an initial value, $n_{\mathrm{e}0}$, and a Boltzmann-like temperature, T_{e}, is assumed to be in thermal equilibrium with the electrostatic potential, $\Phi_{\mathrm{el}}(x,t)$, **for all times $\boldsymbol{t \geq 0}$** during the whole acceleration process:

$$n_{\mathrm{e}}(x,t) = n_{\mathrm{e}0}\cdot \exp\left[\frac{e\Phi_{\mathrm{el}}(x,t)}{k_{\mathrm{B}}T_{\mathrm{e}}}\right] \qquad (7.5)$$

The initial proton distribution can either be step-like or it can drop exponentially with a characteristic density-scale length, L_{p}. The former situation is the same as it was introduced in chapter 2, the latter takes into account the effect of a rear-side expansion due to the prepulse-induced shock wave. Beyond $x_{\max}(0)$, which is the initial position of the proton front before the acceleration starts, the density drops to 0:

$$n_{\mathrm{p}}(x,0) = \begin{cases} n_{\mathrm{e}0} & \text{for} \quad x \leq 0 \\ n_{\mathrm{e}0}\cdot\exp\{-x/L_{\mathrm{p}}\} & \text{for} \quad 0 \leq x \leq x_{\max}(0) \\ 0 & \text{for} \quad x_{\max}(0) < x. \end{cases} \qquad (7.6)$$

As from the prepulse-induced plasma formation at the rear side, that acts over several 100's of ps or even ns, the effective energy gain of the protons is small compared to the subsequent acceleration by the MeV-electrons, the protons in the initial density profile are assumed to be at rest before the acceleration starts, i.e. $v_{\mathrm{p}}(x,0) \equiv 0$.

7.1.3 Calculation of the Electrostatic Potential

At each time step $t_k \geq 0$, the electrostatic potential, $\Phi_{\mathrm{el}}(x,t_k)$, and the electron-density distribution, $n_{\mathrm{e}}(x,t_k)$, that is described by eq. (7.5), are obtained by numerically solving the Poisson equation including the momentary proton-density distribution, $n_{\mathrm{p}}(x,t_k)$. This numerical integration, that is carried out over the distance, x, is devided into two parts.

First the Poisson equation

$$\varepsilon_0 \frac{\partial^2 \Phi_{\mathrm{el}}(x,t_k)}{\partial x^2} = e\left[n_{\mathrm{e0}} \cdot \exp\left[\frac{e\Phi_{\mathrm{el}}(x,t_k)}{k_{\mathrm{B}}T_{\mathrm{e}}}\right] - n_{\mathrm{p}}(x,t_k)\right] \tag{7.7}$$

is integrated in the region where both electrons and protons are present starting from the momentary position of the proton front, $x_{\max} = x_{\max}(t_k)$, to $x \longrightarrow -\infty$. As eq. (7.7) is a second-order differential equation, that does not depend on the first derivative of the potential, $\partial\Phi_{\mathrm{el}}(x,t_k)/\partial x$, Stoermer's rule can be used for integration [119]. For this integration, the boundary conditions are not given at the position of the proton front, $x_{\max}$, what would be necessary for the initialisation of the numerical integration. However, the potential and the electric field have to vanish for $x \longrightarrow -\infty$ to provide charge neutrality in the undisturbed plasma. A so-called *shooting method* is used to overcome this problem [87, 119]. The initial value of the potential, $\Phi_{\mathrm{el}}(x_{\max})$, that also determines the slope of the potential, $\Phi_{\mathrm{el}}{}'(x_{\max})$, as it will be shown in a moment, is guessed and the numerical integration is carried out. Depending on the behaviour of $\Phi_{\mathrm{el}}(x)$ for $x \longrightarrow -\infty$ with the guessed value, the starting value of the potential is varied, until the left boundary conditions, i.e. $\Phi_{\mathrm{el}}(x) \longrightarrow 0$ and $\Phi_{\mathrm{el}}{}'(x) \longrightarrow 0$ for $x \longrightarrow -\infty$, are fulfilled. In the simulation, this is achieved with an accuracy of better than 10^{-7}.

In the second step, the Poisson equation is solved for $x \geq x_{\max}(t_k)$, where a pure electron cloud is present. Here the Poisson equation reads

$$\varepsilon_0 \frac{\partial^2 \Phi_{\mathrm{el}}(x,t)}{\partial x^2} = e n_{\mathrm{e0}} \cdot \exp\left[\frac{e\Phi_{\mathrm{el}}(x,t)}{k_{\mathrm{B}}T_{\mathrm{e}}}\right]. \tag{7.8}$$

As the potential has to be continously differentiable at the proton front, the initial values for the numerical integration in this second step hae to be the same as determined in the first step.

The two parts of the numerical solution together give the potential, $\Phi_{\mathrm{el}}(x,t_k)$, associated to the electron and proton distributions at time, t_k, at all positions, x. The electric field that drives the proton acceleration and changes the proton-density distribution during the next time step is finally obtained by

$$\mathcal{E}(x,t_k) = -\frac{\partial}{\partial x}\Phi_{\mathrm{el}}(x,t_k). \tag{7.9}$$

Figure 7.1 shows the calculated electron densities (red line) and electric fields (dashed blue line in the lower plots) for $t = 0$ for a proton distribution (black line), that is initially step-like (a) and for one having an exponential drop in the density at the back of the target (b). In the simulation, a fully ionised hydrogen plasma is assumed having the same density as the hot electrons for $x \longrightarrow -\infty$, thus assuring charge neutrality.

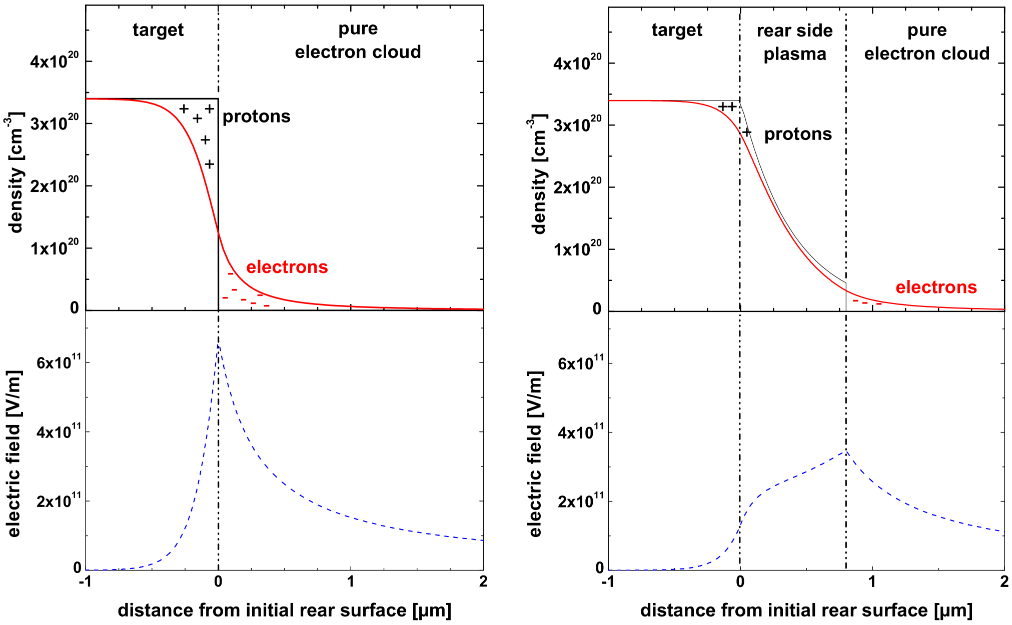

(a) Step-like proton-density (b) Exponential proton-density drop

Figure 7.1: Initial proton- and electron-density distributions and resulting electric fields at the target rear surface with no proton-density gradient (a) and a density gradient with $L_p = 0.8\,\mu$m (b). The undisturbed density of the electron beam in the target is $n_{e0} = 3.4 \times 10^{20}\,\mathrm{cm}^{-3}$ with a temperature of $T_e = 100\,\mathrm{keV}$. The resulting electric field that is peaked at the proton front is significantly reduced in the case with a rear-side proton-density gradient (b), leading to lower final energies of the accelerated protons.

The numerical procedure that gives an accurate description of the acceleration of the protons follows in the next section.

7.1.4 Acceleration of the Proton Distribution

Calculation of the New Proton Velocity Distribution

To describe the acceleration of the protons that have a momentary density and velocity distribution, $n_p(x,t_k)$ and $v_p(x,t_k)$, during the next iterative time step, Δt, the distributions are divided into cells of constant thickness, Δx, starting at the proton front, $x_{\max}(t_k)$. Each boundary between two cells at a position, x_j, has a definite proton density and velocity. During Δt, each boundary is moving due to the velocity, $v_p(x_j,t_k)$, and due to the acceleration by the electric field, $\mathcal{E}(x_j,t_k)$, at this boundary position. This is described by the equation of motion of the protons and it is implemented into the code in the following way:

$$
\begin{aligned}
x_j \quad &\rightarrow \quad x'_j = x_j + v_\mathrm{p}(x_j,t_k)\cdot\Delta t + \frac{e}{2m_\mathrm{p}}\mathcal{E}(x_j,t_k)\cdot\Delta t^2 && (7.10)\\
v_\mathrm{p}(x_j,t_k) \quad &\rightarrow \quad v_\mathrm{p}(x'_j,t_{k+1}) = v_\mathrm{p}(x_j,t_k) + \frac{e}{m_\mathrm{p}}\mathcal{E}(x_j,t_k)\cdot\Delta t && (7.11)
\end{aligned}
$$

The electric field is assumed to be constant over the distance the protons move during the time interval, i.e., a constant force on the protons in a given cell is assumed. The new proton velocities, $v_\mathrm{p}(x'_j,t_{k+1})$, that were calculated at the new boundary positions, x'_j, at time t_{k+1} are used to obtain the new entire proton-velocity distribution by linear interpolation. Note that due to the shift of each boundary the total derivative, $\mathrm{d}v_\mathrm{p}(x,t)/\mathrm{d}t = \partial v_\mathrm{p}(x,t)/\partial t + v_\mathrm{p}\cdot\partial v_\mathrm{p}(x,t)/\partial x$ in eq. (7.3) is taken into account.

Calculation of the New Proton Density Distribution

Due to the different proton velocities at the different cell boundaries, the width of each cell changes. Assuming a constant total number of protons in each cell, the proton density changes accordingly during Δt.

This is solved numerically in the following way, which is also sketched in Figure 7.2. If Δx_j and $\Delta x'_j$ are the thicknesses of a certain cell with the right boundary at x_j and x'_j, respectively, before and after one time interval, then the new density in the shifted cell is

$$
n_\mathrm{p}(x'_j,t_{k+1}) = n_\mathrm{p}(x_j,t_k)\frac{\Delta x_j}{\Delta x'_j} \qquad (7.12)
$$

with the new cell thickness

$$
\begin{aligned}
\Delta x'_j &= x'_j - x'_{j+1}\\
&= x_j - x_{j+1} + \left[v_\mathrm{p}(x_j,t_k) - v_\mathrm{p}(x_{j+1},t_k)\right]\cdot\Delta t\\
&\quad + \frac{e}{2m_\mathrm{p}}\left[\mathcal{E}(x_j,t_k) - \mathcal{E}(x_{j+1},t_k)\right]\cdot\Delta t^2\\
&= \Delta x_j + \Delta v_j\cdot\Delta t + \frac{e}{2m_\mathrm{p}}\Delta\mathcal{E}_j\cdot\Delta t^2. \qquad (7.13)
\end{aligned}
$$

The new densities are, similar to the new velocities, defined at the shifted position, x'_j, of the right boundary. The entire proton-density distribution, $n_\mathrm{p}(x,t_{k+1})$, is again obtained by linear interpolation.

7.1.5 Derivation of the Proton-Energy Spectrum

As the numerical simulation calculates the proton-density distribution, $n_\mathrm{p}(x,t)$, and the proton-velocity distribution, $v_\mathrm{p}(x,t)$, the proton-energy spectrum, $\mathrm{d}n_\mathrm{p}/\mathrm{d}E_\mathrm{p}$, can also be

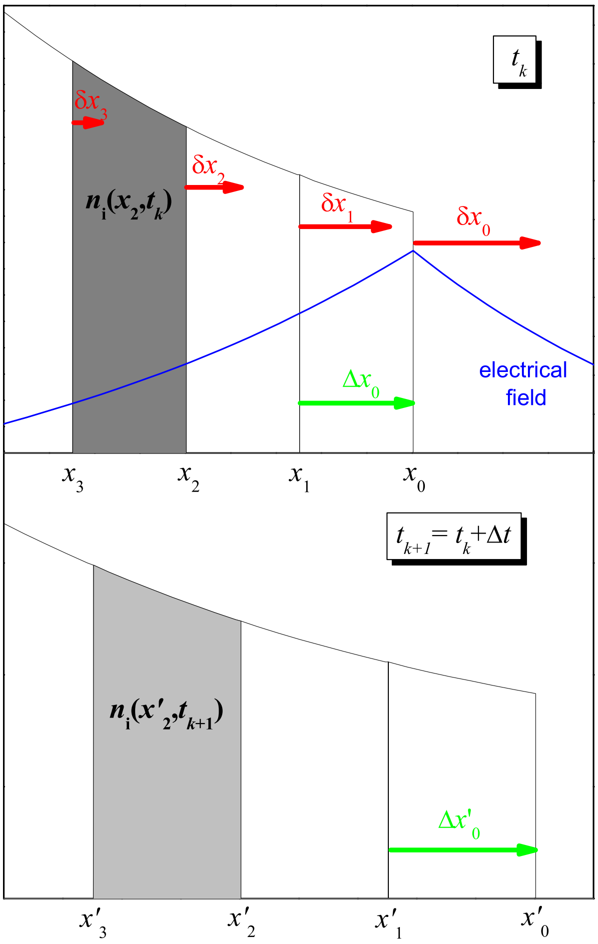

Figure 7.2: Schematic evolution of the proton distribution during one time step, Δt, of the simulation. The proton distribution at $t = t_k$ is devided into cells, that initially have the same thickness, Δx_0. Then the cell boundaries are shifted due to the electric field and the initial velocity of the protons, that were situated at the position of the boundaries. This leads to a new cell configuration at time $t_{k+1} = t_k + \Delta t$. The new proton densities within a shifted cell are calculated assuming particle number conservation within each cell. The entire density distribution is obtained by an interpolation between the values at the cell boundaries.

deduced during the acceleration process. Using the expression $E_p = m_p v_p^2/2$ for the proton kinetic energy, one finds

$$\begin{aligned} \frac{dn_p}{dE_p} &= \frac{dn_p}{dx} \cdot \frac{dx}{dv_p} \cdot \frac{dv_p}{dE_p} \\ &= \frac{dn_p}{dx} \Bigg/ \left(m_p v_p \cdot \frac{dv_p}{dx} \right) . \end{aligned} \tag{7.14}$$

7.2 General Results from the Simulation Code

In this section, first the results for the rear-side proton acceleration, that were obtained using the simulation code described in the last section with a step-like proton distribution, are compared to the analytical formulas derived in chapter 2. After that the code is used to study the effect of a rear-side density gradient on the maximum proton energies. This case cannot be treated analytically.

7.2.1 Comparison with the Analytical Model

Electric Field at the Proton Front

The electric field at the position of the proton front, $\mathcal{E}_{\mathrm{fr}}(t)$, is described by eq. (2.65)

$$\mathcal{E}_{\mathrm{fr}}(t) = \sqrt{\left(\frac{2}{e_{\mathrm{E}}}\right)} \cdot \frac{\mathcal{E}_0}{\sqrt{1+\tau^2}}. \tag{7.15}$$

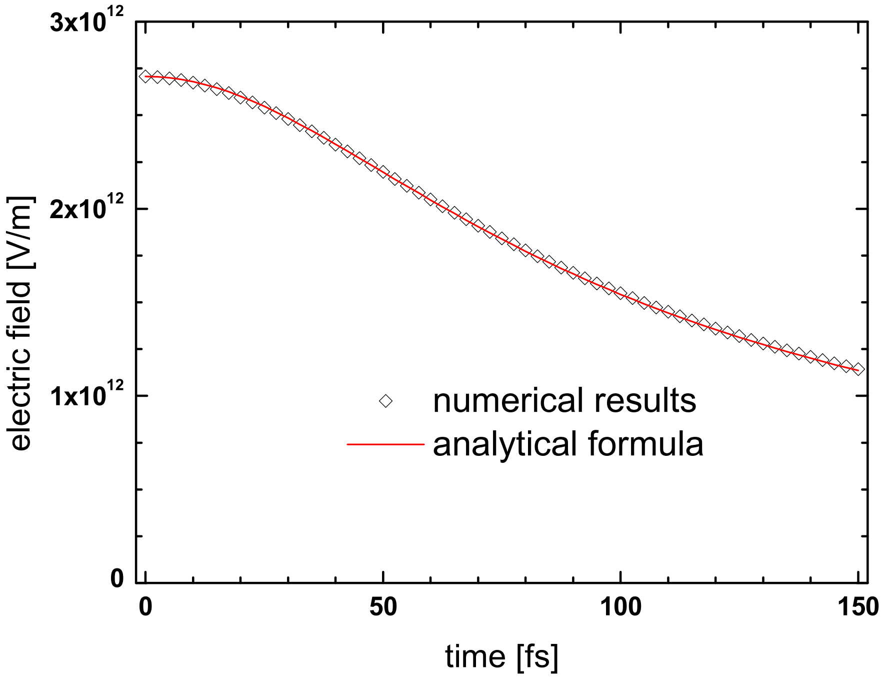

Figure 7.3: Evolution of the peak electric field at the proton front during the acceleration process driven by a hot-electron population with $n_{\mathrm{e0}} = 6.5 \times 10^{20}\,\mathrm{cm}^{-3}$ and $k_{\mathrm{B}}T_{\mathrm{e}} = 840\,\mathrm{keV}$. The diamonds give the numerical results and the solid red line gives the analytical solution described by eq. (7.15). A perfect agreement is found, the relative errors are below 10^{-2}.

Here, $\tau = \omega_{\mathrm{pp}}t/\sqrt{2e_{\mathrm{E}}}$ again denotes the dimensionless interaction time, $e_{\mathrm{E}} = 2.71828\ldots$ is the basis of the natural logarithm. The proton plasma frequency, $\omega_{\mathrm{pp}} = \sqrt{n_{\mathrm{e0}}e^2/\varepsilon_0 m_{\mathrm{p}}}$, depends on the initial electron density, n_{e0}. To compare the analytical solution with the numerical results, an initial electron density of $n_{\mathrm{e0}} = 6.5 \times 10^{20}\,\mathrm{cm}^{-3}$ and a hot-electron temperature of $k_{\mathrm{B}}T_{\mathrm{e}} = 840\,\mathrm{keV}$ are used, which correspond to the situation of an 8.5-μm aluminum target irradiated by a laser intensity of $1.3 \times 10^{19}\,\mathrm{W/cm}^2$, what will be described in detail in chapter 8. The time intervals in the numerical simulation were chosen to be $\Delta t = 2.5\,\mathrm{fs}$. Fig. 7.3 shows the evolution of the peak electric field at the proton front as a function of time, t, obtained with the two different methods.

A perfect agreement between the two methods is found. The relative errors are below

10^{-2}. They weakly depend on the time intervals, Δt, in the simulation, for longer Δt the errors increase slightly.

Proton-Energy Spectrum

In Fig. 7.4, the relative proton-energy spectra are compared that were obtained assuming the same hot-electron population driving the acceleration as above. The black line gives the spectrum described by eq. (2.69) using the self-similar model and assuming that the spectrum only extends up to the peak proton energy, corresponding to a proton distribution only extending to the proton front, as it was discussed in chapter 2 and in [86]. The red diamonds give the energy spectrum obtained from the numerical simulation using eq. (7.14). Although the spectra described by the two methods differ for low energies, a good agreement is found between the two approaches for energies above 1 MeV, as it was also found by Mora [86].

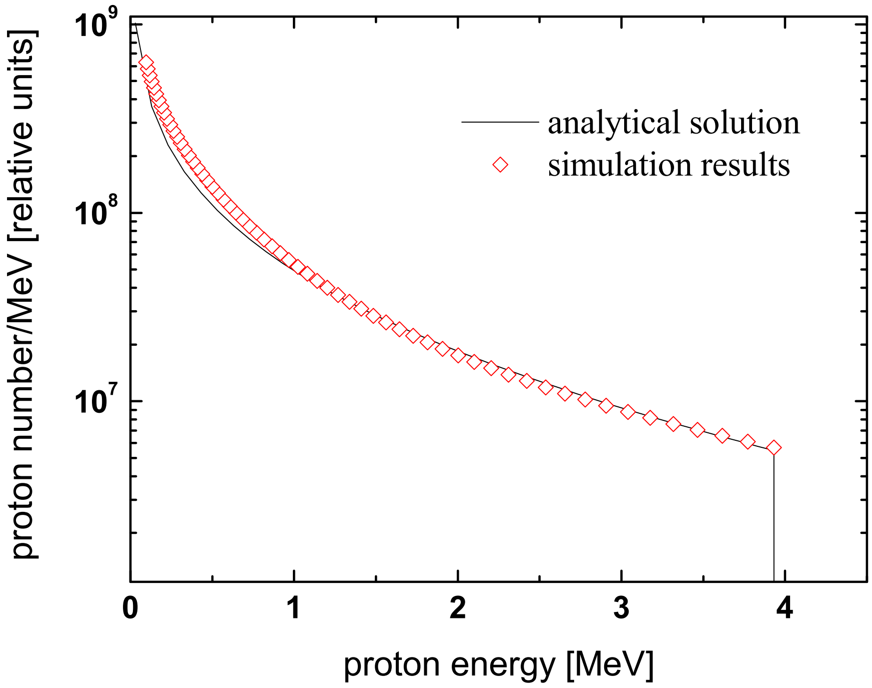

Figure 7.4: Energy spectrum of protons accelerated from the target rear side after the interaction with a laser pulse of $\tau_L = 150\,\mathrm{fs}$ calculated with the analytical formula eq. (2.69) (black line) and derived from the numerical simulation using eq. (7.14) (red diamonds). The hot-electron population was again assumed with $n_{e0} = 6.5 \times 10^{20}\,\mathrm{cm}^{-3}$ and $k_B T_e = 840\,\mathrm{keV}$. Again, a very good agreement between the simulation and the analytical prediction is found.

This confirms that for an initially step-like proton distribution the two methods are equivalent to describe the acceleration process. However, the simulation provides the evolution of the total proton distribution, while the analytical solution only predicts velocity and position of the proton front. Therefore, the evolution of the whole proton population is studied in the next section using the simulation code.

7.2.2 Acceleration of the Proton Distribution

In this section, numercial results for the proton acceleration including the evolution of the total density and velocity distributions of the protons are presented. As an example, the proton expansion driven by the electric fields set up by an electron distribution leaking out of the back of the target with a temperature of 840 keV and an initial density of $6.5 \times 10^{20}\,\mathrm{cm}^{-3}$, again corresponding to the case of an 8.5-μm thick aluminum foil having a thin proton layer on its back surface is investigated. The evolution of the proton density is shown in Fig. 7.5, the evolution ot the proton-velocity distribution is shown in Fig. 7.6. Both densities and velocities are plotted over a time interval of 150 fs. This is also the laser-pulse duration in the experiments.

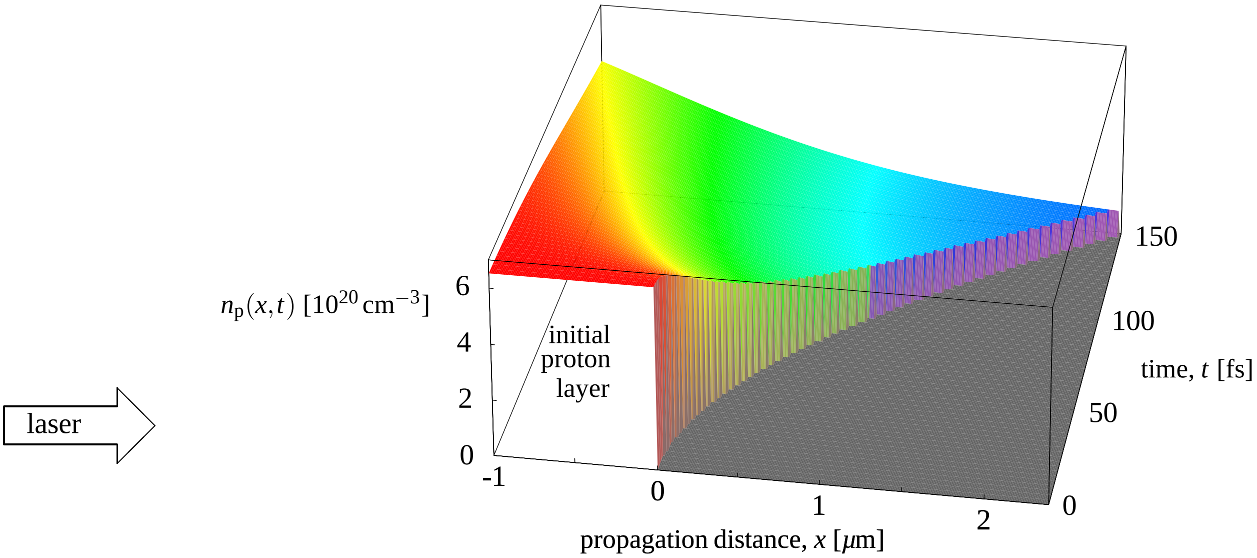

Figure 7.5: Evolution of the proton density distribution, $n_p(x,t)$, at the target rear side during the acceleration process. The laser is coming from the left, impinging on the target front side. The proton front is accelerated away from its initial position at the target rear side at $x = 0$. During the acceleration, the density at the front decreases.

Note that the proton density shows a monotonic decrease from the high-density regions in the target towards the proton front for all times, in agreement with P. Mora [86]. The peak in the proton-density distribution in the vicinity of the proton front, as it was observed in simulations carried out by Crow *et al.* [84] and other authors (see references in [86]), is not present in our simulations.

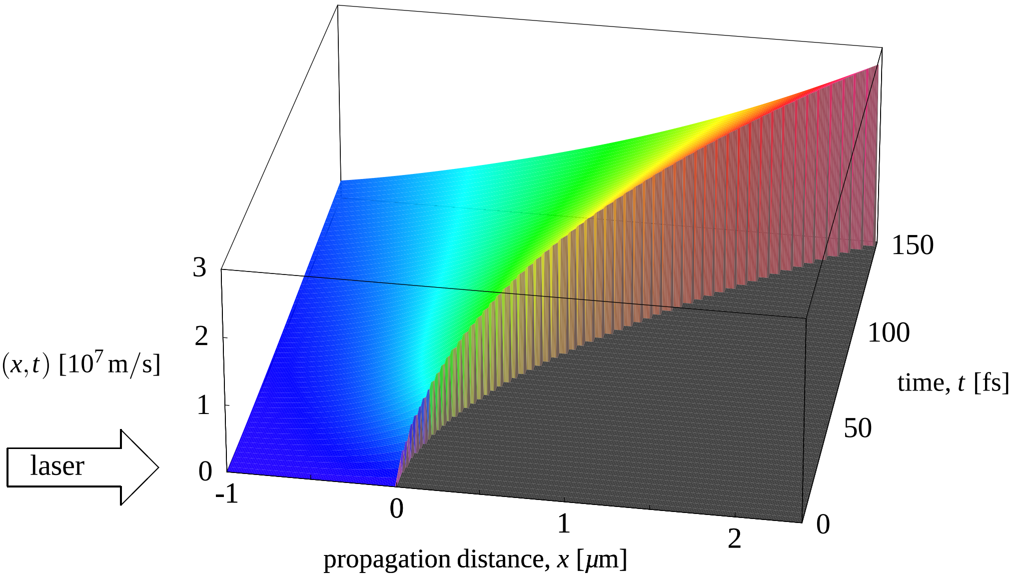

Figure 7.6: Evolution of the proton velocity distribution, $v_p(x,t)$, during the acceleration process. The protons situated at the front are accelerated strongest and gain peak velocities of $2.74 \times 10^7\,\mathrm{m/s}$, i.e. $0.092 \times c$, where c is the velocity of light. This peak velocity corresponds to a kinetic proton energy of 3.93 MeV.

7.2.3 Influence of an Initial Rear-Side Density Gradient

In this section, results from simulations carried out including an initial proton-density gradient at the target rear surface are described. As already depicted in Fig. 7.1, such a density gradient reduces the electric fields at the proton front. This can be explained as follows. Although the *total* potential difference determined by the total charge separation is the same, the potential drops over a larger distance as the charge distribution is distributed over a larger area. Therefore the *local* gradient of the potential (which is the local electric field) is smaller compared to the case of an initially step-like proton distribution. As the life-time of the fields driving the proton acceleration is limited by the laser-pulse duration, the protons gain significantly lower final energies, when the electric field is lower.

Fig. 7.7 shows the influence of a density gradient having different initial scale-lengths, L_p, and different extensions, x_{max}, on the maximum proton energy. As before, x_{max} denotes the initial position of the proton front before the main acceleration starts. Here, a hot-electron population with the same temperature, $T_e = 840\,\mathrm{keV}$, as before but a slightly higher initial density of $9.0 \times 10^{20}\,\mathrm{cm}^{-3}$ is used, corresponding to the case of a 5-μm aluminum foil. The peak proton energy for the step-like case is 4.74 MeV. This cutoff energy for the undisturbed case decreases in a monotonic way both for increasing initial scale length, L_p, and for increasing initial extension, x_{max}, of the preformed rear-side plasma.

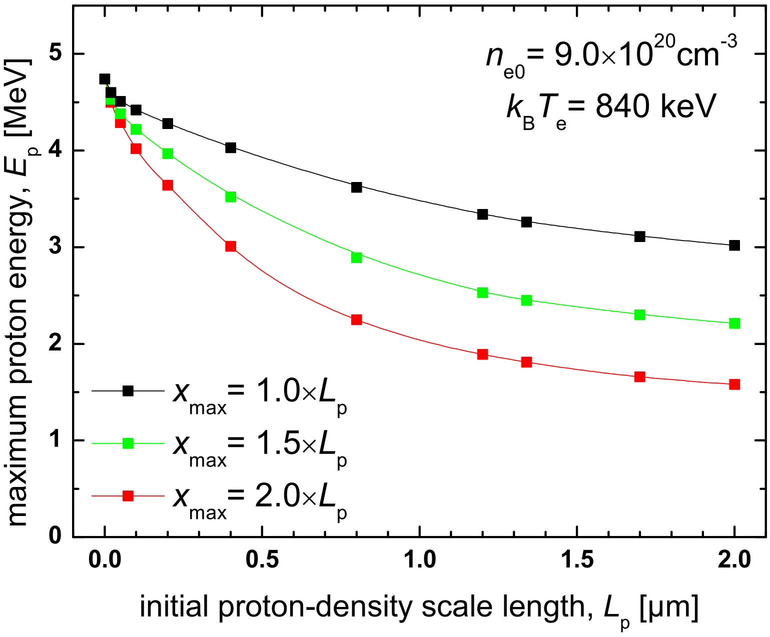

Figure 7.7: Effect of an initial proton-density scale length, L_p, at the rear surface of the target on the maximum proton energy studied with our simulation code. This preformed plasma was formed after the arrival of a heat wave lauched by the ASE-prepulse on the target front side. The proton cutoff energies are plotted as a function of the initial scale length for three different extensions depending on the density scale length, i.e. for $x_{max} = 1.0 \times L_P$ (black dots), for $x_{max} = 1.5 \times L_P$ (green dots), and for $x_{max} = 2.0 \times L_P$ (red dots). The electron population had a temperature of 840 keV and an initial density of $9.0 \times 10^{20}\,\mathrm{cm}^{-3}$.

7.3 Conclusion

In conclusion, a very good agreement between the analytical description of the proton acceleration, as it was derived by P. Mora (cf. chapter 2.4.2) and the results obtained from the simulation code are found. However, to include effects of a rear-side plasma formed by the laser prepulse, numerical simulations are inevitable. The effect of this ion-density gradient on the maximum proton energy accelerated from the target rear side appears to be too large to be negligible.

In the next chapter, the experimental results of the proton energies are compared to the predictions obtained with the simulation code, that was described in this chapter. Furthermore, the prepulse-induced changes in the target properties, as they were simulated by MULTI-FS (cf. chapter 6), will be included.

Chapter 8

Discussion of the Experimental Results

This chapter discusses the experimental results presented in chapter 5 and gives quantitative explanations of the results by the comparison with different numerical simulations that were introduced in chpater 6 and chapter 7. In the first two sections, the results obtained from the thickness scan are compared to two different scenarios for the transport of the electron beam through the target, one assuming a free-streaming propagation and the other including electron-transport effects arising from the collective behaviour of the electrons, as it was discussed in chapter 2.3. In the last section, the results obtained from the angularly-resolved measurements are compared to 3-dimensional PIC simulations [45].

8.1 Results from the Target-Thickness Scan Explained by a "Free-Streaming" Electron-Propagation Model

In this section, a simple quantitative explanation for the experimental results concerning the proton acceleration obtained during the scans of the target thickness is found. For this purpose, both the 1-D simulation code introduced in chapter 7 to describe the proton acceleration at the target rear side and the analytical theory introduced in chapter 2 for the front-side acceleration are used. The necessary parameters for the numerical simulation are the rear-side electron density, n_{e0}, the hot-electron temperature, T_e, and the interaction time, t. In a first step, a *free-streaming* electron beam in the target is assumed to derive these initial parameters.

8.1.1 Approximations for the Assumption of a Free-Streaming Electron Beam

The approximations made in this scenario are as follows. The electrons are accelerated within the laser-focal spot on the front side and propagate normally through the target forming a cone-shaped electron beam.

- The cone formed by the electron beam has a constant divergence, characterised by an initial half opening angle, θ_{in}.

- When the electrons exit the target at the rear side, they still have the same averaged kinetic energy as on the target front side, given by their quasi-temperature, $k_B T_e$.
- The total number of hot electrons in the beam remains constant during its passage through the target.
- The electron pulse length is assumed to be equal to the laser pulse duration.

The simulations were carried out using the experimental parameters. The ATLAS laser, that was described in detail in chapter 3.1, delivers pulses of 150-fs duration (FWHM) and of 790-nm wavelength. The total energy on the target amounts to $E_L = 600\ldots850\,\mathrm{mJ}$, resulting in an averaged laser intensity, I_L, between 1.0 and $1.5\times10^{19}\,\mathrm{W/cm^2}$ within a focal spot of $r_f = 2.6\,\mu\mathrm{m}$ radius, as it was discussed in chapter 3.2.

Determination of the Initial Simulation Parameters

The hot-electron temperature, T_e, is calculated from the averaged laser intensity using the ponderomotive scaling law by Wilks *et al.*, eq. (2.44)

$$k_B T_e = 0.511\,\mathrm{MeV}\cdot\left(\sqrt{1+\frac{I_L\lambda_L{}^2}{1.37\times10^{18}\,\mathrm{W/cm^2}\cdot\mu\mathrm{m}^2}}-1\right). \tag{8.1}$$

The electron density at the target rear surface, n_{e0}, is derived from the total number of electrons, N_e, the focal-spot size on the front side, the target thickness, d_{target}, and the initial half-opening angle, θ_{in}. Again, it is assumed that a fraction of $\eta = 25\%$ of the laser energy, E_L, is converted into hot electrons [9] with a mean energy determined by the hot-electron temperature given by eq. (8.1). This gives a total electron number of

$$N_e \approx \frac{\eta E_L}{k_B T_e}. \tag{8.2}$$

These electrons are emitted in a cone-shaped beam that transverses the target and has a total length of $c\tau_L$, determined by the laser pulse duration, if the velocity of the electrons, $v_e \approx c$, and dispersion effects due to different electron velocities are neglected. This also determines the electron pulse duration and the rear-side acceleration time to $t = \tau_L$.

The radius of the electron spot at the rear side of the target can be deduced from simple geometrical considerations assuming a constant divergence of the beam. This is sketched in Fig. 8.1. Starting with a minimal cross section of the beam at the target front side, which is determined by the focal-spot size of the laser, the cross section increases while the electrons propagate through the target. Depending on the injection angle, α_{in}, of the electron beam into the target that depends on the electron acceleration mechanism on the target front side, the effective thickness of the target through which the electron beam has to propagate is given by $d^*_{\mathrm{target}} = d_{\mathrm{target}}/\cos(\alpha_{\mathrm{in}})$. The radius of the rear-side electron spot is then approximately given by $(r_f + d^*_t \tan\theta_{\mathrm{in}})$. This determines the electron density at the rear surface to

$$n_{e0} \approx \frac{N_e}{c\tau_L\times\pi(r_f + d^*_{\mathrm{target}}\tan\theta_{\mathrm{in}})^2}. \tag{8.3}$$

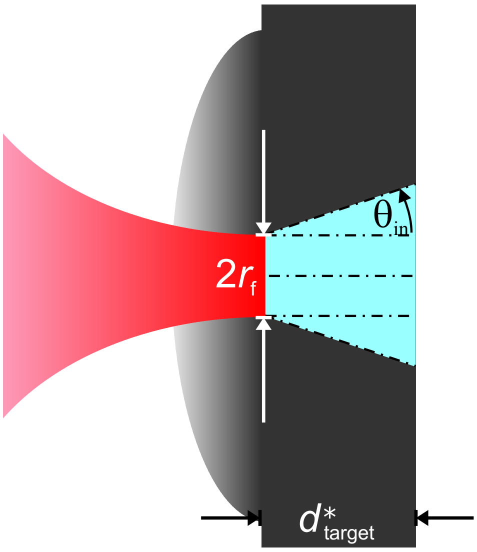

Figure 8.1: Schematic propagation of the hot-electron beam through the target. The laser is focused to a spot with the minimal radius of r_f. Electrons are accelerated within this spot and enter the target in a cone with a constant half-opening angle θ_in. After propagating through the target with the thickness d^*_target, the spotsize of the electrons exiting at the target rear surface is increased. This leads to a lower electron density, n_e0, at the target rear surface.

This is a direct correlation between the target thickness, d_target, and the initial rear-side electron density, n_e0. The two free parameters are the injection angle, α_in, and the half-opening angle, θ_in, of the cone in which the electrons enter the target. These angles can be determined by a comparison with the experimental data.

8.1.2 Comparison of Simulation Results with Experimental Data

In a first step, any prepulse-induced plasma formation on the target rear side due to the prepulse is neglected. This corresponds to targets thicker than d_opt (cf. chapter 6).

Fig. 8.2 compares the experimental results that were obtained for a laser intensity of $1.3\times10^{19}\,\mathrm{W/cm^2}$ and a prepulse duration of $\tau_\mathrm{ASE}=2.5\,\mathrm{ns}$, (cf. Fig. 5.6) with numerical results from the simulation assuming electron injection around the target-normal direction, i.e. $\alpha_\mathrm{in}=0^\circ$ and initial half-opening angles, θ_in, between 7° and 11°, what is indicated by the blue-hatched area. Within the experimental error, an excellent agreement between the numerical simulations and the experimental data is found for targets at and above the optimal thickness, which is $8.5\,\mu\mathrm{m}$ for the prepulse duration of $\tau_\mathrm{ASE}=2.5\,\mathrm{ns}$. To estimate the influence of the electron-incection angle, α_in, an injection in laser forward direction is assumed, which corresponds to $\alpha_\mathrm{in}=30^\circ$. For this case, the experimental results are reproduced for somewhat smaller half-opening angles between 6° and 10°. In the real experiment, the electron injection will occur at an angle between these two cases of $\alpha_\mathrm{in}=0^\circ$ and $\alpha_\mathrm{in}=30^\circ$, as it was discussed in chapter 2.2. The predicted proton energies appear to depend only weakly on this parameter. In the following, normal injection is assumed, i.e. $\alpha_\mathrm{in}=0^\circ$.

Fig. 8.3 (a) – (d) show comparisons of the proton-energy spectra, that were measured in the experiment with the Thomson parabola for a range of target thicknesses between $d_\mathrm{target}=8.5\,\mu\mathrm{m}$ and $30\,\mu\mathrm{m}$ and a laser intensity of $I_\mathrm{L}=1.3\times10^{19}\,\mathrm{W/cm^2}$ with the energy spectra calculated from the numerical simulation for the same initial parameters using an

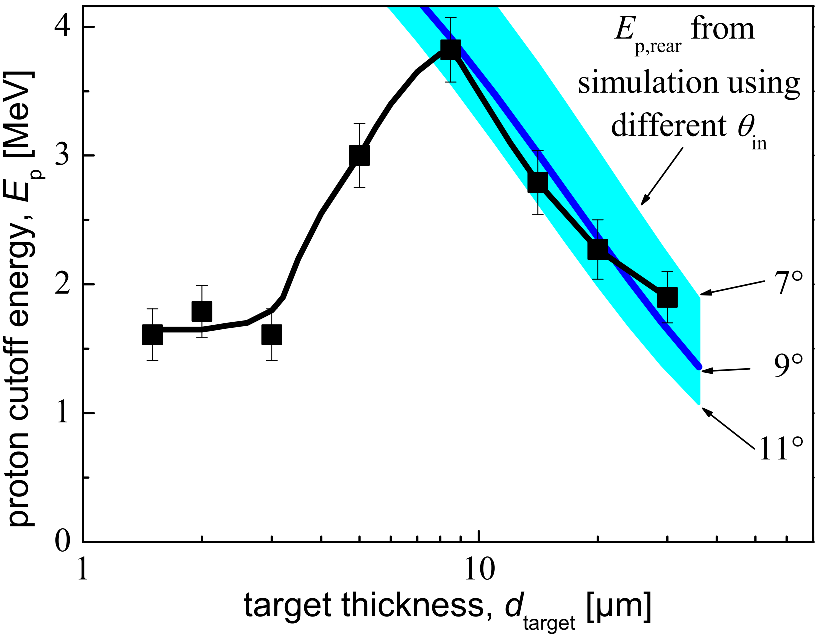

Figure 8.2: Comparison between the maximum proton energy, E_p, obtained in the experiment with a laser intensity of $1.3 \times 10^{19}\,\mathrm{W/cm^2}$, a prepulse duration of 2.5 ns, and different target thicknesses, d_{target}, and the cutoff energies, $E_{p,rear}$, obtained from the numerical simulation for the rear-side acceleration. Normal injection of the electron beam was assumed, $\alpha_{in} = 0°$, and a range of half-opening angles, θ_{in}, between 7° and 11°. This area is hatched in blue.

initial half-opening angle of $\theta_{in} = 9°$. As it can be seen in the plots, also the proton-energy spectra are well reproduced by the simulation in terms of cutoff energy and temperature, but only for the hottest proton component. The cold proton component in the spectrum, that is not reproduced by the simulation for any foil thickness, can either come from a second, colder component in the *electron*-energy spectrum, as it has been observed experimentally by L. M. Wickens *et al.* [120] and explained theoretically by J. Denavit [85], or it indicates that the rear-side acceleration is not the only active mechanism. This point will be addressed below.

In Fig. 8.4, the results for the proton cutoff energies obtained from the numerical simulation are compared to the experimental data for a slightly lower laser intensity of $I_L = 1.0 \times 10^{19}\,\mathrm{W/cm^2}$, as it was present in the experiment. This plot contains the results for three different ASE prepulse durations. For each τ_{ASE}, a very good agreement between experiment and simulation is found at and above the *individual* optimal target thickness depending on the prepulse duration ($d_{opt} = 2\,\mu$m for $\tau_{ASE} = 0.5$ ns, $d_{opt} = 3\,\mu$m for $\tau_{ASE} = 0.7$ ns, and $d_{opt} = 8.5\,\mu$m for $\tau_{ASE} = 2.5$ ns). Below each individual optimal target thickness, the proton cutoff energies remain well below the theoretical prediction. In this range, the experimental observations cannot be explained by the simple model assuming an initially step-like proton distribution at the target rear side.

As it was shown in chapter 6, the values for the optimal target thickness are qualita-

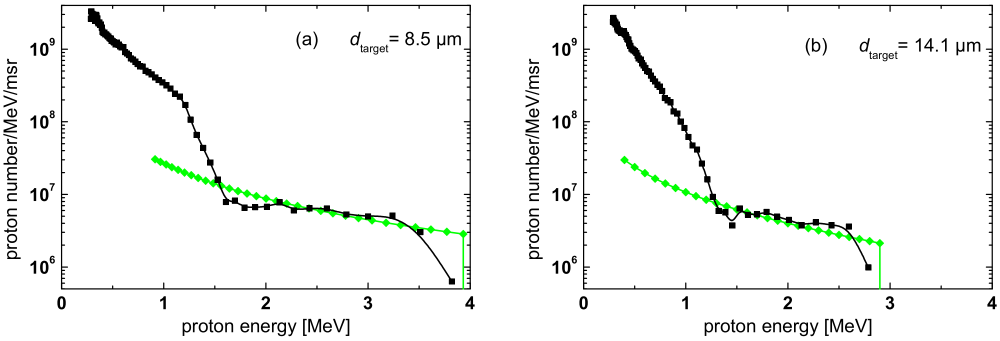

(a) $d_{\text{target}} = 8.5\,\mu\text{m}$ (b) $d_{\text{target}} = 14.1\,\mu\text{m}$

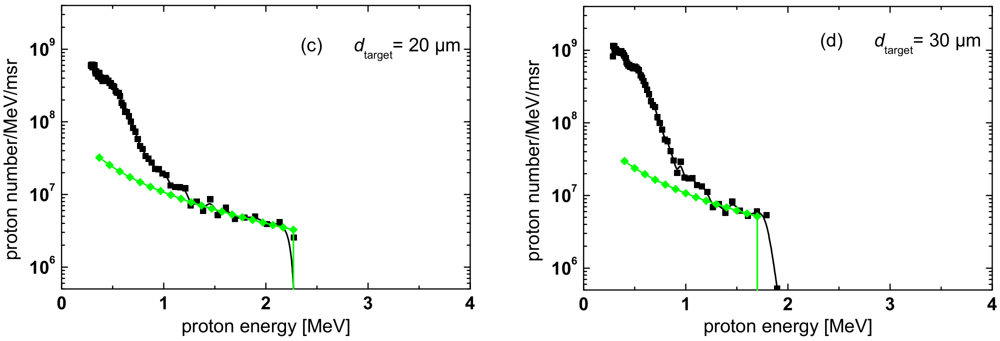

(c) $d_{\text{target}} = 20\,\mu\text{m}$ (d) $d_{\text{target}} = 30\,\mu\text{m}$

Figure 8.3: Comparison between proton-energy spectra measured in the experiment (black squares) and calculated using the simulation code (green diamonds). A very good agreement is found between measured and simulated temperature and cutoff energy of the hottest proton component for all thicknesses. The low-energy part of the spectrum cannot be explained by the simulation, that includes the rear-side acceleration only. Note that the simulation only gives a proton density, n_p, per energy interval and not a total number of protons, N_p. The calculated spectra are all shifted vertically by the same factor to match the experimentally measured total proton numbers.

tively reproduced by MULTI-FS simulations describing the prepulse-induced changes in the target properties. This strongly implies that also the changes in the proton cutoff energies are induced by the prepulse. To give a consistent picture, all effects induced by the prepulse have to be taken into account. This is presented in the next section.

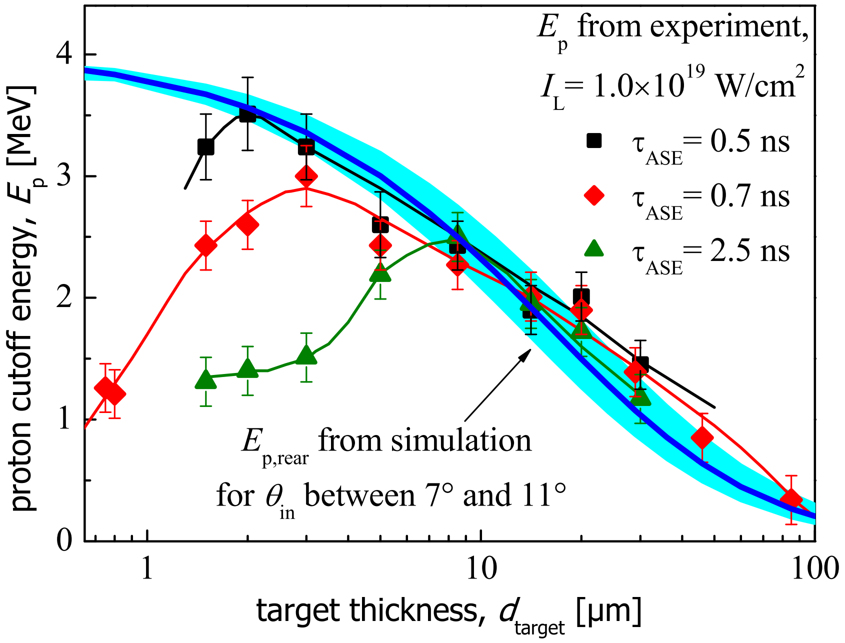

Figure 8.4: Comparison between maximum proton energies from the experiment and from the simulation for a laser intensity of $1.0 \times 10^{19}\,\mathrm{W/cm^2}$, three different prepulse durations of 0.5 ns, 0.7 ns, and 2.5 ns, and different target thicknesses, d_{target}. Again a good agreement between experiment and theory is found but only for targets at and above the *individual* optimal target thicknesses, that depend on the individual prepulse durations. Note that exactly the same range of initial half-opening angles ($7° \leq \theta_{\mathrm{in}} \leq 11°$) was used for the simulation as in Fig. 8.2.

8.2 Prepulse-Induced Effects Relevant for the Rear-Side Proton Acceleration: Numerical Description of the Fast-Electron Transport

In the last section, the “free-streaming” model for the electron propagation in the target was used to interprete the experimental results concerning the rear-side proton acceleration.

A more elaborated picture should additionally include the prepulse-induced changes of the target properties as density and temperature variations, and describe their influence on the proton acceleration. The rear-side proton acceleration is directly influenced by the formation of an ion-density gradient at the target rear side, as it was shown in chapter 7. Furthermore, one would expect that the expansion as well as the associated density and temperature variations inside the target influence the electron transport through the material, too. This indirectly influences the proton acceleration, as the latter depends on the electron density distribution at the rear side of the target, which is likely to be modified by the electron transport.

To include all these aspects, numerical simulations with a fast-electron transport (FET) code were carried out by J. J. Honrubia. This code calculates the density distributions and mean energies of the electrons exiting the target at the rear side. These values are used afterwards in the numerical simulation code for the rear-side proton acceleration, that was described in chapter 7, where also the rear-side density distribution influencing the proton acceleration can be taken into account. This finally yields the peak proton energies including all prepulse induced effects, which are then compared to the experimental results.

8.2.1 The Fast-Electron Transport Code

The FET code is a hybrid code. While the fast electrons are described as "macro" particles each representing a fixed number of 10^6 "real" electrons as in a PIC code, the cold background electrons are treated as a fluid. It describes the propagation of a relativistic electron population through a target that can exhibit any initial ion- and electron-density distribution. These initial target properties are calculated separately by MULTI-FS or an equivalent hydro code, simulating the influence of the laser prepulse on an aluminum foil of a given thickness as described in chapter 6. The return current induced by the fast electron current is computed self-consistently, including the heating of the background plasma due to resistive heating of the return current and due to energy deposition by collisions. These collisions are treated as in standard 3-D Monte-Carlo codes. Additionally, the formation of azimuthal magnetic fields is calculated. These fields can pinch the fast electron beam as a whole.

The electromagnetic fields are calculated by combining Ampere's law without displacement current [121] with the simplest form of Ohm's law and Faraday's law

$$\vec{j}_{\mathrm{r}} = -\vec{j}_{\mathrm{f}} + \frac{1}{\mu_0}\vec{\nabla}\times\vec{B}, \tag{8.4}$$

$$\vec{\mathcal{E}} = \frac{1}{\sigma}\cdot\vec{j}_{\mathrm{r}}, \qquad \text{and} \tag{8.5}$$

$$\frac{\partial\vec{B}}{\partial t} = -\vec{\nabla}\times\vec{\mathcal{E}}, \tag{8.6}$$

where $\vec{j}_{\mathrm{f}}$ and $\vec{j}_{\mathrm{r}}$ are the fast and return current densities, respectively, and $\sigma = 1/\eta$ is the target conductivity, η is the resistivity, both depending on the background ion density and the temperature (see below). In the code, the particle trajectories are simulated in 3-D, but to describe the electromagnetic field generation in the target, cylindrical symmetry around the axis of the injected electron beam is assumed. Therefore, the code takes into account the electric fields in radial and longitudinal direction, $\mathcal{E}_r$ and $\mathcal{E}_x$, respectively, and the azimuthal magnetic fields, B_θ. These fields are generated during the the propagation of the electron beam. To provide charge neutrality, a return current sets in immediately after the onset of the electron-beam injection as described by eq. (8.4). The conductivity of aluminum is computed by the model of Lee and More [122], which allows to calculate transport properties of partially degenerated plasmas. The conductivity of aluminum for different temperatures and two different densities is depicted in Fig. 8.5. Note that the conductivity for low densities, i.e. for an expanded target with temperatures below 100 eV,

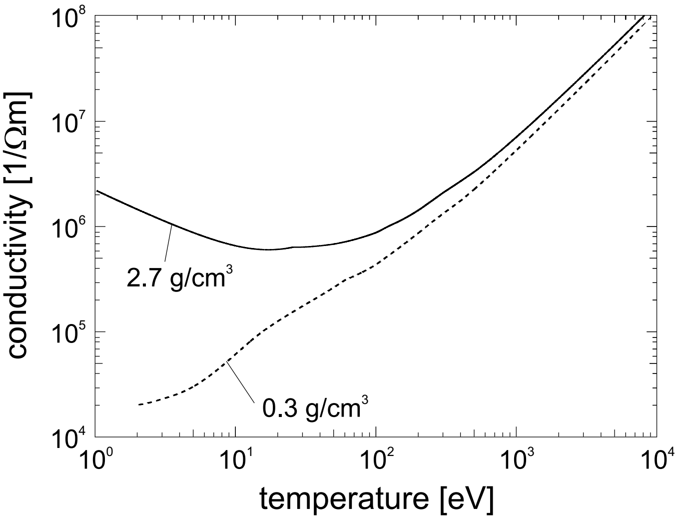

Figure 8.5: Conductivity in aluminum as a function of temperature for two different densities, $\rho = 2.7\,\mathrm{g/cm^3}$ and $\rho = 0.3\,\mathrm{g/cm^3}$, calculated with the model of Lee and More [122].

is reduced compared to the case of a solid target. This can be explained by the lack of ion correlations found in solid conductors.

In the simulation, the laser-generated electron population is injected at the left side of the simulation box. Although the laser-plasma interaction and therefore the explicit electron acceleration is not included in the simulation, the temporal and lateral distributions of the electron population are closely related to the experimental conditions. The population has Gaussian distributions both in time and in radial direction at the target front surface. The FWHM of the focal spot is taken as 4.8 μm, similar to the experiment, and the pulse duration at FWHM of the intensity is 150 fs with a peak intensity of $I_{\mathrm{L,max}} = 1.5 \times 10^{19}\,\mathrm{W/cm^2}$. The mean energy of the electrons follows the temporal evolution and the radial profile of the laser intensity and it is described by the ponderomotive scaling law, eq. (2.44). Again, a conversion efficiency of 25% from laser pulse energy into fast electrons is assumed [9]. The electron population is injected into the target in a beam aligned around the target normal direction with an initial half-opening angle, θ_{in},

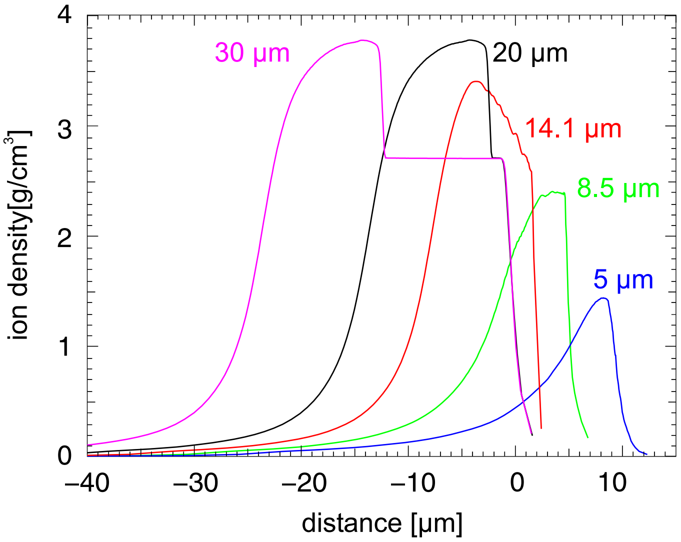

Figure 8.6: Aluminum-foil density profiles for different initial thicknesses after the irradiation with an ASE prepulse of $\tau_{\mathrm{ASE}} = 2.5\,\mathrm{ns}$ coming from the left. These density profiles were used in the FET simulations.

which is the only free parameter in the simulation.

The target is implemented into the code by ion- and electron density distributions and a temperature distribution, that is assumed to be initially 1-dimensional and varying only in the propagation direction of the electron beam. The ion-density profiles used in the FET code are shown in Fig. 8.6. These ion-density distributions are assumed to remain unchanged during the electron-beam propagation.

8.2.2 Simulation Results from the Fast-Electron Transport Code

Fig. 8.7 shows results from an exemplary simulation run for the propagation of an electron population through a target. The electron population is similar to one generated by a 150-fs laser pulse having a peak intensity of $1.5 \times 10^{19}\,\mathrm{W/cm^2}$. It is injected at the left boundary of the simulation box and propagates through an aluminum target that exhibits a density profile increasing from $0.27\,\mathrm{g/cm^3}$ to $2.7\,\mathrm{g/cm^3}$ over the whole length of the simulation box. This target, that has been expanded by the irradiation of a prepulse, corresponds to an initial foil thickness of $30\,\mu$m. The electron pulse is closely related to the current denstity (first row) and propagates to the right. It is injected with a Gaussian radial distribution, correlating to the radial current density at $x = 0$ and $t = 100\,$fs. Due to velocity dispersion, the pulse is elongated in space, what in turn reduces the peak current

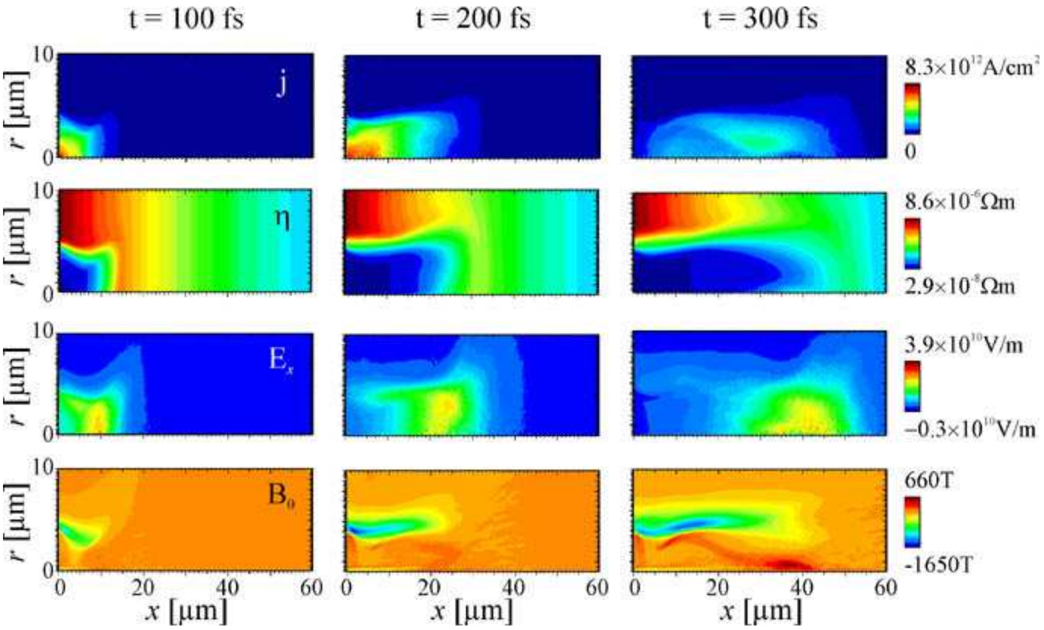

Figure 8.7: Current density, j (first row), resistivity, $\eta = 1/\sigma$ (second row), longitudinal electric field, $\mathcal{E}_x$ (third row), and azimuthal magnetic field, B_θ (last row), during the propagation of an electron pulse through a target consisting of an exponential ion-density profile extending from $x = 0\,\mu$m to $x = 60\,\mu$m at three different time steps: $t = 100\,$fs (first column), $t = 200\,$fs (second column), and $t = 300\,$fs (third column). The plots are two dimensional, cylindrical symmetry around the horizontal axis is assumed.

density at later times. The return current, that is carried by the initially cold background-electron population, that has a much higher density, consists of a much slower drift motion to the left. Due to the lower electron velocities, the return current experiences an enhanced stopping due to collisions, as the cross section for Coulomb collisions increases for decreasing electron velocities, what in turn heats up the background plasma and thereby strongly influences the target resistivity (second row). At the head of the pulse, where the background heating just sets in, the temperature quickly rises to $T_{\mathrm{back}} \approx 50\ldots100\,\mathrm{eV}$, where the resistivity is maximal (i.e. the conductivity is minimal, cf. Fig. 8.5) and thus the longitudinal electric field is peaked (third row). Inside the electron beam, the temperature is much higher and the resistivity is reduced again. The spatial variation of the electric field induces an azimuthal magnetic field around the electron beam (last row). Depending on its strength, the beam injected into the target with an initial half-opening angle, θ_{in}, can be pinched and the propagation occurs in a collimated beam in the target.

It is observed in the simulations that the electrons initially follow a straight line after they are injected into the target. Depending on the initial injection angle, θ_{in}, and the heating rate of the background plasma, $j_{\mathrm{r}}^2\eta/\rho$, the azimuthal magnetic field can grow strongly enough to pinch the electron beam or the electron beam diverges too fast and no pinching occurs as described by A. R. Bell *et al.* [79]. This behaviour is shown in Fig. 8.8, where the collimation is described by the ratio between the electron-spot diameters on the target rear and front side, $d_{\mathrm{rear}}/d_{\mathrm{front}}$. While for the case of $\theta_{\mathrm{in}} = 40°$, the electron beam clearly diverges, it is collimated for the angles of 30° and 20°. It is further found that the electron beam is less collimated when propagating through a density profile than through solid material (compare red an black line for $\theta_{\mathrm{in}} = 30°$). This can be explained, as the higher density present in solid material leads to a lower resistivity and a weaker resistive heating of the target material (cf. Fig. 8.5), i.e. to lower temperatures in the material. These lower temperatures in turn result in higher resistivities compared to the expanded target, what leads to the generation of stronger electric and magnetic fields and therefore a stronger collimation.

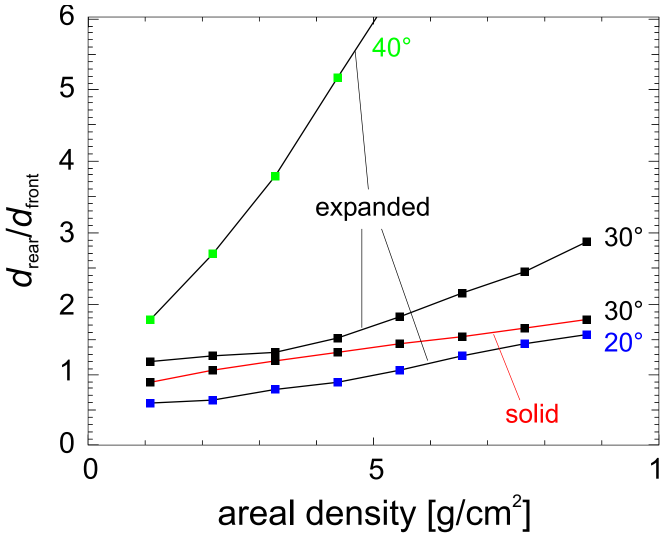

Figure 8.8: Ratio between electron-spot diameters on the target front and rear side, $d_{\mathrm{rear}}/d_{\mathrm{front}}$, characterising the collimation of the electron beam in the target for three different initial half-opening angles, $\theta_{\mathrm{in}} = 20°$ (blue squares), 30° (black squares), and 40° (green squares). For the case of $\theta_{\mathrm{in}} = 30°$, the beam collimation for an expanded target (black line) is compared to the solid target (red line).

8.2.3 Application of Simulation Results for Proton Acceleration

To quantitatively investigate the influence of the electron-transport effects described in the last section on the rear-side proton acceleration, the results from the FET code are used to determine a mean electron density, n_{e0}, a mean electron energy[1], $\langle E_{\mathrm{electron}}\rangle$, and a mean electron-pulse duration, τ_{pulse}, at the target rear side. These quantities are either inserted into Mora's formula, eq. (2.68), for targets that still show a step-like rear-side ion-density gradient as for thicknesses of $8.5\,\mu$m and above or into the numerical simulation code described in chapter 7 including the ion-density gradient for thinner targets. In both cases, the peak energy of protons accelerated at the target rear surface is obtained.

The proton-acceleration time is determined by the effective duration of the electron beam passing through the rear surface of the target. This is shown in Fig. 8.9 for three different target thicknesses. The effective pulse duration, τ_{pulse}, that determines the proton-acceleration time, increases for increasing target thicknesses.

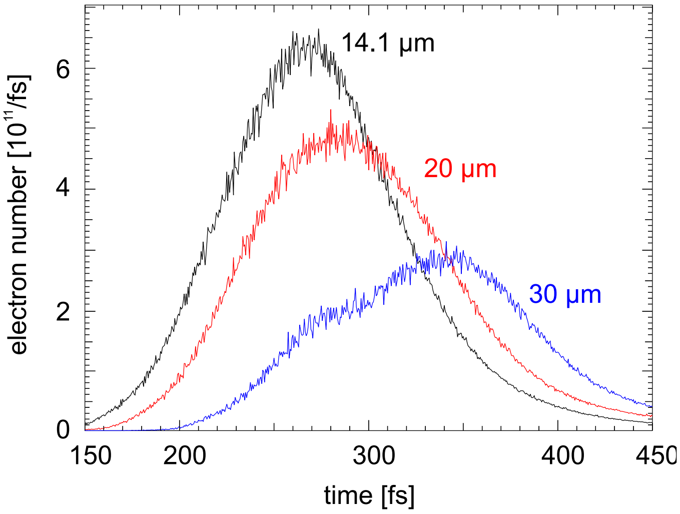

Figure 8.9: This plot gives the number of electrons per fs exiting the rear surface of the target within the FWHM of the rear-side electron spot. For thicker targets, the effectiv pulse duration, τ_{pulse}, is increased.

The averaged electron density, n_{e0}, at the target rear side is determined by the total electron number exiting the target within the FWHM of the rear-side electron spot, d_{rear}. This spot size is strongly influenced by a possible pinching of the electron beam in the target, as it was shown in Fig. 8.8. This number of electrons is devided by the FWHM-area of this spot, $\pi d_{\mathrm{rear}}^2/4$, and the length of the electron pulse, $c \cdot \tau_{\mathrm{pulse}}$, to obtain the averaged electron density, n_{e0}, at the rear side.

As the injected electron beam looses a part of its initial energy during the passage through the target, its mean energy, $\langle E_{\mathrm{electron}}\rangle$, is reduced. The main contributions to the energy losses are the resistive heating of the background plasma by the return current, that takes all of its energy from the fast electron beam, and collisions of the fast electrons.

Table 8.1 summarises the results obtained from the hybrid PIC code describing the electron transport through targets of different thickness using the ion-density profiles shown in Fig. 8.6 and an initial half-opening angle of $\theta_{\mathrm{in}} = 30^\circ$. The last column finally gives

---

[1] The mean electron energy, $\langle E_{\mathrm{electron}}\rangle$, is treated as an effective electron temperature, $k_B T_e$.

target thickness (μm)	d_{rear} (μm)	N_{electron} ($\times 10^{11}$)	τ_{pulse} (fs)	$\langle E_{\text{electron}} \rangle$ (MeV)	E_{proton} (MeV)
1.5	4.6	7.30	185	0.65	0.93 (1.94)
2	4.3	6.42	190	0.67	1.02 (2.05)
3	3.8	5.38	190	0.69	1.15 (2.22)
5	4.8	4.93	175	0.75	2.66 (3.72)
8.5	5.0	5.35	180	0.75	3.87
14.1	6.2	5.81	180	0.75	3.13
20	7.4	5.15	205	0.73	2.46
30	7.6	3.00	220	0.72	1.68

Table 8.1: Parameters for the rear-side proton acceleration obatined from the hybrid PIC simulation. Here, the ion density profiles from Fig. 8.6 and an initial half-opening angle of $\theta_{\text{in}} = 30°$ were used. The last column gives the peak proton energy as predicted by Mora's analytical formula, eq. (2.68) or by the numerical proton simulation. For the first four thicknesses, the energy in brackets gives the proton energy for a step-like ion density distribution at the target rear side. The reduced energy takes into account the effect of the prepulse-induced rear-side gradient.

the proton cutoff energies that were calculated either with Mora's formula, eq. (2.68), or with the numerical simulation for the rear-side acceleration. For the first four thicknesses

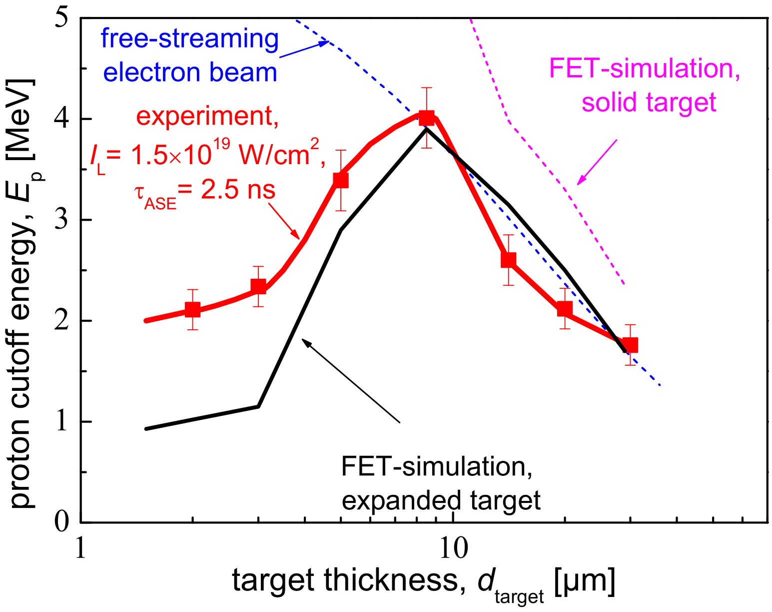

Figure 8.10: This plot compares the simulated proton cutoff energies from three different models with the experimental data (red squares).

($d_{\text{target}} \leq 5\,\mu$m), the two different energy values correspond to the cases (i) including an ion-density gradient, the scale length of which was predicted by MULTI-FS, or (ii) a step-like ion density distribution. The density gradient leads to a significantly reduced proton cutoff energy, as it was also shown in chapter 7 and has to be taken into account. These results are finally compared to the experimental data for the peak proton energy for different target thicknesses and a prepulse duration of 2.5 ns in Fig. 8.10. Here, several different simulation results are shown, each including different effects. While the dashed blue line gives the result from Mora's formula assuming a free-streaming electron beam in the target with $\theta_{\text{in}} = 9^\circ$, as it was discussed in section 8.1, the red and the pink curve correspond to runs with the FET code taking into account the collective effects experienced by the electrons in the target. Both runs start with an initial half-opening angle of 30°. While the run corresponding to the pink curve simulated the transport through solid targets of the initial thickness, the red curve was obtained from simulating the electron transport through "expanded targets". In these latter cases, the target expansion due to the laser prepulse, as it was described by MULTI-FS simulations, was additionally taken into account. For the thinnest targets ($d_{\text{target}} \leq 5\,\mu$m), the the rear-side ion-density gradient strongly reduces the peak proton energies. For the solid red curve, where all effects discussed so far are included, a good agreement with the experimental data is found for $d_{\text{target}} \geq 5\,\mu$m.

While it might first be surprising that both the simple estimation of the free-streaming electron propagation and the much more elaborated numerical simulation of the electron transport through the target give quite similar results for the rear-side proton energies at targets above the optimal thickness, it appears that the additionally included effects in the numerical simulation cancel each other to some extent. While the free-streaming case assumes the same mean energies for the electrons on both target surfaces and should therefore overestimate the proton energies compared to the FET simulation, where energy losses of the electrons are included, the increase of the effective electron pulse length, τ_{pulse}, and therefore the proton acceleration time, slightly increase the proton cutoff energy again. Additionally, the beam pinching acts as to increase the initial electron densities, n_{e0}, at the target rear side, while for the free-streaming case the rear-side electron density steadily decreases with increasing target thickness. On the other hand, taking into account the lower ion densities in the expanded targets reduces the effect of the pinching again, as it is shown in Fig. 8.10. Taking into account these four additional effects in the FET code, two acting as to increase the proton energy and the two others as to decrease the proton energy, the similarity between the two different approaches can be understood.

However, for the thinnest foils ($d_{\text{target}} \leq 3\,\mu$m), the predicted proton energy is lower by at least a factor of 2 compared to the experiment. When the front-side proton acceleration is considered, even those energies can be explained. This will be shown in the next section.

8.2.4 Comparison between Experimental Results and Front-Side Proton Acceleration

In the last section, a good agreement between experiment and the numerical simulations describing the rear-side proton acceleration for targets with thicknesses of $d_{\text{target}} \geq 5\,\mu$m was found. Below this thickness, the predicted proton energies were lower than those measured in the experiment. This is caused by the strong expansion of the target, the associated changes in the electron transport, and the formation of a rear-side ion-density gradient due to the laser prepulse.

However, including the front-side acceleration mechanism gives a natural explanation for this feature. The peak energies of protons, that are accelerated on the target front side by the electric fields set up by the ponderomotive charge-separation in the laser focus, depend on the laser intensity only. The initial energies can be described by eq. (2.53)

$$E_{\text{p,front}} = 1.15\,\text{MeV} \cdot \left(\sqrt{1 + \frac{I_{\text{L}} \lambda_{\text{L}}^2}{1.37 \times 10^{18}\,\text{W/cm}^2 \cdot \mu\text{m}^2}} - 1 \right), \tag{8.7}$$

that was derived in chapter 2. For the three laser intensities corresponding to the different lines in Fig. 5.6, this formula leads to front-side peak proton energies of

$$\begin{aligned} E_{\text{p,front}} &= 1.56\,\text{MeV} \quad \text{for} \quad I_{\text{L}} = 1.0 \times 10^{19}\,\text{W/cm}^2, \\ E_{\text{p,front}} &= 1.87\,\text{MeV} \quad \text{for} \quad I_{\text{L}} = 1.3 \times 10^{19}\,\text{W/cm}^2, \text{ and} \\ E_{\text{p,front}} &= 2.07\,\text{MeV} \quad \text{for} \quad I_{\text{L}} = 1.5 \times 10^{19}\,\text{W/cm}^2. \end{aligned}$$

When protons of these kinetic energies propagate through are finally stopped. This stopping-mechanism is treated numerically using tabulated values for the stopping power, $\mathrm{d}E/\mathrm{d}x$,

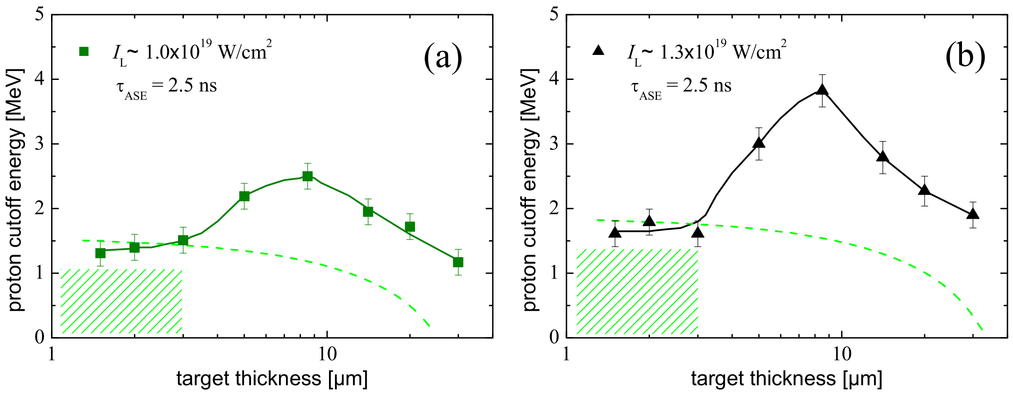

(a) $I_{\text{L}} = 1.0 \times 10^{19}\,\text{W/cm}^2$

(b) $I_{\text{L}} = 1.3 \times 10^{19}\,\text{W/cm}^2$

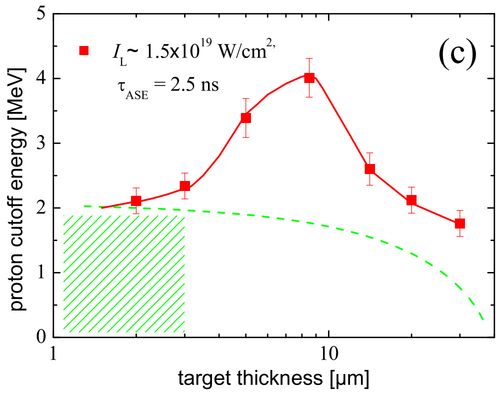

(c) $I_{\text{L}} = 1.5 \times 10^{19}\,\text{W/cm}^2$

Figure 8.11: Comparison between peak proton energies accelerated from the target front side, that are subsequently slowed down in the target material (dashed green lines), and the experimental measurements for three different laser intensities. For the shaded region encompassing thin targets, the experimental data is well explained by the front-side acceleration mechanism, while the rear-side mechanism predicts proton energies that are too low.

for protons in (cold) aluminum from the National Institute of Standards and Technology (NIST, [106]). The kinetic energy of the protons at a given depth, x, of the target is obtained by the following integration:

$$E_{\mathrm{p}}(x) = E_{\mathrm{p,front}} - \int_{0}^{x} \left| \frac{\mathrm{d}E(x')}{\mathrm{d}x'} \right| \mathrm{d}x'. \tag{8.8}$$

The integration is carried out, until the proton is stopped. This stopping distance depends on the initial energy. In Fig. 8.11 the proton energies are shown that were calculated by assuming that the protons are accelerated at the target front side to a peak energy given by eq. (8.7) using the intensity from the experiment. When they propagate through the target material they lose a part of their energy and would leave a target of a certain thickness with the kinetic energy given by the dashed green line.

A good agreement between the theoretical model for the *front-side* acceleration and the experimental data is found for the thinnest foils and long prepulses, while in this region, the model for the *rear-side* acceleration including prepulse effects predicts peak proton energies, that are too low compared to the experiment. On the other hand, the front-side acceleration cannot explain the maximum proton energies at and above the optimal target thickness, as their initial energy is too low and for thicker targets, the stopping in the target material reduces their kinetic energy even more.

8.2.5 Conclusions from the Target-Thickness Scan

Including all the prepulse-induced effects and considering the two different acceleration mechanisms from both target surfaces, the experimental data could well be reproduced by numerical and theoretical predictions. This is summarised in Fig. 8.12. It shows the comparison between the experimentally measured proton cutoff energies for a laser intensity of $I_{\mathrm{L}} = 1.5 \times 10^{19}\,\mathrm{W/cm^2}$ and the theoretically determined values using the two models for the front- and rear-side acceleration. The agreement between these models and different parts of the experimental curve suggests that both acceleration mechanisms have to be taken into account to explain the whole experiment.

The results from the comparison of the experimental data from the target-thickness scans with numerical simulations considering all prepulse-induced effects can be summarised as follows:

- The occurance of the optimal target thickness for the proton acceleration, d_{opt}, and its dependence on the prepulse duration, τ_{ASE}, could be explained for the first time by combining MULTI-FS simulations, that describe the influence of the laser prepulse due to ASE on the target properties, with a fast-electron transport code. For sufficiently thin targets, the prepulse has both reduced the target density and formed a rear-side ion-density gradient. The first effect leads to a less collimated electron transport in the target, as the collimating magnetic fields are weaker for lower target densities. This reduces the electron density in the rear-side sheath. The latter effect further reduces the acceleration fields as described in chapter 7.2.3. Both

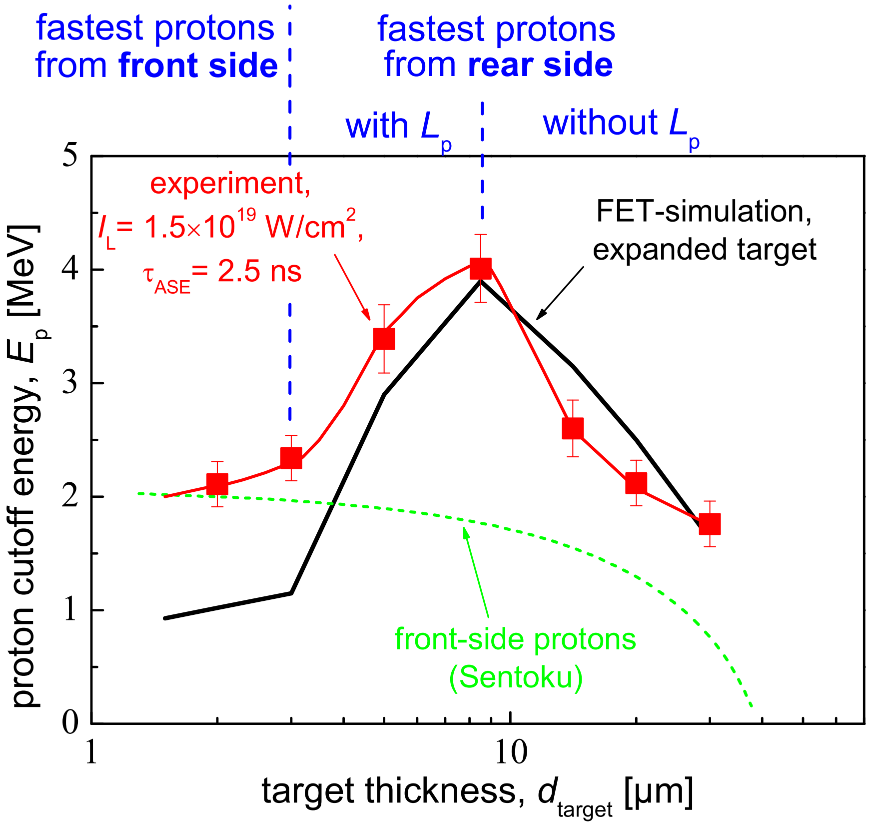

Figure 8.12: Comparison between the experimental results for the proton cutoff energy with the theoretical models for the front- and rear-side acceleration. Neither of the two acceleration mechanisms is able to explain all measured cutoff energies. In the different parameter regimes either the front-side or the rear-side acceleration leads to the peak proton energies.

effects significantly reduce the cutoff energies of protons accelerated at the target rear surface, as it could be shown in a numerical description of the processes.

- The absolute values for the cutoff energies and the temperatures of the hottest component in the measured proton-energy spectra are well reproduced by a combination of a fast-electron transport code and a one-dimensional simulation code for the rear-side proton acceleration. This agreement is only found for targets at and above the optimal thickness.
- The proton energies obtained for thin foils and long prepulse durations cannot be explained by the rear-side acceleration mechanism. However, for these cases the front-side acceleration mechanism predicts peak proton energies, that exactly match the experimental results.

By changing both prepulse duration and target thickness independently, a distinction between protons accelerated from the target front and rear side is possible. It is found that the proton component with the highest kinetic energies and the hottest temperature is accelerated from the target rear surface. By using sufficiently thin targets and long prepulses, the generation of this component in the energy spectrum can be suppressed. In this case, only the proton component accelerated from the target front side remains, having a significantly colder temperature and lower peak energies.

8.3 Results Obtained from the Angular Scan

In chapter 5.4, angularly resolved measurements of the proton-energy spectra were shown. The proton-beam divergence was found to strongly depend on the kinetic energy of the protons. Generally speaking, the low-temperature component in the proton spectrum shows a much smaller divergence, i.e. it is emitted in a very narrow cone, while the hot-temperature component is emitted in a cone with a significantly larger opening angle. A detailed investigation presented in Fig. 5.12 revealed an energy dependence of the beam divergence, that is peaked at $E_\mathrm{p} \approx 1.8\ldots2\,\mathrm{MeV}$. Above this energy, the divergence angle decreases again what is in good agreement with measurements from other groups [28,82]. Furthermore, it was found that the strong collimation of the cold-proton component is reduced for a longer prepulse duration.

These experimental findings will be explained by comparing the experimental results with 3-D particle-in-cell (PIC) simulations carried out by A. Pukhov [45] using the code VLPL (the Virtual Laser Plasma Laboratory) [123].

8.3.1 Description of the Proton Acceleration with 3-D PIC codes

The entire process of proton acceleration from the target rear surface has to be treated in two or even three dimensions. Although it is sufficient to describe the acceleration in 1D for the highest proton energies, that are accelerated in the center of the electron spot on the target rear side, where both temperature and hot-electron density are maximal [18,45,86], the slower protons are likely to be accelerated from regions outside the center of the electron sheath. This phenomenon has been observed by A. Pukhov in 3-D PIC simulations. In a numerical run simulating a “model problem” [45], a laser pulse of 1-μm wave length and an intensity of $10^{19}\,\mathrm{W/cm^2}$ interacts with a 12-μm thick hydrogen-plasma layer with an initial electron density of $16 \times n_\mathrm{cr}$.

The electrons accelerated at the target front side propagate through the target forming a cone that is characterised by its half-opening angle, θ_in, as described in the last section. These electrons leave the target and are pulled back by the arising electric fields that also drive the proton acceleration. As it has been observed in [45], the electrons form a “fountain”-like structure, while they are pulled back, what leads to a large halo in the electron density around the dense spot, where the electrons first exit the target. When these electrons return to the target front surface, where they are again pulled back into the target and come back to the rear side a second time, as it has been described by A. Mackinnon and Y. Sentoku [38], they loose energy, while they heat up the bulk of the target, and quickly spread out sideways further increasing the electron-spot size on the rear side. The hot-electron density distribution calculated from this simulation run is given in Fig. 8.13.

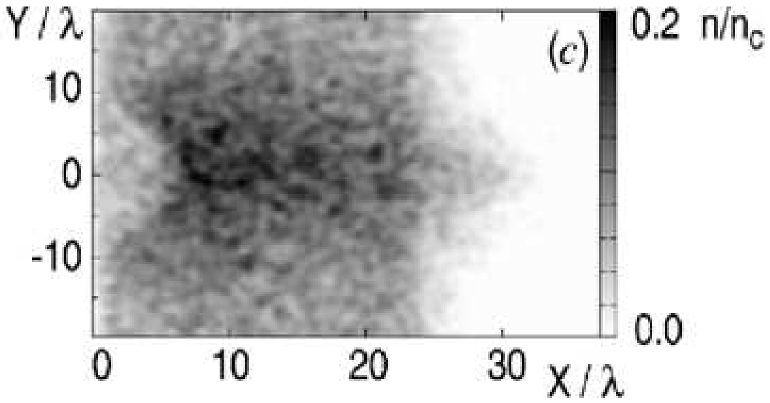

Figure 8.13: Electron density in the target in units of $n_{\mathrm{cr}} = 1.1 \times 10^{21}\,\mathrm{cm}^{-3}$ calculated by A. Pukhov [45]. The laser with an intensity of $I_{\mathrm{L}} = 10^{19}\,\mathrm{W/cm}^2$ and a wave length of $\lambda = 1\,\mu$m impinges on the left side of the target at $x = 0$ and $y = 0$ and accelerates electrons that propagate through the target several times. In this plot, the density distribution of electrons with kinetic energies above 100 keV is shown after the laser pulse has terminated. These electrons form a “fountain”-like structure at the target rear side.

As a consequence of the fountain structure, the electron density remains as high as estimated in eq. (8.3) only in the center of the electron spot and quickly drops towards the outer regions where according to eq. (2.58) also the electric field is significantly lower.

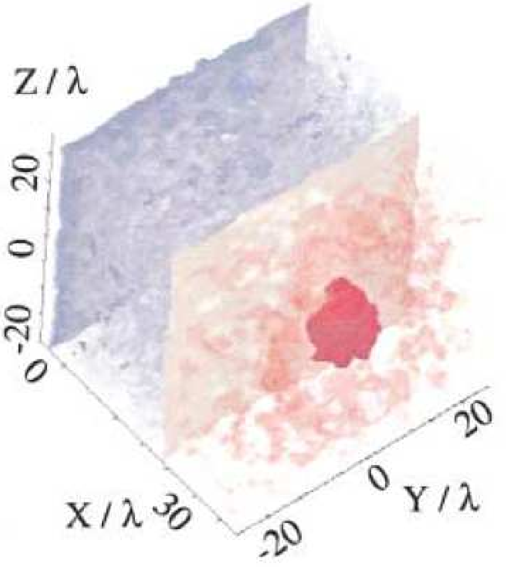

Figure 8.14: 3-D view of the electrostatic field driving the proton acceleration calculated in 3-D PIC simulations in [45]. The blue isosurface has a field value of $-1.6 \times 10^{11}\,\mathrm{V/m}$, the light red isosurface corresponds to $1.6 \times 10^{11}\,\mathrm{V/m}$, and the dark red blob in the center has peak values of $3.2 \times 10^{11}\,\mathrm{V/m}$.

This leads to a spatial distribution of the electric field, as it was calculated in [45] and shown in Fig. 8.14. Note that the center of the electron spot at the target rear side, where the electric field has its peak value, has a diameter of only $\sim 10\,\mu$m. This is in very good agreement with the assumption for the half-opening angle, $\theta_{\mathrm{in}}=(9\pm2)^\circ$ of the electron beam in the target made in section 8.1.1, that predicts an electron-spot with a diameter of $(8.8\pm0.9)\,\mu$m for a target thickness of $12\,\mu$m as it is simulated here and also with the results from the FET code, where a diameter between $10\,\mu$m and $12.4\,\mu$m was predicted for the two target thicknesses of 8.5 μm and 14.1 μm (cf. table 8.1).

Fig. 8.15 gives the corresponding acceleration sketch for the protons. Here the electric field vectors are plotted according to the electron density and temperature distributions. The proton acceleration follows these field lines. In outer regions (*C*) the proton energy remains low but these protons have a stronger collimation due to the plane electron distribution. Moving towards the center of the electron sheath, the electric field increases, but its direction is first tilted compared to the target normal in region *B*, resulting in protons with higher energies but a larger divergence. In the central region, *A*, the electric field is peaked and the lines are again almost parallel to the target normal. Here the fastest protons are accelerated and emitted in a narrow cone again.

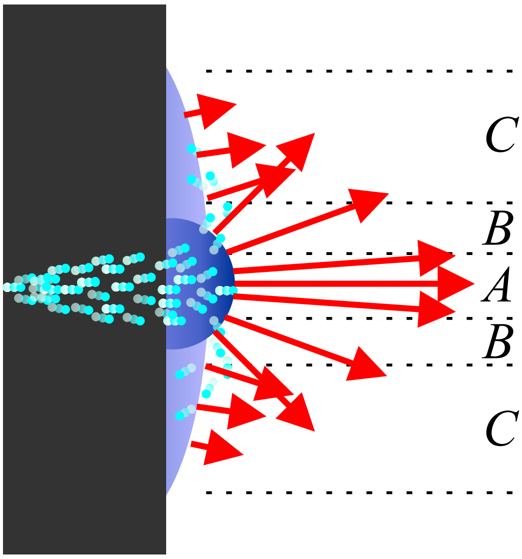

Figure 8.15: Schematic acceleration of protons from the target rear side following the real electron density and the corresponding electric field distribution. The protons with the highest energy are accelerated with a small divergence in the center of the electron sheath (region *A*), where the electric field is peaked, indicated by the red arrows. Going from the center of the electron sheath to outer regions, the divergence first decreases (region *B*) due to the form of the electron distribution and also the proton energy drops. In region *C*, the sheath is plane again leading to a smaller divergence, but due to the low electron density, the electric fields are lower here resulting in lower proton energies.

8.3.2 Conclusions

This comparison with Pukhov's 3-D PIC simulations explains the strongly forward directed cold proton component mainly originating from the outer regions of the electron sheath, *A*, while the divergence first increases for higher proton energies, that come from region *B*. For the fastest protons, that are accelerated exactly in the center of the electron spot, region *C*, the divergence decreases again. This behaviour exactly reproduces the experimentally found energy dependence of the proton-beam divergence. It has also been observed in 3-D PIC-simulations by H. Ruhl [124]. Although the main features of the experimental results can be understood on the basis of the simulations by A. Pukhov, a detailed 3-D simulation that exactly includes all experimental parameters as prepulse-induced effects and the acceleration of all the different ion species including their ionisation process is presently beyond the limit of computational resources.

Furthermore this picture of the rear-side acceleration is also able to explain the changes in the divergence of low-energy protons observed for longer prepulse durations. In this case the prepulse has already started to heat up the back of the target initiating a rear-side expansion that also has to be treated in 2-D, when regions out of the center of the electron spot are taken into account. Then the rear surface is no longer plane but has a convex shape. This leads to a larger divergence also for the low energy protons, in accordance with the experimental observations.

Chapter 9

Summary and Perspectives

During the course of this thesis, experiments were carried out to characterise the proton-acceleration processes that are active during the interaction of high-intensity laser pulses with solid targets. As a whole, the results and their theoretical interpretation answer many questions concerning the physics underlying the acceleration processes.

The results presented here shed new light onto experimental parameters that were found to have a profound effect on the proton acceleration. Together with laser intensity and pulse energy, the target thickness and the duration of the intrinsic prepulse due to amplified spontaneous emission (ASE) were shown to play an important role. Within this work, the occurance of an optimal target thickness was observed and an explanation for its occurance was found. The value of the optimal thickness strongly depends on the prepulse duration that could for the first time both be controlled and varied.

The prepulse-induced changes of the target-density and -temperature distributions were found to significantly influence the electron transport inside the target and as a consequence also the proton acceleration. Including these prepulse-changed target properties in computer simulations yielded a good agreement between the numerically predicted proton energies and the experimental data. However, the peak energies obtained for *all* experimental parameters could only be explained by a physical picture that includes both front-side and rear-side acceleration mechanisms for protons.

It was found that the optimal target thickness delimits two proton acceleration regimes. At and above the optimal target thickness, the fastest protons are accelerated from the rear side, the electron beam propagating through the target is collimated in this regime. For thinner targets, the density in the target is significantly reduced by the prepulse heating, what reduces the collimation of the electron beam in the target and consequently the rear-side acceleration fields. The latter are additionally diminished by an ion-density gradient that was formed at the target rear side. By a further reduction of the target thickness the rear-side mechanism is rendered more and more ineffective. The front-side mechanism, however, only depends on the laser intensity. For the thinnest targets and the longest prepulse durations, the rear-side acceleration is strongly suppressed and the fastest protons come from the target front side.

The changes at the target rear surface are mainly induced by radiative heating due to prepulse-generated X-rays. This depends on the target thickness, as the radiation generated in the focus of the prepulse on the target front side is the more absorbed inside the target the thicker it is. For thicker targets it was found that these changes of the target properties begin at a later time compared to thinner foils. This exactly reproduces the experimental findings.

In conclusion, the experimental results and their theoretical and numerical interpretation reported in this thesis bring about new and relevant aspects concerning the laser-induced acceleration of protons and light ions for future experiments. They can also help to understand and solve apparent discrepancies in the comparison of experiments that have been carried out with different laser systems. It turns out that is is of extreme importance to control the laser prepulse – or at least characterise its temporal evolution – in order to otimise the experimental conditions for proton acceleration.

9.1 Possible Future Experiments on Proton Acceleration

This work has shown that also small-scale table-top laser systems as ATLAS have the potential to be an efficient source of laser-accelerated protons, when all experimental parameters including the prepulse duration can be controlled as accurately as possible. It was shown that it is preferable to reduce the laser prepulse to durations as short as possible to maintain an undisturbed target rear surface also for the thinnest foils.

The MULTI-FS simulations describing the influence of the laser prepulse on the target properties have shown that for prepulse intensities as low as in the experiments described here the radiative heating is the dominant process to destroy the target rear surface before the main pulse arrives at the target front side and the rear-side proton acceleration is initiated. One possibility to reduce this heating is to put a very thin low-Z layer on the front side of the aluminum target that was used here. For such a target configuration, the material of the front layer is also heated by the prepulse but it emits characteristic radiation at lower photon energies compared to the aluminum. This radiation is quickly absorbed in the aluminum layer, leaving the target rear side undisturbed. The layer on the target front side (e.g. plastic or beryllium) should be as thin as possible to leave the electron transport unaffected but thick enough to prevent the aluminum from heating by the prepulse. Other high-Z materials as gold or tungsten could be used for the second layer, too.

Following the road towards shorter and shorter laser-pulse durations, the applicability of such pulses for proton acceleration has to be addressed, too. The effectivity of the rear-side acceleration mainly scales with the product of laser intensity and pulse duration, $I_\mathrm{L} \cdot \tau_\mathrm{L}$, which is proportional to the laser energy, E_L, if an optimal focusability of the laser pusle is assumed. This relation was empirically found by M. Roth by comparing all existing results from different laser systems [125] with pulse durations of $\tau_\mathrm{L} \leq 1\,\mathrm{ps}$. This dependency implies to use lasers with as high pulse energies as possible for an efficient proton acceleration and not to reduce the pulse duration as much as possible. However, with lasers potentially delivering pulses as short as 5 fs and peak intensities in excess of 10^{20} or even $10^{21}\,\mathrm{W/cm^2}$, the generation of electron populations having temperatures in the range of 10 MeV and high total numbers is possible. These electron populations might generate significantly stronger electric fields at the rear side of the target and field-ionise atoms at the surface into much higher charge states. This could be a possibility to generate beams of ions with higher charge states as presently possible. It was shown by M. Hegelich [18] that the ion population that was field ionised to the highest charge state by the electric field at the rear side is preferably accelerated, when surface contaminations including protons are removed by resistively heating the target to several 100's of Kelvin before the laser shot. Thus, the usage of shorter laser pulses generating higher initial fields might help to generate higher charged ion beams. However, it has to be considered that due to the shorter pulse duration, the life time of the acceleration fields is also reduced, what leads to lower peak energies of the ions. Furthermore, the number of electrons in the hot-electron population has to be considered, too. Nevertheless, the utilisation of shorter laser pulses for proton and ion acceleration appears to have an promising potential for future experiments.

Turning to the front side of the target, the peak energy of the protons accelerated here depends on the ponderomotive potential of the laser, as it was shown in chapter 2.4.1. As this scales with $\sqrt{I_\mathrm{L}}$ for high laser intensities, the front-side acceleration should overcome the rear-side acceleration at a certain intensity. Furthermore, it seems possible that the protons that were pre-accelerated at the target front side propagate through the foil and get a second acceleration kick in the rear-side electron sheath. For these purposes, lasers with extremely high intensities would be preferable as the protons at the target front side have to gain sufficiently high velocities to reach the target rear surface before the rear-side sheath breaks down, when the pulse is over. This requires target foils as thin as possible and as a consequence a contrast ratio between laser prepulse and main pulse as high as possible to preserve an undisturbed target rear side as it was found in this thesis. Meeting all these requirements would possibly allow a proton acceleration to even higher energies. In this case, it would no longer make sense to dedicate the origin of the fastest protons to one target surface, but they were accelerated at both sides of the target.

9.2 Suggestions for Future Numerical Simulations of Laser-Plasma Interactions

It was shown in this work that the correct implementation of the initial target properties into numerical simulations is of crucial importance. It is not sufficient to treat the initial target as a cold solid, but prepulse-induced effects were shown to have a profound effect on the simulation results concerning the electron transport and the proton acceleration. The fast-electron transport in the target strongly depends on the resistivity distribution that in turn depends on the initial density and temperature distributions in the target. As a consequence, the rear-side proton acceleration is also strongly influenced. Furthermore, it was shown that an ion-density gradient at the target rear side also has to be taken into account.

For a complete description of all the processes that affect the proton acceleration the development of computer codes is necessary that treat both the electron transport through the target and the rear-side build up of an electrostatic potential driving the proton acceleration in a self-consistent way. It is likely that both processes influence each other, as those electrons, that have left the target, are pulled back by the arising electrostatic field at the rear side, and re-enter the target, modify the transport of those fast electrons that follow subsequently. This modification of the electron transport in turn has consequences for the rear-side acceleration. The development of such a code including all these effects is currently under way [126].

Appendix A

Setup of a Novel Synchronised 2-Colour Probe Beam for Preplasma Diagnostic

In laser-plasma experiments, it is convenient to use probe beams synchronised to the main pulse to backlight the laser-target interaction area from the side to record snapshots of this area with a time resolution that is given by the probe-beam duration (see e.g. [37, 42, 72]). By changing the delay between the main pulse and this probe beam on the target, the plasma evolution can be studied in a sequence of laser shots. In this appendix, we will describe the setup of a novel 2-colour probe beam that was used to study the generation and evolution both of preformed plasmas and of a plasma super channel. With the novel technique using two probe beams, the formation state of the channel can be observed at two different time stages during the very same laser shot.

After a short description of the setup in section A.1, the generation of two probe beams of ~150-fs duration and different wave lengths separated by $\Delta t = 4.1\,\mathrm{ps}$ is described in section A.2. These two beams are used to probe a preplasma that was formed by a synchronised frequency-doubled Nd:Glass-laser delivering pulses of 12-J of energy at 532-nm wave length with a duration of 3 ns. Using a Wollaston prism for interferometry [127], that is introduced in section A.3, the electron density of the preplasma can be deduced from these interferograms, as shown in section A.4. Finally, the formation of a plasma channel is observed [10, 72, 128], that is generated by focusing the synchronised Ti:sapphire-laser ATLAS into the preformed plasma.

A.1 Experimental Setup

The probe-beam setup is sketched in Fig. A.1. After the first multi-pass amplifier, a part of the streched beam is split off, recompressed to 130 fs in the ATLAS-2 grating-compressor chamber and sent into a delay line. This 790-nm pulse contains $\sim 5\,\mathrm{mJ}$ of energy. After that the beam diameter is reduced by a lens telescope. This 1ω-beam is frequency doubled in a 2-mm thick type-1 KDP crystal. Before the pulse enters the crystal, its polarisation is rotated by a $\lambda/2$ wave plate, that its plane of polarisation is tilted by 45° to the vertical axis. The 2ω-pulse generated in the KDP crystal has its plane of polarisation rotated by 90° to the fundamental beam. This choice of polarisations was necessary for the interferometry using a Wollaston prism, what will be described below. These two beams are guided into the target chamber where they both pass the interaction

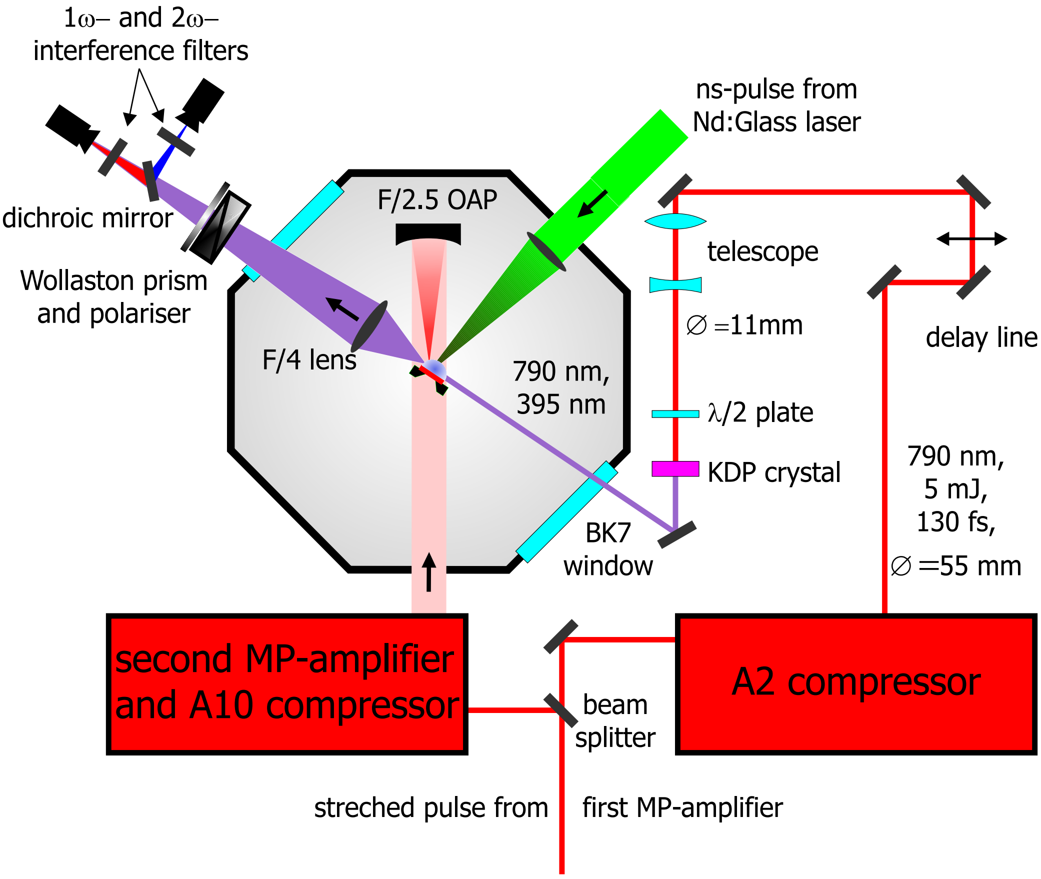

Figure A.1: Schematic setup of the 2ω-probe beam. A part of the streched main pulse is recompressed and frequency-doubled before the two pulses (fundamental and second harmonic) are guided into the vacuum chamber where they pass the target, when the main pulse arrives on the front side. The relative timing between main and probe pulse is adjusted using the delay line. Behind the chamber, the two pulses first pass a Wollaston prism and a polariser to obtain interferograms of the interaction area, and finally they are separated by a dichroic mirror and interference filters to be detected by two CCD-cameras.

area on the target front side. This interaction area is imaged by a $f/4-$lens onto two CCD-cameras that are separated by a dichroic mirror that reflects 2ω-light and transmits 1ω-light. Furthermore, each CCD is equipped with an interference filter either for 1ω- or 2ω-light. Therefore, each CCD only records snapshots of the target backlighted by one of the two probe beams.

Behind the imaging lens, the two beams pass a Wollaston prism and a polariser that enables us to obtain interferometric sideviews of the interaction area of both pulses. This will be described in section A.3. During the generation of the second harmonic and the passage through the first 20-mm thick BK7-window of the vacuum target chamber, the two pulses are separated in time. This will be described in the next section.

A.2 Generation of two fs-Probe Beams Separated by Several ps

When the pulse with the fundamental wave length of 790 nm passes through the type-1 KDP crystal, a second-harmonic pulse with 395-nm wave length is generated. Its plane of polarisation is rotated by 90° with respect to the fundamental. Before the two pulses can pass the target, they have to propagate through a 20-mm thick window of BK7 glass. During their passage through the glass both pulses are slightly stretched and temporally separated due to the dispersion of the group velocities. To estimate the delay, Δt, between the two pulses the Sellmeier equation is used to calculate the refractive index, $\eta(\omega)$:

$$\eta(\omega) = \sqrt{1+\sum_{i=1}^{3} A_i \cdot \frac{\omega_i^2}{\omega_i^2-\omega^2}}, \tag{A.1}$$

using the following tabulated values from Schott [129]:

$$\begin{aligned} A_1 &= 1.0396100, & \omega_1^2 &= 5.912883\times10^{32}\,\mathrm{s}^{-2},\\ A_2 &= 0.2317923, & \omega_2^2 &= 1.772484\times10^{32}\,\mathrm{s}^{-2},\\ A_3 &= 1.0104694, & \omega_3^2 &= 3.426150\times10^{28}\,\mathrm{s}^{-2}. \end{aligned}$$

With this dispersion of the refractive index, the streching and the temporal separation of the two pulses can be calculated. The increase of the initial pulse duration, $\tau_{\mathrm{L}}(0)$, during the passage through BK7 glass of thickness x for each of the two different wave lengths and frequencies is given by

$$\tau_{\mathrm{L}}(x) = \tau_{\mathrm{L}}(0)\cdot\sqrt{1+\left[\frac{4\ln 2}{\tau_{\mathrm{L}}^2(0)}\cdot x\frac{\partial^2}{\partial\omega^2}\left(\frac{\omega\cdot\eta(\omega)}{c}\right)\right]^2}. \tag{A.2}$$

This leads to a relative increase of the pulse durations of 1.1% for 790 nm and of 4.6% for 395 nm, what will be neglected. However, the delay between the two pulses is not negligible. It can be described by the dispersion of the group velocity,

$$v_{\mathrm{gr}}(\lambda) = \frac{c}{\eta(\lambda)-\lambda\frac{\partial\eta(\lambda)}{\partial\lambda}}. \tag{A.3}$$

The delay, Δt, between the two pulses after passing through BK7 glass of $x_{\mathrm{BK7}} = 20\,\mathrm{mm}$ thickness is then

$$\Delta t = x_{\mathrm{BK7}}\left(\frac{1}{v_{\mathrm{gr}}(\lambda_1)}-\frac{1}{v_{\mathrm{gr}}(\lambda_2)}\right) = 3.95\,\mathrm{ps}. \tag{A.4}$$

Furthermore, during the 2ω-generation in the KDP-crystal, the fundamental and second harmonic are separated due to their different group velocities in the crystal, what can be described by a similar Sellmeier equation for KDP. For a crystal thickness of 2 mm, the 790-nm pulse retains its initial duration of $\tau_{1\omega} \approx 130\,\mathrm{fs}$, the 395-nm pulse has $\tau_{2\omega} \approx 160\,\mathrm{fs}$ what is due to the different group velocities of the two wave lengths. After the passage through the crystal, the red pulse leads the blue one by ~160 fs.

Adding this initial delay of 160 fs from the process of frequency doubling, one finally obtains two pulses of 790-nm and 395-nm wave length and ~150-fs duration that both pass the interaction area on the target the vacuum chamber. The red pulse leads the blue one by

$$\Delta t = 4.1\,\mathrm{ps}. \tag{A.5}$$

A.3 Interferometry Using a Wollaston-Prism

A Wollaston prism is a polarising beam splitter [97]. It consists of two birefringent wedges (usually calcite or quartz) put together to form a plane parallel plate. The optic axes of the two wedges are both perpedicular to the front-side normal and perpendicular to each other. Any linearly polarised light ray incident onto the Wollaston prism can be described by a superposition of two linearly polarised rays, where either of them is the ordinary ray (*o*-ray) in one wedge and the extra-ordinary ray (*e*-ray) in the other wedge of the Wollaston prism. At the plane of separation between the two wedges, the one part of the incident ray is deflected to one direction, the other ray is deflected to the other direction by approximately the same angle. After leaving the second wedge, the two beams have a separation angle $\alpha \approx 2(\eta_o - \eta_e) \cdot \tan\gamma$ [130], as it is sketched in Fig. A.2. The separation angle, α, depends on the wedge angle, γ, and the difference of the refractive indices for an *o*- and and *e*-ray, $(\eta_o - \eta_e)$, which in turn depends on the wave length and on the wedge material. For a *parallel* beam of diameter d that consists of both polarisations and enters the Wollaston prism, the two differently polarised parts will be completely separated after the distance $d/[2\sin(\alpha/2)] \approx d/\alpha$. However, for a *diverging* beam with an opening angle β, as it is sketched in Fig. A.2, there is always a region, where the two parts overlap, when $\beta > \alpha$.

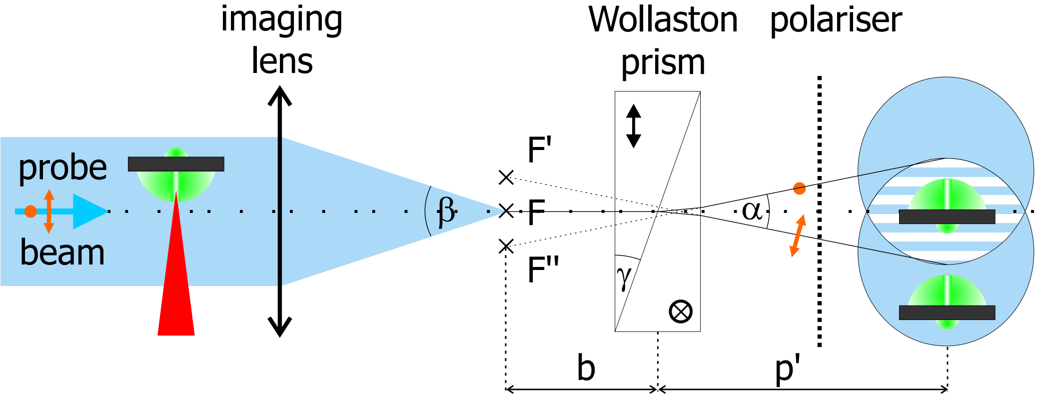

Figure A.2: Sketch of a setup that uses a Wollaston prism for interferometry. The incoming probe beam is polarised in a plane tilted by 45° to the drawing plane and passes the target interaction area and an imaging lens. The Wollaston prism angularly separates the two parts of the incoming beam with different polarisation (one in the drawing plane, one perpendicular). The polariser, that is again rotated by 45°, allows interference between these two parts. In the overlapping region, the upper part of the incoming beam that has passed the plasma on the target front surface, overlaps with the lower part, that has seen no plasma on its way. The plane of the CCD is rotated by 90° for better illustration.

The two separated beams have perpendicular polarisations and thus cannot interfere in the first place. When a polariser rotated by 45° with respect to both polarisations is inserted behind the Wollaston prism, the polariser reduces the intensities of both beams by a factor of 2, but they have parallel polarisations afterwards and can interfere in the overlapping region. As the upper part of the incoming beam overlaps with the lower part, a good spatial coherence over the whole beam is required to obtain interference.[1] The distance of the interference fringes, i, in the plane of the CCD is given by [127]

$$i = \frac{\lambda_\mathrm{L}}{\alpha}\frac{p'}{b} \tag{A.6}$$

and depends on the position of the Wollaston prism between the focal spot, F, of the imaging lens and the plane of the CCD.

A setup sketched in Fig. A.2 can be used for interferometry of a plasma, if the following requirements are met:

- The incoming beam has to have a good spatial coherence, what is usually satisfied for short-pulse lasers having inherently high spatial coherence over the beam.
- To be able to deduce the electron-density distribution from the interference pattern in the overlapping region by Abel-inversion [131,132] what will be described in the next section, the one part of the probe beam has to pass the plasma region, while the other part has to pass vacuum regions only that one obtains overlapping of a disturbed and a completely undisturbed beam.

Therefore the beam diameter has to be be sufficiently large to cover plasma regions as well as undisturbed vacuum regions and the spatial separation between the two differently polarised beams, that depends on the image magnification and the separation angle of the Wollaston prism, has to be large enough. In the setup used here, the probe beam diameter was 11 mm and the separation of the two images of the interaction area was equivalent to $\sim 1.5\,\mathrm{mm}$ in the plane of the target, what is smaller than the preplasma extension as it was simulated by MULTI (see below).

A.4 Preplasma Generation Using a Synchronised Nd:Glass Laser

The 2ω−probe beam described in the last two sections was used to study the preplasma evolution driven by a synchronised frequency-doubled Nd:Glass laser that delivered pulses of 3-ns duration and 12-J of energy at a wave length of 532 nm. This external prepulse was focused to a spot of 200-μm diameter onto thin plastic or metal foils having an averaged intensity of $10^{13}\,\mathrm{W/cm^2}$. This prepulse was capable of producing a long-scale length preplasma extending over several 100's of micrometers on the target front side. Into this preplasma, the synchronised CPA-laser pulse from ATLAS was focused producing a plasma

---

[1] This situation is different to a Mach-Zehnder interferometer, where after splitting and recombination of the beam the same spatial parts overlap again.

channel that also extended over several 100's of micrometers. First, concentrate on the preplasma evolution and its characterisation are described, while the channel formation is discussed in section A.5.

Fig. A.3 (a) shows a typical interferometric image from the preplasma obtained by backlighting the interaction region from the side with the $2\omega-$probe beam. Fig. A.3 (b) gives the electron-density distribution deduced from this interferometric picture. As the probe-beam duration of $\sim 160\,\mathrm{fs}$ was much shorter than the time scale of the preplasma evolution, we obtain a snap shot of the plasma at the time determined by the delay between Nd:Glass-laser pulse and probe pulse.

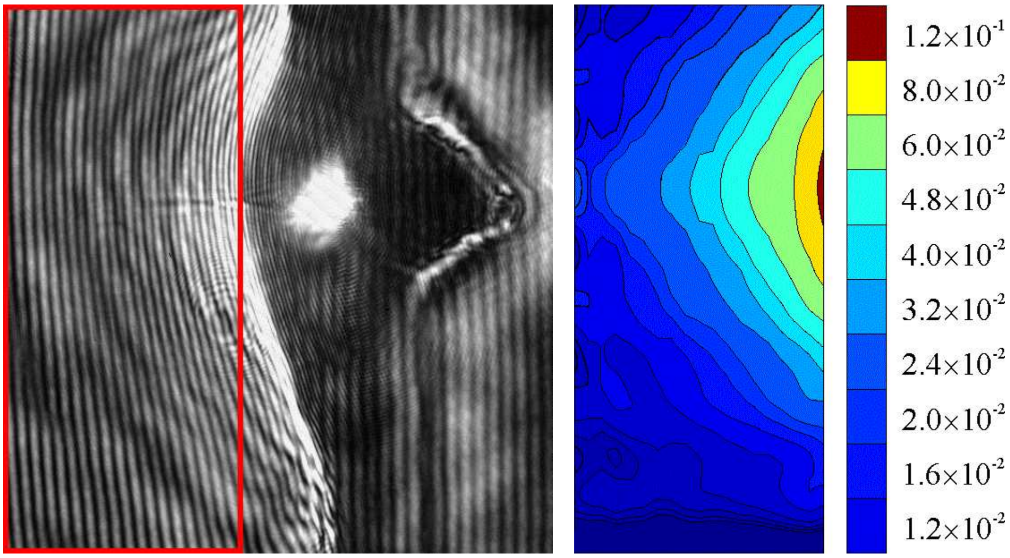

(a) (b)

Figure A.3: $2\omega-$interferogram (a) of a preplasma produced by a Nd:Glass-laser pulse impinging on a polypropylen foil from the left and the deduced electron-density distribution (b) in units of n_{cr}=$1.79\times10^{21}\,\mathrm{cm}^{-3}$. The bending of interference fringes to the left indicates an electron density $n_{\mathrm{e}}>0$. The CPA main pulse coming from the left is not seen in the interferogram, as the probe beam was earlier by $\sim 300\,\mathrm{fs}$. However, the bright spot in the middle of the interaction area is due to $2\omega-$self emission of the plasma. The electron density distribution given in (b) corresponds to the part of (a) indicated by the red box.

Deduction of the Electron-Density Distribution by Abel-Inversion

When a light ray with wave length λ_{L} propagates through a cylindrically symmetric electron density, $n_{\mathrm{e}}(r)$, with a minimal distance, y_0 from the axis of symmetry, O, as it is sketched in Fig. A.4, its phase, $\varphi(y_0)$, differs to that of a ray propagating an equivalent distance through vacuum by

$$\Delta\varphi(y_0)=\Phi(y_0) \quad = \quad \frac{2\pi}{\lambda_{\mathrm{L}}}\int_{x_1}^{x_2}[1-\eta(x)]\,\mathrm{d}x \approx \frac{\pi}{n_{\mathrm{cr}}\lambda_{\mathrm{L}}}\int_{x_1}^{x_2} n_{\mathrm{e}}(x)\mathrm{d}x$$

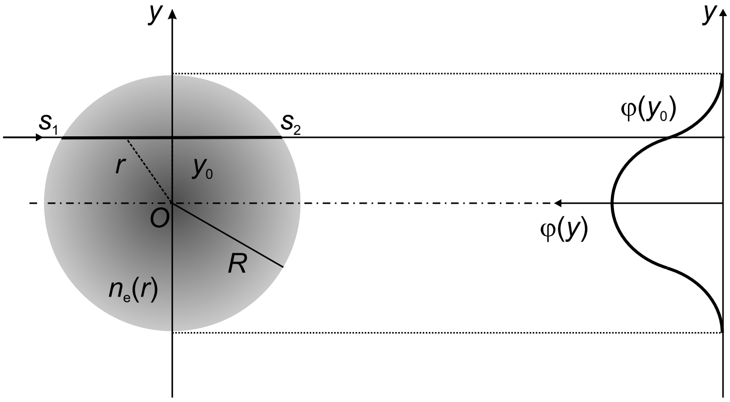

Figure A.4: Sketch for the deduction of the radial electron distribution, $n_e(r)$, from the phase shift distribution, $\varphi(y)$, that is obtained from an interferogram as in Fig. A.3 (a).

$$= \frac{2\pi}{n_{cr}\lambda_L}\int_{y_0}^{R}\frac{n_e(r)r}{\sqrt{r^2-y_0^2}}dr, \tag{A.7}$$

where $\eta(r) = \sqrt{1-n_e(r)/n_{cr}} \approx 1-n_e(r)/2n_{cr}$ is the refractive index at distance r from the center O of the electron distribution. An Abel inversion [131, 132] of this equation leads to

$$n_e(r) = -\frac{n_{cr}\lambda_L}{\pi^2}\int_{r}^{R}\frac{d\Phi(y)}{dy}\cdot\frac{dy}{\sqrt{y^2-r^2}}. \tag{A.8}$$

The phase shift, $\Phi(y)$, can be deduced from the fringe shift in the interferogram. These considerations are valid as long as the fringe shift caused by a deflection of the ray due to the plasma density gradient are small compared to the phase difference caused by the propagation through the electron density [133].

The electron density distribution as it is shown in Fig. A.3 (b) was deduced from the interferograms by M. I. K. Santala using the program IDEA [131] and the $f-$interpolation method [132]. The electron density on the axis of symmetry of the distribution was then compared to simulations carried out with MULTI [114] simulating the preplasma evolution with the same parameters as in the experiment. Here, the delay between Nd:Glass-laser pulse and probe pulse was $\Delta t = 1.9\,\mathrm{ns}$. The result is shown in Fig. A.5, where a good agreement between experiment and simulations is found. The preplasma-scale length is $L_p = 110\,\mu\mathrm{m}$.

A.5 Channel Formation in the Preformed Plasma

Finally, the two probe beams were used to study the formation of a plasma channel generated by relativistic self-focusing of laser light in the preformed plasma.

Figure A.5: Comparison between the experimentally measured electron density distribution with MULTI-simulations. For a delay between 1.2 ns and 2.2 ns, a very good agreement with the experiment is found, where a delay of 1.9 ns was used. In the region measurable in the experiment, the electron density can be described by an exponential distribution with a density-scale length of $L_\mathrm{p} = 110\,\mu\mathrm{m}$.

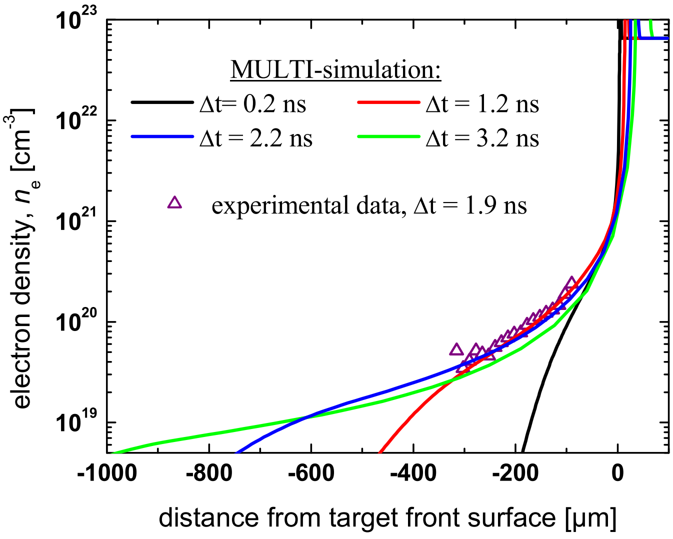

A.5.1 Plasma Channels in Self-Emission

Fig. A.6 shows two images of the same plasma channel recorded at two different wave lengths (790 nm in (a) and 395 nm in (b)) without probe beams. Electrons in the plasma channel scatter laser light sideways via linear and non-linear Thomson scattering, the intensity of the side-scattered light depends on the local laser intensity. The plasma channel extends over a length of more than 400 μm. This is 8-times the confocal parameter of the vacuum focus, which is 50 μm (see chapter 3). This is comparable to results obtained in [10], where electrons were acclerated in a gas jet. Furthermore, the electron energy spectra measured with a 45-channel electron spectrometer [134] also exhibit an exponential decay with a effective temperature between 2 and 5 MeV. It is most likely that the electrons are accelerated in the channel via the mechanism of direct laser acceleration (DLA), that was described in chapter 2.2.2.

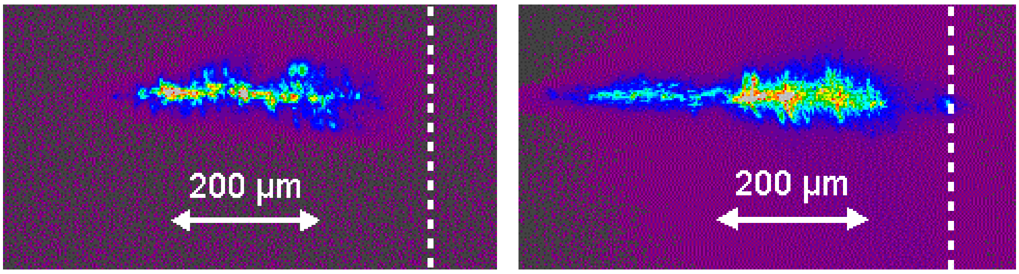

(a) (b)

Figure A.6: Images of a relativistic plasma channel generated by focusing the high-intensity laser pulse of ATLAS 10 into the preformed plasma. The two images of self-emitted light are recorded at 790 nm (a) and 395 nm. The plasma channel extends over more than 400 μm, the initial target front surface is indicated by the vertical dashed line.

A.5.2 Interferometrical Pictures of Plasma Channels

In the last section the plasma channels could be observed by their self-emitted light, which was recorded over the whole exposure time of the CCD-camera, which is of the order of several milliseconds. Therefore, the recorded images are time-integrated, as the channel evolves on a sub-ps time scale. However, using the two synchronised probe beams each having a pulse duration of $\sim 150\,\mathrm{fs}$ allows nearly time-resolved images of the rapid expansion of the plasma channel.

Due to the ponderomotive force of the laser, electrons are radially expelled from the channel leaving behind a region of reduced electron density on the axis of the channel. Furthermore, a shock front, in which the local electron density encreases, propagates radially outwards from the channel axis. Both effects, the reduction of electron density in the center of the channel and the fast propagating shock front forming a cylindrical shell around the central axis, where the local electron density is higher, can be seen in the interferograms. Fig. A.7 shows two interferograms of the preplasma and the channeling region of the same laser shot. While the iterferogram in (a) was generated with the 790-nm pulse, what is indicated by the red background colour, the interferogram in (b) was taken with the blue 395-nm pulse. Depending on the intensity ratio between the light from the channel self-emission and the backlighting probe beam, the self-emission is still visible as in (a) or suppressed as in (b). In (b), only the strong emission from the laser pulse impinging on the overcritical plasma layer is seen as an overexposed spot, while in (a) the self emission of the channel can clearly be distinguished.

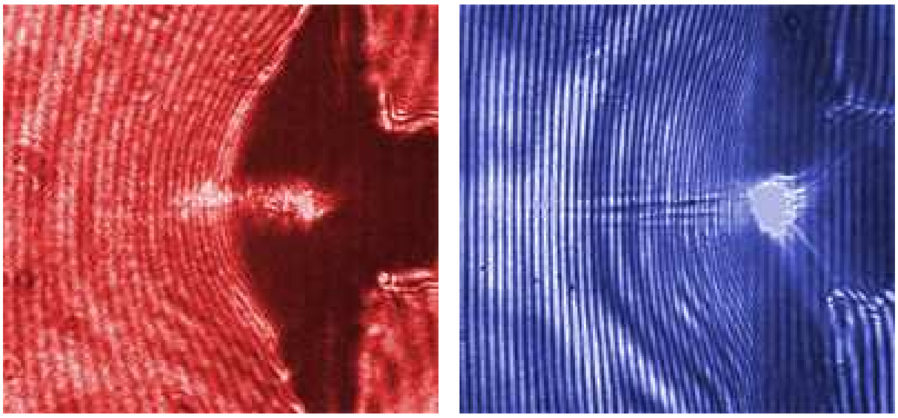
(a) Interferogram with 790-nm probe beam (b) Interferogram with 395-nm probe beam

Figure A.7: Interferograms taken during the same laser shot with two differently-coloured probe beams. The 790-nm beam (a) passes the interaction area shortly before the arrival of the main pulse in the preplasma, the 395-nm beam (b) shortly after the main pulse. Therefore, the channel-induced density modulations in the preplasma are visible in (b) but not in (a).

However, the imprint of the channel on the electron density, i.e. a distortion of the interference fringes that correspond to the electron density of the preplasma, can only be seen in the right picture. To estimate the delay between the two probe pulses, pictures were taken with different delays between the main pulse and the two probe beams. Starting from a certain delay setting, where no channel fringes could be observed in both pictures, the delay was increased in steps of 1.5 ps, first observing the appearance of channel fringes in the 395-nm picture as shown in Fig. A.7 and then in both pictures. The upper limit for the delay between the two probe beams was found to be 6 ps which is the total delay between the two delay settings, where either channel interference was observed in none or in both of the pictures. The lower limit was 3 ps. This is in good agreement with the estimation of $\Delta t = 4.1\,\mathrm{ps}$ from the group-velocity dispersion carried out in section A.2. These measurements show for the first time the generation of the plasma channel with a time resolution of a few ps for one single laser shot. The time delay between the two pulses estimated from the measurements agrees well with the expected value.

Finally, the expansion of the plasma channel was measured in a series of shots with different delays, here using only the pictures obtained with the $2\omega-$probe beam, as it is shown in Fig. A.8.

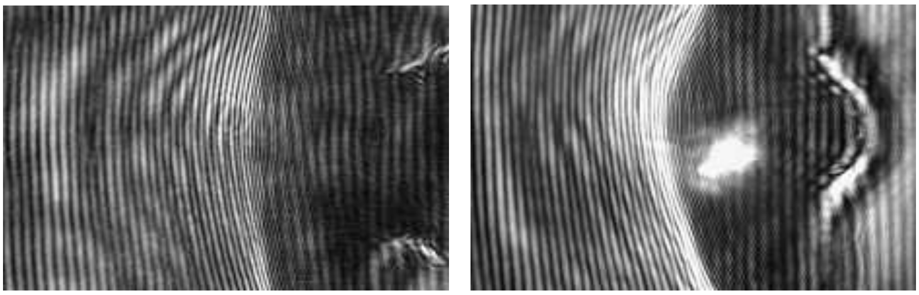

(a) Only Nd:Glass laser, no CPA-laser (b) $\Delta t = -0.3\,\mathrm{ps}$

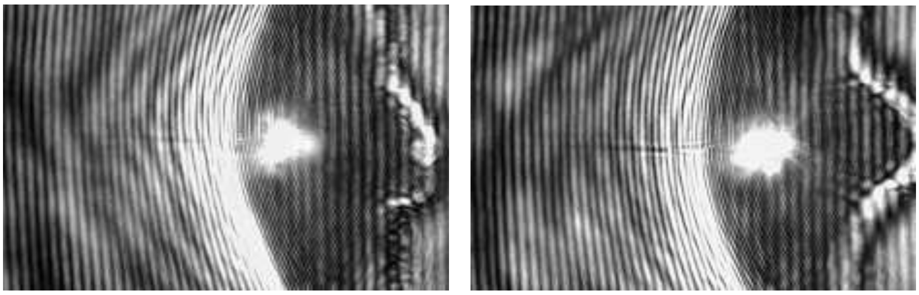

(c) $\Delta t = 0\,\mathrm{ps}$ (d) $\Delta t = +0.6\,\mathrm{ps}$

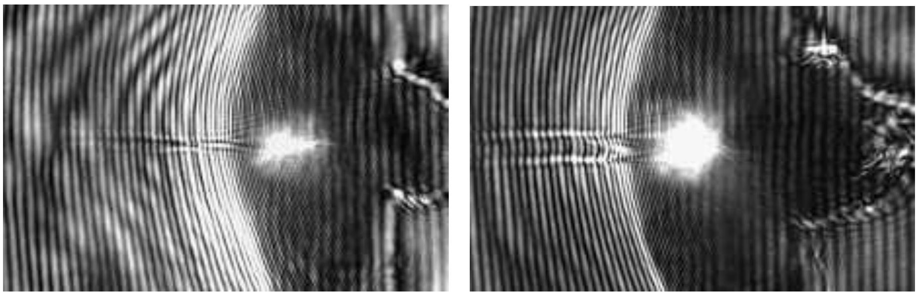

(e) $\Delta t = +1.3\,\mathrm{ps}$ (f) $\Delta t = +12.0\,\mathrm{ps}$

Figure A.8: Series of interferograms with different delays between CPA-laser pulse and $2\omega-$probe pulse. Picture (a) was taken with the prepulse laser only.

Bibliography

[1] D. Strickland and G. Mourou, *Compression of amplified chirped optical pulses*, Opt. Commun. **56**, 219 (1985).

[2] C. B. Edwards, *Vulcan Petawatt Upgrade Overview*, Central Laser Facility (CLF), Annual Report, pg. 164 (2001/2002).

[3] M. Aoyama, K. Yamakawa, Y. Akahane, J. Ma, N. Inoue, H. Ueda, and H. Kiriyama, *0.85-PW, 33-fs Ti:sapphire laser*, Optics Letters **28**, 1594 (2003).

[4] Y. Kitagawa, H. Fujita, R. Kodama, H. Yoshida, S. Matsudo, T. Jistuno, T. Kawasaki, T. Kanabe, S. Sakabe, K. Shigemori, N. Miyanaga, and Y. Izawa, *Prepulse-Free Petawatt Laser for a Fast Ignition*, IEEE Journal of Quantum Electronics **40**, 281 (2004).

[5] K. Krushelnick, private communication (2004).

[6] V. Malka, S. Fritzler, E. Lefebvre, M.-M. Aleonard, F. Burgy, J.-P. Chambaret, J.-F. Chemin, K. Krushelnick, G. Malka, S. P. D. Mangles, Z. Najmudin, M. Pittman, J.-P. Rousseau, J.-N. Scheurer, B. Walton, and A. E. Dangor, *Electron Acceleration by a Wake Field Forced by an Intense Ultrashort Laser Pulse*, Science **298**, 1596 (2002).

[7] E. Esarey, P. Sprangle, J. Krall, and A. Ting, *Overwiew of plasma-based accelerator concepts*, IEEE Trans. Plasma Sci. **30**, 252 (1996).

[8] G. Malka and J. L. Miquel, *Experimental Confirmation of Ponderomotive-Force Electrons Produced by an Ultrarelativistic Laser Pulse on a Solid Target*, Physical Review Letters **77**, 75 (1996).

[9] M. H. Key, M. D. Cable, T. E. Cowan, K. G. Estabrook, B. A. Hammel, S. P. Hatchett, E. A. Henry, D. E. Hinkel, J. D. Kilkenny, J. A. Koch, W. L. Kruer, A. B. Langdon, B. F. Lasinski, R. W. Lee, B. J. MacGowan, A. MacKinnon, J. D. Moody, M. J. Moran, A. A. Offenberger, D. M. Pennington, M. D. Perry, T. J. Phillips, T. C. Sangster, M. S. Singh, M. A. Stoyer, M. Tabak, G. L. Tietbohl, M. Tsukamoto, K. Wharton, and S. C. Wilks, *Hot electron production and heating by hot electrons in fast ignitor research*, Physics of Plasmas **5**, 1966 (1998).

[10] C. Gahn, G. D. Tsakiris, A. Pukhov, J. Meyer-ter-Vehn, G. Pretzler, P. Thirolf, D. Habs, and K. J. Witte, *Multi-MeV Electron Beam Generation by Direct Laser Acceleration in High-Density Plasma Channels*, Physical Review Letters **83**, 4772 (1999).

[11] C. Gahn, G. Pretzler, A. Saemann, G. D. Tsakiris, K. J. Witte, D. Gassmann, T. Schätz, U. Schramm, P. Thirolf, and D. Habs, *MeV γ-ray yield from solid targets irradiated with fs-laser pulses*, Applied Physics Letters **73**, 3662 (1998).

[12] A. Maksimchuk, S. Gu, K. Flippo, D. Umstadter, and V. Yu. Bychenkov, *Forward Ion Acceleration in Thin Films Driven by a High-Intensity Laser*, Physical Review Letters **84**, 4108 (2000).

[13] E. L. Clark, K. Krushelnick, J. R. Davies, M. Zepf, M. Tatarakis, F. N. Beg, A. Machacek, P. A. Norreys, M. I. K. Santala, I. Watts, and A. E. Dangor, *Measurements of Energetic Proton Transport through Magnetized Plasma from Intense Laser Interactions with Solids*, Physical Review Letters **84**, 670 (2000).

[14] E. L. Clark, K. Krushelnick, M. Zepf, F. N. Beg, M. Tatarakis, A. Machacek, M. I. K. Santala, I. Watts, P. A. Norreys, and A. E. Dangor, *Energetic Heavy-Ion and Proton Generation from Ultraintense Laser-Plasma Interactions with Solids*, Physical Review Letters **85**, 1654 (2000).

[15] R. A. Snavely, M. H. Key, S. P. Hatchett, T. E. Cowan, M. Roth, T. W. Phillips, M. A. Stoyer, E. A. Henry, T. C. Sangster, M. S. Singh, S. C. Wilks, A. J. Mackinnon, A. Offenberger, D. M. Penning, K. Yasuike, A. B. Langdon, B. F. Lasinski, J. Johnson, M. D. Perry, and E. M. Campbell, *Intense High-Energy Proton Beams from Petawatt-Laser Irradiation of Solids*, Physical Review Letters **85**, 2945 (2000).

[16] S. P. Hatchett, C. G. Brown, T. E. Cowan, E. A. Henry, J. S. Johnson, M. H. Key, J. A. Koch, A. B. Langdon, B. F. Lasinski, R. W. Lee, A. J. Mackinnon, D. M. Pennington, M. D. Perry, T. W. Phillips, M. Roth, T. C. Sangster, M. S. Singh, R. A. Snavely, M. A. Stoyer, S. C. Wilks, and K. Yasuike, *Electron, photon, and ion beams from the relativistic interaction of Petawatt laser pulses with solid targets*, Physics of Plasmas **7**, 2076 (2000).

[17] S. C. Wilks, A. B. Langdon, T. E. Cowan, M. Roth, M. Singh, S. Hatchett, M. H. Key, D. Pennington, A. Mackinnon, and R. A. Snavely, *Energetic proton generation in ultra-intense laser-solid interactions*, Physics of Plasmas **8**, 542 (2001).

[18] M. Hegelich, S. Karsch, G. Pretzler, D. Habs, K. J. Witte, W. Guenther, M. Allen, A. Blazevic, J. Fuchs, J.-C. Gauthier, M. Geissel, P. Audebert, T. E. Cowan, and M. Roth, *MeV Ion Jets from Short-Pulse-Laser Interaction with Thin Foils*, Physical Review Letters **89**, 085002 (2002).

[19] G. Pretzler, A. Saemann, A. Pukhov, D. Rudolph, T. Schätz, U. Schramm, P. Thirolf, D. Habs, K. Eidmann, G. D. Tsakiris, J. Meyer-ter-Vehn, and K. J. Witte, *Neutron production by 200 mJ ultrashort laser pulses*, Physical Review E **58**, 1165 (1998).

[20] L. Disdier, J.-P. Garçonnet, G. Malka, and J.-L. Miquel, *Fast neutron emission from a high-energy ion beam produced by a high-intensity picosecond laser pulse*, Physical Review Letters **82**, 1454 (1999).

[21] C. Gahn, G. D. Tsakiris, G. Pretzler, K. J. Witte, C. Delfin, C.-G. Wahlström, and D. Habs, *Positron Generation with Table-Top Lasers*, Applied Physics Letters **77**, 2662 (2000).

[22] R. Decoste and B. H. Ripin, *High-Energy Ion Expansion in Laser-Plasma Interactions*, Physical Review Letters **40**, 34 (1978).

[23] C. Joshi, M. C. Richardson, and G. D. Enright, *Quantitative measurements of fast ions from* CO_2*-laser produced plasmas*, Applied Physics Letters **34**, 625 (1979).

[24] G. D. Tsakiris, K. Eidmann, R. Petsch, and R. Sigel, *Experimental Studies of the Bilateral Ion Blowoff from Laser-Irradiated Thin Plastic Foils*, Physical Review Letters **46**, 1202 (1981).

[25] F. Begay and D. W. Forslund, *Acceleration of multi-species ions in* CO_2 *laser-produced plasmas: Experiments and Theory*, Physics of Fluids **25**, 1675 (1982).

[26] S. J. Gitomer, R. D. Jones, F. Begay, A. W. Ehler, J. F. Kephart, and R. Kristal, *Fast ions and hot electrons in the laser-plasma interaction*, Physics of Fluids **29**, 2679 (1986).

[27] M. D. Perry, D. Pennington, B. C. Stuart, G. Tietbohl, J. A. Britten, C. Brown, S. Herman, B. Golick, M. Kartz, J. Miller, H. T. Powell, M. Vergino, and V. Yanovsky, *Petawatt laser pulses*, Optics Letters **24**, 160 (1999).

[28] M. Roth, M. Allen, P. Audebert, A. Blazevic, E. Brambrink, T. E. Cowan, J. Fuchs, J. C. Gauthier, M. Geissel, M. Hegelich, S. Karsch, J. Meyer-ter-Vehn, H. Ruhl, T. Schlegel, and R. Stephens, *The generation of high quality, intense ion beams by ultra intense lasers*, Plasma Physics and Controlled Fusion **44**, B99 (2002).

[29] M. Borghesi, A. J. Mackinnon, D. H. Campbell, D. G. Hicks, S. Kar, P. K. Patel, D. Price, L. Romagnani, A. Schiavi, and O. Willi, *Multi-MeV Proton Source Investigations in Ultraintense Laser-Foil Interactions*, Physical Review Letters **92**, 055003 (2004).

[30] T. E. Cowan, J. Fuchs, H. Ruhl, A. Kemp, P. Audebert, M. Roth, R. Stephens, I. Barton, A. Blazevic, E. Brambrink, J. Cobble, J. Fernández, J.-C. Gauthier, M. Geissel, M. Hegelich, J. Kaae, S. Karsch, G. P. Le Sage, S. Letzring, M. Manclossi, S. Meyroneinc, A. Newkirk, H. Pépin, and N. Renard-LeGalloudec, *Ultralow Emittance, Multi-MeV Proton Beams from a Laser Virtual-Cathode Plasma Accelerator*, Physical Review Letters **92**, 204801 (2004).

[31] P. K. Patel, A. J. Mackinnon, M. H. Key, T. E. Cowan, M. E. Foord, M. Allen, D. F. Price, H. Ruhl, P. T. Springer, and R. Stephens, *Isochoric Heating of Solid-Density Matter with an Ultrafast Proton Beam*, Physical Review Letters **91**, 125004 (2003).

[32] J. A. Cobble, R. P. Johnson, T. E. Cowan, N. Renard-Le Galloudec, and M. Allen, *High resolution laser-driven proton radiography*, Journal of Applied Physics **92**, 1775 (2002).

[33] M. Borghesi, S. Bulanov, D. H. Campbell, R. J. Clarke, T. Z. Esirkepov, M. Galimberti, L. A. Gizzi, A. J. Mackinnon, N. M. Naumova, F. Pegoraro, H. Ruhl, A. Schiavi, and O. Willi, *Macroscopic Evidence of Soliton Formation in Multiterawatt Laser-Plasma Interaction*, Physical Review Letters **88**, 135002 (2002).

[34] A. J. Mackinnon, P. K. Patel, D. W. Price, D. Hicks, L. Romagnani, and M. Borghesi, *Proton moiré fringes for diagnosing electromagnetic fields in opaque materials and plasmas*, Applied Physics Letters **82**, 3188 (2003).

[35] M. Roth, T. E. Cowan, M. H. Key, S. P. Hatchett, C. Brown, W. Fountain, J. Johnson, D. M. Pennington, R. A. Snavely, S. C. Wilks, K. Yasuike, H. Ruhl, F. Pegoraro, S. V. Bulanov, E. M. Campbell, M. D. Perry, and H. Powell, *Fast Ignition by Intense Laser-Accelerated Proton Beams*, Physical Review Letters **86**, 436 (2001).

[36] M. Tabak, J. Hammer, M. E. Glinsky, W. L. Kruer, S. C. Wilks, J. Woodworth, E. M. Campbell, and M. D. Perry, *Ignition and high gain with ultrapowerful lasers*, Physics of Plasmas **1**, 1626 (1994).

[37] M. Roth, T. E. Cowan, J. C. Gauthier, M. Allen, P. Audebert, A. Blazevic, J. Fuchs, M. Geissel, M. Hegelich, S. Karsch, J. Meyer-ter-Vehn, A. Pukhov, and T. Schlegel, *Energetic ions generated by laser pulses: A detailed study on target properties*, Physical Review Special Topics - Accelerators and Beams **5**, 061301 (2002).

[38] A. J. Mackinnon, Y. Sentoku, P. K. Patel, D. W. Price, S. Hatchett, M. H. Key, C. Andersen, R. Snavely, and R. R. Freeman, *Enhancement of Proton Acceleration by Hot-Electron Recirculation in Thin Foils Irradiated by Ultraintense Laser Pulses*, Physical Review Letters **88**, 215006 (2002).

[39] I. Spencer, K. W. D. Ledingham, P. McKenna, T. McCanny, P. Singhal, S. Foster, D. Neely, A. J. Langley, E. J. Divall, C. J. Hooker, R. J. Clarke, P. A. Norreys, E. L. Clark, K. Krushelnick, and J. R. Davies, *Experimental study of proton emission from 60-fs, 200-mJ high-repetition-rate tabletop-laser pulses interacting with solid targets*, Physical Review E **67**, 046402 (2003).

[40] L. Pommier and E. Lefebvre, *Simulations of energetic proton emission in laser-plasma interaction*, Laser and Particle Beams **21**, 573 (2003).

[41] M. Passoni, V. T. Tikhonchuk, M. Lontano, and V. Yu. Bychenkov, *Charge separation effects in solid targets and ion acceleration with a two-temperature electron distribution*, Physical Review E **69**, 026411 (2004).

[42] A. J. Mackinnon, M. Borghesi, S. Hatchett, M. H. Key, P. K. Patel, H. Campbell, A. Schiavi, R. Snavely, S. C. Wilks, and O. Willi, *Effect of Plasma Scale Length on Multi-MeV Proton Production by Intense Laser Pulses*, Physical Review Letters **86**, 1769 (2001).

[43] S. Karsch, S. Düsterer, H. Schwoerer, F. Ewald, D. Habs, M. Hegelich, G. Pretzler, A. Pukhov, K. J. Witte, and R. Sauerbrey, *High-Intensity Laser Induced Ion Acceleration from Heavy-Water Droplets*, Physical Review Letters **91**, 015001 (2003).

[44] M. Zepf, E. L. Clark, F. N. Beg, R. J. Clarke, A. E. Dangor, A. Gopal, K. Krushelnick, P. A. Norreys, M. Tatarakis, U. Wagner, and M. S. Wei, *Proton Acceleration from High-Intensity Laser Interactions with Thin Foil Targets*, Physical Review Letters **90**, 064801 (2003).

[45] A. Pukhov, *Three-Dimensional Simulations of Ion Acceleration from a Foil Irradiated by a Short-Pulse Laser*, Physical Review Letters **86**, 3562 (2001).

[46] Y. Murakami, Y. Kitagawa, Y. Sentoku, M. Mori, R. Kodama, K. A. Tanaka, K. Mima, and T. Yamanaka, *Observation of proton rear emission and possible gigagauss scale magnetic fields from ultra-intense laser illuminated plastic targets*, Physics of Plasmas **8**, 4138 (2001).

[47] M. Kaluza, J. Schreiber, M. I. K. Santala, G. D. Tsakiris, K. Eidmann, J. Meyer-ter-Vehn, and K. J. Witte, *Influence of the Laser Prepulse on Proton Acceleration in Thin-Foil Experiments*, Physical Review Letters **93**, 045003 (2004).

[48] J. J. Honrubia, M. Kaluza, G. D. Tsakiris, and J. Meyer-ter-Vehn, *Fast electron propagation in non-uniform plasmas*, to be submitted to Physical Review E (2004).

[49] H. Baumhacker, G. Pretzler, K. J. Witte, M. Hegelich, M. Kaluza, S. Karsch, A. Kudryashov, V. Samarkin, and A. Roukossouev, *Correction of strong phase and amplitude modulations by two deformable mirrors in a multistaged Ti:sapphire laser*, Optics Letters **27**, 1570 (2002).

[50] K. Eidmann, J. Meyer-ter-Vehn, T. Schlegel, and S. Hüller, *Hydrodynamic simulation of subpicosecond laser interaction with solid-density matter*, Physical Review E **62**, 1202 (2000).

[51] E. S. Sarachik and G. T. Schappert, *Classical Theory of the Scattering of Intense Laser Radiation by Free Electrons*, Physical Review A **1**, 2738 (1970).

[52] L. D. Landau and E. M. Lifschitz, *Lehrbuch der theoretischen Physik: Klassische Feldtheorie, S. 132*, Akademie-Verlag, Berlin, 7. Ed. (1977).

[53] P. Gibbon, *High-Order Harmonic Generation in Plasmas*, IEEE Journal of Quantum Electronics **33**, 1915 (1997).

[54] C. I. Moore, J. P. Knauer, and D. D. Meyerhofer, *Observation of the Transition from Thomson to Compton Scattering in Multiphoton Interactions with Low-Energy Electrons*, Physical Review Letters **74**, 2439 (1995).

[55] F. V. Hartemann, S. N. Fochs, G. P. Le Sage, N. C. Luhrmann, Jr., J. G. Woodworth, M. D. Perry, Y. J. Chen, and A. K. Kerman, *Nonlinear ponderomotive scattering of relativistic electrons by an intense laser field at focus*, Physical Review E **51**, 4833 (1995).

[56] F. V. Hartemann, J. R. Van Meter, A. L. Troha, E. C. Landahl, N. C. Luhmann, Jr., H. A. Baldis, A. Gupta, and A. K. Kerman, *Three-dimensional relativistic electron scattering in an ultrahigh-intensity laser focus*, Physical Review E **58**, 5001 (1998).

[57] G. Malka, E. Lefebvre, and J. L. Miquel, *Experimental Observation of Electrons Accelerated in Vacuum to Relativistic Energies by a High-Intensity Laser*, Physical Review Letters **78**, 3341 (1997).

[58] F. F. Chen, *Introduction to Plasma Physics*, Plenum Press, New York (1974).

[59] W. L. Kruer, *The Physics of Laser Plasma Interactions*, Addison-Wesley, New York (1988).

[60] B. Quesnel and P. Mora, *Theory and simulation of the interaction of ultraintense laser pulses with electrons in vacuum*, Physical Review E **58**, 3719 (1998).

[61] J. Meyer-ter-Vehn, A. Pukhov, and Z. M. Sheng, *Relativistic Laser Plasma Interaction*, in: Atoms, Solids, and Plasmas in Super-Intense Laser Fields (editors: D. Batani, C. J. Joachain, S. Martellucci, and A. N. Chester), Kluwer Academic/Plenum Publishers, New York (2001).

[62] E. Lefebvre and G. Bonnaud, *Transparency/Opacity of a Solid Target Illuminated by an Ultrahigh-Intensity Laser Pulse*, Physical Review Letters **74**, 2002 (1995).

[63] G.-Z. Sun, E. Ott, Y. C. Lee, and P. Guzdar, *Self-focusing of short intense pulses in plasmas*, Physics of Fluids **30**, 526 (1987).

[64] H. Alfvén, *On the motion of cosmic rays in interstellar space*, Physical Review **55**, 429 (1939).

[65] A. Pukhov and J. Meyer-ter-Vehn, *Laser Hole Boring into Overdense Plasma and Relativistic Electron Currents for Fast Ignition of ICF Targets*, Physical Review Letters **79**, 2686 (1997).

[66] H. Ruhl, Y. Sentoku, K. Mima, K. A. Tanaka, and R. Kodama, *Collimated Electron Jets by Intense Laser-Beam-Plasma Surface Interaction under Oblique Incidence*, Physical Review Letters **82**, 743 (1999).

[67] S. C. Wilks, D. L. Kruer, M. Tabak, and A. B. Langdon, *Absorption of Ultra-Intense Laser Pulses*, Physical Review Letters **69**, 1383 (1992).

[68] F. Brunel, *Not-so-Resonant, Resonant Absorption*, Physical Review Letters **59**, 52 (1987).

[69] T. Tajima and J. M. Dawson, *Laser Electron Accelerator*, Physical Review Letters **43**, 267 (1979).

[70] A. Pukhov and J. Meyer-ter-Vehn, *Relativistic laser-plasma interaction by multi-dimensional particle-in-cell simulations*, Physics of Plasmas **5**, 1880 (1998).

[71] A. Pukhov, Z.-M. Sheng, and J. Meyer-ter-Vehn, *Particle acceleration in relativistic laser channels*, Physics of Plasmas **6**, 2847 (1999).

[72] M. Borghesi, A. J. MacKinnon, L. Barringer, R. Gaillard, L. A. Gizzi, C. Meyer, O. Willi, A. Pukhov, and J. Meyer-ter-Vehn, *Relativistic Channeling of a Picosecond Laser Pulse in a Near-Critical Preformed Plasma*, Physical Review Letters **78**, 879 (1997).

[73] M. I. K. Santala, M. Zepf, I. Watts, F. N. Beg, E. Clark, M. Tatarakis, K. Krushelnick, A. E. Dangor, T. McCanny, I. Spencer, R. P. Singhal, K. W. D. Ledingham, S. C. Wilks, A. C. Machacek, J. S. Wark, R. Allott, R. J. Clarke, and P. A. Norreys, *Effect of the Plasma Density Scale Length on the Direction of Fast Electrons in Relativistic Laser-Solid Interactions*, Physical Review Letters **84**, 1459 (2000).

[74] F. Brandl, G. Pretzler, D. Habs, and E. Fill, *Čerenkov radiation diagnostics of hot electrons generated by fs-laser interaction with solid targets*, Europhysics Letters **61**, 632 (2002).

[75] V. T. Tikhonchuk, *Interaction of a beam of fast electrons with solids*, Physics of Plasmas **9**, 1416 (2002).

[76] E. S. Weibel, *Spontaneously growing transverse waves in a plasma due to an anisotropic velocity distribution*, Physical Review Letters **2**, 83 (1959).

[77] M. Honda, J. Meyer-ter-Vehn, and A. Pukhov, *Collective Stopping and Ion Heating in Relativistic-Electron-Beam Transport for Fast Ignition*, Physical Review Letters **85**, 2128 (2000).

[78] H. M. Milchberg, R. R. Freeman, and S. C. Davey, *Resistivity of a Simple Metal from Room Temperature to* 10^6 *K*, Physical Review Letters **61**, 2364 (1988).

[79] A. R. Bell and R. J. Kingham, *Resistive Collimation of Electron Beams in Laser-Produced Plasmas*, Physical Review Letters **91**, 035003 (2003).

[80] J. J. Honrubia, A. Antonicci, and D. Moreno, *Hybrid simulations of fast electrons transport in conducting media*, Laser and Particle Beams **22**, 137 (2004).

[81] Y. Sentoku, T. E. Cowan, A. Kemp, and H. Ruhl, *High energy proton acceleration in interaction of short laser pulse with dense plasma target*, Physics of Plasmas **10**, 2009 (2003).

[82] B. M. Hegelich, *Acceleration of heavy Ions to MeV/nucleon Energies by Ultrahigh-Intensity Lasers*, Dissertation, Ludwig-Maximilians Universität, München (2002).

[83] M. Widner, I. Alexeef, and W. D. Jones, *Plasma Expansion into a Vacuum*, Physics of Fluids **14**, 795 (1971).

[84] J. E. Crow, P. L. Auer, and J. E. Allen, *The expansion of a plasma into a vacuum*, Journal of Plasma Physics **14**, 65 (1975).

[85] J. Denavit, *Collisionless plasma expansion into a vacuum*, Physics of Fluids **22**, 1384 (1979).

[86] P. Mora, *Plasma Expansion into a Vacuum*, Physical Review Letters **90**, 185002 (2003).

[87] M. Kaluza, *Ionisation von Hoch-Z-Atomen in starken Laserfeldern*, Diplomarbeit, Technische Universität, München (2000).

[88] A. V. Gurevich, L. V. Pariiskaya, and L. P. Pitaevskii, *Self-Similar Motion of Rarefied Plasma*, Soviet Physics JETP **22**, 449 (1966).

[89] P. Mora, private communication (2004).

[90] H. Baumhacker, A. Böswald, H. Haas, M. Fischer, W. Fölsner, G. Keller, U. Andiel, X. Dong, M. Dreher, K. Eidmann, E. Fill, M. Hegelich, M. Kaluza, S. Karsch, G. Pretzler, G. D. Tsakiris, and K. J. Witte, *Advanced Titanium:Sapphire Laser ATLAS*, MPQ-Report **272** (2002).

[91] T. Juji, A. Unterhuber, V. S. Yakovlev, G. Tempea, A. Stingl, F. Krausz, and W. Drexler, *Generation of smooth, ultra-broadband spectra directly from a prismless Ti:sapphire laser*, Applied Physics B **77**, 125 (2003).

[92] M. Nisoli, S. Stagira, S. De Silvestri, O. Svelto, S. Sartania, Z. Cheng, M. Lenzner, C. Spielmann, and F. Krausz, *A novel high-energy pulse compression system: generation of multigigawatt sub-5-fs pulses*, Applied Physics B **65**, 189 (1997).

[93] M. D. Perry and G. Mourou, *Terawatt to Petawatt Subpicosecond Lasers*, Science **264**, 917 (1994).

[94] M. Pittman, S. Ferré, J. P. Rousseau, L. Notebaert, J. P. Chambaret, and G. Chériaux, *Design and characterization of a near-diffraction-limited femtosecond 100-TW 10-Hz high-intensity laser system*, Applied Physics B **74**, 529 (2003).

[95] M. P. Kalachnikov, V. Karpov, and H. Schönnagel, *100-terawatt titanium-sapphire laser system*, Laser Phys. **02**, 368 (2002).

[96] T. Brabec, C. Spielmann, P. F. Curley, and F. Krausz, *Kerr lens mode locking*, Optics Letters **17**, 1292 (1992).

[97] E. Hecht, *Optics*, Addison-Wesley, New York, 3. Ed. (1998).

[98] R. Tommasini, private communication (2004).

[99] Kentech Instruments Ltd., Harrow, U.K., http://www.kentech.co.uk.

[100] R. P. Godwin, C. G. M. van Kessel, J. N. Olsen, P. Sachsenmaier, R. Sigel, and K. Eidmann, *Reflection Losses from Laser-Produced Plasmas*, Zeitschrift für Naturforschung **32a**, 1100 (1977).

[101] Centronic Ltd., New Abingdon, Surrey, U.K., http://www.kentech.co.uk.

[102] Tektronix Inc., Beaverton, Oregon, U.S.A., http://www.tek.com.

[103] Laser 2000 GmbH, Wessling, Germany, http://www.laser2000.de.

[104] Track Analysis Systems Limited, H. H. Wills Physics Laboratory, Bristol, UK, http://www.phy.bris.ac.uk/research/TASL/home.html.

[105] S. A. Durrani and R. K. Bull, *Solid State Nuclear Track Detection*, Pergamon Press, Oxford (1987).

[106] National Institute of Standards and Technology, http://physics.nist.gov.

[107] J. S. Pearlman, *Faraday cups for laser plasmas*, Review of Scientific Instruments **48**, 1048 (1977).

[108] B. H. Ripin and R. Decoste, *Secondary Electron Supression in Charge Collectors and Analyzers*, Naval Research Laboratory, Memorandum Report 3494, Washington, D.C. (1977).

[109] S. Karsch, *High-intensity laser generated neutrons: A novel neutron source and new tool for plasma diagnostics*, Dissertation, Ludwig-Maximilians Universität, München (2002).

[110] J. Schreiber, private communication (2004).

[111] Computer Simulation Technology (CST), EM STUDIO$^{\mathrm{TM}}$.

[112] Goodfellow GmbH, Bad Nauheim, Germany, http://www.goodfellow.com.

[113] D. A. Lide, *CRC Handbook of Chemistry and Physics 1973-1974*, CRC Press, Boca Raton, 54. Ed. (1973).

[114] R. Ramis, R. Schmalz, and J. Meyer-ter-Vehn, *MULTI: A computer code for one-dimensional multigroup radiation hydrodynamics*, Computer Physics Communications **88**, 475 (1988).

[115] Y. B. Zel'dovich and Y. P. Raizer, *Physics of Shock Waves and High-Temperature Hydrodynamic Phenomena*, Academic Press, New York (1966).

[116] T4 Group, SESAME *Equation Of State*, Los Alamos National Laboratory, Report LALP-83-4, Los Alamos, NM (1983).

[117] K. Eidmann, *Radiation transport and atomic physics modeling in high-energy-density alser-produced plasmas*, Laser and Particle Beams **12**, 223 (1994).

[118] J. Stein, private communication (2004).

[119] W. Press, B. Flannery, S. Teukolsky, and W. Vetterling, *Numerical Recipes in C: The Art of Scientific Computing*, Cambridge University Press, New York, 2. Ed. (1992).

[120] L. M. Wickens, J. E. Allen, and P. T. Rumsby, *Ion emission from Laser-Produced Plasmas with Two Electron Temperatures*, Physical Review Letters **41**, 243 (1978).

[121] J. Davies, A. R. Bell, and M. Tatarakis, *Magnetic focusing and trapping of high-intensity laser-generated fast electrons at the rear of solid targets*, Physical Review E **59**, 6032 (1999).

[122] Y. T. Lee and R. M. More, *An electron conductivity model for dense plasmas*, Physics of Fluids **5**, 1273 (1984).

[123] A. Pukhov, *Three-dimensional electromagnetic relativistic particle-in-cell code VLPL (Virtual Laser Plasma Lab)*, Journal of Plasma Physics **61**, 425 (1999).

[124] H. Ruhl, private communication (unpublished) (2003).

[125] M. Roth, private communication (2004).

[126] J. J. Honrubia, private communication (2004).

[127] R. Benattar, C. Popovics, and R. Sigel, *Polarized light interferometer for laser fusion studies*, Review of Scientific Instruments **50**, 1583 (1979).

[128] A. Pukhov and J. Meyer-ter-Vehn, *Relativistic Magnetic Self-Channeling of Light in Near-Critical Plasma: Three-Dimensional Particle-in-Cell Simulation*, Physical Review Letters **76**, 3975 (1996).

[129] Schott Glaskatalog, http://www.schott.de.

[130] M. Françon and S. Mallick, *Polarization Interferometers*, Wiley-Interscience, London, 1. Ed. (1971).

[131] M. Hipp and P. Reiterer, *User Manual for IDEA 1.00: Software for Interferometrical Data Evaluation*, http://optics.tu-graz.ac.at, Institut für Experimentalphysik, Technische Universität Graz (1999).

[132] G. Pretzler, H. Jäger, T. Neger, H. Phillip, and J. Woisetschläger, *Comparison of Different Methods of Abel Inversion Using Computer Simulated and Experimental Side-On Data*, Zeitschrift für Naturforschung **47a**, 955 (1992).

[133] K.-U. Amthor, *Plasmadiagnose in Experimenten zur Wechselwirkung intensiver Laserimpulse mit Materie*, Diplomarbeit, Friedrich-Schiller Universität, Jena (2002).

[134] C. Gahn, G. D. Tsakiris, K. J. Witte, P. Thirolf, and D. Habs, *A novel 45-channel electron spectrometer for high intensity laser-plasma interaction studies*, Review of Scientific Instruments **71**, 1642 (2000).

Appendix P

Publication List

1. **M. Kaluza**, J. Schreiber, M. I. K. Santala, G. D. Tsakiris, K. Eidmann, J. Meyer-ter-Vehn, and K. J. Witte: *Influence of the Laser Prepulse on Proton Acceleration in Thin-Foil Experiments*, Physical Review Letters, **93**, 045003 (2004)

2. H. Baumhacker, G. Pretzler, K.-J. Witte, M. Hegelich, **M. Kaluza**, S. Karsch, A. Kudryashov, V. Samarkin, and A. Roukossouev: *Correction of strong phase and amplitude modulations by two deformable mirrors in a multistaged Ti:sapphire laser*, Optics Letters, **27**, 1570-1572 (2002)

3. J. J. Honrubia, **M. Kaluza**, G. D. Tsakiris, and J. Meyer-ter-Vehn: *Fast-electron propagation in non-uniform plasmas*, to be submitted to Physical Review E

The first two publications are attached to this work.

Correction of strong phase and amplitude modulations by two deformable mirrors in a multistaged Ti:sapphire laser

H. Baumhacker, G. Pretzler, K. J. Witte, M. Hegelich, M. Kaluza, and S. Karsch

Max-Planck-Institut für Quantenoptik, Hans-Kopfermann-Strasse 1, D-85748 Garching, Germany

A. Kudryashov, V. Samarkin, and A. Roukossouev

Adaptive Optics for Industrial and Medical Applications Group, Institute on Laser and Information Technology of the Russian Academy of Science (ILIT RAS), Svyatoozerskaya Street 1, Shatura, Moscow Region, 140700 Russia

Received May 23, 2002

We describe a novel scheme consisting of two deformable bimorph mirrors that can free ultrashort laser pulses from simultaneously present strong wave-front distortions and intensity-profile modulations. This scheme is applied to the Max-Planck-Institut für Quantenoptik 10-TW Advanced Titanium-Sapphire Laser (ATLAS) facility. We demonstrate that with this scheme the focusability of the ATLAS pulses can be improved from 10^{18} to 2×10^{19} W/cm^2 without any penalty in recompression fidelity.

OCIS codes: 010.1080, 140.3590, 220.1000.

In high-power multistage Nd:glass and Ti:sapphire (TiS) laser systems, wave-front aberrations (WFAs) that result in deterioration of beam quality are common. These WFAs originate from imperfections in the many optical components that are present in the beamline as a result of optical figure errors, pump-induced thermal distortions in the amplifiers, and the third-order nonlinear n_2 effect. In TiS lasers, cooling the crystals to the temperature of liquid nitrogen can essentially eliminate pump-induced distortions.[1–3] A more versatile approach, however, is to use adaptive optics, which can counteract each of the three WFA sources, regardless of whether they occur individually, in pairs, or all together simultaneously. This was demonstrated in Refs. 4–7 by use of just a single deformable mirror (SDM).

In the SDM concept, only the WF of the pulse is corrected, not the intensity profile. This scheme works well as long as the WF perturbing action of each individual optical element is so weak that the shortest local radius of curvature, R, of the WF of the exiting pulse is many times the distance to the adaptive mirror. In addition, the pulse should not pick up strong intensity modulations, e.g., by nonuniform amplification. However, when an optical element such as a multipass amplifier causes a single-pass WFA with an associated R value of the order of the pass-to-pass propagation distance, the pulse intensity profile becomes increasingly modulated from pass to pass. On further propagation, these modulations may get even worse. If one stays with the SDM concept, the beam loading would then have to be reduced so that the optical components placed downstream from the amplifier are not damaged. In chirped-pulse amplification laser systems, the compressor gratings are then particularly endangered because of their low damage threshold. The system efficiency is thereby decreased considerably, too.

In this Letter we study this heavy-perturbation case, which to our knowledge has not been investigated experimentally before and is characterized here by the simultaneous presence of strong phase and amplitude modulations. We show that by invoking two DMs one can cancel the modulations without any sacrifice in beam loading. In our concept, the compressor is placed between two DMs and thus has to be operated with a distorted WF. For this situation, we present conditions that, when met, maintain the pulse recompressibility and focusability within reasonable limits.

The two-DM concept has also been investigated for applications in areas others than the one studied here, so far only theoretically. These other applications include beam shaping for high-power laser beams in laser photochemistry and material processing[8] as well as delivering a high-quality pulse on a remote target after propagation through turbulent atmosphere.[9] In astronomy, the use of two DMs may enable one to overcome turbulence-induced phase and amplitude modulations for widely enlarged fields of view (Refs. 10 and 11, and references therein). The algorithms developed in Refs. 8–11 for control of the DM surfaces are not applicable to our situation because of the presence of the gratings between the two DMs, which limits beam loading.

The heavy-perturbation case that we are confronted with arises in the final disk amplifier of our Advanced Titanium:Sapphire Laser (ATLAS) facility (Fig. 1). The front end of the laser[12] delivers a 300-mJ pulse that is centered at 790 nm and stretched from 100 fs to 200 ps with a smooth intensity profile and a well-behaved WF. After four passes, the fluence pattern of the pulse inside the compressor is heavily modulated (Fig. 2, left) due to crystal-growth defects (Fig. 3) and pump-induced aberrations. At a pulse energy of 1.3 J at the compressor entrance, the peak fluence reaches 0.3 J/cm^2 on the first grating, far beyond its damage threshold of 0.15 J/cm^2. Under these loading conditions, the energy that is transmittable through the compressor is limited to only 0.5 J. Because of the simultaneous presence of WFAs and intensity modulations, the SDM concept is no longer applicable. To increase the amount of energy that is transportable through the compressor, we must first smooth the fluence profile. This is achieved with deformable mirror DM1 (17 electrodes, 30-mm diameter, bimorph),[13] which replaces the plane mirror in the beamline before the pulse makes its final transit through the amplifier

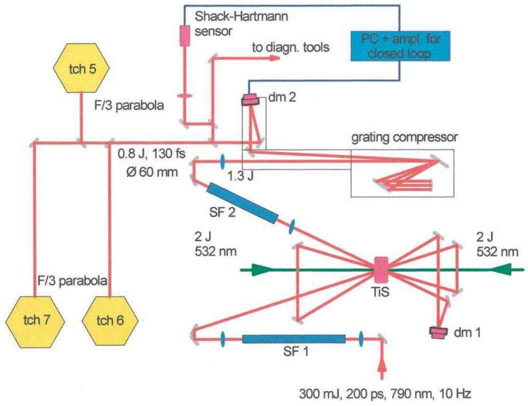

Fig. 1. Setup of the final amplifier in the ATLAS facility with two deformable mirrors, DM1 and DM2, closed loop, and three target chambers (TCH5–TCH7). The TiS crystal of 40-mm outer diameter is pumped from two sides. The TiS pulse provided by the front end passes through the crystal four times and is thereby amplified from 0.3 to 1.5 J. The pulse then runs through spatial filter SF2, and the pulse diameter increases from 18 to 63 mm. The pulse is then recompressed to 130 fs in an evacuated compressor chamber that houses two holographic gold gratings and is connected to the target chambers by evacuated tubes.

(Fig. 1). The best electrode voltage settings for DM1 can be found manually with a few iterations by use of a real-time beam-profile analyzer. For the same energy of 1.3 J as before, the peak fluence of the smoothed profile is then reduced to 90 mJ/cm^2 so that the 1.3-J energy can be safely transmitted through the compressor. At constant voltage settings, the smoothed beam profile remains stable over weeks and changes little on propagation inside the compressor and a few meters downstream.

The action of DM1 modifies the WFAs originating in the amplifying crystal but does not generate a plane WF. A plane WF is generated with a second deformable mirror, DM2 (33 electrodes, 80-mm diameter, bimorph).[13] DM2 is placed behind the compressor so that it is able to compensate for the optical figure errors of the gratings and to ensure that highly peaked intensity patterns that might occur when DM2 is optimized cannot damage the gratings. The compressor is thus fed with a chirped pulse whose WF is distorted. In this situation, which was investigated theoretically in Ref. 14, the following three effects are of major importance: loss of compression fidelity, astigmatism, and chromatic aberration. For an estimate of the level of WFAs that are tolerable without too high a loss in beam quality, the rigorous theory[14] is not needed. It is sufficient to replace the real pulse with a spherical WF whose curvature is chosen to be equal to the maximum local curvature in the real distorted WF. The focus of the model WF is downstream DM2.

From measurements, we find that the recompression fidelity in terms of pulse duration and contrast is hardly affected as long as any local radius of curvature of the WF exceeds 15 m. The condition is met in the ATLAS for pulse energies of up to 1 J after compression.

The originally spherically convergent beam turns astigmatic when it leaves the compressor, leading to the occurrence of two focal lines instead of a single point focus because the beam behaves differently in the dispersion and nondispersion planes of the compressor. With $R \geq$ m, the compressor-induced astigmatism turns out to be weak and is hence easily correctable with DM2, since the necessary displacement is $\leq 1\ \mu$m. The compensation of the original beam convergence is not a problem, either.

The chromatic aberration originates from the different path lengths of the individual spectral components on their way through the compressor. When they are exiting, the individual spectral beam components still have the same cone angle, but at a fixed position in space the radii of curvature are different. This effect cannot be compensated for with DM2. The beam emerging from DM2 will hence be parallel for the spectral component near λ_0 but divergent for the components with $\lambda < \lambda_0$ and convergent for those with $\lambda > \lambda_0$. The focus of such a beam is hence no longer pointlike but exhibits longitudinal spreading, with each spectral component having its own focus located at a different position. This spreading is tolerable when the foci of all colors inside the spectral range $4\Delta\lambda_{\mathrm{FWHM}}$ lie within the Rayleigh length of the spectral beam component at λ_0. For the ATLAS, this criterion requires $R > 15$ m, which is met. The theoretical analysis reveals that $R \propto \Delta\lambda_{\mathrm{FWHM}}$. Very short pulses with $\Delta\lambda_{\mathrm{WFHM}} \geq 50$ nm thus need to be rather well collimated if one wishes to avoid intensity degradation in the focus. This conclusion is in fair agreement with the results of the rigorous theory.[14]

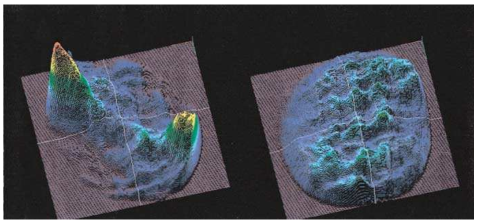

Fig. 2. Fluence patterns in the plane of the first compressor grating. Left, DM1 is replaced with a plane mirror; peak fluence, 300 mJ/cm^2. The double-peak pattern is due to the coarse two-half structure of the WFAs shown in Fig. 3. Right, DM1 is optimized; peak fluence reduced to 90 mJ/cm^2. The remaining fluence modulation arises from the fine structure of the WFAs (Fig. 3). The very high spatial frequencies, which carry little energy, are lost on propagation through the spatial filter SF2 (Fig. 1).

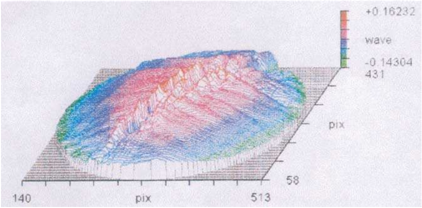

Fig. 3. WFAs that are due to growth defects in the final disk amplifier of 40-mm diameter, 17-mm thickness, and $\alpha l = 2.3$ at 532 nm.

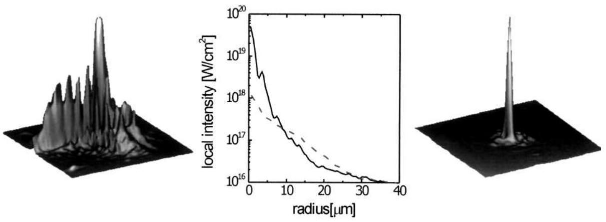

Fig. 4. Fluence profile in the focus of the $F/3$ off-axis parabola. Left, DM1 and DM2 are on, but DM2 acts as a plane mirror. Middle; local intensity as a function of radius for the fluence profiles shown to the left (- - -) and right (——). Right, DM1 and DM2 are on, but DM2 is locked to operation for minimal WFAs.

We generate a parallel beam with DM2 by comparing the actual WF as measured with a Shack–Hartmann sensor that has a 12×12 lenslet array with a reference WF obtained from a diode laser running at 790 nm and expanded to a parallel beam of 63-mm diameter. Edge points with an intensity of less than 10% of the maximal intensity are disregarded. The reference WF is stored in the computer for subsequent use. The voltage settings to be assigned to the electrodes of DM2 then have to be found so that the WF of the ATLAS pulse matches the reference WF as closely as possible. This is achieved by application of a closed loop. The algorithm employed for this purpose is the same as that developed in Ref. 5. The deviations between the actual and the reference WFs are minimized by use of the peak-to-valley optical-path difference as a criterion. Usually, approximately five iterations are needed to decrease the peak-to-valley value from the original 10λ to $\lambda/4$. The voltage settings corresponding to minimal WF distortion are stored. They can be used for hours because of the high thermomechanical stability of the ATLAS and the correspondingly low shot-to-shot fluctuations of the WF. For routine operation of the ATLAS, the closed loop is no longer needed once the WF correction is complete. We can then remove the beam splitter feeding the Shack–Hartmann sensor from the beam line to keep the B integral low. In case of performance deterioration, e.g., because of thermal drift, the whole WF correction procedure, which takes ~15 s, has to be redone.

We check the quality of the corrected WF in each target chamber by measuring the fluence patterns in the foci of the $F/3$ off-axis parabolas, using an 8-bit CCD camera and a set of calibrated filters. This combination provides an effective dynamic range of $>10^4$. The focus is viewed at 50× magnification. Because of the 1-mm-diameter pinhole SF2, there can be no energy outside the sensor chip (6 mm × 4 mm). Hence, the amount of energy that can possibly be hidden in the pixels showing no direct response is at most 10% of the total pulse energy. In each chamber, we obtain the same result for thousands of shots. With DM1 on and DM2 acting as a plane mirror, we find the multiple-peak fluence pattern depicted in the left-hand part of Fig. 4. The Strehl ratio (for its definition, see Ref. 15) is only ~0.04. However, when DM2 is locked to operation for minimal WFA, we find a dramatic improvement (Fig. 4, right). A single peak appears that contains 65% of the pulse energy within the diffraction-limited diameter. The mean intensity inside the diffraction-limited diameter is raised by a factor of ~20 from $\sim 10^{18}$ to 2×10^{19} W/cm^2. The Strehl ratio increases to 0.7. The Strehl ratio estimated from the corrected WF with a peak-to-valley optical path difference of $\lambda/4$ is 0.8. The difference in the two ratios is attributed to the fact that the real WF has higher-order abberrations that are not measurable with our Shack–Hartmann sensor and are not correctable with our adaptive optics.

We have shown that a combination of two DMs can free ultrashort laser pulses from simultaneously present heavy phase and amplitude modulations without any penalty in recompression fidelity and focusability.

This work was supported by the Commission of the European Union (EU) within the framework of the Association Euratom–Max-Planck-Institut für Plasmaphysik and the EU project ADAPTOOL (contract HPRI-CT-1999-50012). K. Witte's e-mail address is klaus.witte@mpq.mpg.de.

References

1. G. Erbert, L. Bass, R. Hackel, S. Jenkins, K. Kanz, and J. Paisner, in *Conference on Lasers and Electro-Optics*, Vol. 10 of 1991 OSA Technical Digest Series (Optical Society of America, Washington, D.C., 1991), pp. 390–391.
2. M. Pittmann, J. Rousseau, L. Notebaert, S. Ferré, J. Chambaret, and G. Cheriaux, in *Conference on Lasers and Electro-Optics*, Vol. 56 of OSA Trends in Optics and Photonics Series (Optical Society of America, Washington, D.C., 2001), p. 83.
3. S. Backus, R. Bartels, S. Thompson, R. Dollinger, H. Kapteyn, and M. Murnane, Opt. Lett. **26,** 465 (2001).
4. B. Van Wonterghem, J. Murray, J. Campbell, D. Speck, C. Barker, I. Smith, D. Browning, and W. Behrend, Appl. Opt. **36,** 4932 (1977).
5. K. Akaoka, S. Harayama, K. Tei, Y. Marayuma, and T. Arisawa, Proc. SPIE **3265,** 219 (1997).
6. F. Druon, G. Cheriaux, J. Faure, J. Nees, M. Nantel, A. Maksimchuk, J. Chanteloup, and G. Vodvin, Opt. Lett. **23,** 1043 (1998).
7. J. Chanteloup, H. Baldis, A. Migus, G. Mourou, B. Loiseaux, and J. Huignard, Opt. Lett. **23,** 475 (1998).
8. K. Nemoto, T. Fujiti, and N. Goto, Proc. SPIE **2119,** 155 (1994).
9. G. Roger, J. Phys. Colloq. **41,** 399 (1980).
10. K. Li You, Q. C. Dong, and W. D. Xiang, High-Power Laser Particle Beams **12,** 665 (2000).
11. A. Tokovinin, M. Le Louarn, E. Viard, N. Hubin, and R. Conan, Astron. Astrophys. **378,** 710 (2001).
12. K. Yamakawa, P. Chin, A. Magano, and J. Kmetec, IEEE J. Quantum Electron. **37,** 2698 (1994).
13. DM1 and DM2 were produced in the mainframe of Max-Planck-Institut–ILIT RAS collaboration. See also J. Dainty, A. Koryabin, and A. Kudryashov, Appl. Opt. **37,** 4663 (1998).
14. Z. Wang, Z. Xu, and Z.-Q. Zhang, IEEE J. Quantum Electron. **37,** 1 (2001).
15. W. J. Smith, *Modern Optical Engineering*, 2nd ed. (McGraw-Hill, New York, 1990), p. 337.

Influence of the Laser Prepulse on Proton Acceleration in Thin-Foil Experiments

M. Kaluza, J. Schreiber, M. I. K. Santala, G. D. Tsakiris, K. Eidmann, J. Meyer-ter-Vehn, and K. J. Witte
Max-Planck-Institut für Quantenoptik, Hans-Kopfermann-Straße 1, D-85748 Garching, Germany

(Received 8 December 2003; published 20 July 2004)

We investigate the influence of the laser prepulse due to amplified spontaneous emission on the acceleration of protons in thin-foil experiments. We show that changing the prepulse duration has a profound effect on the maximum proton energy. We find an optimal value for the target thickness, which strongly depends on the prepulse duration. At this optimal thickness, the rear side acceleration process leads to the highest proton energies, while this mechanism is rendered ineffective for thinner targets due to a prepulse-induced plasma formation at the rear side. In this case, the protons are primarily accelerated by the front side mechanism leading to lower cutoff energies.

DOI: 10.1103/PhysRevLett.93.045003 PACS numbers: 52.38.Kd, 29.30.Ep, 41.75.Jv

Proton and ion acceleration using high-intensity lasers is a field of rapidly growing interest. For possible applications of proton beams produced in laser-solid interactions like the imaging of electromagnetic fields in overdense plasmas [1] and the envisaged usage of proton beams in the fast-ignitor scenario [2], the generation of beams with controllable parameters such as energy spectrum, brightness, and spatial profile is crucial. Hence, for the reliable generation of proton beams, the physics underlying the acceleration processes has to be well understood. After the first proof-of-principle experiments [3–6], systematical studies were carried out to examine the influence of target material and thickness [7–9]. To establish the influence of the main laser parameters such as intensity, pulse energy, and duration over a wide range, results from different laser systems have to be compared, since usually each system covers a small parameter range only. Besides these parameters, strength and duration of the prepulse due to amplified spontaneous emission (ASE) play an important role, too [7], but until now a detailed investigation has not yet been carried out.

In most experiments, protons with energies exceeding 1 MeV have been observed. They originate from water and hydrocarbon molecules adsorbed at the target surfaces due to the unavoidable presence of water and pump oil vapor in the target chamber. The origin of the most energetic protons is still debated. There are at least two acceleration scenarios able to explain the occurrence of MeV protons. (i) They may come from the *front* surface of the target, i.e., the side irradiated by the laser pulse [3,4,10] or (ii) from the *rear* surface [5,11,12]. Recent results indicate that both mechanisms act simultaneously [13,14], in accordance with the predictions of multidimensional particle-in-cell (PIC) codes [15,16].

In this Letter, we report on experiments performed to investigate the effect both of the ASE prepulse duration and the target thickness on the acceleration of protons. The proton cutoff energy depends very sensitively on the combination of these two parameters. For a fixed prepulse duration, the highest proton energies are obtained at an optimal target thickness, which in turn is determined by the ASE prepulse duration. The results can be consistently interpreted if one assumes that above this thickness, the fastest protons are accelerated at the target rear side, while for thinner targets this mechanism is rendered ineffective and only the front side acceleration is active, resulting in lower proton cutoff energies. Furthermore, our results allow a comparison of the experimental results obtained with different laser systems.

The experiments were carried out with the ATLAS laser system at the Max-Planck-Institut für Quantenoptik. It consists of a MIRA oscillator delivering 100-fs pulses of 790-nm wavelength. The pulses are stretched to 160 ps followed by a regenerative amplifier (RA), two multipass amplifiers, and a grating compressor. The output pulses have a duration of $\tau_L = 150$ fs (FWHM) with an on-target energy, E_L, between 600 and 850 mJ. The p-polarized beam is focused under 30° incident angle by a $f/2.5$ off-axis parabolic mirror onto Al foils of 0.75 to 86-μm thickness. About 60% of the pulse energy is contained in a spot of $r_f \approx 2.5$ μm radius, resulting in an averaged intensity, I_L, slightly above 10^{19} W/cm^2 within this spot. The high-intensity part of the pulse is preceded by a 6-ns long low-intensity pedestal due to ASE mainly generated in the RA. The prepulse duration can be controlled by means of an ultrafast Pockels cell located after the RA with a top-hat-like temporal gate of 6-ns duration. The rise time of the leading edge is 300 ps and the gate jitter is 150 ps. By changing the position of the gate relative to the main pulse, the pedestal is either fully or partially transmitted or almost fully suppressed to a minimum prepulse duration of (500 ± 150) ps. The intensity ratio between main and prepulse is better than 2×10^7 and the increase of the intensity above the pedestal level, as measured by a third-order autocorrelator [17], starts 11 ps before the peak intensity.

Two different proton detectors were used. Pieces of CR 39 were placed 82 mm behind the target to record the spatial profile of the proton beam. Covering a half-opening angle of ~20°, they were wrapped with a 12-μm

Al foil to filter out heavier ions and protons with energies below 900 keV. Through a small hole around the target normal direction, ions could pass to be detected by a Thomson parabola. In such a spectrometer, ions with different charge-to-mass ratios are dispersed by parallel electric and magnetic fields onto distinct parabola tracks in the plane of the detector (CR 39). After etching the CR 39, the ion pits were counted under a computer-controlled microscope, revealing the exact energy spectra.

We have performed several series of measurements, varying the ASE duration, $\tau_{\rm ASE}$, the laser intensity, I_L, and the target thickness. Figure 1 shows the measured proton cutoff energies versus the target thickness for $I_L = 1.0 \times 10^{19}\ {\rm W/cm^2}$ and ASE durations of 0.5, 0.7, and 2.5 ns, respectively. For each duration we find that with increasing target thickness the cutoff energy first increases and then drops again. The highest proton energies are achieved at an optimal target thickness. When the prepulse duration is changed, this optimal value changes correspondingly, as it is shown in the inset. For thicker targets, the prepulse duration appears to have no effect on the proton cutoff energies, whereas for thinner targets and longer $\tau_{\rm ASE}$ the cutoff energies are reduced.

To check the influence of the laser intensity, we have performed shots with constant prepulse duration of 2.5 ns but slightly different laser intensities by changing the laser energy (Fig. 2). While the proton cutoff energies strongly depend on I_L, the optimal thickness appears to depend on the prepulse duration only (cf. Fig. 1).

The proton spectra around the optimal target thickness measured with an intensity of $1.3 \times 10^{19}\ {\rm W/cm^2}$ and a prepulse duration of 2.5 ns are plotted in Fig. 3. In addition to the rather cold proton component dominating the spectrum of the 2-μm foil with a Boltzmann-like temperature of 250 ± 30 keV, a population with a significantly higher temperature of 800 ± 200 keV and 4.0 ± 0.6 MeV appears in the 5 and 8.5-μm foil spectra, respectively. The temperatures of the hottest proton component, given in the inset, exhibit a similar behavior as the cutoff energies, i.e., the proton temperature drastically decreases below the optimal target thickness.

The spatial profiles of the proton beam also change around the optimal thickness. Figures 4(a)–4(c) show the proton beam profiles obtained with targets 2, 5, and 8.5 μm thick. While the first profile is rather blurred, a collimated feature aligned along the target normal appears in Figs. 4(b) and 4(c), persisting for all thicker targets.

The significant changes in proton spectra and beam profiles described above can be interpreted as a transition between two regimes delimited by the optimal thickness: (i) Only the front side acceleration is active for targets thinner than the optimal thickness and (ii) protons are accelerated from both target surfaces for target thicknesses above the optimal value. In this second regime, the rear side acceleration leads to higher cutoff energies. This mechanism is suppressed in the first regime due to the formation of an ASE-induced density gradient at the rear side of the target.

On the target front side, the high-intensity part of the laser pulse interacts with a plasma created by the ASE prepulse. Electrons are expelled from high-intensity regions by the ponderomotive potential of the laser, $\varphi_p = m_e c^2(\gamma_{\rm os} - 1)$, until it is balanced by the electrostatic potential arising from the charge separation. Here, $\gamma_{\rm os} = \sqrt{1 + I_L \lambda_L^2/(1.37 \times 10^{18}\ {\rm W\,cm^{-2}}\ \mu{\rm m}^2)}$ is the relativistic factor, $m_{\rm e}$ the rest mass of the plasma electrons. Sentoku *et al.* showed [18] that protons can initially gain kinetic energies approaching this potential, when the laser pulse

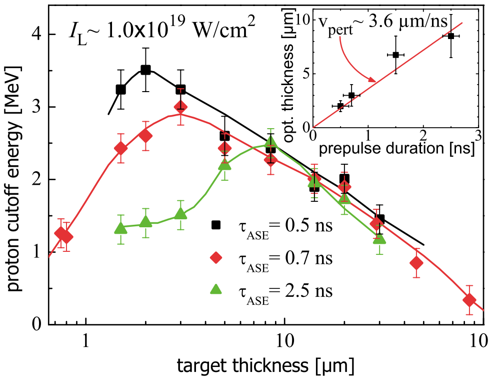

FIG. 1 (color). Proton cutoff energies for differently thick targets and prepulse durations, $\tau_{\rm ASE}$, of 0.5, 0.7, and 2.5 ns, respectively, at $I_L = 1.0 \times 10^{19}\ {\rm W/cm^2}$. For longer $\tau_{\rm ASE}$, the maximum proton energies are achieved with thicker foils. The inset gives the optimal thickness, depending on $\tau_{\rm ASE}$.

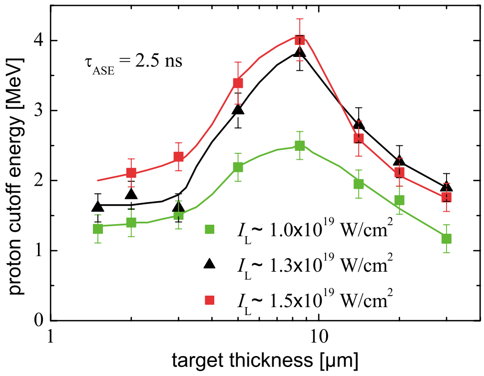

FIG. 2 (color). Proton cutoff energies for differently thick targets and different laser intensities for a prepulse duration of $\tau_{\rm ASE} = 2.5$ ns. The cutoff energies vary with the laser intensity, but the optimal target thickness depends on $\tau_{\rm ASE}$ only (cf. Fig. 1).

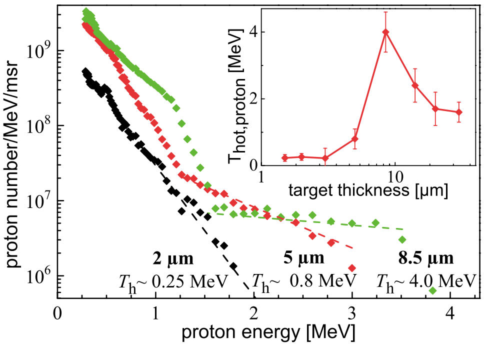

FIG. 3 (color). Proton spectra at $I_L = 1.3 \times 10^{19}$ W/cm^2 for $\tau_{\mathrm{ASE}} = 2.5$ ns and 2, 5, and 8.5 μm thick foils. With increasing target thickness, a second hotter proton population with much higher cutoff energies appears. The inset gives the temperatures of the hot proton component for all measured thicknesses. A similar behavior is observed for all different τ_{ASE}.

is longer than the acceleration time $\tau_a = \lambda_L/c \times \sqrt{m_p/m_e\gamma_{\mathrm{os}}}$, where m_p is the proton mass. For our conditions, we have $\tau_a = 70$ fs, which is shorter than our pulse duration, and φ_p varies between 0.72 and 0.92 MeV, depending on I_L. During the acceleration, a sharp proton front is formed, that expands afterwards due to an electrostatic repulsion within this front, additionally increasing the peak proton velocity by 50% [18], and thus resulting in cutoff energies of $1.5^2 \times \varphi_p \approx 1.6 \ldots 2.1$ MeV for protons accelerated at the front side of the target.

The target normal sheath acceleration (TNSA) mechanism is responsible for proton acceleration from the target rear side [15]. At the front side, a fraction of $\eta \approx 25\%$ of the laser energy is converted into fast electrons having a mean energy of $k_BT_e \approx m_ec^2(\gamma_{\mathrm{os}} - 1)$ [19], resulting in a total number $N_e \approx \eta E_L/k_BT_e$ of hot electrons that propagate through the target. Arriving at the rear side, only a small fraction of the fastest electrons can escape, while the target charges up. Most of the electrons are held back by the arising electic field and form a sheath at the rear side with a Debye length of $\lambda_D = \sqrt{\varepsilon_0 k_BT_e/n_ee^2}$. This field ionizes atoms at the rear surface and accelerates them in target normal direction. Mora described the acceleration process with 1D simulations [20]. Here, the target consists of preionized hydrogen. The electrons, having a mean energy of k_BT_e during the laser pulse duration, are assumed to be in thermal equilibrium with the electrostatic potential Φ at the target rear side, i.e., $n_e = n_{e0} \times \exp(e\Phi/k_BT_e)$. On the other hand, Φ can be obtained from the Poisson equation $\varepsilon_0\partial^2\Phi/\partial x^2 = e(n_e - n_p)$, taking into account the electron and proton densities. Initially, the proton density, n_p, is steplike with $n_p = n_{e0}$ in the target. By iteratively solving the equation of motion and the continuity equation for the protons, their new density in the next time step is obtained, leading to a new potential and electric field. As the field is always peaked at the proton front, the fastest protons are also located there. Mora also found an analytical expression for the evolution of the maximum proton energy, E_p, as a function of the interaction time, t_i, depending only on the electron temperature, T_e, and the initial electron density, n_{e0}:

$$E_p \approx 2k_BT_e\left\{\ln\left[\frac{t_i\omega_{pp}}{\sqrt{2e_E}} + \sqrt{1 + \left(\frac{t_i\omega_{pp}}{\sqrt{2e_E}}\right)^2}\right]\right\}^2. \tag{1}$$

$\omega_{pp} = \sqrt{n_{e0}e^2/\varepsilon_0 m_p}$ is the proton plasma frequency, that depends on n_{e0}, and $e_E = 2.71828\ldots$. We assume $t_i \approx \tau_L$, the same electron numbers and temperatures on both target surfaces, and a constant divergence of the electron beam propagating through the target. The hot electron density at the rear side, n_{e0}, is estimated as follows. Accelerated in the laser focus with an initial radius of $r_f = 2.5$ μm and a half-opening angle of θ_{in}, the electron beam travels through an effective target thickness of $d_t^* = d_t/\cos 30°$ and leaves it within an area of $\pi(r_f + d_t^* \tan\theta_{\mathrm{in}})^2$. Assuming an electron bunch length of $c\tau_L$, the averaged electron density at the rear side is

$$n_{e0} \approx \frac{N_e}{c\tau_L \times \pi(r_f + d_t^* \tan\theta_{\mathrm{in}})^2}. \tag{2}$$

The peak proton energies for differently thick targets calculated with Eqs. (1) and (2) are compared in Fig. 5 with the experimental results for $I_L = 1.3 \times 10^{19}$ W/cm^2 and $\tau_{\mathrm{ASE}} = 2.5$ ns. The cutoff energies for targets optimally thick and thicker are well described by this model for an initial half-opening angle of $\theta_{\mathrm{in}} = (8 \pm 2)°$, which is comparable to the value found in [21]. For the same θ_{in}, this model describes also well the results from Fig. 1, when the reduced laser intensity is taken into account.

The cutoff energies for thinner targets cannot be explained by the TNSA mechanism assuming a steplike density gradient at the rear side. Because of the ASE prepulse, a plasma is formed at the target rear surface,

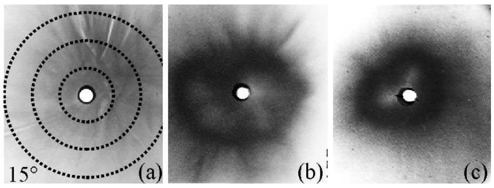

FIG. 4. Proton beam profiles for $\tau_{\mathrm{ASE}} = 2.5$ ns recorded on CR 39 for 2, 5, and 8.5 μm thick targets, respectively. While in (a) the profile is blurred, we observe in (b) and (c) that the major part of the beam is well collimated along the target normal direction. This collimated feature appears only for targets at and above the optimal thickness. The circles in (a) give half-opening angles of 5°, 10°, and 15°, respectively.

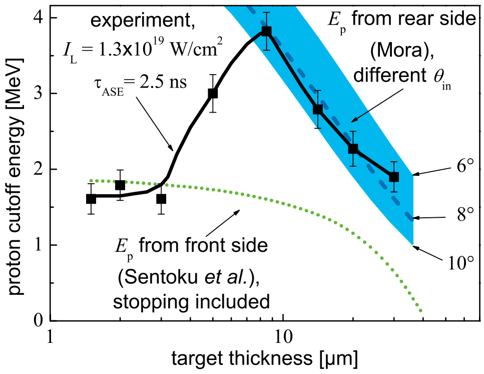

FIG. 5 (color). Comparison of experimental data for $\tau_{ASE} = 2.5$ ns and $I_L = 1.3 \times 10^{19}$ W/cm^2 with theoretical predictions. The dotted line gives the cutoff energy for front side accelerated protons including their stopping in the target, while the broad area gives the maximum rear side proton energies for a range of opening angles $\theta_{in} = (8 \pm 2)°$ of the electron beam.

reducing the acceleration fields [12,19]. We investigated the evolution of this rear side density gradient using the 1D-hydro code MULTI-FS [22]. A simulation for the rear side proton acceleration as described above, that starts with the same rear side density gradient as predicted by MULTI-FS, gives much lower proton cutoff energies for the thinnest foils than those observed in the experiment. Therefore, the rear side acceleration process alone is not able to explain the measured proton energies for all foil thicknesses. On the other hand, protons accelerated at the target front side are not affected by a plasma at the rear side [12]. The maximum energy for front side protons predicted by Sentoku *et al.* [18] reproduces the experimental data much better. Their initial energy is determined by the laser intensity only. The comparison with this model including proton stopping in the target [23] is shown in Fig. 5, yielding a good agreement for the thinnest foils. The increase of the proton cutoff energy for thin targets due to electron recirculation in the target [8] could not be observed, because in our experiment the laser contrast ratio was 500 times lower.

The optimal target thickness is found to depend on the ASE duration only (cf. Figs. 1 and 2). This dependency can be approximated linearly with a slope of $v_{\text{pert}} \approx 3.6\,\mu\text{m/ns}$ (cf. Fig. 1). MULTI-FS simulations show that (i) the prepulse launches a shock wave into the target and (ii), the bulk of the target is radiatively heated due to x rays generated in the focus of the prepulse on the target front side. Both effects can cause an expansion of the target. While the shock wave is weak for our prepulse conditions, the radiative heating is sufficiently strong to form a rear side density gradient for the thinnest foils. In contrast, due to the absorption of radiation in the bulk of the target, the formation of a rear side density gradient sets in at later times for thicker targets. The onset of this plasma formation as observed in MULTI-FS simulations defines the optimal thickness for proton acceleration. The simulation results reproduce the experimentally found value of $3.6\,\mu\text{m/ns}$. Although slightly dependent on the ASE intensity, which could not be varied during the experiment, this value can be used to estimate the effect of the prepulse in various laser systems, each having a fixed prepulse duration, on the rear side ion acceleration [9].

In conclusion, we demonstrated a strong influence of the ASE prepulse on the laser-initiated acceleration of protons. An optimal target thickness for the proton acceleration was found. This optimal value depends linearly on the ASE duration and it is determined by a prepulse-induced formation of an ion-density gradient at the rear side of the target. Furthermore, we were able to distinguish between the two main proton acceleration mechanisms, the fastest protons are accelerated from the rear side of the target having the optimal thickness. Analytical estimates support this interpretation. The determination of the optimal target thickness allows a better comparison between existing experimental results and can help to optimize the conditions for proton acceleration for a large range of laser systems in the future.

We thank S. Karsch and P. Mora for fruitful discussions and H. Haas and A. Böswald for the technical support. This work was supported by Euratom-IPP and the EU project SHARP (Contract No. HPRI-CT-2001-50012).

---

[1] M. Borghesi *et al.*, Phys. Rev. Lett. **88**, 135002 (2002).
[2] M. Roth *et al.*, Phys. Rev. Lett. **86**, 436 (2001).
[3] A. Maksimchuk *et al.*, Phys. Rev. Lett. **84**, 4108 (2000).
[4] E. Clark *et al.*, Phys. Rev. Lett. **84**, 670 (2000).
[5] R. Snavely *et al.*, Phys. Rev. Lett. **85**, 2945 (2000).
[6] S. Hatchett *et al.*, Phys. Plasmas **7**, 2076 (2000).
[7] M. Roth *et al.*, Phys. Rev. ST Accel. Beams **5**, 061301 (2002).
[8] A. Mackinnon *et al.*, Phys. Rev. Lett. **88**, 215006 (2002).
[9] I. Spencer *et al.*, Phys. Rev. E **67**, 046402 (2003).
[10] E. Clark *et al.*, Phys. Rev. Lett. **85**, 1654 (2000).
[11] M. Hegelich *et al.*, Phys. Rev. Lett. **89**, 085002 (2002).
[12] A. Mackinnon *et al.*, Phys. Rev. Lett. **86**, 1769 (2001).
[13] S. Karsch *et al.*, Phys. Rev. Lett. **91**, 015001 (2003).
[14] M. Zepf *et al.*, Phys. Rev. Lett. **90**, 064801 (2003).
[15] S. Wilks *et al.*, Phys. Plasmas **8**, 542 (2001).
[16] A. Pukhov, Phys. Rev. Lett. **86**, 3562 (2001).
[17] S. Karsch, Ph.D. thesis [MPQ-Report 279 (2003)].
[18] Y. Sentoku *et al.*, Phys. Plasmas **10**, 2009 (2003).
[19] S. Wilks *et al.*, Phys. Rev. Lett. **69**, 1383 (1992).
[20] P. Mora, Phys. Rev. Lett. **90**, 185002 (2003).
[21] J. Santos *et al.*, Phys. Rev. Lett. **89**, 025001 (2002).
[22] K. Eidmann *et al.*, Phys. Rev. E **62**, 1202 (2000).
[23] http://physics.nist.gov/

Danksagung

An dieser Stelle möchte ich allen, die zum Gelingen meiner Arbeit beigetragen haben, ein ganz herzliches Dankeschön aussprechen.

- Besonders danke ich meinem Doktorvater Herrn Prof. Dr. Jürgen Meyer-ter-Vehn für die äußerst kompetente Betreuung der Arbeit, für die Hilfe bei theoretischen Überlegungen und für das stete Interesse am Fortgang meiner Arbeit.
- Ich danke Herrn Prof. Dr. Alfred Lauberau für die bereitwillige Übernahme des Zweitgutachtens.
- Ebenso möchte ich mich bei Herrn Prof. Dr. Klaus-Jürgen Witte für die herzliche Aufnahme in die Laser-Plasma-Gruppe am MPQ bedanken, sowie für die zahlreichen und sehr ausführlichen Diskussionen über meine Arbeit, die mir sehr geholfen und mich zusätzlich motiviert haben.
- Mein besonderer Dank gilt Herrn Dr. Georges D. Tsakiris für die außerordentlich gute Zusammenarbeit während der gesamten Zeit. Zum einen hat er mich zum wissenschaftlichen Arbeiten angeleitet, zum anderen hat er mir die nötigen Freiräume zum Arbeiten gelassen.
- Ein großes Dankeschön an Herrn Dr. Javier Honrubia für die Durchführung der numerischen Simulationen zum Elektronentransport im Target, die wichtige Erklärungen zu den Experimenten liefern konnten.
- Herrn Dr. Klaus Eidmann danke ich für die geduldige Hilfe bei den Simulationen mit MULTI und MULTI-FS.
- Herrn Dr. Marko Santala und Herrn Jörg Schreiber sei herzlich für ihre Mitwirkung beim Experiment, für die vielen guten Ideen und für die Unterstützung bei der Auswertung der Daten gedankt.
- Herrn Dr. Riccardo Tommasini möchte ich für die Hilfe bei der Berechnung der theoretischen Intensitätsverteilung im Fokus danken.
- Bei Herrn Matthias Dreher möchte ich mich besonders für die Hilfe auch bei den kniffeligsten physikalischen und computertechnischen Fragen bedanken aber auch für alle Diskussionen, die nur im weiteren Sinne mit Physik zu tun hatten.
- Herrn Dr. Stefan Karsch möchte ich für die Überlassung seiner Thomson-Parabel zum Experimentieren danken, sowie für zahlreichen Anregungen zu meiner Arbeit.

- Für die Mitarbeit im Labor danke ich den Herren Dr. Istvan Földes, Ervin Racz und Dr. Hideaki Habara. Herrn Dr. Michael Jost, Herrn Dr. Michael Geissler, Herrn Jürgen Stein, Herrn Dr. Ulrich Andiel, Herrn Dr. Paris Tzallas, Frau Dr. Francesca Pisani, Herrn Prof. Dr. Georg Pretzler, Herrn Dr. Manuel Hegelich, Herrn Dr. Ernst Fill, Herrn Dr. Andrius Marcinkevičius, Herrn Felix Brandl und Frau Annika Krenz sei gedankt für die zahlreichen physikalischen und nicht-physikalischen Gespräche.

- Ich danke den Herren Alois Böswald, Harald Haas und Horst Baumhacker für den hervorragenden ATLAS-Laserbetrieb. Besonders bei Herrn Haas möchte ich mich an dieser Stelle für die Hilfe beim Einbau und beim Betrieb der schnellen Pockelszelle bedanken.

- Allen weiteren Mitarbeitern der Laser-Plasma Gruppe, insbesondere den Herren Günther Keller, Manfred Fischer und Walter Fölsner, sowie der gesamten Werkstatt des MPQ gilt mein besonderer Dank für die Hilfe bei kleineren und größeren mechanischen Problemen.

- Nicht zuletzt danke ich meinen Eltern, meiner Schwester Wiebke und ganz besonders natürlich meiner Miri für den persönlichen Rückhalt während der gesamten Zeit.